

Measurement of charm and beauty production in deep inelastic scattering at HERA

Dissertation
zur Erlangung des Doktorgrades
des Department Physik
der Universität Hamburg

vorgelegt von
Philipp Roloff
aus Lippstadt

Hamburg
2011

Gutachter der Dissertation: Dr. Achim Geiser
Prof. Dr. Robert Klanner
Prof. Dr. Stefan Tapprogge

Gutachter der Disputation: Prof. Dr. Peter Schleper
Dr. Olaf Behnke

Datum der Disputation: 20. April 2011

Vorsitzender des Prüfungsausschusses: Dr. Georg Steinbrück
Vorsitzender des Promotionsausschusses: Prof. Dr. Joachim Bartels

Leiterin des Departments Physik: Prof. Dr. Daniela Pfannkuche
Dekan der MIN-Fakultät: Prof. Dr. Heinrich Graener

Abstract

In this thesis two measurements of heavy quark production in deep inelastic scattering at HERA are presented. Cross sections for the production of heavy quarks can be calculated in quantum chromodynamics (QCD). The heavy quark masses represent hard scales, which allow to apply perturbative methods.

Charm production has been measured with the ZEUS detector using an integrated luminosity of 120 pb^{-1} . The hadronic decay channels $D^+ \rightarrow K_S^0 \pi^+$, $\Lambda_c^+ \rightarrow p K_S^0$ and $\Lambda_c^+ \rightarrow \Lambda \pi^+$ were reconstructed. The presence of a neutral strange hadron in the final state reduces the combinatorial background and extends the measured sensitivity into the region $p_T(D^+, \Lambda_c^+) < 1.5 \text{ GeV}$. The inclusive cross section and differential cross sections in $p_T^2(D^+)$, $\eta(D^+)$, Q^2 and x for the production of D^+ mesons are in reasonable agreement with predictions from perturbative QCD. The fraction of c quarks hadronising into Λ_c^+ baryons was extracted from a combination of both investigated Λ_c^+ decay channels. The result is consistent with a previous measurement in the photoproduction regime and with the average e^+e^- value.

The production of charm and beauty quarks has been measured with the ZEUS detector using the data collected between 2004 and 2007. This data sample corresponds to an integrated luminosity of 354 pb^{-1} . The charm and beauty contents in events with a jet were determined using the decay-length significance and invariant mass of the reconstructed secondary decay vertices. Differential cross sections in E_T^{jet} , η^{jet} , Q^2 and x are in reasonable agreement with predictions from perturbative QCD. The open charm and beauty contributions to the inclusive proton structure function F_2 were extracted from double differential cross sections in x and Q^2 . The obtained $F_2^{c\bar{c}}$ and $F_2^{b\bar{b}}$ values are in good agreement with previous measurements and theoretical predictions. This measurement represents the most precise determination of $F_2^{b\bar{b}}$ at the HERA collider in a large part of the accessible phase space.

First test beam measurements using the EUDET pixel telescope were performed in 2007 and 2008. Measurements performed at DESY and CERN to estimate the precision of the so-called demonstrator telescope and its sensors are described. The spatial resolution of the full telescope consisting of six MAPS sensors is $1.2 \mu\text{m}$.

Kurzfassung

In dieser Arbeit werden zwei Messungen der Produktion schwerer Quarks in tiefunelastischer Streuung bei HERA vorgestellt. Wirkungsquerschnitte für die Produktion schwerer Quarks können im Rahmen der Quantenchromodynamik (QCD) berechnet werden. Die Massen der schweren Quarks stellen harte Skalen dar, die die Anwendung perturbativer Methoden ermöglichen.

Charm-Produktion wurde mit dem ZEUS-Detektor unter Verwendung einer integrierten Luminosität von 120 pb^{-1} gemessen. Die hadronischen Zerfallskanäle $D^+ \rightarrow K_S^0 \pi^+$, $\Lambda_c^+ \rightarrow p K_S^0$ und $\Lambda_c^+ \rightarrow \Lambda \pi^+$ wurden rekonstruiert. Die Präsenz eines neutralen Strange-Hadrons im Endzustand reduziert den kombinatorischen Untergrund und erweitert die gemessene Sensitivität in den Bereich $p_T(D^+, \Lambda_c^+) < 1.5 \text{ GeV}$. Der inklusive Wirkungsquerschnitt und differentielle Wirkungsquerschnitte in $p_T^2(D^+)$, $\eta(D^+)$, Q^2 und x für die Produktion von D^+ -Mesonen befinden sich in sinnvoller Übereinstimmung mit Vorhersagen der perturbativen QCD. Der Anteil der c -Quarks, welcher in ein Λ_c^+ -Baryon fragmentiert, wurde aus einer Kombination beider untersuchter Λ_c^+ -Zerfälle bestimmt. Das Ergebnis ist konsistent mit vorherigen Messungen in Photoproduktion und mit dem Mittelwert aus Messungen in e^+e^- -Wechselwirkungen.

Die Produktion von Charm- und Beauty-Quarks wurde mit dem ZEUS-Detektor unter Verwendung der zwischen 2004 und 2007 aufgezeichneten Daten gemessen. Dieser Datensatz entspricht einer integrierten Luminosität von 354 pb^{-1} . Die Charm- und Beauty-Anteile in Ereignissen mit einem Jet wurden mit Hilfe der Signifikanz der Zerfallslänge und mit Hilfe der Masse von rekonstruierten sekundären Zerfallsvertices bestimmt. Differentielle Wirkungsquerschnitte in E_T^{jet} , η^{jet} , Q^2 und x stehen in sinnvoller Übereinstimmung mit Vorhersagen der perturbativen QCD. Die Beiträge von offener Charm- und Beauty-Produktion zur inklusiven Protonstrukturfunktion F_2 wurden aus doppelt differenziellen Wirkungsquerschnitten in x und Q^2 extrahiert. Die gemessenen Werte für $F_2^{c\bar{c}}$ und $F_2^{b\bar{b}}$ sind in guter Übereinstimmung mit vorherigen Messungen und theoretischen Vorhersagen. Diese Messung stellt die präziseste Bestimmung von $F_2^{b\bar{b}}$ am HERA-Beschleuniger in einem großen Teil des erreichbaren kinematischen Bereichs dar.

Erste Teststrahlmessungen mit dem EUDET Pixelteleskop wurden in den Jahren 2007 und 2008 durchgeführt. Messungen bei DESY und CERN zur Bestimmung der Präzision des sogenannten Demonstrator-Teleskops und seiner Sensoren werden beschrieben. Die räumliche Auflösung des kompletten Teleskops, bestehend aus sechs MAPS-Sensoren, beträgt $1.2 \mu\text{m}$.

Contents

1. Introduction	1
2. Theoretical overview	5
2.1. Deep inelastic scattering at HERA	5
2.1.1. Kinematics	5
2.2. Inclusive cross sections	7
2.3. Quark-parton model	8
2.4. Quantum chromodynamics	11
2.4.1. Perturbative calculations	12
2.4.2. Quark masses	14
2.4.3. Factorisation and parton density functions	15
2.5. Treatment of heavy quark production in QCD	18
2.5.1. Fixed flavour number scheme	19
2.5.2. Zero-mass variable flavour number scheme	20
2.5.3. General-mass variable flavour number scheme	20
2.5.4. Heavy flavour treatment in global PDF analyses	21
2.6. Event simulation	22
2.6.1. Parton showers	23
2.6.2. Fragmentation models	23
2.7. Monte Carlo event generators	24
2.7.1. ARIADNE	25
2.7.2. RAPGAP	26
2.8. Properties of charmed and beauty hadrons	26
2.9. Decays of charmed and beauty hadrons	27
3. Heavy flavour production at HERA	29
3.1. Charm production at HERA	29
3.1.1. Hadronic decay channels	29
3.1.2. Fragmentation parameters from hadronic decays	32
3.2. Beauty production at HERA	35
3.3. Measurements of heavy flavour production based on lifetime information	36

4. Experimental set-up	39
4.1. DESY	39
4.2. HERA	39
4.3. The ZEUS detector	42
4.3.1. Overview	42
4.3.2. The tracking system	44
4.3.3. The uranium calorimeter	49
4.3.4. The luminosity detectors	50
4.3.5. The trigger system	52
4.4. Offline reconstruction and detector simulation	54
5. Event reconstruction	55
5.1. HERA I tracking and vertex reconstruction	55
5.1.1. Track finding	56
5.1.2. Track fitting	57
5.1.3. Vertex reconstruction	57
5.1.4. Usage of HERA I tracking for measurements of heavy flavour production	57
5.1.5. Overall magnetic field correction	58
5.2. HERA II tracking and vertex reconstruction	58
5.2.1. Vertex reconstruction and beam spot	58
5.2.2. Usage of HERA II tracking for measurements of heavy flavour production	60
5.3. Energy loss via ionisation	60
5.4. Energy flow objects	60
5.4.1. Calorimeter clustering	61
5.4.2. Track matching	62
5.4.3. Energy measurement	62
5.5. Electron reconstruction	63
5.6. Jet reconstruction	64
5.7. Kinematic reconstruction	65
6. Measurement of D^+ and Λ_c^+ production	67
6.1. Data samples and Monte Carlo sets	67
6.1.1. Data samples	67
6.1.2. Monte Carlo samples	67
6.2. Event selection	70
6.2.1. Online event selection	70
6.2.2. Offline event selection	73
6.3. Strange-particle reconstruction	76
6.3.1. K_S^0 meson candidate selection	76
6.3.2. Λ candidate selection	76
6.4. Reconstruction of charmed hadrons	77
6.4.1. Reconstruction of the decay $D^+ \rightarrow K_S^0 \pi^+$	78

6.4.2.	Reconstruction of the decay $\Lambda_c^+ \rightarrow pK_S^0$	85
6.4.3.	Reconstruction of the decay $\Lambda_c^+ \rightarrow \Lambda\pi^+$	85
6.5.	Cross sections and acceptance corrections	86
6.6.	Systematic uncertainties	89
6.7.	NLO QCD predictions for D^+ production	91
6.8.	Cross sections and extraction of $f(c \rightarrow \Lambda_c^+)$	93
6.8.1.	D^+ cross sections	93
6.8.2.	Λ_c^+ cross sections and fragmentation fractions	96
6.9.	Conclusions	98
7.	Measurement of $F_2^{b\bar{b}}$ and $F_2^{c\bar{c}}$ using lifetime information	99
7.1.	Data samples and Monte Carlo sets	99
7.1.1.	Data samples	99
7.1.2.	Monte Carlo samples	100
7.2.	Event selection	102
7.2.1.	Online event selection	102
7.2.2.	NC DIS selection	104
7.3.	Signal determination	104
7.3.1.	Secondary vertex reconstruction	105
7.3.2.	Decay length and significance	107
7.3.3.	Extraction of the charm and beauty fractions	109
7.3.4.	Corrections	112
7.3.5.	Control distributions	115
7.4.	Measurement of beauty production and extraction of $F_2^{b\bar{b}}$	120
7.4.1.	Cross sections	120
7.4.2.	Systematic uncertainties	121
7.4.3.	NLO QCD predictions from HVQDIS	123
7.4.4.	Results	125
7.4.5.	Extraction of $F_2^{b\bar{b}}$	138
7.5.	Measurement of charm production and extraction of $F_2^{c\bar{c}}$ in an extended kinematic region	146
7.5.1.	Systematic uncertainties	146
7.5.2.	NLO QCD predictions from HVQDIS	147
7.5.3.	Results	147
7.5.4.	Extraction of $F_2^{c\bar{c}}$	156
7.6.	Conclusions and outlook	161
8.	First test beam measurements with the EUDET pixel telescope	163
8.1.	Introduction	163
8.2.	The demonstrator telescope	164
8.2.1.	The sensor	164
8.2.2.	The DAQ system	166
8.2.3.	User integration	168
8.3.	The EU Telescope software	168

8.4.	Signal extraction	169
8.4.1.	Pedestal and noise	169
8.4.2.	Cluster reconstruction	170
8.4.3.	Cluster position	170
8.5.	Alignment	172
8.5.1.	Alignment parameters	172
8.5.2.	Implementation of the alignment procedure	173
8.5.3.	Alignment of the demonstrator telescope	174
8.6.	Laboratory tests	175
8.6.1.	Calibration with low-energy X-rays	175
8.6.2.	Temperature dependence of the noise	176
8.7.	First test beam measurements in 2007	178
8.7.1.	Analysed data samples	178
8.7.2.	Cluster selection	179
8.7.3.	Sensor characterisation with MIPs	179
8.7.4.	Track reconstruction	181
8.7.5.	Resolution studies	183
8.7.6.	Sensor efficiency	188
8.8.	Improvements in 2008	188
8.8.1.	Data taking in ZS mode	189
8.8.2.	Analysis of example data	189
8.9.	Conclusions and outlook	190
A.	Matching of charmed hadrons	193
B.	D^+ signals in bins of $p_T(D^+)$, $\eta(D^+)$, Q^2 and x	195
C.	D^+ cross sections for $Q^2 > 5 \text{ GeV}^2$	199
D.	Detailed list of Monte Carlo samples for the HERA II period	201
E.	Example beauty signals	205
F.	Control distributions for $E_T^{\text{jet}} > 4.2 \text{ GeV}$	211
G.	Uncertainties of the HVQDIS NLO QCD predictions	217

1. Introduction

All interactions between elementary particles, i.e. particles without substructure, observed so far can be explained by the *Standard Model* (SM) of Particle Physics [1]. Matter is composed of fundamental particles of spin $\frac{1}{2}$ called *fermions* in the SM. These fermions are grouped into three *families* of *quarks* and *leptons*. An overview of the quarks and leptons is shown in Fig. 1.1.

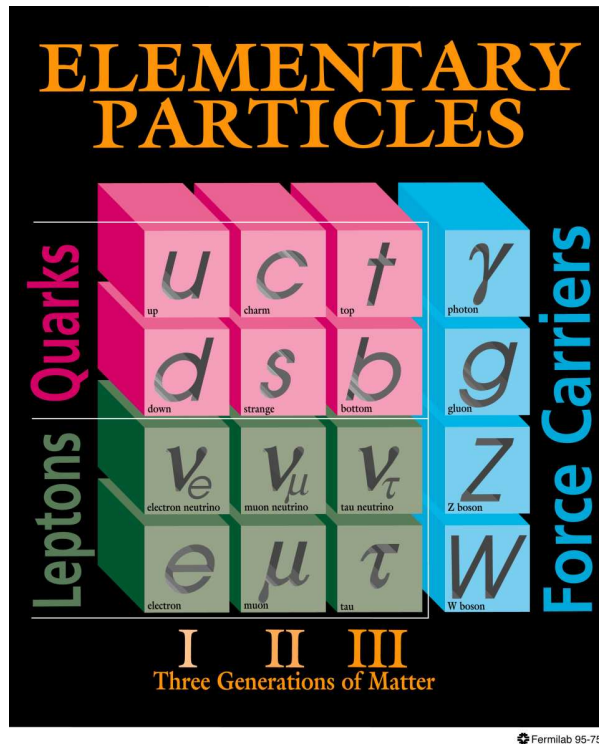


Figure 1.1.: Particle content of the Standard Model of particle physics.

The interactions between the fermions are mediated through the exchange of gauge *bosons* with integer spin. All fermions are sensitive to the weak interaction mediated through the exchange of the massive Z^0 and W^\pm bosons. Electrically charged particles interact electromagnetically via the exchange of photons.

Hadrons like protons or neutrons are not elementary particles since they are composed of quarks. Quarks inside the hadrons interact through the exchange of *gluons* which are the gauge bosons of the strong interaction. This interaction keeps the quarks together inside the hadrons. The charge of the strong interaction is referred to as *colour*.

In the SM, the interactions are described by *quantum field theories*. For example, electrodynamics is described by *quantum electrodynamics* (QED) which is an Abelian gauge theory, i.e. its symmetry group is commutative. On the other hand, the combination of the electromagnetic with the weak force in the electroweak theory by Glashow, Salam and Weinberg (GSW) [2] as well as *quantum chromodynamics* (QCD), the theory of the strong interaction, are non-Abelian gauge theories. As a consequence, the exchanged bosons can not only interact with fermions, but also with themselves. The SM is a combination of the electroweak theory and of QCD. Its symmetry group is given by:

$$SU(3) \times SU(2) \times U(1).$$

The last un-detected particle of the SM is the Higgs boson which is a scalar field with a non-vanishing vacuum expectation value [3]. The coupling to the Higgs field generates the masses of the W^\pm and Z^0 bosons.

The inner structure of the proton can be investigated using electromagnetic probes in scattering experiments. Sufficient energies are needed to resolve the inner structure of the proton. At the energies reached at the HERA collider, deep inelastic lepton-proton scattering can be described as the interaction of a virtual boson (γ , Z^0 or W^\pm) emitted from the electron with the constituents of the proton. The usage of leptons to investigate hadron structure is advantageous since the electromagnetic part of the interaction is well understood.

The production of the heavy charm and beauty quarks in lepton-proton interactions provides an interesting test of perturbative QCD. The large masses of the heavy quarks allow to perform reliable calculations in the whole accessible kinematic region. On the other hand, a large part of the cross section for charm and beauty production is due to events where the virtual photon interacts with a gluon from the proton. Hence the measurement of heavy quark production in lepton-proton collisions is directly sensitive to the gluon content of the proton. Heavy quark production allows to check the gluon density in the proton obtained using other processes.

In this thesis, two measurements of heavy flavour production in deep inelastic lepton-proton scattering are described. Both studies are based on data collected using the ZEUS detector at the HERA collider. The physics motivations for both analyses are discussed in the following.

Charm production was measured using the decay channels $D^+ \rightarrow K_S^0 \pi^+$, $\Lambda_c^+ \rightarrow p K_S^0$ and $\Lambda_c^+ \rightarrow \Lambda \pi^+$, and their charge conjugates. The presence of a neutral strange hadron in the final state reduced the combinatorial background and extended the measured sensitivity into the low transverse momentum region. Hence charm production could be measured for the first time without an explicit cut on $p_T(D^+, \Lambda_c^+)$. This allowed to test QCD calculations in a new kinematic region.

A comparison of the cross sections for the production of D^+ and Λ_c^+ hadrons allowed to extract the fragmentation fraction $f(c \rightarrow \Lambda_c^+)$ for the first time in deep inelastic scattering at HERA. This measurement helps to investigate if the charm fragmentation fractions are universal in different processes.

All of the reconstructed decay channels were used for the first time to extract cross

sections at HERA. First results were already shown in [4]. The results presented here contain substantial improvements and extensions and were recently published [5].

The main topic of this thesis is a measurement of cross sections for jet production in beauty and charm events. The decay-length significance and the invariant mass of inclusive secondary vertices were used to extract the beauty and charm content in the investigated data sample. Inclusive lifetime information was used for the first time to measure cross sections in deep inelastic scattering using ZEUS data.

Since the analysis is not limited to a specific decay channel, the statistical precision is significantly improved compared to previous measurements. This is especially important for beauty, because measurements of semileptonic beauty quark decays are limited by large statistical uncertainties. Charm jet production was investigated for the first time in the forward direction, i.e. in the direction of the incoming proton, at HERA.

Double differential cross sections in Q^2 and x were used to extract F_2^{bb} and $F_2^{c\bar{c}}$. The required extrapolation to the full kinematic range in E_T^{jet} and η^{jet} is smaller than in any previous determination of F_2^{bb} at ZEUS. Compared to measurements of F_2^{bb} and $F_2^{c\bar{c}}$ by the H1 collaboration, the extrapolation in η^{jet} is smaller.

An introduction to the theoretical background is given in **chapter 2**. Previous measurements of charm and beauty quark production in lepton-proton scattering are discussed in **chapter 3**. The ZEUS detector and its most important components are discussed in detail in **chapter 4**. The reconstruction of physics observables from the measurements of the individual detector components is reviewed in **chapter 5**. The measurements summarised above are described in **chapter 6** and **chapter 7**. Conclusions and an outlook for future improvements are given at the end of these chapters.

The technical part of this thesis was to participate in the first measurements using a new pixel beam telescope and to analyse the collected data. The main goals of the Large Hadron Collider (LHC), which recently started operation at CERN in Geneva, are to observe the Higgs boson and to search for physics beyond the SM. To complement the LHC and to allow more detailed investigations of possible discoveries, a future linear electron-positron collider is planned [6, 7]. The detectors at this accelerator are very complex devices. To fulfil the special requirements, sensor technologies for different components of the intended experiments need to be developed. Prototypes for new detectors are studied in so-called *test beam* measurements. Within the EUDET project, a pixel beam telescope was developed to measure particle trajectories with high spacial resolution in test beam experiments. First results from measurements using the EUDET pixel beam telescope are given in **chapter 8**.

2. Theoretical overview

In this chapter the theoretical concepts important for the analyses presented in this thesis are summarised. After a brief introduction to kinematics at HERA and inclusive cross sections in deep inelastic scattering, the quark-parton model is explained. The main characteristics of the theory of quantum chromodynamics are discussed in the following. Finally, the production of heavy quarks at HERA and different schemes for the treatment of the charm and beauty quark masses in perturbative QCD are reviewed.

2.1. Deep inelastic scattering at HERA

Deep inelastic lepton scattering off nucleons provides a rich source of information on hadron structure. A probe, i.e. a charged lepton or a neutrino, which does not participate in the strong interaction, scatters off a constituent quark in the nucleon. The precise measurement of this reaction allows to investigate the inner structure of the target nucleons. Historically, deep inelastic scattering experiments have played an important role in establishing QCD as the theory of the strong interaction. While in all previous deep inelastic scattering experiments the lepton beams were collided with fixed nucleon targets, beams of electrons or positrons¹ and protons were collided at HERA. This allowed to increase the centre-of-mass energy by about an order of magnitude compared to fixed-target experiments. Distances down to 10^{-18} m were probed at HERA which corresponds to about $\frac{1}{1000}$ of the proton radius. Additionally, the electron beam was polarised longitudinally for a part of the data taking to perform electroweak measurements.

2.1.1. Kinematics

The general electron-proton scattering process:

$$ep \rightarrow l'X, \tag{2.1}$$

where l' is the scattered lepton and X the hadronic system in the final state, proceeds via the exchange of a virtual vector boson (γ , Z^0 or W^\pm). The corresponding Feynman diagram is shown in Fig. 2.1. In *neutral current* (NC) processes a photon or a Z^0 boson is exchanged. The reaction exchanging a W^\pm boson is called *charged current* (CC). In this case, the lepton in the final state is an electrically uncharged neutrino.

Given the incoming and scattered lepton four-momenta, k and k' , and the four-momenta of the incoming proton and the hadronic final state, P and P' , the event kinematics can be described by the following Lorentz invariant variables:

¹Hereafter, both electrons and positrons are referred to as electrons, unless explicitly stated otherwise.

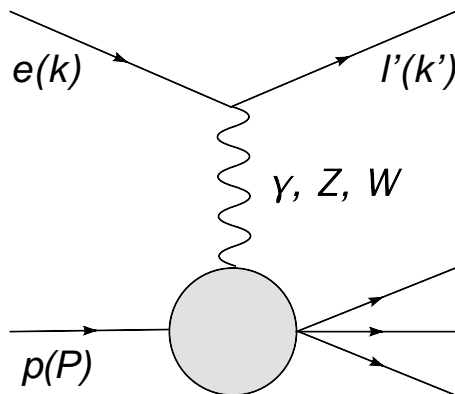


Figure 2.1.: Schematic diagram of the process $ep \rightarrow l'X$.

- $s = (k + P)^2$, centre-of-mass energy squared of the electron-proton system
- $Q^2 = -q^2 = -(k - k')^2$, negative squared four-momentum exchange at the lepton vertex
- $x = \frac{Q^2}{2P \cdot q}$, $0 \leq x \leq 1$, Bjorken scaling variable: fraction of the proton momentum carried by the struck quark in the framework of the quark-parton model (see Sec. 2.3)
- $y = \frac{P \cdot q}{P \cdot k}$, $0 \leq y \leq 1$, inelasticity: relative energy transfer from the lepton to the hadronic system in the proton rest frame
- $W^2 = (P + q)^2$, centre-of-mass energy squared of the boson-proton system

If Q^2 is large enough that the incoming electron and proton masses can be neglected, then the virtuality of the exchanged boson can be expressed as:

$$Q^2 = sxy. \quad (2.2)$$

Since \sqrt{s} is fixed at HERA due to the constant energies of the lepton and proton beams, only two of the variables Q^2 , x , y and s are independent and are sufficient to describe the kinematics of the scattering process. The kinematic variables x , y and Q^2 can be calculated from any two of the following quantities: the angles and the energies of the scattered electron and the struck quark. The variable W can be expressed as:

$$W^2 = (P + q)^2 = P^2 + q^2 + 2P \cdot q \approx -Q^2 + ys. \quad (2.3)$$

In the last step $m_p^2 \approx 0$ is assumed, where m_p is the proton mass. The scattering processes are divided into two regions of phase space. Events with quasi-real photons ($Q^2 \approx 0 \text{ GeV}^2$) are called *photoproduction* (PHP). If Q^2 is greater than a few GeV^2 , the wavelength of the exchanged boson, $\lambda \approx \frac{hc}{|Q|}$, becomes smaller than the size of the proton ($\approx 10^{-15} \text{ m}$). In this case the exchanged boson is able to probe the structure of the proton. The process is classified as *deep inelastic scattering* (DIS) for events where the invariant mass of the hadronic final state is much larger than the proton mass ($W^2 \gg m_p^2$).

2.2. Inclusive cross sections

The general form of the NC DIS differential cross sections as functions of x and Q^2 for longitudinally unpolarised beams can be written at leading order in the electroweak interaction in terms of three structure functions F_2 , F_L and xF_3 [8]:

$$\frac{d^2\sigma_{Born}^{NC}(e^\pm p)}{dx dQ^2} = \frac{2\pi\alpha^2}{Q^4 x} [Y_+ F_2^{NC}(x, Q^2) - y^2 F_L^{NC}(x, Q^2) \mp Y_- x F_3^{NC}(x, Q^2)]. \quad (2.4)$$

Mass terms related to the interacting proton or lepton are ignored as appropriate at high Q^2 , α is the fine structure constant and Y_\pm is given by:

$$Y_\pm = 1 \pm (1 - y)^2. \quad (2.5)$$

The parity violating structure function xF_3 is non-zero only for weak interactions and therefore negligible if $Q^2 \ll M_Z^2$, where M_Z is the mass of the Z^0 boson. Further discussion of the structure functions can be found below in the framework of the quark-parton model and its extensions by QCD. For CC DIS the corresponding formula for the differential cross section reads as:

$$\frac{d^2\sigma_{Born}^{CC}(e^\pm p)}{dx dQ^2} = \frac{G_F^2}{4\pi x} \frac{M_W^4}{(Q^2 + M_W^2)^2} [Y_+ F_2^{CC}(x, Q^2) - y^2 F_L^{CC}(x, Q^2) \mp Y_- x F_3^{CC}(x, Q^2)],$$

where $G_F = \frac{\pi\alpha}{\sqrt{2}\sin^2\theta_W M_W^2}$ is the Fermi coupling constant and M_W the mass of the W^\pm boson.

At lower values of Q^2 than the mass of the exchanged boson, Z^0 or W^\pm , the weak interaction contribution to the cross section is suppressed relative to γ exchange:

$$\frac{\sigma(Z^0, W^\pm)}{\sigma(\gamma)} \sim \left(\frac{Q^2}{Q^2 + M_{Z,W}^2} \right)^2. \quad (2.6)$$

Hence in the low Q^2 region the photon mediated NC DIS process dominates. In this region the cross sections for electrons and positrons are similar. The contribution from the weak interaction becomes relevant with increasing Q^2 . Differences between the cross sections for electrons and positrons at high Q^2 are caused by the different strengths of the weak force for the individual quark flavours in the proton. Thus the NC cross sections for electrons and positrons start to differ significantly.

Figure 2.2 shows measurements of the NC and CC cross sections from the H1 and ZEUS experiments as functions of Q^2 for electron and positron beams [9]. The suppression of the CC cross section compared to the NC cross section is visible for $Q^2 \lesssim 10^4 \text{ GeV}^2$. The CC and NC cross sections become comparable in the region where Q^2 is similar to M_W^2 and M_Z^2 which can be interpreted as a manifestation of the electroweak unification.

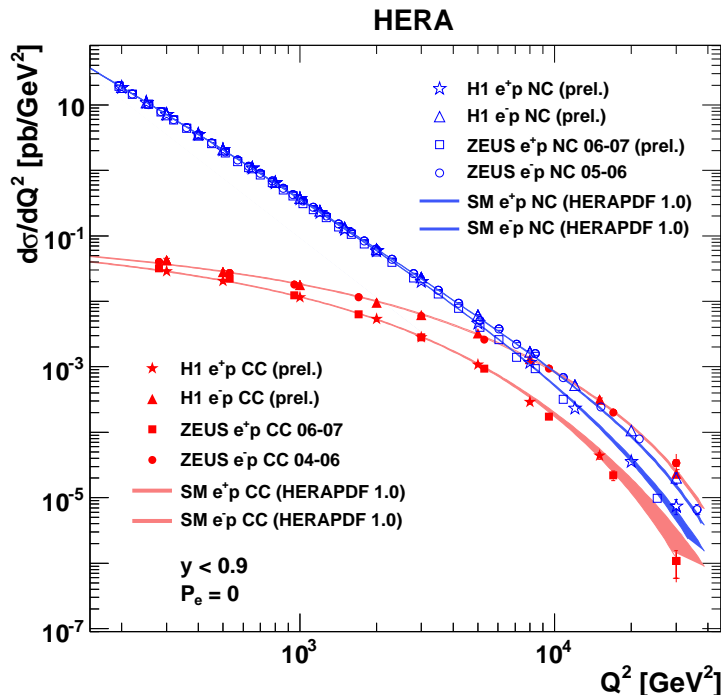


Figure 2.2.: Inclusive differential NC and CC cross sections as functions of Q^2 from H1 and ZEUS for electron and positron beams. Predictions from the Standard Model are shown as bands.

2.3. Quark-parton model

A simple interpretation of DIS is given by the *parton model*, which is based on the assumption that the proton is built of non-interacting, point-like partons. Each parton carries a fraction ξ of the proton four-momentum P :

$$p = \xi P, \quad (0 < \xi < 1). \quad (2.7)$$

In the *infinite momentum frame*, defined by:

$$P^\mu \approx (P, 0, 0, P), \quad P \gg M, \quad (2.8)$$

where M is the mass of the proton, all transverse momenta of the partons can be neglected. At HERA, the laboratory frame can be approximately treated as an infinite momentum frame. The squared four-momentum of the outgoing parton is given by:

$$p'^2 = (\xi P + q)^2 = q^2 + (\xi P)^2 + 2q\xi P = m^2 \approx 0. \quad (2.9)$$

Since the masses of the incoming partons, m , are also neglected ($(\xi P)^2 = p^2 = m^2 \approx 0$), this simplifies to:

$$\xi = -\frac{q^2}{2q \cdot P} = \frac{Q^2}{2q \cdot P} = x. \quad (2.10)$$

Thus x is the fraction of the proton momentum carried by the massless struck quark in the simple parton model described here. For leptons scattered incoherently on single partons, the differential cross section can be formulated as the sum of elastic scattering processes:

$$\frac{d^2\sigma}{dQ^2 dx} = \frac{4\pi\alpha^2}{Q^4} \left(1 - y + \frac{y^2}{2}\right) \sum_i Q_i^2 f_i(x). \quad (2.11)$$

Q_i is the electric charge in units of the elementary charge of parton i and the *parton density functions* (PDFs) $f_i(x)dx$ give the probability of finding a parton of type i in the proton, in the momentum range between xP and $(x + dx)P$.

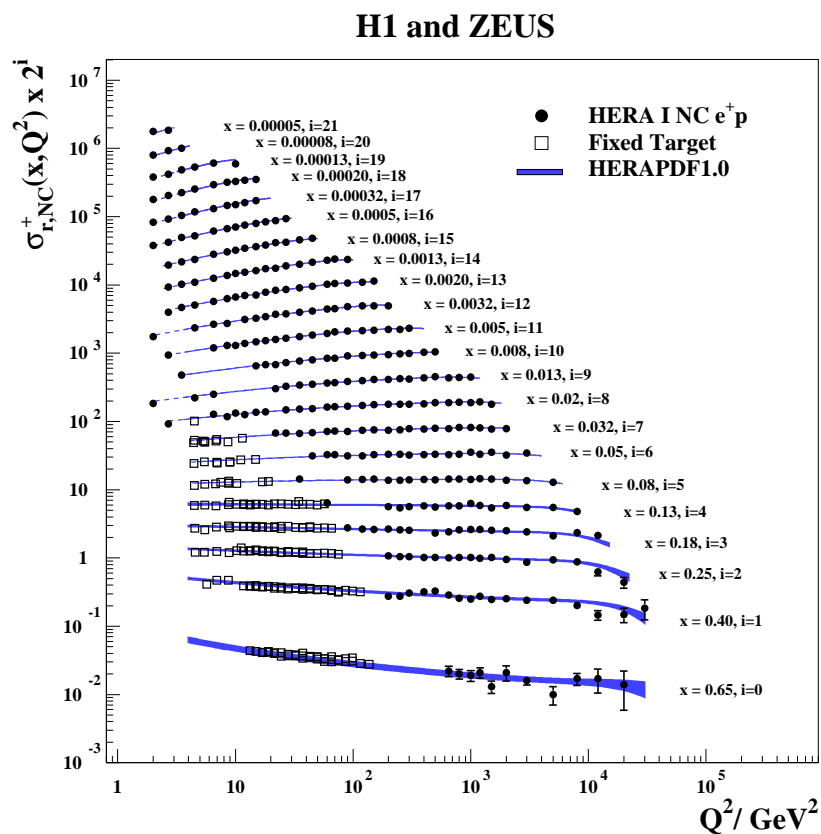


Figure 2.3.: NC e^+p reduced cross sections as a function of Q^2 for fixed values of x from a combination of H1 and ZEUS data and from fixed target experiments.

It was predicted by Bjorken already in the late sixties that in the DIS regime the structure

functions are functions of x alone [10]. This behaviour is known as *scaling*. In Fig. 2.3 the reduced cross section defined as:

$$\sigma_{r,NC} = \frac{d^2\sigma}{dx dQ^2} \cdot \frac{Q^4 x}{2\pi\alpha^2 Y_+} = F_2^{NC} \mp \frac{Y_-}{Y_+} x F_3^{NC} - \frac{y^2}{Y_+} F_L^{NC}, \quad (2.12)$$

is shown for positron-proton collisions [11]. The data at low Q^2 and high x were taken by several fixed target experiments [12] while the points at high Q^2 and low x were obtained from a combination of several measurements by the H1 and ZEUS collaborations. For $x \approx 0.1$, σ_r is nearly independent of Q^2 and the data show scaling behaviour.

A comparison of (2.4) and (2.11) for not too high values of Q^2 ($x F_3 \approx 0$) leads to²:

$$F_2(x) = x \sum_i Q_i^2 f_i(x) \text{ and} \quad (2.13)$$

$$F_L = 0. \quad (2.14)$$

(2.14) is called the *Callan-Gross relation* and is a direct consequence of the spin- $\frac{1}{2}$ nature of the quarks [13]. This was confirmed in fixed target experiments using an electron beam at SLAC³. The prediction for spin-0 particles, $F_2 = F_L$, is clearly excluded by the data [14].

The identification of quarks as the partons in the parton model led to the *quark-parton model* (QPM). Here F_2 can be expressed as the sum of quark and anti-quark densities.

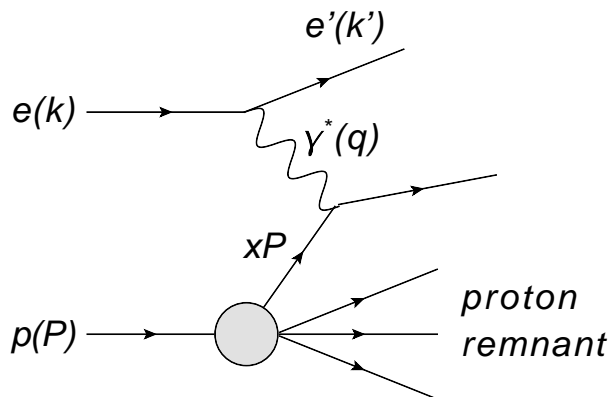


Figure 2.4.: Feynman diagram for the QPM process.

The Feynman diagram of the so-called *QPM process* is shown in Fig. 2.4. This process represents the lowest-order contribution to NC DIS. The QPM process is a purely electroweak interaction.

If the proton consisted only of quarks (and antiquarks), the sum of their momenta would be equal to the momentum of the proton. However, it was shown experimentally [15]

² F_2^{NC} is referred to as F_2 in the following.

³The SLAC National Accelerator Laboratory was founded as Stanford Linear Accelerator Center in 1962.

that:

$$\sum_i \int_0^1 x f_i(x) dx \approx 0.5. \quad (2.15)$$

Only half of the proton's momentum is carried by charged quarks. The other half is carried by *gluons* which are the gauge bosons of quantum chromodynamics as described in the next section. Gluons were first observed directly in 1979 at the PETRA collider in three-jet events [16].

2.4. Quantum chromodynamics

The strong interactions between quarks and gluons are described by QCD which is a non-Abelian gauge theory⁴. The gauge group of QCD is an SU(3) group⁵ where the unitary transformations are acting on a degree of freedom called *colour*. The Dirac equation of a quark in the vacuum can be written as:

$$(i\gamma_\mu \partial^\mu - m)\Psi = 0. \quad (2.16)$$

A local SU(3)_c transformation is given by:

$$\Psi' = \exp\left(i\frac{g_s}{2}\lambda_j\beta_j(x)\right)\Psi, \quad (2.17)$$

where g_s is the coupling constant of the strong interaction and the λ_i are the eight *Gell-Mann matrices*. The following sum convention is used:

$$\lambda_j\beta_j = \lambda_1\beta_1 + \dots + \lambda_8\beta_8. \quad (2.18)$$

The transformation in Eq. 2.17 acts only on the colour part of the wave function and is characterised by eight independent transformations $\beta_i(x)$. To ensure the invariance of the Dirac equation under local SU(3)_c transformations, eight gauge fields G_j^μ are introduced and ∂^μ is replaced by the SU(3)_c covariant derivative:

$$D^\mu = \partial^\mu + i\frac{g_s}{2}(\lambda_1 G_1^\mu + \dots + \lambda_8 G_8^\mu). \quad (2.19)$$

In parallel to the SU(3)_c transformation of the spinors, a transformation of the gauge fields needs to be performed to ensure the invariance of the Lagrangian. The eight gauge fields G_j^μ are related to the fields of the eight gluons.

The field-strength tensor is defined as:

$$F_j^{\mu\nu} = \partial_\mu G_j^\nu - \partial_\nu G_j^\mu - g_s f_{jkl} G_k^\mu G_l^\nu, \quad (2.20)$$

where f_{jkl} are the SU(3)_c structure constants. This leads to the Lagrangian density of

⁴For an introduction to perturbative QCD, see, e.g. [17].

⁵The gauge group of QCD is referred to as SU(3)_c in the following.

QCD:

$$\mathcal{L} = \sum_f \bar{\Psi}_{f,\alpha} (i\gamma_\mu D^\mu - m_f)_{\alpha\beta} \Psi_{f,\beta} - \frac{1}{4} F_{j,\mu\nu} F_j^{\mu\nu}, \quad (2.21)$$

where the sum runs over all six quark flavours f and the quark colour indices α and β run from 1 to 3.

The main difference between QCD and QED is the fact that the gluons are carrying colour charge while photons are electrically neutral. Thus the gluons interact with themselves via three-gluon and four-gluon vertices.

Apart from the six quark masses, the coupling $\alpha_s = g_s^2/4\pi$ is a fundamental parameter of QCD. The size of α_s strongly depends on the energy scale of the interaction as discussed in Sec. 2.4.1. If the scale of the interaction is large, corresponding to small distances, the coupling becomes small and the quarks behave like free particles (*asymptotic freedom*). On the other hand, the strength of the coupling rises for increasing distances. Thus quarks are not observed as free particles because at a certain distance between two quarks it becomes energetically favourable to produce new quark pairs before the original quarks are separated (*confinement*).

2.4.1. Perturbative calculations

Since the QCD Lagrangian is known, Feynman rules for the perturbative calculation of predictions for amplitudes of scattering processes can be derived. Any cross section can be written as a power series in α_s :

$$\sigma = c_0\alpha_s^0 + c_1\alpha_s^1 + c_2\alpha_s^2 + \dots = \sum_{i=0}^n c_i\alpha_s^i, \quad (2.22)$$

where n is the order of the calculation and the coefficients c_i have to be determined from the appropriate Feynman diagrams. In the lowest order in α_s which contributes to a given QCD process, referred to as *leading order*, only tree-level diagrams contribute to the cross section. In contrast, at higher orders also virtual loops need to be considered (see Fig. 2.5) which lead to divergencies caused by the integration over infinite internal loop momenta. These *ultraviolet divergencies* can be made temporarily finite using a *regularisation* procedure, e.g. by dimensional regularisation [18]. The regularised divergencies can be removed by absorbing them in the definition of α_s . The prescription for this is referred to as *renormalisation scheme*. Most commonly the modified minimal subtraction ($\overline{\text{MS}}$) scheme is used [19].

The renormalisation procedure introduces an arbitrary and unphysical parameter called *renormalisation scale* μ_R . Predictions of perturbative QCD are expressed in terms of the renormalised coupling $\alpha_s(\mu_R^2)$. In general, any physical observable \mathcal{R} has to be independent of μ_R . This requirement is expressed by the renormalisation group equation:

$$\mu_R^2 \cdot \frac{d\mathcal{R}}{d\mu_R^2} = 0. \quad (2.23)$$

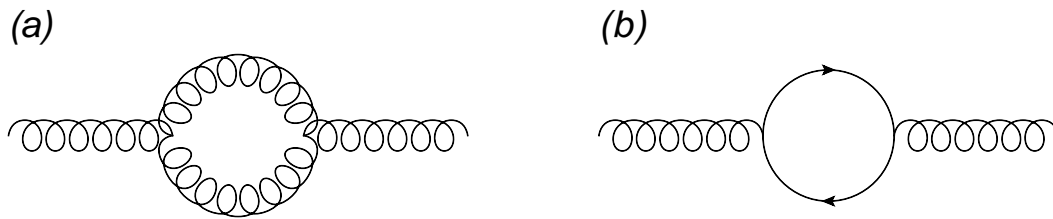


Figure 2.5.: One-loop corrections to the gluon propagator. The gluon loop (a) is unique for QCD while the quark loop (b) has its pendant in QED.

To ensure that \mathcal{R} is independent of the choice of μ_R , changes in μ_R have to be compensated by changes in the renormalised strong coupling constant $\alpha_s(\mu_R^2)$. The renormalisation group equation for the coupling is given by:

$$\mu_R^2 \frac{d\alpha_s}{d\mu_R^2} = \beta(\alpha_s) = -(b_0\alpha_s^2 + b_1\alpha_s^3 + b_2\alpha_s^4 + \dots), \quad (2.24)$$

where the β function of QCD describes the change of the coupling with the renormalisation scale. The minus sign in Eq. 2.24 is the origin of asymptotic freedom. The β function coefficients are calculable in QCD and are given by [20]:

$$b_0 = \frac{33 - 2n_f}{12\pi}, \quad b_1 = \frac{153 - 19n_f}{24\pi^2} \quad \text{and} \quad b_2 = \frac{2857 - \frac{5033}{9}n_f + \frac{325}{27}n_f^2}{128\pi^3}, \quad (2.25)$$

where the b_i are valid for an effective theory with n_f light flavours ($m_q \ll \mu_R$) and in which the other heavier quark flavours decouple from the theory. b_2 is dependent on the renormalisation scheme and is given here for the $\overline{\text{MS}}$ scheme. In an energy range where n_f is constant, the leading-order solution of Eq. 2.24 is given by:

$$\alpha_s(\mu_R^2) = \frac{1}{b_0 \ln(\frac{\mu_R^2}{\Lambda^2})} = \frac{12\pi}{(33 - 2n_f) \ln(\frac{\mu_R^2}{\Lambda^2})}, \quad (2.26)$$

where Λ is a constant of integration corresponding to the scale where the perturbatively-defined coupling would diverge. The parameter Λ is not predicted by QCD but has to be determined experimentally and is dependent on n_f , on the order of the calculation and on the renormalisation scheme. In determinations of the QCD coupling it has become standard not to quote Λ but the value of α_s at the scale $\mu_R^2 = M_Z^2$. The renormalisation scale dependence of α_s is demonstrated in Fig. 2.6 [21]. Measurements from different processes are shown at their respective energy scales. The running of α_s follows the expectation from perturbative QCD. The following average was obtained from the different measurements:

$$\alpha_s(M_Z) = 0.1184 \pm 0.0007. \quad (2.27)$$

Only if a given observable is calculated to all orders in α_s , the renormalisation group equation (see Eq. 2.23) is fulfilled. Any truncation in the expansion in powers of α_s causes

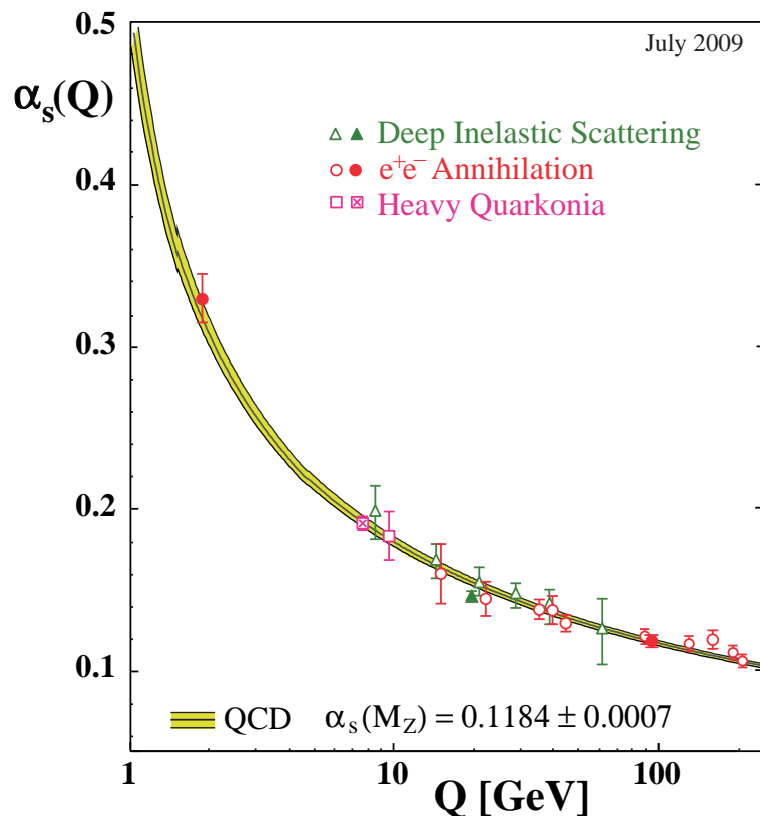


Figure 2.6.: Different measurements of α_s as a function of the respective energy scale Q .

dependencies of the observable on μ_R . Several prescriptions how to choose reasonable renormalisation scales were proposed [22]. One commonly used ansatz requires that the choice of μ_R should be related to the scale of the investigated process. Hence for inclusive DIS the renormalisation scale is often set to Q^2 while for the production of heavy quarks in DIS $Q^2 + 4m_Q^2$ is a possible choice.

2.4.2. Quark masses

On a timescale of $1/\Lambda \approx 3 \times 10^{-24}$ s all quarks⁶ *hadronise*, i.e. become part of a meson or baryon. Hence any definition of the quark masses is dependent on a specific prescription. A possible choice is the *pole mass*, m_Q , which is given by the position of the divergence of the propagator. The pole mass is commonly used in perturbative calculations because it is introduced in a gauge invariant way and defined at any finite order of perturbative theory. On the other hand, the pole mass prescription suffers from non-perturbative ambiguities of the order Λ when it is related to observable quantities [23].

An alternative choice is the $\overline{\text{MS}}$ mass, $\overline{m}_Q(\mu_R^2)$, which is free of ambiguities of the order

⁶The top quark does not form colourless hadrons since its lifetime is smaller than the timescale for hadronisation.

A. Its scale dependence is given by:

$$\mu_R^2 \frac{d\overline{m}_Q(\mu_R^2)}{d\mu_R^2} = \left(-\frac{\alpha_s(\mu_R^2)}{\pi} + \mathcal{O}(\alpha_s^2) \right) \overline{m}_Q(\mu_R^2). \quad (2.28)$$

Results of determinations of the charm and beauty quark masses are often quoted either using the pole mass prescription or as the $\overline{\text{MS}}$ mass evaluated at the scale equal to the mass, $\overline{m}_Q(m_Q^2)$. Both prescriptions are related by:

$$m_Q = \overline{m}_Q(m_Q^2) \left(1 + \frac{4\alpha_s(\overline{m}_Q^2)}{3\pi} + \mathcal{O}(\alpha_s^2) + \dots \right), \quad (2.29)$$

where the coefficients of the perturbative expansion in α_s are known to three-loop order [24].

2.4.3. Factorisation and parton density functions

Electron-hadron interactions are treated as an incoherent sum of the partonic processes in QCD calculations. At present, it is not possible to predict the parton distributions within hadrons from first principle since no hard scale is available to apply a perturbative approach. Future developments in lattice QCD might allow to predict the partonic structure of hadrons some day [25]. However, it is possible to separate the hard (short range) interactions from the soft (long range) processes. This approach is called *factorisation* [26]. The structure function F_2 can be written as a convolution of a perturbatively calculable part, the *coefficient functions* C_2^i , and experimentally determined parton density functions f_i :

$$F_2(x, Q^2) = \sum_i \int_x^\infty C_2^i \left(\frac{x}{\xi}, \frac{Q^2}{\mu_R^2}, \frac{\mu_F^2}{\mu_R^2}, \alpha_s(\mu_R) \right) f_i(\xi, \mu_F, \mu_R) d\xi, \quad (2.30)$$

where ξ is the momentum fraction of the parton i . The sum runs over all partons (quarks, antiquarks and gluons). The use of factorisation can be interpreted as a generalisation of the simple parton model (see Eq. 2.13). Divergencies arising from the emission of collinear gluons from the partons are absorbed in the definition of the PDFs using the *factorisation scale* μ_F . This scale defines the separation between short-range and long-range effects. A propagator that is off-shell by more than μ_F^2 contributes to C_2^i while it is absorbed into f_i below this scale.

In the following, the quark PDFs are referred to as $q_i(x, Q^2)$ and the gluon density is called $g(x, Q^2)$. The evolution of the parton densities in Q^2 can be calculated using *parton evolution schemes*. The *Dokshitzer-Gribov-Lipatov-Altarelli-Parisi* (DGLAP) equations have the form [27]:

$$\frac{dq_i(x, Q^2)}{d \ln Q^2} = \frac{\alpha_S(Q^2)}{2\pi} \int_x^1 \frac{d\xi}{\xi} \left[\sum_j q_j(\xi, Q^2) P_{q_i q_j} \left(\frac{x}{\xi} \right) + g(\xi, Q^2) P_{q_i g} \left(\frac{x}{\xi} \right) \right] \text{ and} \quad (2.31)$$

$$\frac{dg(x, Q^2)}{d \ln Q^2} = \frac{\alpha_S(Q^2)}{2\pi} \int_x^1 \frac{d\xi}{\xi} \left[\sum_j q_j(\xi, Q^2) P_{gq_j}\left(\frac{x}{\xi}\right) + g(\xi, Q^2) P_{gg}\left(\frac{x}{\xi}\right) \right]. \quad (2.32)$$

Equation 2.31 describes the change of the quark densities with Q^2 caused by gluon radiation and gluon splitting while Eq. 2.32 describes the evolution of the gluon density with Q^2 due to gluon radiation off quarks and gluons.

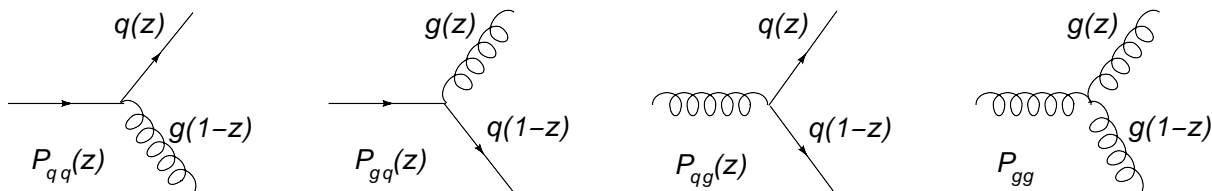


Figure 2.7.: The DGLAP splitting functions.

The $P_{p'p}(\frac{x}{\xi})$ are called *splitting functions* (see Fig. 2.7). They represent the probability of a parton p to emit a gluon or quark and become parton p' carrying a fraction $z = \frac{x}{\xi}$ of the momentum of the parent parton p . At the order α_S , the splitting functions are given by:

$$P_{qq}(z) = \frac{4}{3} \frac{1+z^2}{1-z}, \quad (2.33)$$

$$P_{gq}(z) = \frac{4}{3} \frac{1+(1-z)^2}{z}, \quad (2.34)$$

$$P_{qg}(z) = \frac{1}{2} [z^2 + (1-z)^2] \text{ and} \quad (2.35)$$

$$P_{gg}(z) = 6 \left[\frac{z}{1-z} + \frac{1-z}{z} + z(1-z) \right]. \quad (2.36)$$

It is easy to see that the splitting functions obey:

$$P_{gq}(z) = P_{qg}(1-z) \text{ and } P_{gg}(z) = P_{gg}(1-z). \quad (2.37)$$

Though the DGLAP equations are suspected to fail at very low values of x since terms proportional to $\alpha_s \ln(\frac{1}{x})$ may become large and spoil the accuracy of the approach, no significant deviations have been found experimentally so far. Other evolution schemes are BFKL [28] or CCFM [29]. The difference between the schemes is the ordering of the chain of partons that are emitted from the quark before entering the hard interaction with the photon.

The PDFs are usually extracted in global analyses based on the DGLAP equations using several observables. Apart from inclusive DIS cross sections, also other processes are used in a combined fit. Since the inclusive DIS cross sections are only sensitive to the gluon density in the proton via scaling violations ($\partial F_2 / \partial(\ln Q^2) \sim \alpha_s \cdot x \cdot g$), cross sections for processes more strongly dependent on the gluon density like the production of jets or heavy quarks are used to improve the precision. Additionally, measurements of the

Drell-Yan process ($q\bar{q} \rightarrow l^+l^-$, where l is a lepton), which is sensitive to the anti-quark densities, are often included in the fits. Measurements of W^\pm asymmetries measured at the Tevatron can constrain the ratio of the d quark density to the u quark density at high x . The dependence of the parton densities on x is usually parametrised at a starting scale Q_0^2 . The parton densities are evolved accordingly to any scale of interest. Examples for recent results include the HERAPDF 1.0 [11], CTEQ6.6 [30], CT10 [31], MSTW 2008 [32], ABKM09 [33], GJR08 [34] and NNPDF2.0 [35] parton densities. These and other PDF sets are available through common interfaces, e.g. [36]. As an example, Fig. 2.8 shows the parton distributions from the HERAPDF 1.0 analysis.

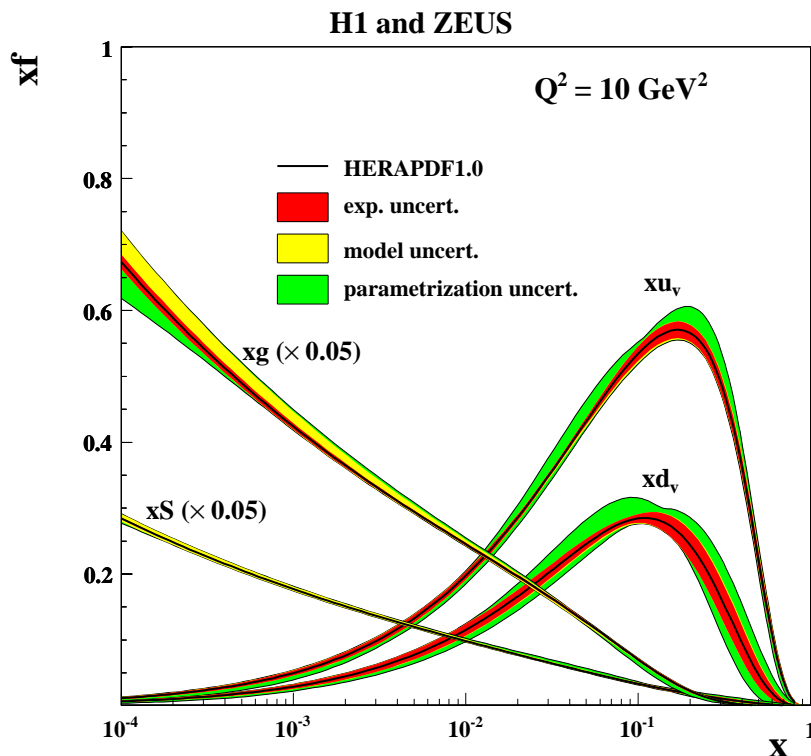


Figure 2.8.: Parton distributions from HERAPDF 1.0 at $Q^2 = 10 \text{ GeV}^2$. The gluon and sea quark ($xS = 2x(\bar{U} + \bar{D})$) distributions are scaled down by a factor 20. Different contributions to the uncertainty are shown separately.

QCD predicts that quarks can radiate gluons, which in turn can split into a pair of so-called *sea* quarks. As a consequence, the number of partons is increasing while the average momentum of the partons is decreasing. Due to gluon radiation the quarks have a transverse momentum component and coupling to longitudinally polarised virtual photons is possible. The Callan-Gross relation is not satisfied and F_L is not zero any more in a variant of the quark-parton model improved by QCD.

At high values of x , the cross section is mainly sensitive to valence quarks. Since the momentum fraction of the valence quarks decreases with increasing Q^2 , caused by gluon

radiation, scaling is violated. This effect is found in the experimental data. For high values of x , the cross section falls with increasing Q^2 (see Fig. 2.3).

At higher values of Q^2 , smaller distances can be resolved. Here the number of sea quarks and gluons in the proton becomes larger. Thus the cross section rises with increasing Q^2 at low values of x . Also this behaviour can be seen in Fig. 2.3. As shown in Fig. 2.8, the densities of the valence quarks have a maximum at about 0.2 while the densities of gluons and sea quarks are relatively small for high x and rise steeply towards smaller values of x .

2.5. Treatment of heavy quark production in QCD

The production of the *heavy quarks* charm and beauty⁷ in ep collisions can not be explained by the simple QPM. The lowest order process to produce heavy quarks in DIS is the so-called *boson-gluon fusion* (BGF) mechanism where the exchanged virtual photon interacts with a gluon from the proton (see Fig 2.9).

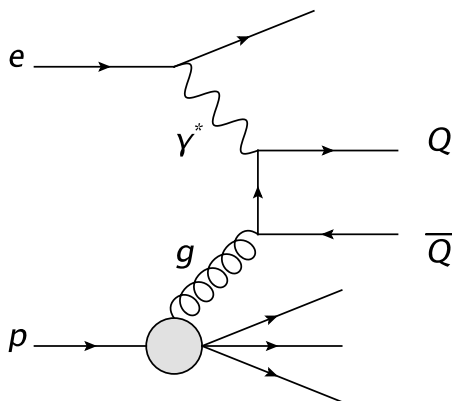


Figure 2.9.: Feynman diagram for boson-gluon fusion at leading order.

A heavy quark pair can be produced by the BGF process if the centre-of-mass energy squared of the photon-gluon system, \hat{s} , is larger than the squared mass of the $Q\bar{Q}$ pair:

$$\hat{s} = (q + \xi P)^2 > (2m_Q)^2. \quad (2.38)$$

The high pole masses of the charm and beauty quarks ($m_c \approx 1.5$ GeV, $m_b \approx 4.75$ GeV) provide hard scales which allow to obtain reliable predictions using perturbative QCD even in the \hat{s} threshold region. On the other hand, the mass competes with other hard scales in the interaction like the transverse momenta of the produced quarks or the photon virtuality Q^2 . Hence the measurement of heavy quark production allows to study multi-scale problems in QCD. Since the cross section is directly sensitive to the gluon density in

⁷The production of top quark pairs is kinematically not accessible at HERA.

the proton, heavy quark production provides an independent check of the gluon density obtained from scaling violations.

The reconstruction of heavy flavour production allows to extract the charm and beauty structure functions $F_2^{c\bar{c}}$ and $F_2^{b\bar{b}}$, which represent the fractions of the inclusive structure function F_2 related to charm and beauty production, respectively. The double differential cross section for charm (beauty) production in NC DIS for not too high values of Q^2 can be written in an analogous way to Eq. 2.4:

$$\frac{d^2\sigma^{c\bar{c}(b\bar{b})}}{dx dQ^2} = \frac{2\pi\alpha^2}{xQ^4} \left[Y_+ F_2^{c\bar{c}(b\bar{b})}(x, Q^2) - y^2 F_L^{c\bar{c}(b\bar{b})}(x, Q^2) \right]. \quad (2.39)$$

Several schemes exist to include the production of heavy quarks in the framework of perturbative QCD. These schemes are reviewed in the following subsections.

2.5.1. Fixed flavour number scheme

In the *fixed flavour number scheme* (FFNS) the initial state protons contain only light quarks (u , d and s) as partons, whose distributions fulfil the DGLAP equations. Charm and beauty quarks are produced by the BGF process and other higher order processes. The threshold region is correctly handled in the FFNS. On the other hand, the presence of different large scales, Q^2 , p_T^2 and m_Q^2 , can spoil the convergence of the perturbative series because terms of higher order in α_s contain $\log \frac{Q^2}{m_c^2}$ terms which can become large. Thus results based on the FFNS are expected to be most precise for $Q^2 \approx m_Q^2$. However, no significant deviations from FFNS predictions at high Q^2 were observed at HERA so far.

At leading order, inclusive [37] and differential [38] calculations for heavy quark production by the BGF process are known since a long time. Additionally, the *next-to-leading order* (NLO), i.e. $\mathcal{O}(\alpha_s^2)$, corrections for the inclusive structure functions [39] and for differential cross sections [40] are available. Any differential parton level cross section at NLO can be obtained using the HVQDIS program [41] in the FFNS. The corresponding corrections at the next order in α_s , referred to as NNLO, are not known.

At not too large values of Q^2 , the convolution of the coefficient function and the gluon density for $F_2^{Q\bar{Q}}$ is dominated by rather low values of \hat{s} . Hence estimates of the NNLO corrections obtained using threshold resummation [42] can provide useful information on the dominant contribution to $F_2^{Q\bar{Q}}$. To demonstrate the effect of the soft gluon resummation, Fig. 2.10 shows $dF_2^{c\bar{c}}/dp_T$ estimated using the ABKM09 PDFs, where p_T is the transverse momentum of the detected quark in the rest frame of the virtual photon-boson system. A comparison at NLO of the exact result to the NLL expanded prediction for $Q^2 = 10 \text{ GeV}^2$ indicates that the NLL approximation is reliable at $x \approx 0.01$, but not at $x \approx 0.001$. The NNLO corrections are large and positive in the peak region. The NLL approximation for visible charm and beauty cross sections at NNLO is not yet available. In the asymptotic limit $m_Q^2/Q^2 \rightarrow 0$, fully analytic NLO results were obtained [43]. These were recently extended to NNLO for the lowest even-integer Mellin moments [44].

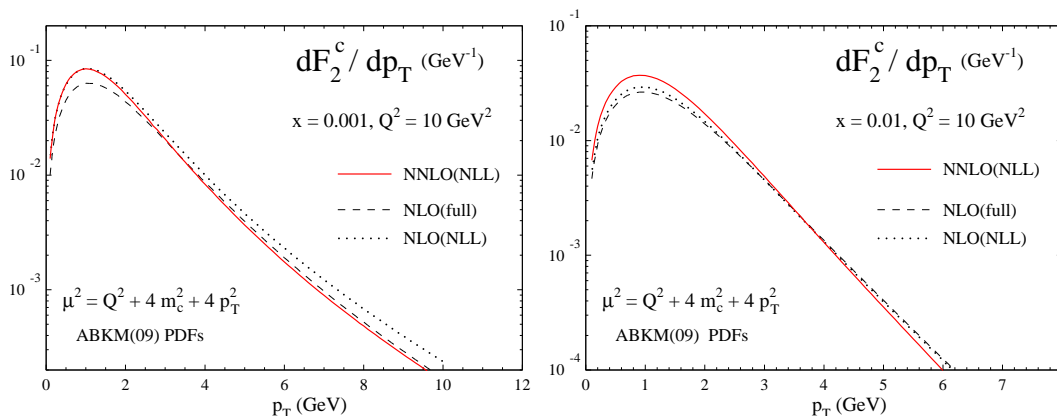


Figure 2.10.: NLL estimates for $F_2^{c\bar{c}}$ at NNLO as a function of p_T evaluated at two values of x . At NLO, the exact results are compared to the NLL approximation.

2.5.2. Zero-mass variable flavour number scheme

At very high values of Q^2 , where $Q^2 \gg m_Q^2$, the heavy quark mass becomes almost negligible and it is appropriate to treat the heavy quarks as massless partons. This scheme is referred to as *zero-mass variable flavour number scheme* (ZM-VFNS). The large $\log \frac{Q^2}{m_Q^2}$ terms are resummed via the DGLAP equations. The leading order contribution in this scheme is the simple quark-parton model process (see Fig. 2.4).

However, the physical threshold is not treated correctly. The heavy quark parton density $f_Q(x, Q^2)$ vanishes below a certain threshold, which is chosen so that $F_2^{Q\bar{Q}}(x, Q^2) = 2e_Q^2 x f_Q(x, Q^2)$ gives a reasonable description of the data.

2.5.3. General-mass variable flavour number scheme

The *general-mass variable flavour number scheme* (GM-VFNS) was proposed to treat charm production correctly for all values of Q^2 . At low values of Q^2 , heavy quark production is described using the FFNS while the procedure at larger values of Q^2 is based on the ZM-VFNS. Hence this formalism uses different numbers of active flavours in the proton depending on Q^2 . Several possibilities exist how to implement the GM-VFNS. They differ in the prescription how to treat the transition region between the two well-defined regions at low and very high Q^2 . The most common schemes include the ACOT(χ) scheme [45], the Thorne-Roberts (TR) scheme [46] and the Buza, Matiounine, Smith, van Neerven (BMSN) scheme [47]. The implications of the chosen scheme on PDF fits and cross section predictions are discussed in [48].

The effect of different variants of the GM-VFNS in the TR scheme on predictions for $F_2^{c\bar{c}}$ is illustrated in Fig. 2.11. Different choices of the GM-VFNS are shown at NLO and NNLO using the MSTW 2008 PDFs in each case. At NLO, a sizable spread between the predictions based on the different schemes is visible. The ZM-VFNS prediction vanishes below a certain threshold by definition and rises steeper in Q^2 than the GM-VFNS curves. The ZM-VFNS is not really feasible at NNLO since it leads to huge discontinuities in $F_2^{c\bar{c}}$ and even sizeable discontinuities in the inclusive structure function F_2 [49]. The different

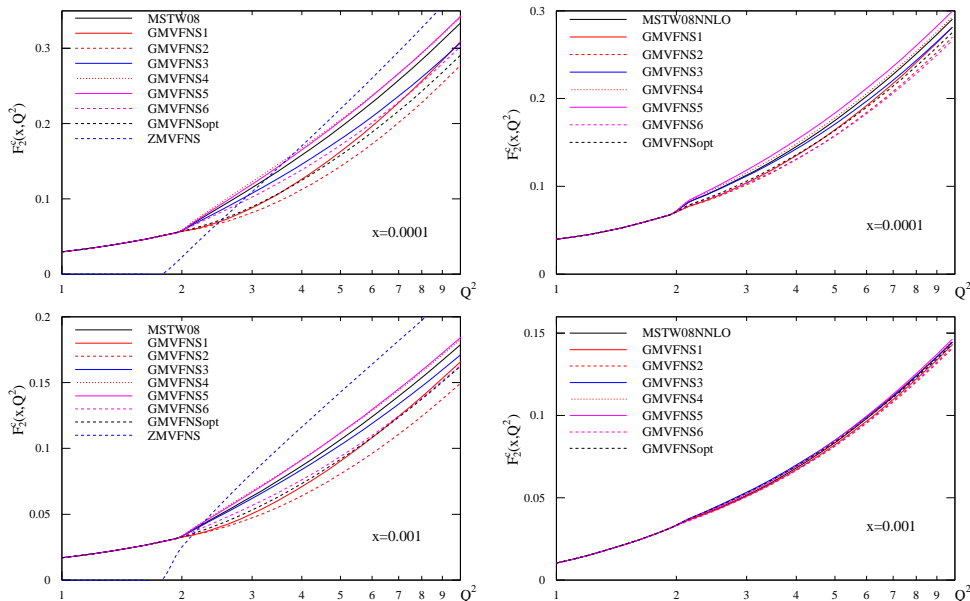


Figure 2.11.: The structure function $F_2^{c\bar{c}}$ obtained using different variants of the GM-VFNS at NLO (left) and NNLO (right). The MSTW 2008 PDFs were used for all predictions. The charm quark mass was set to 1.4 GeV.

GM-VFNS predictions at NNLO are reasonably similar, especially at higher Bjorken x .

2.5.4. Heavy flavour treatment in global PDF analyses

All recent global PDF fits (see Sec. 2.4.3) are based either on the GM-VFNS (e.g. CT10, MSTW 2008, NNPDF2.0, HERAPDF) or on the FFNS (e.g. ABKM09, HERAPDF). The ZM-VFNS is disfavoured theoretically (see Fig. 2.11) and by the data since predictions based on the ZM-VFNS are for example not able to describe the $F_2^{c\bar{c}}$ and $F_2^{b\bar{b}}$ measurements at HERA. Some PDF sets are available in several versions using different heavy flavour treatments. If the parton densities are used as an input for a perturbative calculation like the HVQDIS program, an appropriate PDF set obtained in the same scheme has to be used. Additionally, other parameters like the heavy quark masses or the choice of $\alpha_s(M_Z)$ should be identical in the PDF fit and in the perturbative part of the calculation to obtain a consistent prediction.

To investigate the effect of the choice of heavy flavour treatment, PDF fits of the same data were performed using different variants of the GM-VFNS [50]. Neutral and charged current cross sections as well as $F_2^{c\bar{c}}$ measurements from HERA were fitted. An optimal value for the charm quark mass was determined for each heavy flavour scheme. It is interesting to notice that the predictions obtained for W^\pm and Z^0 production cross sections at the LHC are very similar for the different heavy flavour schemes if the optimised mass values are used. The extracted optimal values of the charm quark mass range between 1.26 and 1.68 GeV.

2.6. Event simulation

In the discussion so far the production of coloured partons in hard QCD interactions was described. Due to confinement, these partons have to form colourless hadrons. This process is referred to as *hadronisation* or *fragmentation*. All well-established hadrons can be classified either as quark-antiquark pairs called *mesons* or as *baryons* consisting of three quarks or antiquarks. Since the hadronisation process can not be calculated perturbatively, the usual approach is to use Monte Carlo (MC) *event generators* to simulate the transition from the final state partons of the hard interaction described by perturbative QCD into hadrons which correspond to the signatures observed in experiments.

Event generators provide all stable final-state particles for an event. The radiation of additional partons before and after the hard subprocess can be calculated perturbatively. These *parton showers* provide an approximation of higher order processes not considered in the fixed order calculation of the hard subprocess. The non-perturbative step from the partons to hadrons is approximated using phenomenological *hadronisation models*. Both aspects, parton showers and hadronisation models, are discussed in the following subsections. A more detailed overview is given in [51]. An example illustrating the different aspects of event generators in a BGF event is shown in Fig. 2.12.

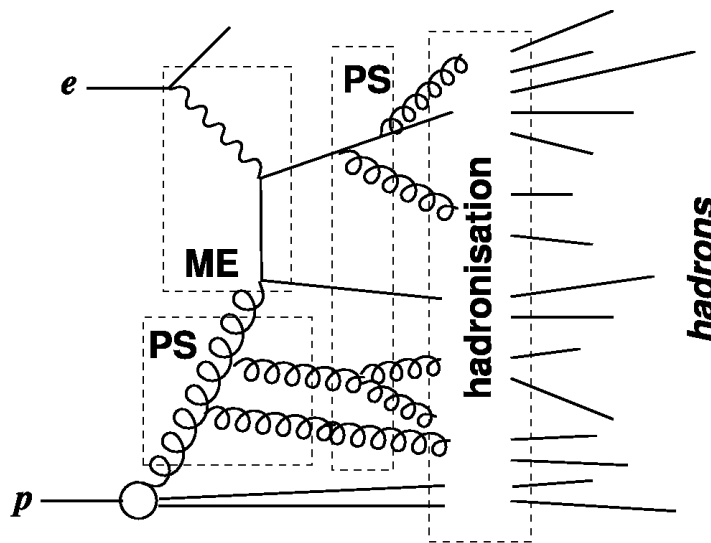


Figure 2.12.: Principle of event generators for the BGF process. Different parts of the simulation are shown by dashed boxes. The hard interaction in the box labelled “ME” (matrix element) is calculated perturbatively. The parton showers are applied in the boxes called “PS”. Finally, the outgoing partons are transformed into colourless hadrons.

2.6.1. Parton showers

In the parton shower approach, the parton cascade is modelled as a sequence of particle branchings $q \rightarrow qq$, $g \rightarrow gg$ and $g \rightarrow q\bar{q}$ in the leading log (LL) approximation. This iterative procedure allows simple expressions for these branchings to be combined to form complex multiparton final states. The probabilities for the splittings are given as so-called Sudakov form factors which provide a physical way to handle the cancellation between real and virtual divergencies.

In the following, the evolution of a parton shower in an event generator is illustrated. The probability for each parton not to split into other partons between the hard scale Q_0 and some smaller scale Q_1 is called $\Delta(Q_0, Q_1)$. A random number n is chosen uniformly in the range $0 < n < 1$. By solving $n = \Delta(Q_0, Q_1)$, the event generator determines the scale of the first emission. This procedure is repeated to evaluate the scale of the next emission, Q_2 , and so forth. The sequence is stopped at a scale ~ 1 GeV separating the perturbative and the non-perturbative parts of the simulation.

2.6.2. Fragmentation models

Since the transformation of the final state partons into hadrons can not be calculated perturbatively, phenomenological models have to be used instead. Typically, these models contain one or several free parameters which were adjusted to describe previous measurements. Two approaches relevant for this thesis are summarised here.

- **Independent fragmentation:** This is the simplest model to describe hadronisation. All partons fragment independently and the flight direction of the produced hadrons is identical to that of the original partons. The fraction of the momentum of the parton which is transferred to the hadron, z , is described by *fragmentation functions* $D(z)$. A commonly used fragmentation model for heavy quark production is the *Peterson function* [52]:

$$D(z) \propto \frac{1}{z[1 - 1/z - \epsilon/(1 - z)]^2}, \quad (2.40)$$

where ϵ is a free parameter dependent on the quark mass. Fig 2.13 shows $D(z)$ for typical choices of the ϵ parameter for charmed and beauty hadrons. The fragmentation for beauty quarks is significantly harder than for charm quarks, i.e. on average a larger fraction of the transverse momentum of the beauty quarks is transferred to the hadrons. Different measurements of the charm fragmentation function at HERA are reviewed in Sec. 3.1.2.

Another parametrisation was proposed by the Kartvelishvili et al. [53]:

$$D(z) \propto z^\alpha(1 - z), \quad (2.41)$$

where α is a free parameter.

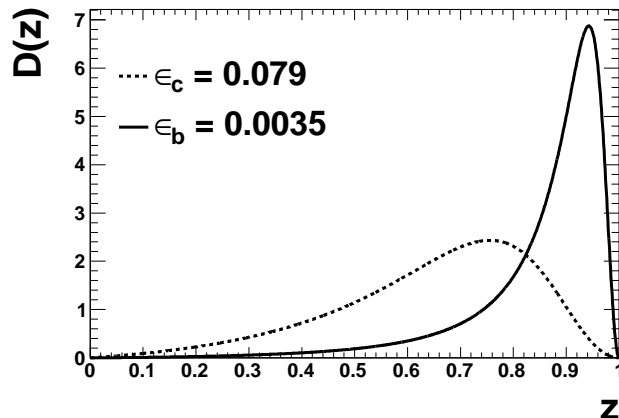


Figure 2.13.: Peterson function for typical choices of the ϵ parameter for charm ($\epsilon_c = 0.079$) and beauty ($\epsilon_b = 0.0035$). The distributions are area normalised to unity.

A fragmentation function for heavy quarks was developed by Bowler [54] within the framework of the Artru-Mennessier model [55] which has the form:

$$D(z) \propto \frac{1}{z^{1+r_Q b m_\perp^2}} (1-z)^a \exp\left(\frac{-b m_\perp^2}{z}\right), \quad (2.42)$$

where a and b are free parameters. The transverse mass of the hadron, m_\perp , is defined by: $m_\perp^2 = m^2 + (p_T^{\text{rel}})^2$, where m is the hadron's mass and p_T^{rel} is the transverse momentum relative to the direction of the quark. For massive quarks r_Q is predicted to be unity. The parameter r_Q allows to extrapolate smoothly between the Bowler function and the symmetric Lund form [56] ($r_Q = 0$) which is suitable for massless quarks.

- **String fragmentation:** In this approach, *colour strings* are connecting the partons [57]. When these are stretched, more and more energy is stored in the strings. If the stored potential energy in a string is sufficient to produce a $q\bar{q}$ pair, it breaks up and two substrings are formed. This process continues until all energy to produce more $q\bar{q}$ pairs is used up. The string fragments are accordingly grouped into hadrons. The string fragmentation model is illustrated in Fig. 2.14.

2.7. Monte Carlo event generators

For the analyses presented in this thesis, two Monte Carlo programs were used to generate ep scattering events in the DIS regime. Inclusive DIS events were obtained using ARIADNE while dedicated charm and beauty samples to estimate the detector acceptances

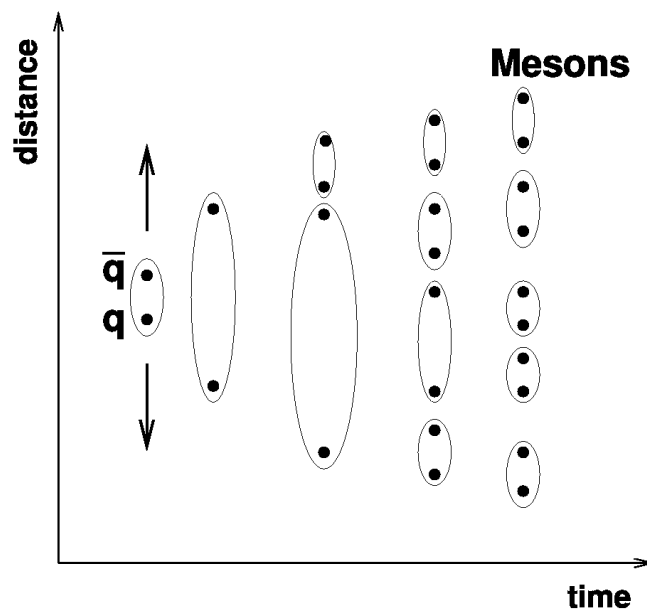


Figure 2.14.: Schematic view of the string fragmentation model.

were produced using the RAPGAP program. Both event generators are discussed in the following subsections.

2.7.1. ARIADNE

NC DIS events were simulated using the DJANGO [58] event generator, which is an interface between the HERACLES [59] and LEPTO [60] programs. LEPTO simulates the QCD part of the hard interaction while QED corrections are provided by HERACLES. Corrections for initial- and final-state radiation, vertex and propagator terms, and two-boson exchange are included in HERACLES. The QCD parton shower cascade was simulated using the ARIADNE [61] program.

The ARIADNE program is based on the *colour dipole model* (CDM) [62]. In this model, higher-order processes are approximated by the emission of gluons from so-called colour dipoles formed by the final-state partons from the hard interaction carrying colour charge. Additionally, these emitted gluons can form further colour dipoles that can radiate more gluons or split into $q\bar{q}$ pairs. These processes continue as long as the dipoles have not reached a certain minimum energy.

The hadronisation of the coloured particles from the QCD cascade into colourless hadrons was performed using the JETSET program [63] based on the string model (see Sec. 2.6.2). The decays of unstable hadrons are simulated using a table of known particle decays and their properties by JETSET.

The event samples generated as described above are referred to as ARIADNE MC in the following. In this approach charm and beauty quarks were treated as massless partons.

Hence the charm and beauty events in the inclusive Ariadne MC samples are not expected to reproduce the properties of charm and beauty events in the data correctly.

2.7.2. RAPGAP

The RAPGAP [64] program was used to generate charm and beauty event samples. Also RAPGAP uses HERACLES to simulate QED corrections. While first order QCD processes are simulated using the exact matrix elements, the simulation of higher order corrections is based on parton showers (see Sec. 2.6.1) using the DGLAP splitting functions.

Charm and beauty quark production by the BGF process are simulated using massive matrix elements. Thus predictions for this process are valid also in the threshold region. On the other hand, the so-called *resolved* photon processes:

$$\begin{aligned}
 Qg &\rightarrow Qg, \\
 gg &\rightarrow Q\bar{Q} \text{ and} \\
 q\bar{q} &\rightarrow Q\bar{Q}
 \end{aligned}$$

are simulated using massless matrix elements. For the first process, the charm quark was treated as a part of the structure of the photon. The cross sections for non-BGF processes diverge for low values of p_T^2 . Hence a cutoff in p_T^2 needs to be specified to obtain finite predictions. Due to this cutoff, the non-BGF Monte Carlo samples generated using RAPGAP are not expected to reproduce the data in the threshold region.

The Lund string model was used for the hadronisation as implemented in PYTHIA 6.2 [65], which is a successor of the JETSET package. In this approach, the transverse momenta of the produced heavy quarks are determined using the Bowler function while the symmetric Lund form was used for light quarks. The decay of hadrons is again based on a table containing the particle properties.

2.8. Properties of charmed and beauty hadrons

An overview of the most relevant charmed and beauty hadrons produced at HERA is given in Tab. 2.1. Except for the D^{*+} meson, all of these particles are ground states whose decays are mediated by the weak interaction. For all hadrons, the constituents in the quark model are listed. The mass of charmed hadrons is typically about 2 GeV while the masses of the beauty hadrons are typically in the range 5 – 6 GeV.

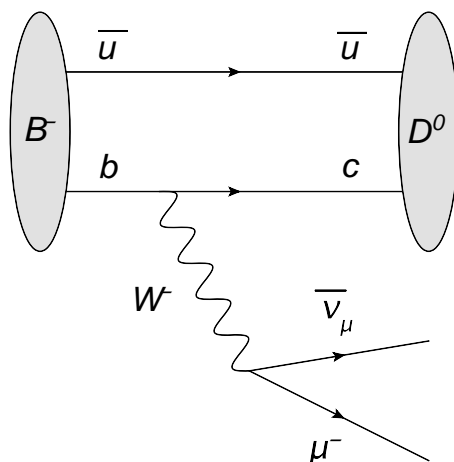
Charmed and beauty ground states are rather long lived due to the high mass of the W^\pm bosons mediating the weak decays of heavy quarks. The somewhat longer lifetime of beauty hadrons compared to charm hadrons is caused by the smaller transition probability for the transition $b \rightarrow c$ compared to the transition $c \rightarrow s$. This is expressed by the sizes of the Cabbibo-Kobayashi-Maskawa (CKM) matrix elements $|V_{cb}| \approx 0.04$ and $|V_{cs}| \approx 1.0$ [66].

Hadron	Quark content	Mass [MeV]	Decay length $c\tau$ [μm]	$I(J^P)$
B^+	$u\bar{b}$	5279.17 ± 0.29	491.1	$\frac{1}{2}(0^-)$
B^0	$d\bar{b}$	5279.50 ± 0.30	457.2	$\frac{1}{2}(0^-)$
B_s^0	$s\bar{b}$	5366.3 ± 0.6	411	$0(0^-)$
Λ_b^0	udb	5620.2 ± 1.6	417	$0(\frac{1}{2}^+)$
D^+	$c\bar{d}$	1869.60 ± 0.16	311.8	$\frac{1}{2}(0^-)$
D^0	$c\bar{u}$	1864.83 ± 0.14	122.9	$\frac{1}{2}(0^-)$
D_s^+	$c\bar{s}$	1968.47 ± 0.33	149.9	$0(0^-)$
Λ_c^+	udc	2286.46 ± 0.14	59.9	$0(\frac{1}{2}^+)$
D^{*+}	$c\bar{d}$	2010.25 ± 0.14		$\frac{1}{2}(1^-)$

Table 2.1.: Properties of charmed and beauty hadrons [66].

2.9. Decays of charmed and beauty hadrons

The charmed and beauty mesons and baryons produced in the hadronisation process decay weakly into lighter hadrons. These decays can be understood in the *spectator model*. In this picture, the heavy b or c quarks decay independently of the other valence quarks.

Figure 2.15.: Quark level diagram for the decay $B^- \rightarrow D^0 \mu^- \bar{\nu}_\mu$.

As an example, Fig.2.15 shows the decay $B^- \rightarrow D^0 \mu^- \bar{\nu}_\mu$ in the spectator model. In this case, the virtual W^- boson decays leptonically. About 11% of all beauty hadrons decay into $l^- \mu_l + X$ for each lepton flavour, where l is a lepton (e^- , μ^- or τ^-) and ν_l the neutrino from the same family [66]. All other beauty hadron decays are fully hadronic, i.e. no leptons are produced in these decays.

The spectator model gives a better description of beauty hadron decays than of charmed hadron decays since the large b quark mass suppresses higher-order QCD effects. Fig. 2.16 shows the hadronic decay $D^0 \rightarrow K^- \pi^+$ where the virtual W^+ boson decay into a quark

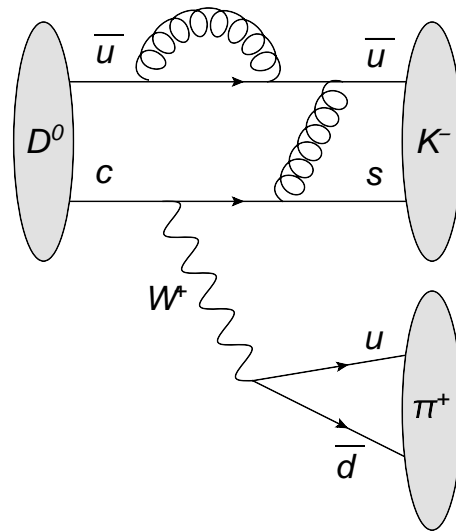


Figure 2.16.: Quark level diagram for the decay $D^0 \rightarrow K^- \pi^+$.

and an antiquark. Examples for QCD corrections are also illustrated in the figure. The branching ratios for the individual decay channels of charmed and beauty hadrons were extensively studied at different experiments [66]. Most measurements were performed using e^+e^- interactions. All available information can be combined. This allows to simulate inclusive charm and beauty production where the probabilities for the different decays are chosen according to the measurements. Event generators usually contain a list of known decays for this purpose.

3. Heavy flavour production at HERA

The production of charmed and beauty hadrons in ep collisions has been intensively studied by the H1 and ZEUS collaborations over the last 15 years. In this chapter a brief overview of previous measurements is given. Due to the large number of results, the discussion is restricted to measurements of *open* charm and beauty production, i.e. the measured hadrons contain only one heavy quark. The focus of this chapter is on heavy quark production in DIS. Results in photoproduction are only mentioned if they are relevant for the measurements presented in this thesis.

3.1. Charm production at HERA

The production of charm quarks in NC DIS was first observed in fixed-target muon-nucleon interactions [67] using semileptonic decays into muons. At HERA, charm production in DIS has been studied using various techniques. The measurements can be classified by the decay products of the considered charmed hadrons. In most studies, appropriate hadronic decays of charmed hadrons were fully reconstructed. Additionally, charm quarks were identified using semileptonic decays into muons and inclusively based on lifetime information. Results based on these different approaches are presented in the following subsections.

3.1.1. Hadronic decay channels

The production of charm via the identification of D and D^* mesons has been extensively studied in the kinematic range $1 < Q^2 < 1000 \text{ GeV}^2$ and $p_T(D, D^*) > 1.5 \text{ GeV}$. The most precise results were obtained using D^{*+} mesons in the so-called *golden* decay mode¹:

$$D^{*+}(2010) \rightarrow D^0 \pi_s^+ \text{ with } D^0 \rightarrow K^- \pi^+. \quad (3.1)$$

The *slow pion*, π_s^+ , has a very low momentum in the centre-of-mass system of the D^{*+} since the mass of the D^{*+} is only slightly greater than the masses of the D^0 and the π_s^+ combined. The accuracy of the mass difference:

$$\Delta M = M(D^{*+}) - M(D^0), \quad (3.2)$$

is proportional to the π_s^+ energy. Hence the mass difference can be measured more precisely than the masses of the D^{*+} or the D^0 mesons (see Fig. 3.1). This method to measure D^{*+} production was proposed in [69] and first applied in [70]. A disadvantage of

¹Charge conjugation is always implied in this thesis.

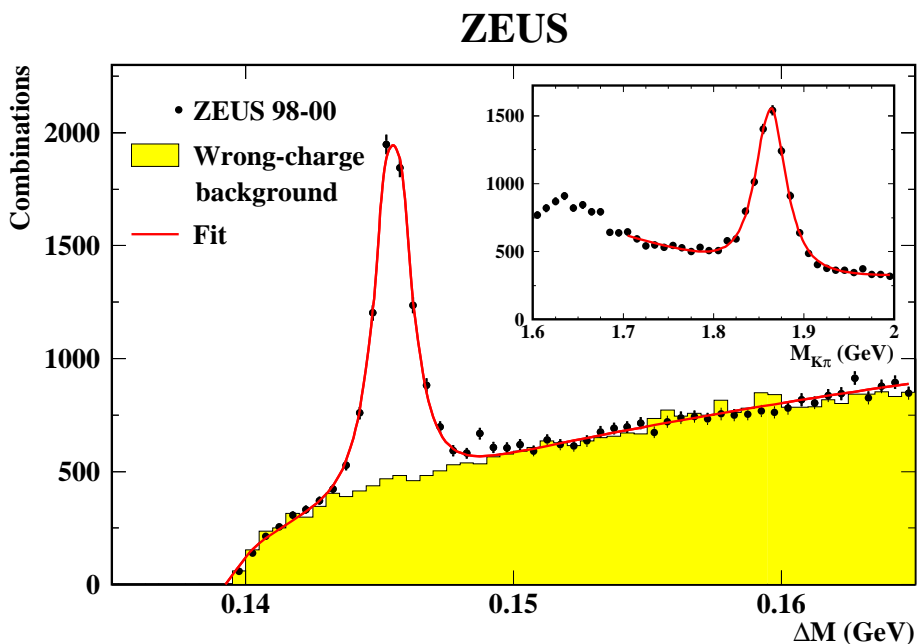


Figure 3.1.: ΔM distribution as measured by the ZEUS collaboration using data taken between 1998 and 2000. The small histogram shows the corresponding D^0 peak.

the mass difference method is that the kinematic region is limited to $p_T(D^{*+}) \gtrsim 1.5$ GeV at the HERA experiments because otherwise the transverse momentum of the slow pion is too small for it to be reconstructed. Hence the extraction of $F_2^{c\bar{c}}$ from visible D^{*+} cross sections always requires an extrapolation to the full transverse momentum range using some theory prediction.

As an example, Fig. 3.2 shows differential cross sections for D^{*+} production in the range $1.5 < Q^2 < 1000$ GeV², $0.02 < y < 0.7$, $1.5 < p_T(D^*) < 15$ GeV and $|\eta(D^*)| < 1.5$ as functions of Q^2 , x , $p_T(D^*)$ and $\eta(D^*)$. The data were taken using the ZEUS detector from 1998 till 2000. All measured cross sections are in agreement with the NLO QCD predictions from the HVQDIS.

Furthermore, cross sections for the production of D^+ and D^0 and D_s^+ mesons were measured by the H1 and ZEUS collaborations [71, 72, 73] using the decay channels:

$$D^+ \rightarrow K^- \pi^+ \pi^+, \quad (3.3)$$

$$D^0 \rightarrow K^- \pi^+ \text{ and} \quad (3.4)$$

$$D_s^+ \rightarrow \phi \pi^+ \rightarrow K^+ K^- \pi^+. \quad (3.5)$$

These D meson decays were fully reconstructed. The signals are visible as peaks in the invariant mass spectra obtained from the decay tracks at the masses of the respective mesons. All measurements are described by NLO QCD predictions obtained using the HVQDIS program. In all previous measurements cuts on the transverse momenta of

the reconstructed D mesons were applied due to different reasons. If the D mesons are reconstructed using only the momentum vectors of the decay tracks [72], then the combinatorial background rises steeply towards lower values of $p_T(D)$. Hence a lower cut on $p_T(D)$ needs to be applied since otherwise the signals are hidden by the fluctuations of the large background. The background can be significantly reduced using lifetime information [71, 73]. But also the usage of lifetime information requires that the D mesons have certain minimal transverse momenta to provide measurable decay lengths in the plane perpendicular to the beam axis. The lowest cut so far of $p_T > 1.5$ GeV, which was used in the ZEUS measurement of D^+ and D^0 production based on the data taken in 2005 [71], is similar to the cuts applied in studies of D^{*+} production.

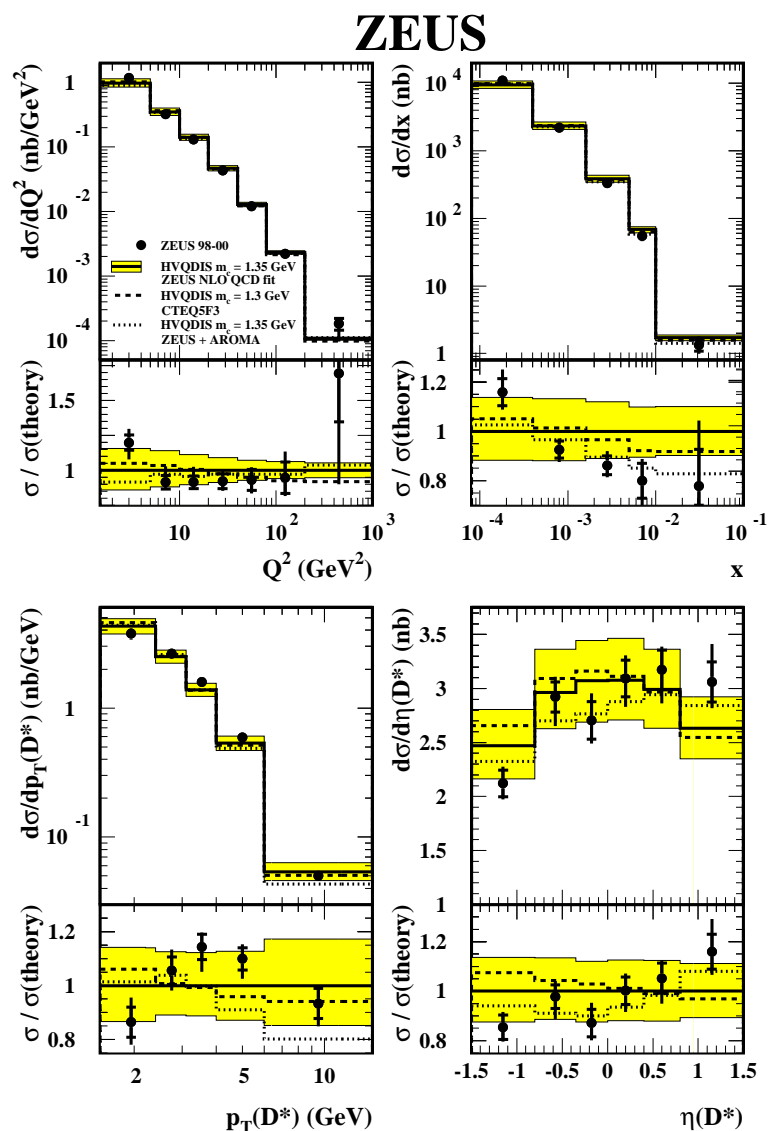


Figure 3.2.: Single differential cross sections for D^{*+} production in DIS as a function of Q^2 , x , $p_T(D^{*+})$ and $\eta(D^{*+})$.

The most precise measurements of charm production in DIS by the H1 and ZEUS collaborations were used to obtain averaged $F_2^{c\bar{c}}$ values in the range $2 < Q^2 < 1000 \text{ GeV}^2$ and $10^{-5} < x < 0.1$ [75]. In Fig. 3.3 the combined $F_2^{c\bar{c}}$ points are compared to various theoretical predictions. Especially at low Q^2 the precision of the data is better than the differences between the predictions.

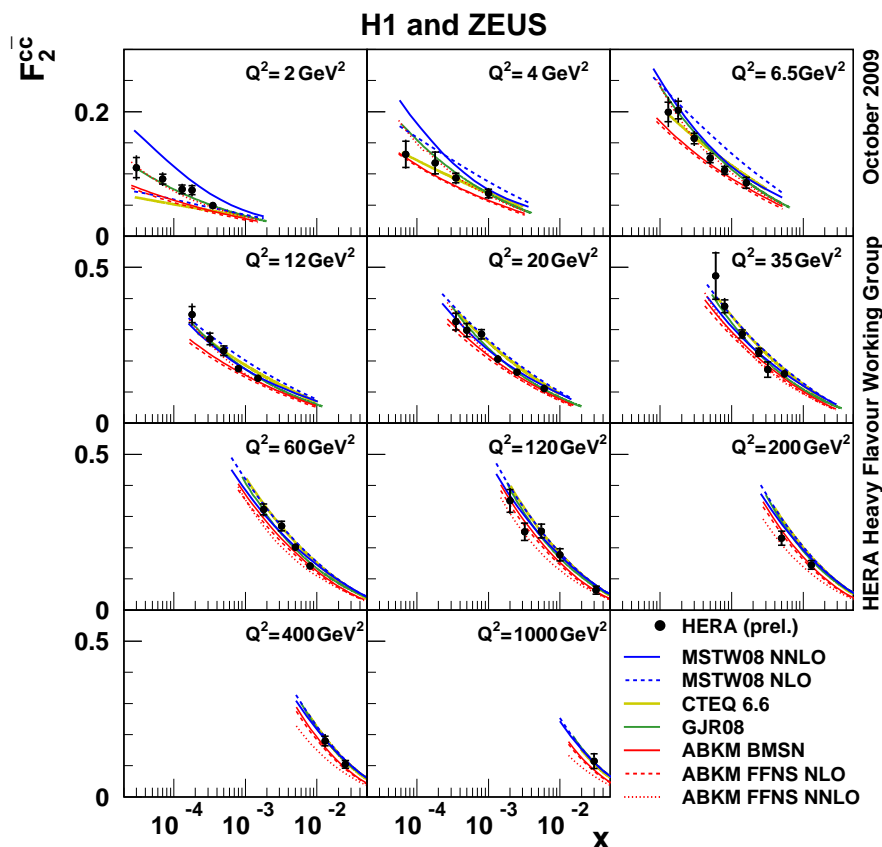


Figure 3.3.: Average $F_2^{c\bar{c}}$ as a function of x for fixed values of Q^2 compared to various theoretical predictions.

3.1.2. Fragmentation parameters from hadronic decays

Fragmentation fractions

The probability that a charm quark fragments into a specific hadron, e.g. a D^+ meson, is not calculable by perturbative QCD. Thus the *fragmentation fractions* have to be derived experimentally. Average values obtained from e^+e^- annihilation data recorded by the CLEO, ARGUS, ALEPH, DELPHI and OPAL experiments are listed in [74].

The charm fragmentation fractions were extracted from visible cross sections measured in photoproduction events with $Q^2 < 1 \text{ GeV}^2$ in the range $130 < W < 300 \text{ GeV}$ by

the ZEUS collaboration. Charmed hadrons were reconstructed in the kinematic region $p_T(D, \Lambda_c^+) > 3.8$ GeV and $|\eta(D, \Lambda_c^+)| < 1.6$ [76]. The cross sections for the pseudoscalar mesons D^+ and D^0 , the vector meson D^* , the charmed strange meson D_s^+ and the Λ_c^+ baryon have been measured. The Λ_c^+ hadrons were reconstructed using the following decay channel:

$$\Lambda_c^+ \rightarrow K^- p \pi^+. \quad (3.6)$$

The fragmentation fractions were calculated under the assumption that every charm quark fragments and/or decays into one of the hadrons mentioned above, or into Ξ_c^+ , Ξ_c^0 or Ω_c^0 particles.

In DIS, the charm fragmentation fractions were measured by both experiments, H1 [73] and ZEUS [72]. The kinematic region in the H1 analysis is defined by $2 < Q^2 < 100$ GeV², $0.05 < y < 0.7$, $p_T(D) > 2.5$ GeV and $|\eta(D)| < 1.5$. For the ZEUS result charm hadrons were selected in the region $1.5 < Q^2 < 1000$ GeV², $0.02 < y < 0.7$, $p_T(D) > 3.0$ GeV and $|\eta(D, \Lambda_c^+)| < 1.6$. In both analyses the Λ_c^+ baryon was not measured directly, but results for charmed baryon production obtained in other processes were used to calculate the fragmentation fractions for D mesons.

All measurements are summarised in Table 3.1. The results for D^+ mesons and Λ_c^+ baryons are relevant for measurements presented in this thesis. Hence the published results from previous measurements are discussed in the following. For the D^+ meson, all above-mentioned measurements obtained in DIS, photoproduction and e^+e^- collisions are in good agreement within the given uncertainties. The ZEUS result for $f(c \rightarrow \Lambda_c^+)$ measured in photoproduction lies around 2 standard deviations above the average from e^+e^- interactions.

Fragmentation function

Additionally, the charm fragmentation function was measured using D^{*+} decays. For this purpose, the cross section for D^{*+} production was measured as a function of z . The free parameters of fragmentation functions (see Sec. 2.6.2) were obtained accordingly from a fit to the measured distribution.

The ZEUS collaboration has measured the fragmentation function in photoproduction events in the range $130 < W < 280$ GeV, $Q^2 < 1$ GeV², $|\eta(D^{*+})| < 1.5$ and $p_T(D^{*+}) > 2$ GeV [79]. The D^{*+} mesons were associated to jets with $|\eta^{\text{jet}}| < 2.4$ and $E_T^{\text{jet}} > 9$ GeV. The Peterson parameter, ϵ , was extracted using the formula $z = (E + p_{\parallel})/2E^{\text{jet}}$, where E is the energy and p_{\parallel} is the longitudinal momentum of the D^{*+} meson relative to the axis of the associated jet of energy E^{jet} . From a comparison of the data with an NLO QCD prediction [80], the following value for the parameter of the Peterson function was obtained:

$$\epsilon = 0.079 \pm 0.008(\text{stat.})_{-0.005}^{+0.010}(\text{syst.}). \quad (3.7)$$

The fragmentation function for D^{*+} mesons was extracted by the H1 collaboration in DIS [81]. The kinematic range of the measurement is given by $2 < Q^2 < 100$ GeV², $0.05 < y < 0.7$, $|\eta(D^{*+})|$ and $1.5 < p_T(D^{*+}) < 15$ GeV. The measurement was performed in two different regions. Similar to the ZEUS measurement, the z variable was calculated

	ZEUS γp			ZEUS DIS			HI DIS	Combined e^+e^- data	
	stat.	syst.	br.	stat.	syst.	br.	total	stat. \oplus	syst. br.
$f(c \rightarrow D^+)$	0.217 ± 0.014	$+0.013+0.014$	$-0.005-0.016$	0.216 ± 0.019	$+0.002+0.008$	$-0.020-0.010$	0.203 ± 0.026	0.226 ± 0.010	$+0.016$ -0.014
$f(c \rightarrow D^0)$	0.523 ± 0.021	$+0.018+0.022$	$-0.017-0.032$	0.605 ± 0.020	$+0.009+0.015$	$-0.052-0.023$	0.560 ± 0.046	0.557 ± 0.023	$+0.014$ -0.013
$f(c \rightarrow D_s^+)$	0.095 ± 0.008	$+0.005+0.026$	$-0.005-0.017$	0.092 ± 0.011	$+0.007+0.012$	$-0.008-0.010$	0.151 ± 0.055	0.101 ± 0.009	$+0.034$ -0.020
$f(c \rightarrow \Lambda_c^+)$	0.144 ± 0.022	$+0.013+0.037$	$-0.022-0.025$					0.076 ± 0.007	$+0.027$ -0.016
$f(c \rightarrow D^{*+})$	0.200 ± 0.009	$+0.008+0.008$	$-0.006-0.012$	0.229 ± 0.011	$+0.006+0.007$	$-0.021-0.010$	0.263 ± 0.032	0.238 ± 0.007	$+0.003$ -0.003

Table 3.1.: Charm fragmentation fractions as measured by different experiments. The ZEUS measurement in DIS took the values for all branching ratios from [77], the rest of the listed measurements took them from [78].

using the jet containing the D^{*+} meson using $z_{\text{jet}} = (E^* + p_L^*)^{D^{*+}} / (E^* + p^*)^{\text{jet}}$, where the longitudinal momentum p_L^* of the D^{*+} meson is defined with respect to the direction of the three-momentum of the jet with $E_T^* > 3$ GeV. The jet reconstruction and the calculation of z_{jet} were performed in the γ^*p rest-frame. For the NLO QCD prediction from HVQDIS the following result was obtained:

$$\epsilon = 0.034 \pm 0.004. \quad (3.8)$$

To perform a measurement close to the charm production threshold, the events were divided into two hemispheres, one approximately containing the fragmentation products of the charm quark and the other approximately containing those of the anti-charm quark. In this case the quantity z was defined as $z = (E^* + p_L^*)^{D^{*+}} / \sum_{hem} (E^* + p^*)$, where in the denominator the energy E^* and the momentum p^* of all particles falling in the D^{*+} meson hemisphere are added up. The longitudinal momentum p_L^* of the D^{*+} meson was calculated with respect to the vectorial sum of the three-momenta of all particles in the hemisphere where the D^{*+} was reconstructed. This allowed to extract the fragmentation function even if no jets were reconstructed. Considering only events where no jet was associated to the D^{*+} meson, the following result was obtained:

$$\epsilon = 0.007 \pm 0.001. \quad (3.9)$$

From a comparison of all three discussed measurements of the ϵ parameter, it can be concluded that the fragmentation of D^{*+} mesons is harder for charm quarks produced close to the threshold, i.e. at low values of \hat{s} . This is presumably an effect of the (neglected) perturbative evolution of the fragmentation function combined with a reduction of the available phase space, and should be considered when a value for ϵ is chosen to obtain a prediction for D meson production for a given kinematic range.

3.2. Beauty production at HERA

The measurement of beauty production cross sections reconstructing individual hadronic decay modes is not feasible at HERA since no decay channel with sufficient events is available. Thus the extraction of fragmentation parameters is also not possible. However, beauty quarks can be tagged by their semileptonic decays into muons [82, 83, 84] or electrons [85]. Before the installation of vertex detectors into the H1 and ZEUS experiments, the reconstruction of semileptonic decays provided the only possibility to measure beauty production in ep collisions at HERA.

The beauty production cross sections can be extracted using the distribution of the transverse momentum of the muon with respect to the momentum of the associated jet, p_T^{rel} , which is defined as:

$$p_T^{\text{rel}} = \frac{|\vec{p}^\mu \times \vec{p}^{\text{jet}}|}{|\vec{p}^{\text{jet}}|}, \quad (3.10)$$

where \vec{p}^μ is the muon and \vec{p}^{jet} the jet momentum vector. The measured distributions of p_T^{rel} from the ZEUS collaboration are shown in Fig. 3.4. The distribution from beauty

decays tends to larger values of p_T^{rel} than the expectations for charm or light quark decays due to the large mass of the B hadrons. The beauty content in a given dataset can be extracted on a statistical basis by fitting the MC templates for beauty and lighter quarks to the data.

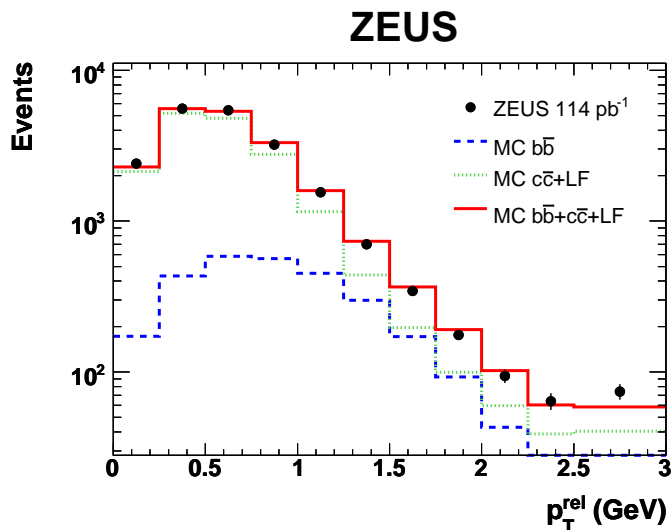


Figure 3.4.: p_T^{rel} distribution measured by the ZEUS collaboration using the data collected from 1996 till 2000.

As an example, Fig. 3.5 shows the beauty cross section as a function of Q^2 for events with at least one jet and one muon in the range $Q^2 > 2 \text{ GeV}^2$ and $0.05 < y < 0.7$. The data are reasonably described by the NLO QCD prediction obtained using the HVQDIS program. However, at low Q^2 the data are about 2 standard deviations higher than the HVQDIS prediction. In other analyses, the visible cross sections are described similarly well by NLO QCD.

3.3. Measurements of heavy flavour production based on lifetime information

Charmed and beauty hadrons exhibit lifetimes large enough to observe signatures of their decays using the H1 and ZEUS silicon vertex detectors. The H1 collaboration has measured the charm and beauty content in an inclusive DIS data sample [86] in the range $5 < Q^2 < 2000 \text{ GeV}^2$ and $0.0002 < x < 0.05$. In this analysis no visible cross sections were measured, but the structure functions $F_2^{c\bar{c}}$ and $F_2^{b\bar{b}}$ were extracted directly.

Lifetime information was used to extend the sensitivity of other properties of semileptonic muon decays like p_T^{rel} or the missing momentum parallel to the muon direction by the ZEUS collaboration [87]. Visible cross sections were extracted in the kinematic range $Q^2 > 20 \text{ GeV}^2$, $0.01 < y < 0.7$, $p_T^\mu > 1.5 \text{ GeV}$ and $-1.6 < \eta^\mu < 2.3$. The structure functions $F_2^{c\bar{c}}$ and $F_2^{b\bar{b}}$ were obtained from double differential cross sections in Q^2 and x .

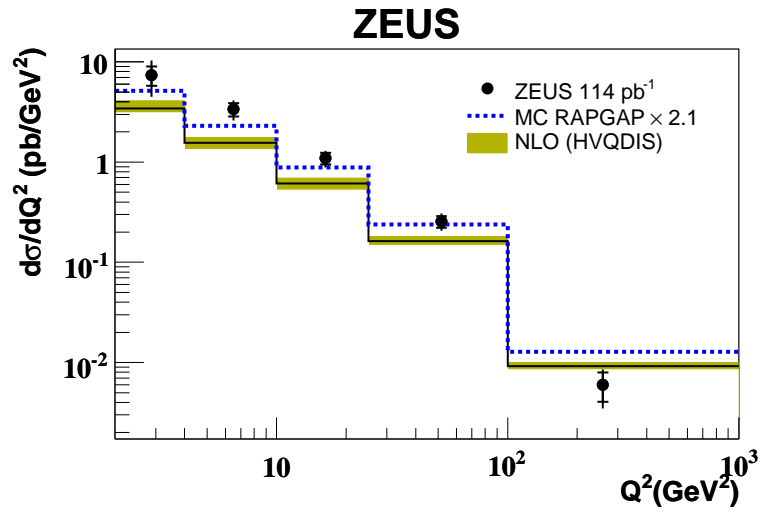


Figure 3.5.: Differential beauty cross section as a function of Q^2 for events with at least one jet and one muon. The measurement is compared to the RAPGAP PS+LO MC normalised to the data and to the NLO QCD prediction from the HVQDIS program.

All measurements of $F_2^{b\bar{b}}$ mentioned in this chapter are summarised in Fig. 3.6. The data are compared to different predictions from perturbative QCD. All predictions are able to describe the data. The uncertainties of the data are too large to discriminate between different predictions.

The H1 collaboration has also measured visible cross sections for events with charm and beauty jets in the range $Q^2 > 6 \text{ GeV}^2$ and $0.07 < y < 0.625$ [88]. Jets of transverse energy $E_T^{\text{jet}} > 6 \text{ GeV}$ and $-1.0 < \eta^{\text{jet}} < 1.5$ in the laboratory frame were considered in this study. Cross sections were also extracted in the Breit frame. The measurements are described by NLO QCD.

ZEUS

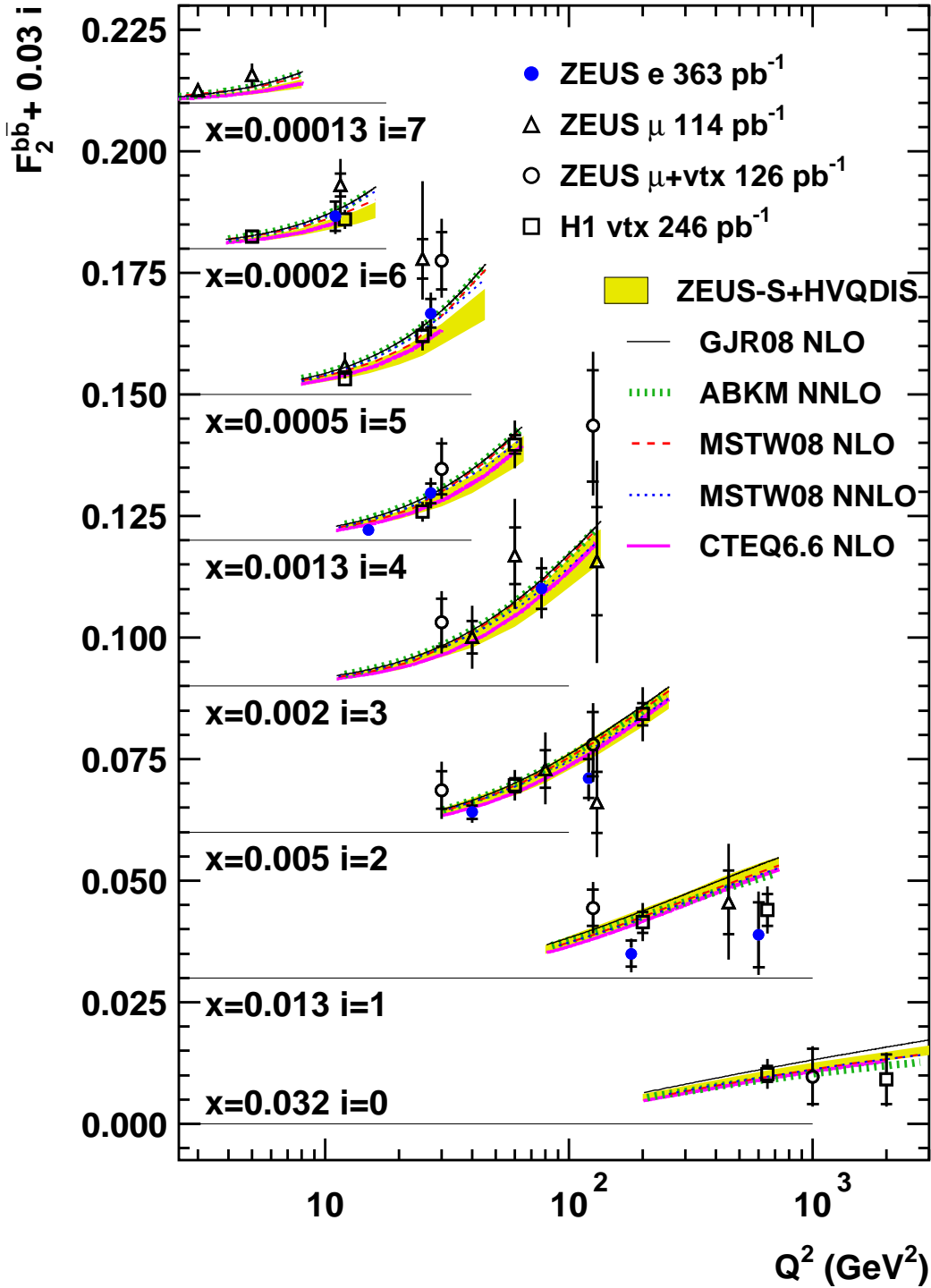


Figure 3.6.: Previous measurements of F_2^{bb} as a function of Q^2 . Different results [84, 85, 86, 87] are compared to QCD predictions.

4. Experimental set-up

In this chapter the ZEUS experiment is described. After a short introduction to the DESY research centre, the HERA accelerator is discussed. All components relevant for the studies presented in this thesis are explained in the following sections.

4.1. DESY

The Deutsches Elektronen-Synchrotron (DESY) research centre was founded in 1959 to develop and operate large particle accelerators in Hamburg, Germany. At present, DESY performs research in the areas of particle physics, photon science and accelerator development. To provide synchrotron radiation, DESY operates the electron ring accelerators DORIS III and PETRA III. The latter is the most brilliant storage-ring based source of hard X-rays in the world. FLASH, which is used for photon science since 2005, was the first free electron laser for X-rays operated in the SASE mode. The European X-ray Free Electron Laser (XFEL) will start operation in 2015.

4.2. HERA

The Hadron Elektron Ring Anlage (HERA) [89], operated at DESY between 1992 and 2007, was the only electron-proton collider in the world. HERA therefore represents a unique facility to study QCD and hadron structure. Electrons and protons circulated in two different rings mounted on top of each other in a 6.3 km long tunnel 15 – 30 m below ground (see Fig 4.1).

Electrons at an energy of 27.5 GeV were brought into collision with protons at 920 GeV (820 GeV before 1998), resulting in a centre-of-mass energy of $\sqrt{s} = 318$ GeV (300 GeV before 1998). Electron-proton collisions were recorded by the ZEUS experiment located in the south hall and by the H1 experiment in the north hall. Additionally, two fixed-target experiments made use of only one of the HERA beams. From 1995, the HERMES collaboration collided a polarised electron beam with a polarised or unpolarised gas jet target to study the spin structure of the nucleon. The HERA-B experiment running from 1999 till 2003 used an aluminium wire target located in the halo of the proton beam. The experiment was originally optimised to study CP violation in the $B^0\bar{B}^0$ system.

Before the injection into the HERA accelerator, electrons and protons pass through a system of several pre-accelerators. Protons were produced by shooting H^- ions from the LINAC III accelerator through a thin foil to remove the electrons. The obtained protons were first accelerated to an energy of 7.5 GeV in the DESY III synchrotron and then injected into PETRA II where their energy was increased to 40 GeV. Finally, the protons

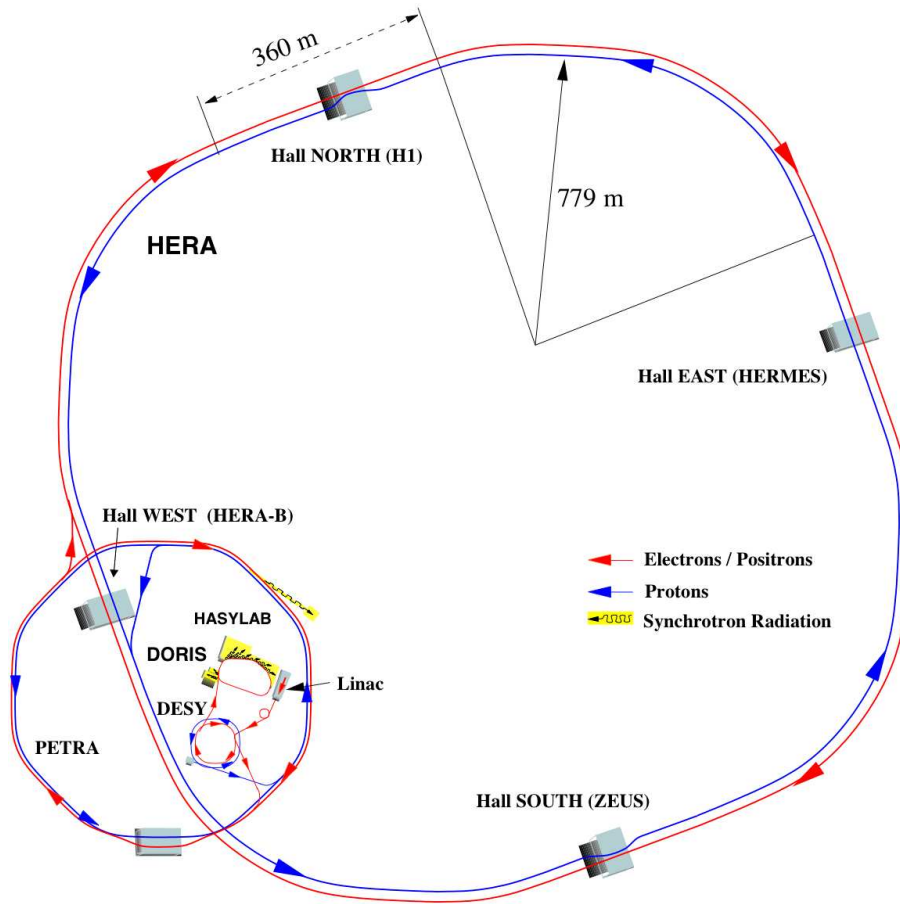


Figure 4.1.: Schematic diagram of the HERA collider and its pre-accelerators. The straight sections are 360 m long and the circular sections have a radius of 779 m. Experiments were located in underground halls at each straight section. The chain of pre-accelerators is shown at the lower left corner.

were transferred into the HERA proton ring. On the other hand, electrons or positrons were accelerated to an energy of 450 MeV in the LINAC II. Similar to the protons, the electrons or positrons were accelerated further in the DESY II and PETRA II rings until they were injected into HERA at an energy of 12 GeV.

For the lower momentum electrons, normal conducting dipole magnets with a field strength of 0.16 T were used to force the particles on orbit. For the higher momentum protons, superconducting magnets operating at a temperature of 4.4 K providing a field of 4.68 T were used. Electrons were collided in the years 1998 and 1999 as well as in 2005, while positrons were used in all remaining periods.

Electrons and protons were grouped in so-called *bunches* which were collided in the experiments. At HERA, the time difference between two bunches was 96 ns corresponding to a distance between two neighbouring bunches of about 30 m. Up to 210 bunches were stored simultaneously in the HERA collider. Unpaired and empty bunches were used to monitor beam related backgrounds.

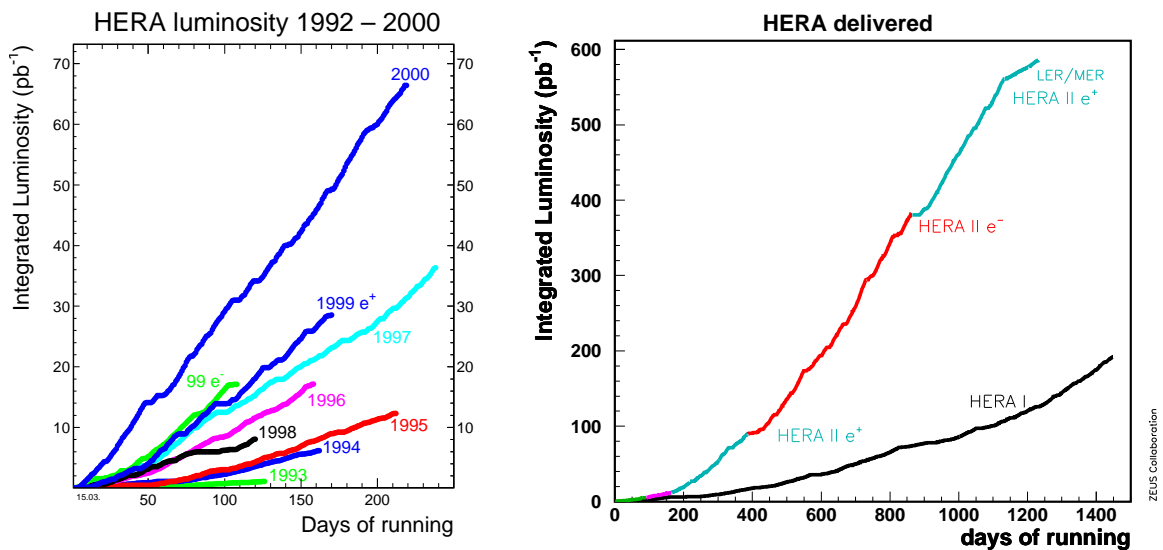


Figure 4.2.: The luminosity delivered by the HERA from 1992-2000 (HERA I, left) and from 2002-2007 (HERA II, right). In the right figure the luminosity collected before the upgrade is shown for comparison.

In 2000/2001, the HERA collider and the H1 and ZEUS experiments were upgraded to increase the specific luminosity by a factor five [90]. Additionally, new components were installed in the detectors to enable higher precision measurements. In addition, the electrons were longitudinally polarised in both collider experiments after the upgrade. The electron beam at HERA was naturally polarised transversely due to the Sokolov-Teller effect [91]. After the upgrade, spin rotators [92] were placed at each side of the H1 and ZEUS experiments to rotate the transverse polarisation of the electron beam into longitudinal polarisation and back to ensure the preservation of the polarisation in the ring. Two independent devices were used to measure the polarisation, the TPOL [93] and the LPOL [94]. In both cases the polarisation was measured using the spin dependence of Compton scattering of circularly polarised photons off electrons.

After HERA was proposed in 1981, the accelerator was built between 1984 and 1990. Physics operation started in 1992. First, protons were accelerated to an energy of 820 GeV and positrons to 27.5 GeV. The proton beam energy was increased to 920 GeV and the lepton beam was switched to electrons in 1998. From 1999 till 2000 positrons were accelerated again. The data taken before the upgrade is referred to as HERA I data in the following. The running period after the upgrade is called HERA II. Severe problems due to high backgrounds in the ZEUS detector were solved in 2002/2003 [95]. These backgrounds were mostly caused by doubly scattered synchrotron radiation, by electron beam-gas scattering and by proton beam-gas scattering. In October 2003 physics data taking started again. During the last three months of HERA operation, data were collected at the reduced proton beam energies of 460 and 575 GeV to measure the longitudinal structure function F_L directly [96]. An overview of the data taking periods relevant to the analyses presented in this thesis is given in Tab. 4.1. The luminosities delivered by HERA for the

Period	Lepton beam	Proton energy (GeV)	\sqrt{s} (GeV)	Integrated Luminosity	Average polarisation
HERA I					
1996-1997	e^+	820	300	38.6 pb ⁻¹	0
1998-1999	e^-	920	318	16.7 pb ⁻¹	0
1999-2000	e^+	920	318	65.1 pb ⁻¹	0
HERA II					
2003-2004	e^+	920	318	40.6 pb ⁻¹	+0.03
2004-2005	e^-	920	318	133.7 pb ⁻¹	-0.07
2006	e^-	920	318	52.7 pb ⁻¹	+0.09
2006-2007	e^+	920	318	137.3 pb ⁻¹	+0.04

Table 4.1.: Data taking periods of HERA from 1996 till 2007.

different periods as a function of the number of days of running are shown in Fig. 4.2.

4.3. The ZEUS detector

In this section the ZEUS detector [97] is described. Starting from a general overview, the tracking systems, the uranium calorimeter, the luminosity monitors and the trigger system are explained in more detail.

4.3.1. Overview

As a hermetic general purpose detector, ZEUS was designed to study various aspects of electron-proton scattering. Because of the higher energy of the protons compared to the electrons, the centre-of-mass system was boosted relative to the laboratory system. To take this boost into account, the detector had an asymmetry in the forward-backward¹ direction. This can be seen in Fig. 4.3. The main part of the detector had a weight of 3600 tons and a size of 12 m × 10 m × 19 m.

The right-handed ZEUS coordinate system has its origin at the interaction point. The X axis is pointing to the centre of the HERA collider while the direction of the Z axis is given by the proton beam. The polar angle θ is measured relative to the Z axis and the azimuth angle φ is measured relative to the X axis. It is common to use the *pseudorapidity* η instead of θ given by:

$$\eta = -\ln \tan \frac{\theta}{2}. \quad (4.1)$$

Since the ZEUS detector was installed in 1992, several new detector components have been added and others were removed. In the following, the different components of the

¹The *forward* direction is given by the direction of the proton beam, the *backward* direction is given by the electron beam.

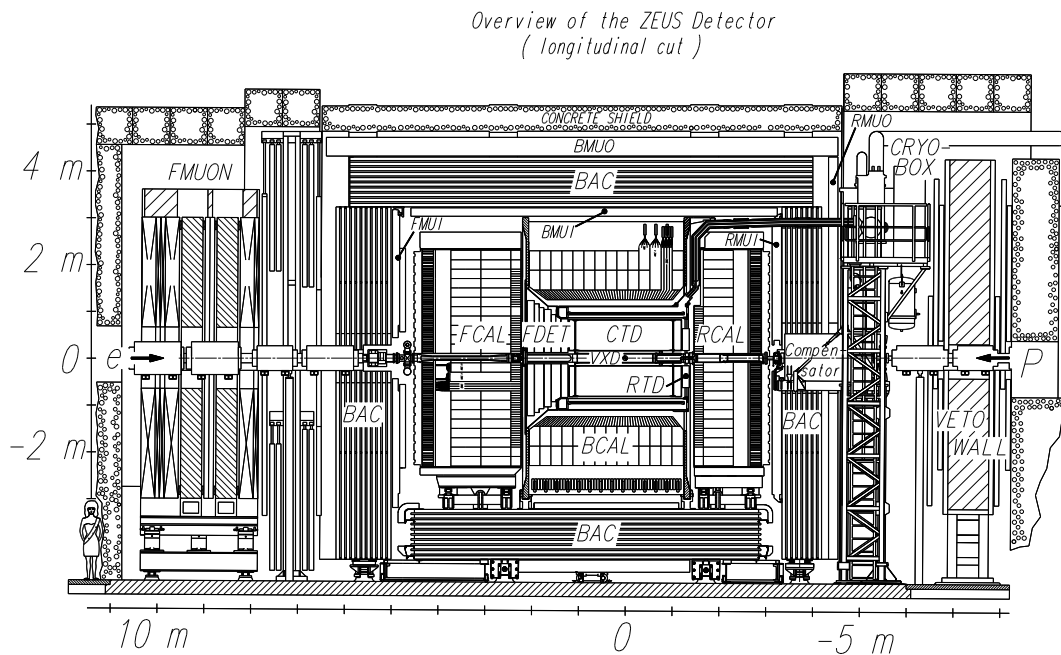


Figure 4.3.: Cross section of the ZEUS detector along the beam pipe.

detector are described starting from the innermost parts close to the beam pipe.

Figure 4.4 shows an overview of the ZEUS detector. At the centre of ZEUS, a vertex detector (VXD) was situated till the shutdown 1995/1996. It was removed because a continuous operation was not possible due to high beam backgrounds. A silicon microvertex detector (MVD) was installed at the same position during the HERA upgrade in 2001. Charged tracks were measured using a cylindrical drift chamber, the central tracking detector (CTD). The tracking detectors were surrounded by a superconducting solenoid that provided a magnetic field of 1.43 T parallel to the beam pipe. The magnetic field was used to determine the momentum and charge of charged particles. In the forward region three sets of planar drift chambers (FTD) with interleaved transition radiation detectors (TRD) were operated as additional tracking detectors (FDET in Fig. 4.3). One planar drift chamber consisting of three layers (RTD) was positioned in the rear direction. In 2001 the forward TRD was replaced by a new detector called straw tube tracker (STT). The tracking detectors and the magnet were surrounded by a high-resolution compensating uranium-scintillator calorimeter (CAL) used as the main device for energy measurements. The CAL was divided into forward (FCAL), barrel (BCAL) and rear (RCAL) parts. To determine the position of the scattered electron near the beam pipe with a better resolution than possible using the RCAL, the small angle rear tracking detector (SRTD) [98] was used. The SRTD consisted of two layers of scintillator strips, one mounted in the vertical and the other mounted in the horizontal direction. To avoid the high magnetic field near the beam pipe, the photomultipliers were located 2.5 m away from the scintillators. The SRTD covered the angular range $162^\circ < \theta < 176^\circ$.

The CAL was enclosed by an iron yoke to provide the return path for the magnetic

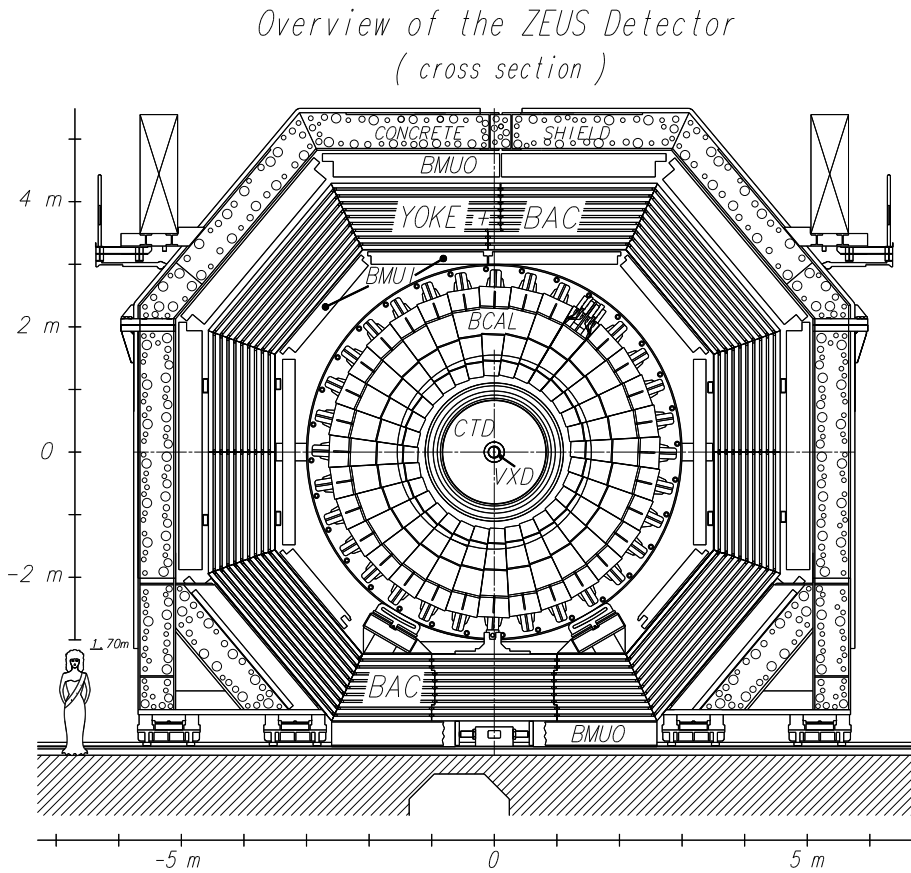


Figure 4.4.: Cross section of the ZEUS detector perpendicular to the beam pipe.

field. It was instrumented with proportional chambers to measure the energy of particles penetrating through the CAL and is therefore referred to as backing calorimeter (BAC). The BAC was also used to detect muons. Further dedicated muon identification chambers were mounted on the inner (FMUI, BMUI and RMUI) and outer (FMUON, BMUO and RMUO) surfaces of the BAC.

To reject beam related backgrounds, the VETO wall was located at $Z = -7.3$ m. It was composed of iron and scintillators. The luminosity was monitored by dedicated luminosity detectors using the well known bremsstrahlung process ($ep \rightarrow ep\gamma$).

The HERA beams were monitored using the C5 counter. It consisted of 2×2 scintillator layers interleaved with layers of tungsten positioned 1.2 m away from the interaction point in the electron flight direction.

4.3.2. The tracking system

The micro vertex detector MVD

The MVD was a silicon-strip vertex detector [99] to improve the spatial and momentum resolutions of the tracking system. Its main purpose was to identify heavy quark decays

from track impact parameters or secondary vertices. A major constraint for the design of the MVD was that the available space was limited by the inner bore of the CTD with a diameter of 32.4 cm.

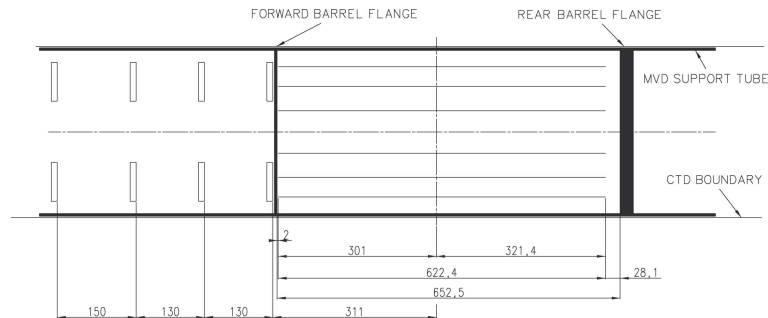


Figure 4.5.: Layout of the MVD. The barrel region is visible on the right while the wheels in the forward direction are shown on the left. The proton beam goes from right to left. All distances are given in mm.

The MVD consisted of two regions, the barrel (BMVD) and the forward (FMVD) section (see Fig. 4.5). The barrel section, centred at the nominal interaction point, was 63 cm long and consisted of three layers (*cylinder* 0, 1 and 2) of silicon-strip detectors mounted on so-called *ladders* parallel to the beam axis. For tracks with three hits, polar angles in the range $30^\circ < \theta < 150^\circ$ were covered. The arrangement of the ladders is illustrated in Fig. 4.6. Due to limited space, about 25% of the azimuthal angle is covered by only two sensors. In the forward section, the sensors were arranged in four vertical planes to extend the angular coverage down to 7° . Cables and cooling were connected from the backward direction.

The MVD sensors [100] consisted of $300 \mu\text{m}$ thick n-type Silicon. The $14 \mu\text{m}$ thick p^+ readout strips were arranged with a pitch of $120 \mu\text{m}$. Between two neighbouring readout strips five p^+ interstrips with a width of $12 \mu\text{m}$ were located. Due to *capacitive charge sharing* a good resolution of less than $20 \mu\text{m}$ was achieved [101] despite the large distance between the readout strips. The structure of an MVD sensor is shown in Fig. 4.7.

In the barrel section, two strip sensors of $64.2 \times 64.2 \text{ mm}$ formed a so-called *half module*. Each sensor had 512 readout channels. The sensors were connected by a Kapton foil with etched copper strips to the frontend readout which was based on the HELIX 128-v3.2 chip [102]. Pairs of adjacent channels from two sensor strips perpendicular to each other were read out using one single channel. Hence 512 channels were read for every half module. Two combinations of X and Y positions were possible for every hit. This ambiguity is resolved by the track reconstruction algorithm.

In the barrel section of the MVD, 300 half modules formed the 30 ladders. The wheels in the forward section were constructed from 112 half modules mounted in two back-to-back layers on four carbon fiber wheels. In total, the MVD had about 210000 readout channels.

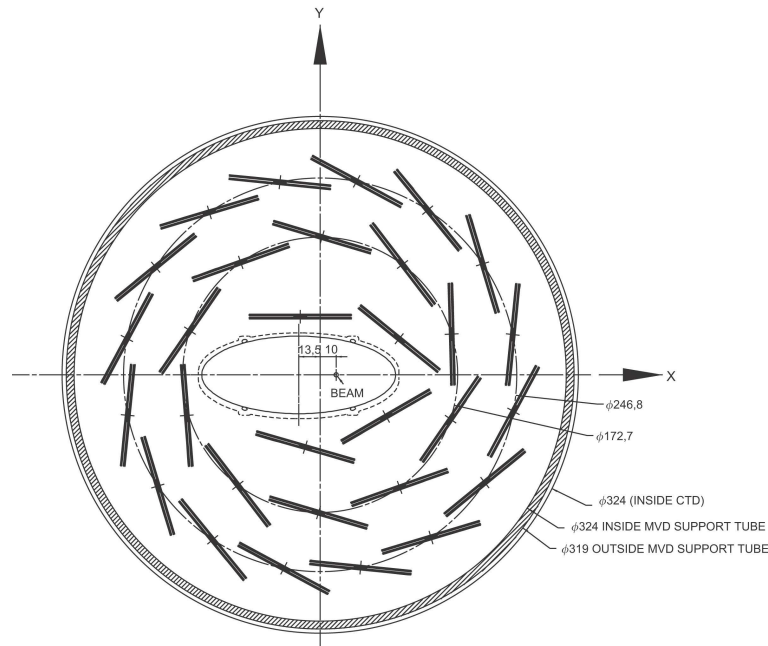


Figure 4.6.: Cross section of the barrel MVD perpendicular to the beam pipe.

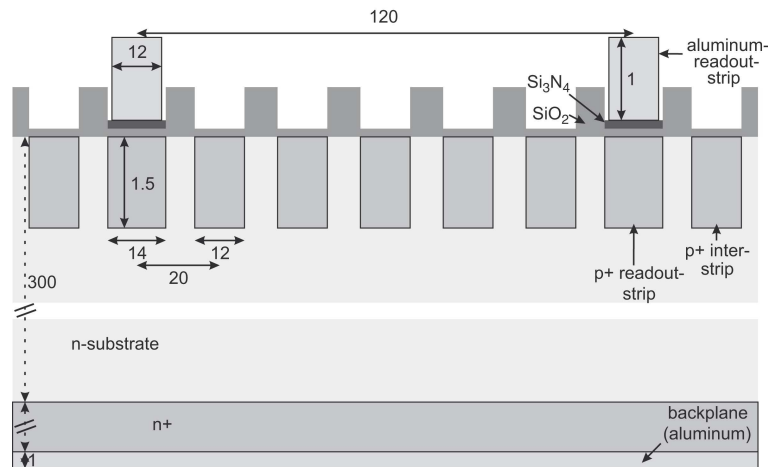


Figure 4.7.: Cross section of an MVD sensor. All distances are given in μm .

The central tracking detector CTD

The main component of the ZEUS detector used for the reconstruction of charged-particle tracks was the CTD [103], a cylindrical drift chamber measuring the direction, momentum and energy loss dE/dx . The latter is needed for particle identification. The fiducial volume of the CTD had a length of 203 cm, an inner radius of 18.2 cm and an outer radius of

79.4 cm. This resulted in an angular coverage of $15^\circ < \theta < 164^\circ$. The CTD was filled with a gas mixture of argon, carbon dioxide and ethane.

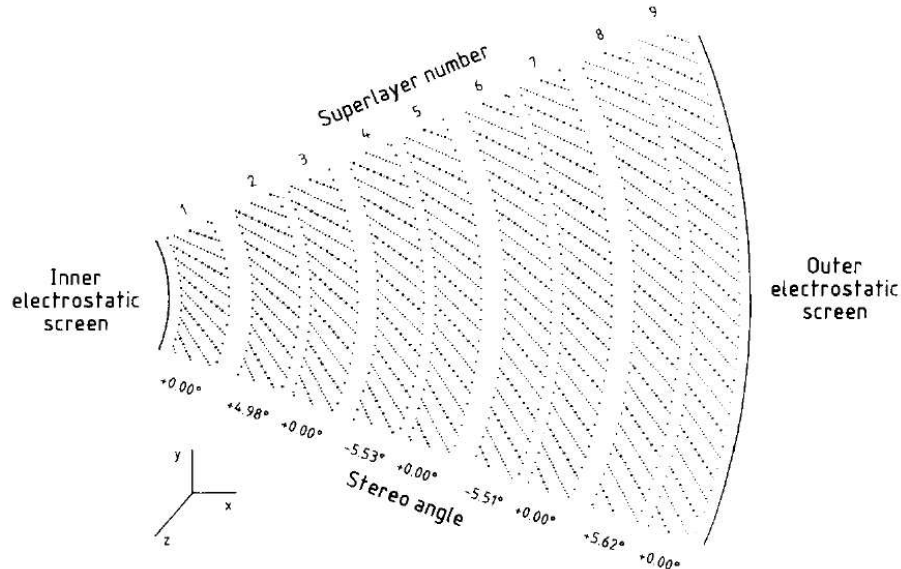


Figure 4.8.: Cross section of a CTD octant perpendicular to the beam pipe. Larger dots indicate sense wires.

When charged particles travelled through the CTD, they ionised the gas along their path. The electrons were attracted to the positively charged sense wires and the positive ions drifted towards the negative field wires. In the field of the sense wires, the electrons ionised further atoms. Thus the signal was amplified and could be measured by electronic read out systems.

Figure 4.8 shows the XY cross section of a CTD octant. 4608 sense wires were grouped in nine *superlayers*. Each superlayer (SL) consisted of 8 sense wire layers. The wires in odd-numbered superlayers were oriented parallel to the beam axis. To allow an accurate determination of the Z position, the wires in the even-numbered superlayers were inclined by about $\pm 5^\circ$. Furthermore, the Z position was measured using timing information. In total, 16 sense wire layers were instrumented for this purpose, eight in SL1 and four each in SL3 and SL5. Timing yielded a resolution of only about 4.5 cm and was mainly used for the trigger decision since it was already available at the first trigger level. The trigger will be discussed in more detail below.

For the HERA I data taking period, the CTD tracking resolution for full-length tracks can be parameterised as [104]:

$$\frac{\sigma(p_T)}{p_T} = 0.0058 \cdot p_T \oplus 0.0065 \oplus \frac{0.0014}{p_T}, \quad (4.2)$$

with p_T in GeV. This value was derived from Monte Carlo events which have passed through the simulation of the ZEUS detector for the 1996 configuration. The first term

reflects the position resolution, whereas the second and third terms give the contributions from multiple scattering before and inside the CTD, respectively.

For the combined system of MVD and CTD used during the HERA II period, the following momentum resolution for full-length tracks was found [105]:

$$\frac{\sigma(p_T)}{p_T} = 0.0029 \cdot p_T \oplus 0.0081 \oplus \frac{0.0012}{p_T}, \quad (4.3)$$

with p_T in GeV. From a comparison of Eqs. 4.2 and 4.3, it can be concluded that the transverse momentum resolution of the combined tracking in HERA II is better than the resolution of the CTD alone. On the other hand, more material between the interaction point and the CTD was added. Hence the probability for multiple scattering had increased after the upgrade.

The straw tube tracker STT

After the upgrade, the tracking capabilities of the ZEUS experiment in the forward direction were improved by the STT [106] which consisted of 48 sectors of two different sizes. The layout of the STT is shown in Fig. 4.9.

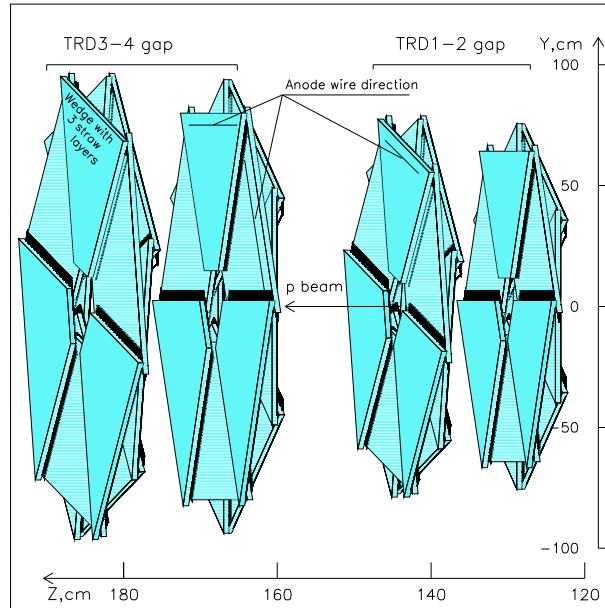


Figure 4.9.: Layout of the STT.

The STT was subdivided into two modules consisting of 24 sectors mounted between the FTDs. The sectors consisted of three layers of straws. Each straw had a diameter of 7.5 mm and acted as an independent drift chamber with an anode wire in the middle. In total, the STT consisted of 10944 straws and covered the polar-angle region $5^\circ < \theta < 23^\circ$.

4.3.3. The uranium calorimeter

The most important device to measure energies was the CAL [107]. As a compensating sampling calorimeter, it consisted of alternating layers of absorbing uranium and active scintillator material. It was designed to be hermetic providing a nearly full solid angle coverage. The absorber consisted of 3.3 mm thick plates of depleted uranium made of 98.1% U^{238} , 1.7% Nb and 0.2% U^{235} covered in stainless steel foils. Plastic scintillator plates (SCSN38) with a thickness of 2.6 mm were positioned between the absorber plates to measure the energy of particles.

In general, the ratio of the measured energy compared to the energy of the incoming particle is higher for electromagnetic showers compared to hadronic showers because some energy is lost due to nuclear processes, which do not result in a measurable signal, and due to muons, neutrinos and slow neutrons. The fraction of lost energy is smaller for electrons. Since hadronic showers always contain a certain electromagnetic component, it is difficult to correct for these effects after the measurement.

Uranium as an absorber provides a high yield of spallation neutrons. These neutrons can be detected using plastic scintillators in which they create recoil protons upon scattering on hydrogen nuclei. Photons from neutron capture additionally help to compensate the signal loss for hadronic showers. By tuning the uranium to scintillator ratio, equal pulse heights for electrons and hadrons can be achieved. This idea is the basis of *compensating* calorimeters like the ZEUS CAL.

The energy resolutions of the CAL for electrons and hadrons were measured under test-beam conditions:

$$\frac{\sigma_{\text{elec}}(E)}{E} = \frac{18\%}{\sqrt{E}} \quad \text{and} \quad \frac{\sigma_{\text{had}}(E)}{E} = \frac{35\%}{\sqrt{E}}, \quad (4.4)$$

with E in GeV.

Fig. 4.10 shows an overview of the CAL. It was divided geometrically into three main regions: forward (FCAL), barrel (BCAL) and rear (RCAL) calorimeter. Due to the boost of the particles in the final state to the forward direction, the forward region was thicker than the rear part of the CAL. This resulted in a depth in interaction lengths of about 7λ for the FCAL, 5λ for the BCAL and 4λ for the RCAL. All regions were subdivided into modules. The modules were groups of towers of $20 \text{ cm} \times 20 \text{ cm}$ containing stacks of absorber and scintillator material.

The towers consisted of one electromagnetic (EMC) and one or two hadronic sections. The RCAL contained only a single hadronic section (RHAC) while the BCAL and the FCAL consisted of two hadronic subsections (HAC1 and HAC2). The EMC sections were subdivided further into two or four transverse cells. In the forward and the barrel region there were four such cells. The electromagnetic part of the rear calorimeter contained only two cells. The EMC had a depth of about 26 radiation lengths, X_0 , in the FCAL and in the RCAL and a depth of 22 X_0 in the BCAL. The layout of an FCAL module is shown in Fig. 4.11.

In total, the CAL contained 5918 cells, which were read out on two sides using photomultiplier tubes with wavelength shifters. Hence the ratio of both signals gave an

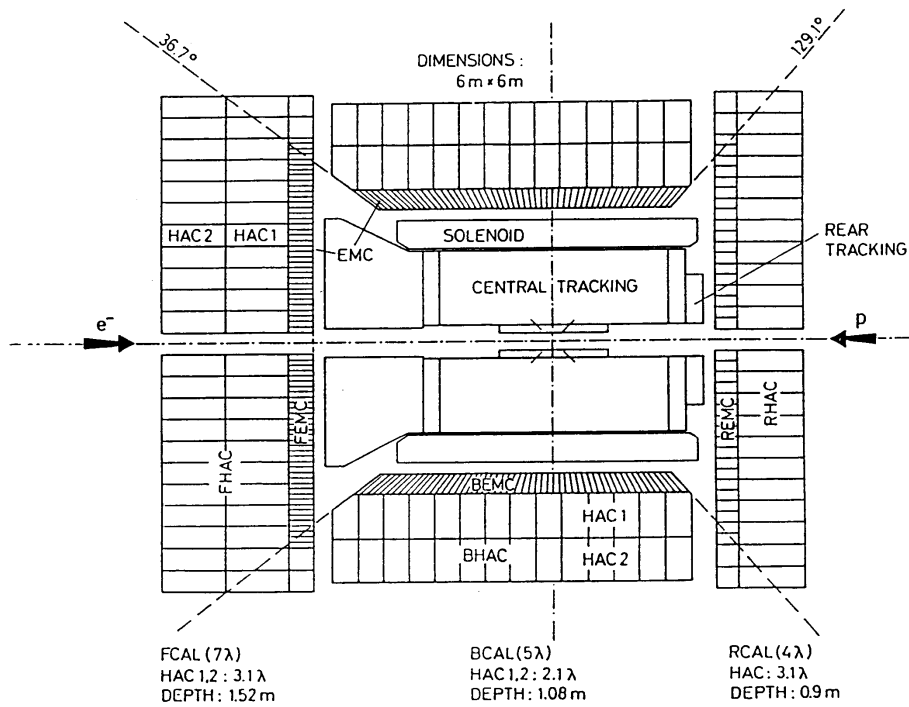


Figure 4.10.: Cross section of the CAL parallel to the beam pipe. The different regions (FCAL, BCAL and RCAL) are shown with their electromagnetic (EMC) and hadronic (HAC) parts.

approximation of the transverse location of the shower in a cell. Because hardware failures rarely occur on both sides at the same time, there were not many completely dead cells in the detector using two photomultiplier tubes.

The excellent timing resolution of the CAL allowed to reject non- ep background events with characteristic timing patterns. The signal originating from the radioactive decay of U^{238} was used to calibrate the CAL on a daily basis. Additionally, the photomultiplier tubes and the readout electronics were calibrated using LED, LASER and test pulses.

4.3.4. The luminosity detectors

The integrated luminosity \mathcal{L} is given by:

$$\mathcal{L} = \frac{N}{\sigma}, \quad (4.5)$$

where N is the number of events observed for a given process with the cross section σ . Hence a precise determination of the luminosity is crucial to measure cross sections in a particle physics experiment. At ZEUS, the luminosity was determined using the well-known Bethe-Heitler process $ep \rightarrow ep\gamma$. This reaction occurs at a high rate and the theoretical cross section can be calculated with good precision in QED. The Bethe-Heitler formula describing the dependence of the cross section on the photon energy E_γ is known

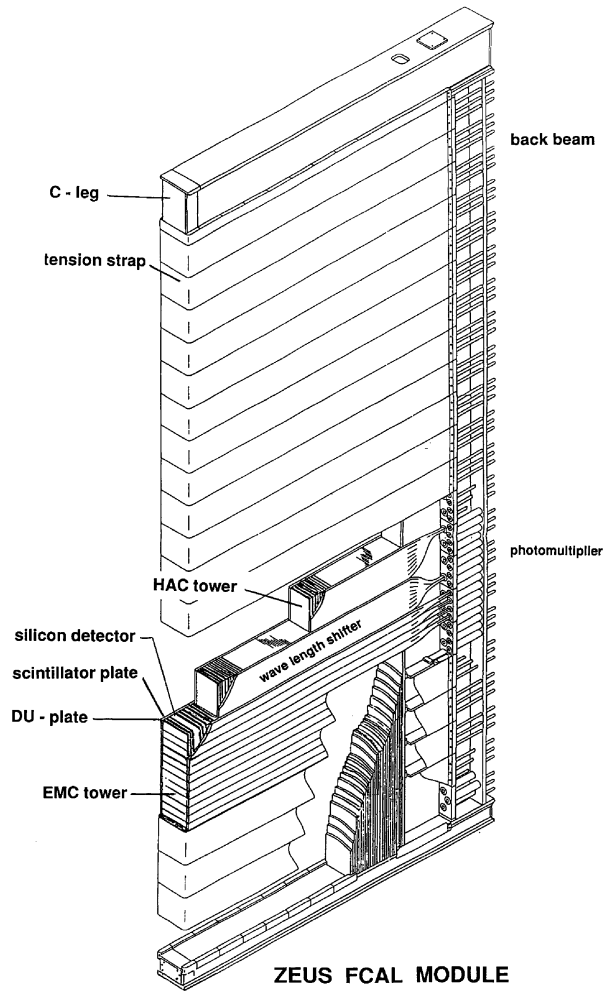


Figure 4.11.: A module of the FCAL.

since 1934 [108]:

$$\frac{d\sigma}{dE_\gamma} = 4\alpha r_e^2 \frac{E'_e}{E_\gamma E_e} \left(\frac{E_e}{E'_e} + \frac{E'_e}{E_e} - \frac{2}{3} \right) \left(\ln \frac{4E_p E_e E'_e}{m_p^2 E_\gamma} - \frac{1}{2} \right), \quad (4.6)$$

where α is the fine structure constant, $r_e = \alpha/m_e$ is the classical electron radius, E_e is the energy of the incoming electron and E'_e the energy of the scattered electron. So far, this formula was used to calculate the luminosity measured by the ZEUS detector. Recently one-loop QED radiative corrections for the Bethe-Heitler process were calculated [109]. The photons were emerging at a very small angle θ_γ with respect to the incident electron direction [110]:

$$\frac{d\sigma}{d\theta_\gamma} \sim \frac{\theta_\gamma}{((m_e/E_e)^2 + \theta_\gamma^2)^2}. \quad (4.7)$$

During the HERA I period, the photons from the Bethe-Heitler process were measured in a

lead–scintillator calorimeter [111] placed outside the ZEUS detector in the direction of the electron beam at $Z = -107$ m. After the upgrade of the ZEUS detector, the luminosity was measured additionally using a spectrometer [112] located at $Z = -104$ m. The bremsstrahlung photons were detected using their conversion $\gamma \rightarrow e^+e^-$ in the material of a beam pipe exit window at $Z = -92$ m. Converted e^+e^- pairs were separated vertically by a dipole magnet at $Z = -95$ m.

4.3.5. The trigger system

The bunch structure of the HERA collider (see Sec. 4.2) led to a beam crossing in the ZEUS detector every 96 ns. This corresponds to a nominal bunch crossing rate of 10.4 MHz. Only a small fraction of these contained interesting ep events. The dominant part of the background was caused by so-called *beam gas interactions*. These are collisions of electrons or protons with nuclei of the residual gas and with the beam pipe. Beam gas events occurred at a typical rate of 10 kHz. An additional background was caused by cosmic muons passing the CTD.

The rate that could be written to tape was about 10 Hz. Thus a significant reduction of the rate was needed. This was achieved by a three level, pipelined trigger system [97, 113]. The complexity of the trigger selection increased from level to level while data throughput was reduced. The different levels of the trigger system are described in the following. Figure 4.12 shows a schematic diagram of the ZEUS trigger and data acquisition chain.

First Level Trigger (FLT)

At the first level, a hardware trigger was used to reduce the event rate to below 1 kHz. Trigger decisions were based on properties like energy sums, thresholds or timing information. Every detector component had its own FLT electronics [114]. The information from the individual components was stored in a pipeline and prepared for the trigger decision within about $2 \mu\text{s}$ after the bunch crossing. The data from the local FLT's were passed to the global first level trigger (GFLT) to perform the trigger decision within a time interval of $4.4 \mu\text{s}$. This decision was returned to the readout systems of the different detector components.

Second Level Trigger (SLT)

Events passing the GFLT were analysed further by the SLT which was a software trigger implemented using a transputer² network to reduce the rate to below 100 Hz. The second level triggers of the individual components provided information on charged-particle tracks, the interaction vertex, calorimeter timing and global energy sums [115]. The outputs of the local subtriggers were passed to the global second level trigger (GSLT), which provided a decision after a few milliseconds. Because the time available for the SLT decision was much longer than for the FLT, more detailed data from the components were available and more sophisticated algorithms were possible.

²Microprocessor design to be used in parallel computing systems from INMOS.

The eventbuilder [116] combined the data from all components into a single record of ADAMO [117] database tables and passed them to the third trigger level. In 2001 an additional tracking trigger, the global tracking trigger (GTT) [118], was installed to supplement the SLT.

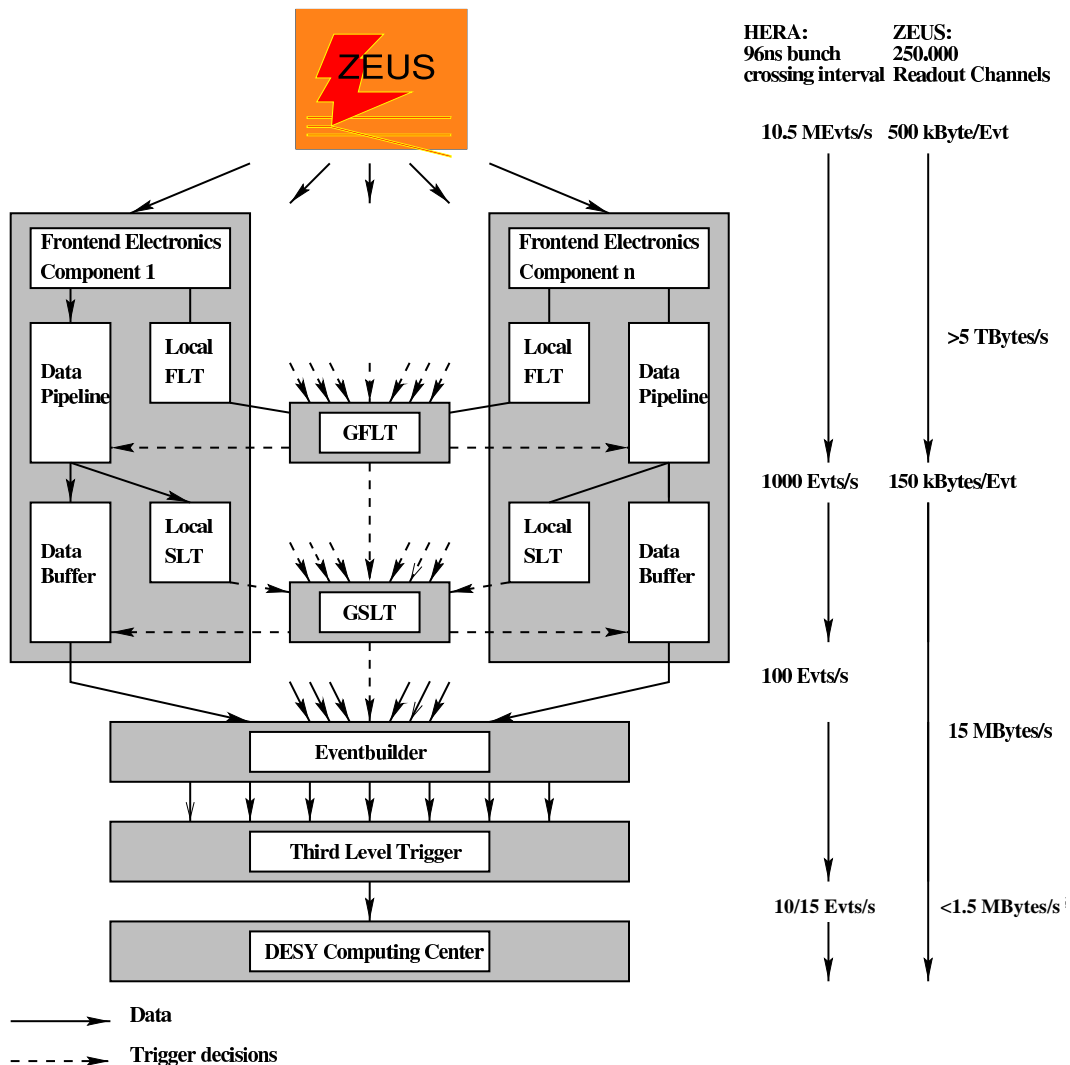


Figure 4.12.: Overview of the data flow through the ZEUS trigger and data acquisition system.

Third Level Trigger (TLT)

The third level trigger was a software trigger running on a farm of personal computers [119]. The offline reconstruction software was used to calculate physical quantities of the events. Thus kinematic variables like the output of jet or vertex finding algorithms

and the topology of hadronic final states could be used for the trigger decision. Accepted events were written to disk and later to tape to be fully reconstructed offline. The final output rate after the TLT was typically only a few Hz before the upgrade and about 10 Hz during the HERA II period.

4.4. Offline reconstruction and detector simulation

Once the data were stored on tape, the events could be processed using the offline reconstruction software in order to precisely reconstruct each event. Some aspects of the reconstruction were too slow to be applied at the TLT. Additionally, final calibration constants like alignment parameters were often only available months or years after the data were collected.

To obtain a realistic simulation of the detector response to dedicated physics processes, the output of Monte Carlo event generators (see Sec. 2.7) was used as an input to a full simulation of the ZEUS detector. Within the ZEUS software framework, the supported Monte Carlo event generators are gathered in the AMADEUS program. It is possible to include user defined *event filters* in the AMADEUS source code to select events based on the generator output before the events are passed to the rather slow detector simulation. For example, the user can select events that fulfil certain kinematic criteria or contain certain interesting particle decays.

The output of AMADEUS is passed to a simulation program of the ZEUS detector based on the GEANT package [120] called MOZART³. GEANT contains a description of all relevant physics processes for electromagnetic and hadronic interactions of particles travelling through an arbitrary detector geometry. To simulate the ZEUS detector before the upgrade GEANT 3.13 was used while version 3.21 was used to simulate the detector configuration after the upgrade. The output of MOZART has the same format as the data collected by the ZEUS detector. Hence the same reconstruction software can be used in both cases. After MOZART, the trigger logic used during data taking is simulated by CZAR⁴ package which combines the FLT and SLT simulation called ZGANA⁵ with the TLT simulation software TLTZGANA.

Data as well as Monte Carlo events are processed using the offline reconstruction package ZEPHYR⁶. From the measurements of the different detector components, ZEPHYR generates event variables like particle momenta or energies. Finally, the processed data can be accessed by the ORANGE framework which produces Ntuples based on a configuration file provided by the user.

³Monte Carlo for ZEUS Analysis, Reconstruction and Trigger

⁴Complete ZGANA Analysis Routines

⁵ZEUS Geant Analysis

⁶ZEUS Physics Reconstruction

5. Event reconstruction

In this chapter the reconstruction of physical quantities from the measurements of the individual detector components by the ZEUS offline software is described. First, the measurement of charged-particle tracks and secondary decay vertices is reviewed. To exploit the full potential of the MVD and STT detectors installed during the upgrade in 2001, the track and vertex reconstruction procedure was substantially improved for the data collected during the HERA II period. In the first section of this chapter the reconstruction of tracks and vertices used for the data recorded during the HERA I period using only the CTD is described. The extended procedure used for the data collected after the upgrade is explained in the second section. Accordingly, the measurement of the energy loss of charged particles in the CTD is explained briefly.

In the following sections a procedure to improve the energy measurement combining tracking and calorimeter information and the algorithm used to identify the scattered electron are discussed in detail. The different steps of the KTCLUS algorithm used to reconstruct jets are described. Finally, different procedures to reconstruct the kinematic variables Q^2 , x and y from the scattered electron and hadronic system are compared.

5.1. HERA I tracking and vertex reconstruction

For data taken during the HERA I period, tracks and vertices were reconstructed by the VCTRACK software package [121]. VCTRACK is part of the offline reconstruction program ZEPHYR, but can also be called from user analysis code. Two variants of the track reconstruction procedure are available. In the so-called “regular mode” information from the CTD, FTD, RTD and SRTD were used while the “CTD only” mode, which was used for this analysis, relies only on measurements in the CTD. The following discussion is limited to the tracking procedure using only CTD information.

Tracks are described by a five parameter helix. The following parametrisation suited to describe trajectories of charged particles in a magnetic field parallel to the beam pipe was chosen:

- φ_H : the azimuthal angle of the helix tangent at its point of closest approach to the reference point (0,0);
- Q/R : ratio of the charge, Q , to the radius closest to the reference point, R ;
- $Q \cdot D_H$: product of the charge Q and the distance of closest approach to the reference point;
- Z_H : the Z position of the track at its closest approach to the reference point;

- $\cot \theta$, where θ is the polar angle of the track.

A circle in the $X - Y$ plane is described by the first three parameters and the latter two parameters specify the location and pitch in Z . The helix parameters are illustrated in Fig. 5.1.

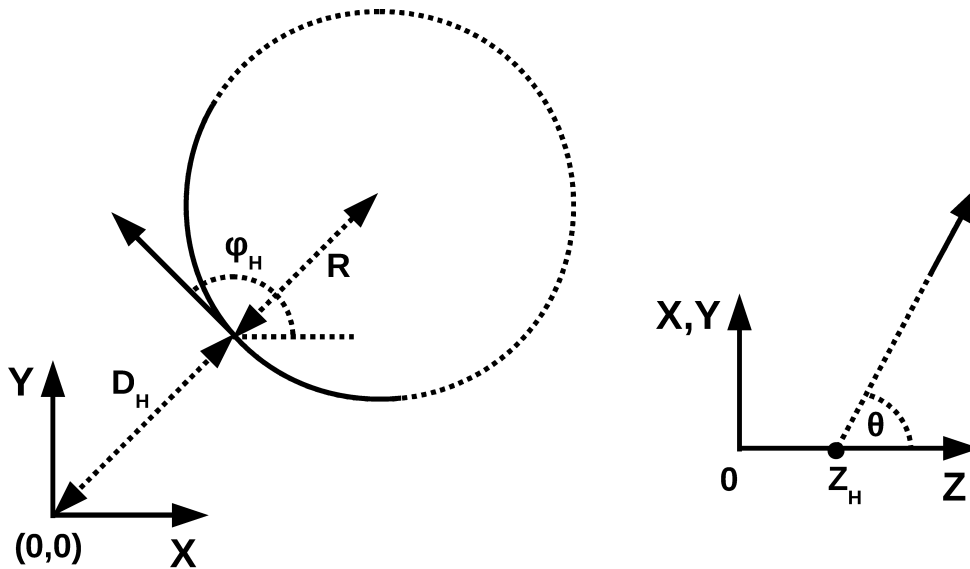


Figure 5.1.: The parameters of the helix model used by the VCTRAK package.

The track reconstruction was performed in two steps, track finding and track fitting. These two aspects are described in the following two subsections.

5.1.1. Track finding

Track candidates started from seeds consisting of three hits in the CTD from an axial superlayer (SL9, SL7, SL5, SL3 or SL1). The beam crossing position was used as an additional constraint to help guide the trajectory. Track seeds were extrapolated inwards gathering additional hits. The precision increased during the extrapolation since the trajectory parameters were updated when hits were added to the track candidate. The extrapolation was based only on information from the innermost three superlayers once the trajectory spanned several axial superlayers.

In the next step, the arcs in the $X - Y$ plane were used for the pattern recognition in the Z direction. Timing measurements provided a coarse first estimate where to search for stereo hits if available. Every track candidate was required to have 3D information, either from stereo hits or from timing information, or both.

Tracks with too many shared hits were removed periodically. In a first iteration of the track finding procedure, only tracks continued down to SL1 were accepted. First, the longest tracks were found, then the slightly shorter ones and so on. This process was

repeated until the shortest tracks reconstructed only from hits in SL1 remained. In the second iteration of the pattern recognition, the tracks not reaching down to SL1 were considered. These were required to cover at least two axial superlayers and one intermediate stereo superlayer.

5.1.2. Track fitting

Each track candidate was fitted to the 5 parameter helix model described above. During the fit, hits could be dropped or swapped between tracks. The track momentum was estimated first from the slope and curvature provided by the pattern recognition. Trajectories were established by swimming through the magnetic field starting from the innermost hit. Residuals and their derivatives with respect to the helix parameters were calculated from the swum trajectory. Finally, the trajectory was propagated to the reference point (0,0). During the track fitting procedure, corrections for magnetic field effects, and for Coulomb scattering inside the beam pipe and at the inner wall of the CTD were considered. The track fit provided a covariance matrix for each track which was used to reconstruct vertices.

5.1.3. Vertex reconstruction

VCTRACK performed a so-called *multi-vertex* reconstruction where the primary interaction vertex and additional secondary vertices were considered. Secondary vertices were caused by decays of long-lived particles such as $K_S^0 \rightarrow \pi^+\pi^-$ or $\Lambda \rightarrow p\pi^-$, but also by photon conversions ($\gamma \rightarrow e^+e^-$) and nuclear interactions in the detector material.

The vertex reconstruction procedure is briefly outlined here. Track pairs were tested for loose compatibility with forming a common vertex. From track pairs passing this requirement clusters were formed. Clusters consisted of tracks loosely consistent with a common vertex. Tracks were allowed to be associated to several clusters.

The tracks associated to a cluster were filtered using a simple fit procedure. The weighted centre of gravity in X , Y and Z was found. Tracks contributing too much to the χ^2 of the vertex were discarded one by one until the fit quality was acceptable. All clusters passing the selection up to this stage were considered as vertex candidates.

The final multi-vertex pattern recognition where every track was associated to exactly one vertex was performed inside a loop over all tracks. Tracks were dropped from vertices until no track was associated to multiple vertices any more. Finally, a full fit was performed for every vertex. The simple and the full vertex fit are described in more detail in [122].

5.1.4. Usage of HERA I tracking for measurements of heavy flavour production

The resolution of the CTD alone was not sufficient to identify secondary vertices caused by charmed or beauty hadron decays. On the other hand, the resolution and efficiency for low-momentum tracks was very good since no material was present between the beam

pipe and the CTD. Hence the data collected during the HERA I period are well suited to study hadronic decays using invariant mass spectra.

5.1.5. Overall magnetic field correction

It was shown by studies of mass peaks of particles like J/ψ , D^* or K_S^0 that the magnetic field used by VCTRAK is low by about 0.3%. To correct for this effect, the transverse momenta of all tracks were scaled by a factor of 1.003 by the ZEUS software.

5.2. HERA II tracking and vertex reconstruction

To exploit the full potential of the MVD and STT detectors, new track reconstruction procedures needed to be developed for the analysis of the HERA II dataset.

The reconstruction of tracks was performed in several steps. First, the hit positions in the individual subdetectors were reconstructed using the mvrecon (for the MVD), vcrecon (for the CTD) and strecon (for the STT) packages. For example, mvrecon combined the signals from the individual MVD readout strips to clusters.

In the second step, the vcrecon program performed a combined pattern recognition, i.e. a combined track finding, using information from the MVD, CTD and STT detectors [121, 123]. Track seeds were formed from groups of hits in the outermost available component which was the STT in the forward direction and the CTD elsewhere. Seeds in the STT were required to consist of at least eight hits. Otherwise the CTD was also used in the forward direction to provide the track seeds. Accordingly, the seeds were connected to the interaction point collecting more hits from the inner parts of the tracking system using an approximate estimation of the trajectory. Finally, a road of hits from the STT or CTD through the MVD to the interaction point was formed. The hits selected in this way were used as an input to the track fit.

In the third step, a so-called rigorous track fit was performed [124]. In this approach inhomogeneities of the magnetic field, multiple scattering and the energy loss of particles were considered. The fitting procedure was based on the Kalman filter [125] technique. Outlier hits were rejected during the track fit and hence the track quality was improved further.

5.2.1. Vertex reconstruction and beam spot

A *deterministic annealing filter* (DAF) [126] was used to fit the primary and secondary vertices. In this approach, the fixed χ^2 cut applied to the tracks was replaced by a smooth weight function given by:

$$w(\chi^2, T) = \frac{1}{1 + \exp\left(\frac{\chi^2 - \chi_{\text{cut}}^2}{2T}\right)}, \quad (5.1)$$

where T is referred to as temperature and χ_{cut}^2 is a parameter. The vertex reconstruction started from the vertices obtained using fixed χ^2 cuts. These vertices were refined using

the DAF. Initially, a weight with a high temperature was assigned to each track. After updating the fit using the weighted tracks, the temperature was reduced. This step was repeated until a certain T or convergence was reached. The dependence of $w(\chi^2, T)$ on χ^2 for several values of T is shown in Fig. 5.2. The procedure described above provides a more robust vertex determination.

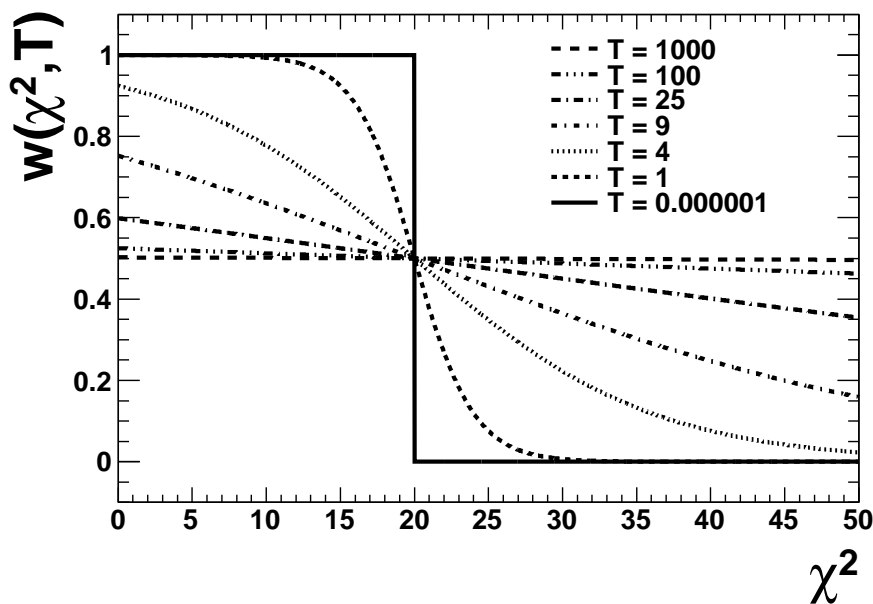


Figure 5.2.: Weight $w(\chi^2, T)$ used by the deterministic annealing filter for several values of the temperature T and $\chi_{\text{cut}}^2 = 20$.

The overlap region between the colliding beams is referred to as *beam spot*. The centre of the elliptical beam spot was determined every 2000 well measured events [127]. Gaussian curves were fitted to the X , Y and Z distributions of the primary vertex. The RMS widths of the beam spot were $80 \mu\text{m}$ ($88 \mu\text{m}$) in the X and $22 \mu\text{m}$ ($24 \mu\text{m}$) in the Y directions for the e^-p (e^+p) data [128]. In the Z direction, the beam spot was roughly 8 cm wide.

Additionally, the *beam tilt*, i.e. the slopes of the beams in X and Y with respect to the Z axis, was evaluated. This was achieved slicing the X and Y vertex distributions into several Z intervals and fitting those with Gaussian distributions. The mean values of the Gaussians were accordingly fitted to straight lines to extract the slopes in X and Y .

The position of the beam spot was used as an additional constraint in the primary vertex fit. The beam spot constrained DAF method was established as the default primary vertex finding in ZEUS since it improved the precision and resolution considerably.

5.2.2. Usage of HERA II tracking for measurements of heavy flavour production

The precision of the MVD+CTD system allows to use lifetime information for the identification of heavy quark decays. The reconstruction of secondary vertices or track impact parameters can be used to improve the precision of measurements based on semileptonic decays or hadronic D meson decay channels. Additionally, fully inclusive measurements not restricted to a particular final state are possible.

5.3. Energy loss via ionisation

In an absorber charged particles other than electrons mainly lose energy due to ionisation and atomic excitation. The mean rate of energy loss, $\langle dE/dx \rangle$, by moderately relativistic charged heavy particles is described by the *Bethe-Bloch formula* [66]:

$$-\left\langle \frac{dE}{dx} \right\rangle = K z^2 \frac{Z}{A} \frac{1}{\beta^2} \left[\frac{1}{2} \ln \frac{2m_e c^2 \beta^2 \gamma^2 T_{max}}{I^2} - \beta^2 - \frac{\delta(\beta\gamma)}{2} \right], \quad (5.2)$$

where K is a constant, ze is the charge of the incident particle, I is the mean excitation energy of the absorber in eV, T_{max} is the maximum kinetic energy which can be transferred to a free electron in a single collision and $\delta(\beta\gamma)$ is a density effect correction. Eq. 5.2 describes the mean rate of energy loss with an accuracy of a few % in the region $0.1 \lesssim \beta\gamma \lesssim 1000^1$.

The ionisation energy loss of charged particles, dE/dx , was reconstructed in the CTD [129] using the pulse sizes observed at the individual wires caused by electrons. All sense wires were read out using 8-bit flash analog-to-digital converters (FADCs). For every track the so-called *truncated mean* of the anode-wire pulse heights was calculated, which removed the lowest 10% and at least the highest 30% depending on the number of saturated hits. The measured dE/dx values were corrected by normalising to the average dE/dx for tracks around the region of minimum ionisation for pions with momentum p satisfying $0.3 < p < 0.4$ GeV. Henceforth, dE/dx is quoted in units of minimum ionising particles (mips).

5.4. Energy flow objects

The energy of charged and neutral particles was measured in the calorimeter. The momenta of charged particles were additionally reconstructed by the tracking detectors. At low momentum the precision of the measurement in the CTD is often better than that of the energy measurement in the calorimeter for charged particles. The reconstruction of the hadronic final state was significantly improved combining tracking and calorimeter information to obtain *Energy Flow Objects* (EFOs). Especially for low-energy objects a

¹For protons this corresponds to a momentum range between 100 MeV and 1 TeV.

better precision was achieved. The procedure to reconstruct EFOs called ZEUS Unidentified Flow Objects (ZUFOS) [130] is described in the following.

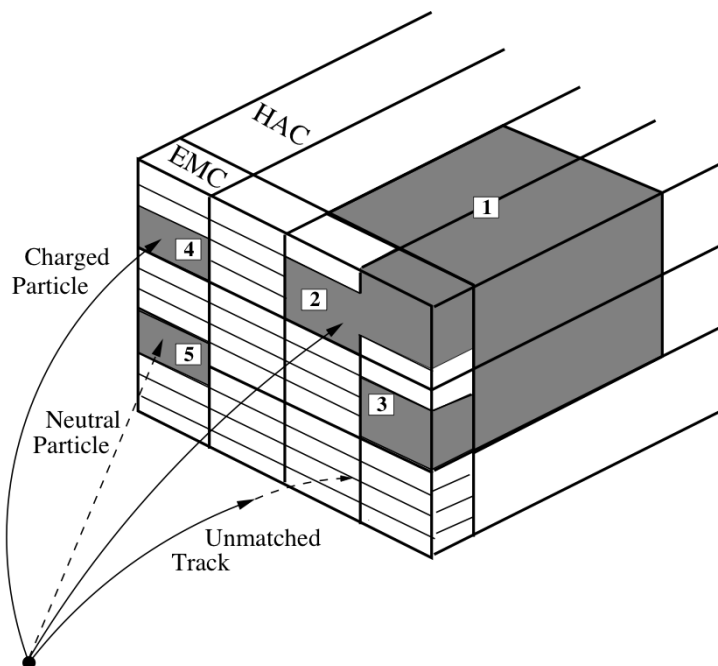


Figure 5.3.: Overview of the ZUFOS procedure. One HAC and four EMC cell islands are shown. The HAC cell island 1 and the EMC cell islands 2 and 3 were joined to a cone island. Then the cone islands were matched to tracks.

5.4.1. Calorimeter clustering

Particles absorbed in the ZEUS calorimeter usually deposited energy in several adjacent cells (see Sec. 4.3.3). Cells were merged using the clustering algorithm described in the following. Ideally, each cluster corresponds to the shower caused by a single particle.

First, adjacent cells were clustered into *cell islands* separately in the different sections of the calorimeter (EMC, HAC1 and HAC2). Each cell with sufficient energy was connected to the neighbouring cell with the highest energy. This simple procedure provided an unambiguous assignment of every cell to an island. In the next step, the cell islands were clustered in the $\theta - \phi$ space. The obtained three dimensional objects are referred to as *cone islands*. The clustering procedure is illustrated in Fig 5.3. Finally, the positions of the cone islands were determined using the logarithmically weighted centre of gravity of the shower. As proposed in [131], the following weights were used:

$$w_i = \max \left\{ 0, \left[W_0 + \ln \left(\frac{E_i}{E_{\text{tot}}} \right) \right] \right\}, \quad (5.3)$$

where E_i is the energy deposited in a cell, $E_{\text{tot}} = \sum_i E_i$ is the total energy of the shower

and W_0 is a free parameter. The motivation to use logarithmic energy weights instead of linear weights was the exponential falloff of the shower energy distribution from the maximum. Different values for W_0 were used for the EMC and HAC sections of the calorimeter due to the different geometries.

Cells surrounding the FCAL beam hole were allowed to be joined into one cell or cone island. The resulting island was assigned a polar angle pointing inside the beam hole.

5.4.2. Track matching

Tracks in the range $0.1 < p_T < 20$ GeV passing at least 4 CTD superlayers and tracks in the high momentum range $20 < p_T < 25$ GeV passing at least 7 CTD superlayers were considered for the matching to cone islands. The tracks were extrapolated to the inner surface of the calorimeter and accordingly associated to cone islands. A track was matched to an island if the distance of closest approach between the extrapolated track and the cone island was less than 20 cm, or if the distance of closest approach was smaller than the maximum radius of the island in the plane perpendicular to the vector connecting the primary vertex and the island.

5.4.3. Energy measurement

The CTD information was used to determine the energy and momentum of an object assuming the pion mass if a track was matched to a cone island and the following two requirements were fulfilled:

- $\frac{E_{\text{cal}}}{p} < 1.0 + 1.2 \cdot \sigma\left(\frac{E_{\text{cal}}}{p}\right)$, where p is the track momentum, E_{cal} is the energy measured in the calorimeter and $\sigma\left(\frac{E_{\text{cal}}}{p}\right)$ is the resolution of the measured ratio $\frac{E_{\text{cal}}}{p}$. This requirement ensured that the energy measured in the calorimeter is due to the track alone;
- $\frac{\sigma(p)}{p} < \frac{\sigma(E_{\text{cal}})}{E_{\text{cal}}}$ where $\sigma(p)$ is the uncertainty of the track momentum and $\sigma(E_{\text{cal}})$ is the uncertainty of the energy measurement in the calorimeter.

Otherwise the energy measurement in the calorimeter was used.

The energy of tracks which were not matched to cone islands was calculated assuming the pion mass. Cone islands not matched to tracks were assumed to be caused by photons. The calorimeter energy was used in this case. Also for energy deposits in the calorimeter that were associated with more than three tracks the calorimeter energy was used.

In the analysis described here, ZUFOs were used to calculate the $E-p_z$ values of the events as well as the kinematic variables from the Jacquet-Blondel and from the double-angle methods as described in the next section.

5.5. Electron reconstruction

NC DIS events were identified by the presence of a scattered electron found in the calorimeter. The SINISTRA [132] algorithm, which is based on a neural network, was used to reconstruct electrons offline.

The scattered electron typically deposited energy in several neighbouring calorimeter cells. Hence the electron finding process began by grouping calorimeter cells into islands. The energy distribution of an island can be described by an infinite series of moments. The longitudinal shower profile was expressed by complex Zernike moments up to the second order which are invariant under rotation. The standard Legendre functions up to the third order were used to describe the longitudinal shower profile. These moments were used as an input to SINISTRA. Additionally, the total energy of the island was used resulting in 17 input variables to the neural network. This approach allowed to properly handle the non-projective regions of the calorimeter.

The neural network was trained on a sample of low- Q^2 events. The output of SINISTRA represents the probability that an energy deposit is of electromagnetic origin. In Fig. 5.4 the probability for hadronic and electromagnetic clusters is compared. The algorithm was optimised for the electron identification in the RCAL.

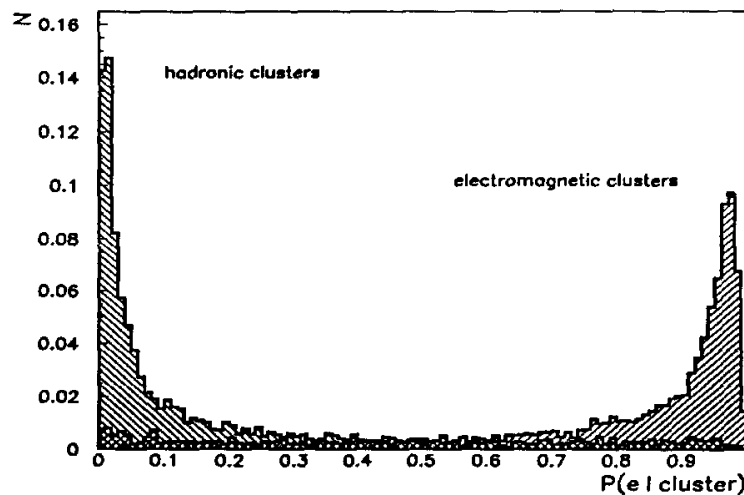


Figure 5.4.: Probability for a given cluster to be an electromagnetic cluster, $P(e|\text{cluster})$, from the SINISTRA electron finder.

If the probability of the candidate with the highest probability exceeded 0.9, this calorimeter island was assumed to be an electron. Here only the candidate with the highest probability was considered further if several candidates with a probability greater than 0.9 were present in an event. The sum of all cell energies in the island represented the energy of the surviving electron candidate, which was corrected for energy losses in the inactive material before the calorimeter. Only electrons with an energy of more than 10 GeV were used in this analysis. Additional cuts on the electron probability and energy will be described later.

5.6. Jet reconstruction

Due to confinement, quarks and gluons are not directly observable in experiments. The hadrons produced in the fragmentation process of a hard parton form a collimated flow of particles which is referred to as *jet*. Hence quarks and gluons have to be measured indirectly exploiting the strong correlation between the hard partons and the observed jets in the detector. A meaningful comparison of experimental measurements and theoretical predictions requires well defined jets. For this purpose different *jet algorithms* were proposed.

Several criteria to be fulfilled by jet algorithms were formulated at Snowmass in 1990 [133] to obtain reasonable jet definitions. The jet algorithm should be simple to implement in experimental analyses and theoretical calculations. The jets have to be well-defined at any order of perturbation theory. The obtained cross sections should be infrared² and collinear³ safe. Finally, the jet definition should yield cross sections which are relatively insensitive to hadronisation effects.

For *ep* collisions these criteria are matched by the k_T cluster algorithm KTCLUS [134]. Typically, jet definitions consist of an algorithm to combine the final state objects into jets and of a *recombination scheme* describing how the four-momenta of the final state objects are combined. In the analysis of inclusive secondary vertices, the KTCLUS algorithm was used in its *massive mode*. The E_T recombination scheme was used to minimise the hadronisation corrections which had to be applied to the theoretical calculation [135]. Energy flow objects as described in Sec. 5.4 were used as input to the KTCLUS algorithm. The algorithm consists of the following steps:

1. A list of all measured objects and a list of reconstructed jets are used. The latter is empty at the beginning.
2. For every object i , i.e. for every EFO, the distance to the beam axis is calculated as $d_i = E_{T,i}^2$.
3. For every pair of objects i and j the distance between the two objects is calculated according to $d_{i,j} = \min(E_{T,i}^2, E_{T,j}^2) R_{i,j}^2$, where $R_{i,j}$ is the distance between both objects in the $\eta - \phi$ plane, $R_{i,j} = \sqrt{(\eta_i - \eta_j)^2 + (\phi_i - \phi_j)^2}$.
4. The smallest distance, d_{\min} , in the list of all d_i and $d_{i,j}$ is determined.
5. If d_{\min} is an element of the list $\{d_i\}$, the object i is removed from the clustering procedure and is added to the list of reconstructed jets.
6. If d_{\min} belongs to the list $\{d_{i,j}\}$, the objects i and j are combined to a new object k :

$$\eta_k = \frac{E_{T,i} \cdot \eta_i + E_{T,j} \cdot \eta_j}{E_{T,i} + E_{T,j}}, \quad \phi_k = \frac{E_{T,i} \cdot \phi_i + E_{T,j} \cdot \phi_j}{E_{T,i} + E_{T,j}} \quad \text{and} \quad E_{T,k} = E_{T,i} + E_{T,j}.$$

²The resulting jets have to be independent of the emission of very low energy particles.

³The resulting jets have to be independent of collinear parton splittings.

The new object k replaces the objects i and j .

7. This procedure is iterated until the smallest object in the list $\{d_i, d_{i,j}\}$ is above a certain threshold, d_{cut} , with $\Lambda_{\text{QCD}}^2 \ll d_{\text{cut}} \ll s$. For the analysis presented in this thesis d_{cut} was set to 1 GeV².

An advantage of the k_T cluster algorithm is that it avoids overlapping jets. Only those jets which did not contain the flagged DIS electron EFO [136] were considered further.

5.7. Kinematic reconstruction

The ZEUS detector allowed to measure the angles and energies of the final state electron and hadronic system as described in the previous sections. Hence the kinematic variables x , y and Q^2 could be reconstructed in different ways. The optimal reconstruction method has to be chosen for a certain kinematic region. It is also possible to use a combination of different reconstruction methods. The reconstruction methods relevant for this thesis are discussed in the following.

Electron method

This method relies on the measurement of the angle, θ_e , and the energy, E'_e , of the scattered electron [137]. The kinematic variables for given electron and proton beam energies, E_e and E_p , are given by:

$$Q_e^2 = 2E_e E'_e \cdot (1 + \cos \theta_e) = 4E_e E'_e \cos^2 \frac{\theta_e}{2}, \quad (5.4)$$

$$y_e = 1 - \frac{E'_e}{2E_e} \cdot (1 - \cos \theta_e) = 1 - \frac{E'_e}{E_e} \sin^2 \frac{\theta_e}{2} \text{ and} \quad (5.5)$$

$$x_e = \frac{Q_e^2}{s y_e} = \frac{E'_e \cos^2 \frac{\theta_e}{2}}{E_p (1 - \frac{E'_e}{E_e} \sin^2 \frac{\theta_e}{2})}. \quad (5.6)$$

Since only one particle needs to be reconstructed, the electron method is conceptually the simplest way to derive the event kinematics. It is also used for fixed target experiments where the hadronic final state can not be reconstructed.

Photons from final-state QED radiation are usually almost parallel to the scattered electron. These photons are clustered into the same island as the scattered electron. Hence the electron method is little affected by final-state QED radiation. On the other hand, initial-state QED radiation reduces the energy of the incoming electron and thus leads to a shift in the reconstructed variables.

Jacquet-Blondel method

This method uses only variables from the hadronic system and is thus independent of the electron [138]. It is the only method that can also be used in CC DIS and photoproduction

(for y) because the scattered lepton can not be measured. All particles in the hadronic final state are summed up. An important quantity is δ_h which is defined as:

$$\delta_h = \sum_i (E_i - p_{z,i}), \quad (5.7)$$

where the sum runs over all particles excluding the electron. Since E and p_z of particles tend to cancel along the positive Z axis, δ_h is hardly affected by energy losses through the forward beam hole. The kinematic variables are given by:

$$y_{\text{JB}} = \frac{\delta_h}{2E_e}, \quad (5.8)$$

$$Q_{\text{JB}}^2 = \frac{p_{T,h}^2}{1 - y_{\text{JB}}} \text{ and} \quad (5.9)$$

$$x_{\text{JB}} = \frac{Q_{\text{JB}}^2}{s \cdot y_{\text{JB}}}, \quad (5.10)$$

where $p_{T,h} = \sqrt{(\sum_i p_{x,i})^2 + (\sum_i p_{y,i})^2}$ is the transverse momentum of the hadronic system. Despite the fact that this method does not provide the best resolution, y_{JB} provides a measurement of the hadronic activity in the event. Since the presence of a charmed or beauty hadron represents some hadronic energy, y_{JB} is useful to suppress background.

Double-angle method

Here the polar angles of the electron, θ_e , and of the hadronic system, γ_h , are used [137]. In the naive QPM γ_h can be interpreted as the angle of the scattered quark and is given by:

$$\cos \gamma_h = \frac{p_{T,h}^2 - \delta_h^2}{p_{T,h}^2 + \delta_h^2}. \quad (5.11)$$

Now the kinematic variables can be written as follows:

$$Q_{\text{DA}}^2 = 4_e^2 \frac{\sin \gamma_h (1 + \cos \theta_e)}{\sin \gamma_h + \sin \theta_e - \sin(\theta_e + \gamma_h)}, \quad (5.12)$$

$$y_{\text{DA}} = \frac{\sin \theta_e + (1 - \cos \gamma_h)}{\sin \gamma_h + \sin \theta_e - \sin(\theta_e + \gamma_h)} \text{ and} \quad (5.13)$$

$$x_{\text{DA}} = \frac{E_e \sin \gamma_h + \sin \theta_e + \sin(\theta_e + \gamma_h)}{E_p \sin \gamma_h + \sin \theta_e - \sin(\theta_e + \gamma_h)}. \quad (5.14)$$

Since angles were in general measured more precisely than energies with the ZEUS detector, this method gives the most precise results in a large fraction of the phase space. While the electron method has a good resolution at low Q^2 , the double-angle method has a better precision at high values of Q^2 .

6. Measurement of D^+ and Λ_c^+ production

In this chapter a measurement of charm production in DIS using 120 pb^{-1} of data collected before the upgrades of ZEUS and HERA in 2001 is described. Cross sections for D^+ and Λ_c^+ production were measured using decay channels with a K_S^0 or Λ hadron in the final state. The data taken between 1996 and 2000 are particularly suitable for this study since a fully inclusive DIS trigger with a very low Q^2 threshold was available.

First, the analysed data set and the Monte Carlo samples used to determine the detector acceptance are described. After a detailed description of the D^+ and Λ_c^+ candidate selection, the investigated sources of systematic uncertainty are reviewed. Cross sections were extracted and are compared to theoretical predictions and previous measurements. Finally, the fraction of c quarks hadronising into Λ_c^+ baryons is extracted.

The aim of the analysis was to extend the measurement of charm quark production to the low transverse momentum region and to test if charm fragmentation is universal. The results presented in this chapter were recently published [5].

6.1. Data samples and Monte Carlo sets

In the following subsections, all data and Monte Carlo samples that were used for the measurement of D^+ and Λ_c^+ production are described in detail.

6.1.1. Data samples

Data collected using the ZEUS detector during the HERA I period were analysed. Events were preselected using the EVTAKE routine, which requires good data quality from the CTD, CAL, trigger chain and luminosity measurement. The luminosity values after the EVTAKE selection are shown in Tab. 6.1.

In the year 2000 data corresponding to an integrated luminosity of 815 nb^{-1} were taken where the primary interaction vertex was shifted to $\pm 0.8 \text{ m}$. The corresponding runs were excluded from the analysis. A combination of all listed samples yields an integrated luminosity of $120.4 \pm 2.4 \text{ pb}^{-1}$. This value was used for the calculation of all cross sections presented in this chapter.

6.1.2. Monte Carlo samples

To obtain acceptance corrections for the calculation of cross sections, charm events were generated using RAPGAP (see Sec. 2.7.2). The CTEQ5L PDFs [139] were used for the

Year	Interaction	\sqrt{s} (GeV)	\mathcal{L} (pb $^{-1}$)	$\sigma_{\text{syst.}}$ (%)
1996	e^+p	300	10.77	1.1
1997	e^+p	300	27.85	1.8
1998	e^-p	318	4.60	1.8
1999	e^-p	318	12.08	1.8
1999	e^+p	318	19.65	2.25
2000	e^+p	318	45.41	2.25
Total			120.36	1.98

Table 6.1.: Data samples collected at the ZEUS detector between 1996 and 2000. The shifted vertex runs have been excluded (see text).

proton and the charm-quark mass was set to 1.5 GeV. Events were generated in the range $Q^2 > 0.8$ GeV 2 . Charm fragmentation was simulated using the Lund string model (see Sec. 2.6.2). Filters were added to AMADEUS to select events that contain at least one of the relevant hadronic charm decays. To calculate the central values of the extracted cross sections, charm quarks were produced by the BGF process only. An overview of the corresponding samples is given in Tab. 6.2. Three different versions of the ZEUS detector simulation were used (“1996/1997”, “1998/1999” and “1999/2000”) to account for changes in the detector geometry, primary vertex distribution and trigger configuration.

Decay	Period	Interaction	\sqrt{s} (GeV)	Events	\mathcal{L} (pb $^{-1}$)
$D^+ \rightarrow K_S^0 \pi^+$	1996/1997	e^+p	300	119995	315.8
	1998/1999	e^-p	318	79980	198.6
	1999/2000	e^+p	318	159989	395.8
$D_s^+ \rightarrow K^+ K_S^0$	1996/1997	e^+p	300	59992	237.9
	1998/1999	e^-p	318	40000	150.5
	1999/2000	e^+p	318	80000	300.7
$\Lambda_c^+ \rightarrow p K_S^0$	1996/1997	e^+p	300	29998	316.9
	1998/1999	e^-p	318	20000	198.1
	1999/2000	e^+p	318	39995	398.9
$\Lambda_c^+ \rightarrow \Lambda \pi^+$	1996/1997	e^+p	300	30000	434.5
	1998/1999	e^-p	318	20000	276.3
	1999/2000	e^+p	318	39994	549.4

Table 6.2.: Monte Carlo samples for charm quark production by the BGF process. All samples were generated for $Q^2 > 0.8$ GeV 2 .

Additional samples where charm was produced by the process $cg \rightarrow cg$ were generated and used to study the model dependence of the simulation. These samples are listed in Tab. 6.3. The processes $gg \rightarrow c\bar{c}$ and $q\bar{q} \rightarrow c\bar{c}$ were not included because their contribution estimated using the RAPGAP program was found to be less than 1% in the studied kinematic range.

Decay	Period	Interaction	\sqrt{s} (GeV)	Events	\mathcal{L} (pb ⁻¹)
$D^+ \rightarrow K_S^0 \pi^+$	1996/1997	e^+p	300	60000	329.2
	1998/1999	e^-p	318	40000	200.4
	1999/2000	e^+p	318	80000	405.5
$D_s^+ \rightarrow K^+ K_S^0$	1996/1997	e^+p	300	30000	247.5
	1998/1999	e^-p	318	20000	152.2
	1999/2000	e^+p	318	40000	304.9
$\Lambda_c^+ \rightarrow p K_S^0$	1996/1997	e^+p	300	15000	327.2
	1998/1999	e^-p	318	10000	202.0
	1999/2000	e^+p	318	20000	405.8
$\Lambda_c^+ \rightarrow \Lambda \pi^+$	1996/1997	e^+p	300	15000	453.3
	1998/1999	e^-p	318	10000	277.0
	1999/2000	e^+p	318	20000	556.7

Table 6.3.: Monte Carlo samples for charm quark production by the process $cg \rightarrow cg$. All samples were generated for $Q^2 > 0.8 \text{ GeV}^2$.

The D^+ and Λ_c^+ hadrons originating from beauty decays were accounted for using RAPGAP MC samples where beauty quark pairs were produced by the BGF process in the range $Q^2 > 1 \text{ GeV}^2$. An overview of the beauty samples is given in Tab. 6.4. Due to the much smaller cross section, the beauty samples were not restricted to any specific decay channel.

Period	Interaction	\sqrt{s} (GeV)	Events	\mathcal{L} (pb ⁻¹)
1996/1997	e^+p	300	400000	497.0
1998/1999	e^-p	318	240000	264.3
1999/2000	e^+p	318	940000	988.3

Table 6.4.: Monte Carlo samples for beauty quark production by the BGF process. All samples were generated for $Q^2 > 1.0 \text{ GeV}^2$.

To perform various checks, inclusive ARIADNE MC (see Sec. 2.7.1) samples were used. An overview is given in Tab. 6.5.

Period	Interaction	\sqrt{s} (GeV)	Events	\mathcal{L} (pb ⁻¹)
1996/1997	e^+p	300	$8 \cdot 10^6$	19.61
1999/2000	e^+p	318	$23 \cdot 10^6$	55.04

Table 6.5.: Monte Carlo samples for the simulation of NC DIS events. Both samples were generated for $Q^2 > 0.8 \text{ GeV}^2$.

Both ARIADNE MC samples were generated in the range $Q^2 > 2 \text{ GeV}^2$. Since no dedicated sample was available for the 1998/1999 detector configuration, the sample generated for

the 1999/2000 period was used for all data taken at $\sqrt{s} = 318$ GeV. The ARIADNE MC was not used to extract any cross sections.

6.2. Event selection

6.2.1. Online event selection

As described in Sec. 4.3.5, a three-level trigger system was used to select events online. The complexity of the trigger decision increased from level to level as more detailed information from the individual detector components became available.

To select NC DIS events, two TLT slots were used for the analysis described in this chapter. A fully inclusive DIS trigger (DIS01) had a high acceptance for $Q^2 \gtrsim 1$ GeV². This trigger was prescaled, i.e. only one out of every n events accepted by the trigger was written to tape. Here n is the *prescale factor*. On the other hand, the medium- Q^2 trigger (DIS03) was never prescaled, but is only sensitive above $Q^2 \approx 20$ GeV².

These triggers do not apply cuts on the transverse momenta of the reconstructed charmed hadrons. Dedicated triggers for the analysed charmed hadron decays were not available during the HERA I period. In the following subsections the logic of the FLT and SLT slots required by the DIS01 and DIS03 triggers as well as the cuts applied at the third trigger level are briefly summarised.

First level trigger

To reject beam gas events, the FLT slots could be vetoed by signals from the C5, Veto Wall, SRTD or CTD detectors. If there was no veto, events were selected by the logical OR of the following conditions [140]:

- total EMC energy deposit in the BCAL greater than 4.8 GeV or total EMC energy deposit in the RCAL excluding the ring of towers surrounding the beam hole greater than 3.4 GeV;
- an *isolated electron condition* (*isoE*) in the RCAL. The *isoE* condition required an isolated EMC energy deposit of more than 2.08 GeV and that the HAC energy behind it was less than one third of the EMC energy or smaller than 0.95 GeV. Furthermore, a signal had to be found in the SRTD and the total energy in the calorimeter was required to be greater than 0.464 GeV.
- total transverse energy in the CAL greater than 30 GeV;
- total transverse energy in the CAL greater than 11.6 GeV and at least one track candidate in the CTD;
- total EMC energy deposit in the CAL greater than 10 GeV and at least one track candidate in the CTD.

The average trigger efficiency was above 99% for events passing an offline selection similar to the one presented below [140, 141].

Second level trigger

The background was reduced further at the second trigger level using timing information from the calorimeter cells and energy sums. For fully contained NC DIS events and a perfect detector resolution the quantity:

$$\delta = E - p_z = \sum_i E_i(1 - \cos \theta_i), \quad (6.1)$$

where E_i and θ_i are the energies and polar angles of all energy deposits in the calorimeter, is equal to two times the energy of the electron beam, i.e. 55 GeV. For photoproduction events, where the scattered electron escapes down the beam pipe, the value of δ is much lower. For proton beam-gas events originating from inside the detector the energy is mostly absorbed in the forward direction and thus δ is small. Events were accepted at the SLT if they satisfied the following condition:

$$\delta_{\text{SLT}} = \sum_i E_i(1 - \vartheta_i) > (29 \text{ GeV} - 2E_\gamma), \quad (6.2)$$

where the ϑ_i are the measured polar angles of the energy deposits with respect to the nominal vertex and E_γ is the measured photon energy in the luminosity detector.

Third level trigger

The complete event information was available at the third trigger level. Algorithms to remove beam-halo muons and cosmic rays as well as tighter timing cuts than on the previous trigger levels were applied. Events were taken if they were accepted by the DIS01 and DIS03 slots. The following conditions had to be fulfilled:

- an electron with an energy $E'_e > 4 \text{ GeV}$ had to be found;
- $\delta_{\text{TLT}} > (30 \text{ GeV} - 2E_\gamma)$ and $\delta_{\text{TLT}} < 100 \text{ GeV}$, where δ_{TLT} was calculated using the reconstructed vertex;
- cuts on the position of the electron candidate on the face of the RCAL were applied:
 - **DIS01:** electrons in the RCAL were required to be outside a box centred around the beam pipe of $24 \times 12 \text{ cm}^2$;
 - **DIS03:** electrons in the RCAL were required to be outside a box centred around the beam pipe of $28 \times 28 \text{ cm}^2$, or outside a circle centred around the beam pipe with a radius of 25 cm, or outside a circle around the beam pipe with a radius of 35 cm, depending on the run range.

Cuts like these are referred to as *box cuts* in the following.

- for the DIS01 slot a prescale factor of $n = 1, 10$ or 100 was applied depending on the run range.

6. Measurement of D^+ and Λ_c^+ production

The prescale factors used for the DIS01 slot and the box cuts of the DIS03 slot are summarised in Tab. 6.6.

Time period	Run Range	DIS01 prescale	\mathcal{L}_{eff} (nb ⁻¹)	DIS03 box cut	\mathcal{L} (nb ⁻¹)
1996 e^+p	20718 - 21631	1	1620.75	28×28	1621
	21634 - 21853	OFF	0.0	28×28	1326
	21871 - 22447	100	44.40	28×28	4440
	22451 - 22462	1	148.24	$R > 25$	148
	22466 - 22662	100	8.06	$R > 25$	806
	22673 - 22954	1	2431.66	$R > 25$	2432
1997 e^+p	25190 - 25336	1	749.67	$R > 25$	750
	25344 - 27889	100	270.96	$R > 25$	27096
Total			5273.74		38618
1998 e^-p	30758 - 31544	100	31.24	$R > 25$	3124
	31557 - 31752	1	1473.81	$R > 25$	1474
1999 e^-p	31784 - 32213	1	3220.44	$R > 25$	3220
	32214 - 32906	100	88.58	$R > 25$	8858
Total			4814.07		16677
1999 e^+p	33125 - 34486	10	1968.88	$R > 35$	19649
2000 e^+p	35031 - 37715 ^a	10	4540.06	$R > 35$	45406
Total			6508.94		65055
Total 1996 - 2000			16596.75		120350 ^b

Table 6.6.: Overview of DIS01 prescales and DIS03 box cuts.

^aDuring the runs 37588 - 37639 were taken, the position of the primary vertex was shifted. Hence these events were excluded.

^bThe marginal difference of this value compared to the 120.36 pb⁻¹ listed in Tab. 6.1 was caused by rounding errors when all runs were summed up.

The prescale factors for the DIS01 slot were not included in the trigger simulation. Hence those events accepted only by the DIS01 slot but not by the DIS03 slot were weighted to compensate for this effect. The weights for the three different MC configurations are given by:

$$w_{1996/1997} = \frac{\mathcal{L}_{\text{eff},1996/1997}}{\mathcal{L}_{1996/1997}} = 0.1366 \text{ and} \quad (6.3)$$

$$w_{1998/1999} = \frac{\mathcal{L}_{\text{eff},1998/1999}}{\mathcal{L}_{1998/1999}} = 0.2887 \text{ and} \quad (6.4)$$

$$w_{1999/2000} = \frac{\mathcal{L}_{\text{eff},1999/2000}}{\mathcal{L}_{1999/2000}} = 0.1000. \quad (6.5)$$

6.2.2. Offline event selection

The following requirements were imposed offline:

- at least 15% of all tracks were required to originate from the primary interaction vertex. This cut removed events not originating from ep collisions;
- $38 < \delta < 65$ GeV, where $\delta = \sum_i E_i(1 - \cos \theta_i)$ and E_i and θ_i are the energy and the polar angle of the i^{th} EFO. The sum i runs over all EFOs. The lower cut reduced the background from photoproduction events further while events caused by cosmic particles were removed by the upper cut on δ ;
- $E'_e > 10$ GeV, where E'_e is the energy of the scattered electron. This cut ensures a good purity and efficiency of the SINISTRA electron finder. Additionally, photoproduction events tend to lower values of E'_e and were thus suppressed;
- an energy dependent cut on the SINISTRA electron probability, \mathcal{P}_e , was applied as suggested by previous studies [142]:
 - $\mathcal{P}_e > 0.94 + 0.0025 \cdot E'_e$ for $10 < E'_e < 20$ GeV;
 - $\mathcal{P}_e > 1.17 - 0.0090 \cdot E'_e$ for $20 < E'_e < 30$ GeV;
 - $\mathcal{P}_e > 0.9$ for $E'_e < 30$ GeV.
- $E_{\text{cone}} < 5$ GeV, where E_{cone} is the calorimeter energy measured in a cone around the electron position that was not assigned to the electron cluster. The cone was defined by $R_{\text{cone}} < 0.8$ with $R_{\text{cone}} = \sqrt{(\Delta\phi)^2 + (\Delta\eta)^2}$;
- a match between the calorimeter information and a track with $p > 5$ GeV for electrons well within the CTD acceptance, $17^\circ < \theta_e < 149^\circ$. The distance of closest approach between the calorimeter cluster and the endpoint of the track extrapolated to the calorimeter was required to be smaller than 10 cm. For θ_e outside this region, the cut $\delta > 44$ GeV was imposed;
- box cuts slightly bigger than those implemented at the third trigger level were applied offline. The following requirements were imposed for the two TLT trigger slots:
 - **DIS01:** for events with the scattered electron reconstructed within the SRTD acceptance, the impact position of the electron on the face of the RCAL had to be outside the region 26×14 cm² centred on $X = Y = 0$. If the electron position was reconstructed without using SRTD information, a box cut of 26×20 cm² was imposed;
 - **DIS03:** for the time periods 1999 e^+p and 2000 e^+p the position of the scattered electron on the RCAL face had to lie outside a circle centred around the beam pipe of radius $R > 36$ cm. For the earlier periods this cut was changed to $R > 26$ cm.

To treat events with more than one electron candidate correctly, the box cuts were applied separately for the two TLT trigger slots;

- $1.5 < Q_e^2 < 1000 \text{ GeV}^2$;
- $y_{\text{JB}} > 0.02$ and $y_e < 0.7$;
- a primary vertex position in the range $|Z_{\text{vertex}}| < 50 \text{ cm}$.

Control distributions of event variables

As an approximate check of the event selection, the data are compared to the inclusive ARIADNE MC (see Tab. 6.5). Since no ARIADNE MC sample was available for the 1998/1999 e^-p data taking period, the sample generated for the period 1999/2000 e^+p was used for all data taken at $\sqrt{s} = 318 \text{ GeV}$. Hence the cut $R > 36 \text{ cm}$ for the DIS03 slot was imposed also for the e^-p data. To reduce migration effects, the cut on the photon virtuality was increased to $Q_e^2 > 5 \text{ GeV}^2$. The comparison was performed after all event selection and D^+ reconstruction cuts (see Sec. 6.4.1). Additionally, the mass of the D^+ candidates was restricted to the range $1.6 < M(D^+) < 2.1 \text{ GeV}$.

Control plots for different event variables are shown in Fig. 6.1. The Monte Carlo distributions were area normalised to the data. The agreement is reasonable given the limitations of this comparison. The integrated luminosity of the ARIADNE MC corresponds to only about 75 pb^{-1} .

Three peaks are visible in the distribution of the electron scattering angle θ_e . The two left peaks correspond to the two different radius cuts used for the DIS03 trigger. The third peak is caused by the box cut of the DIS01 trigger.

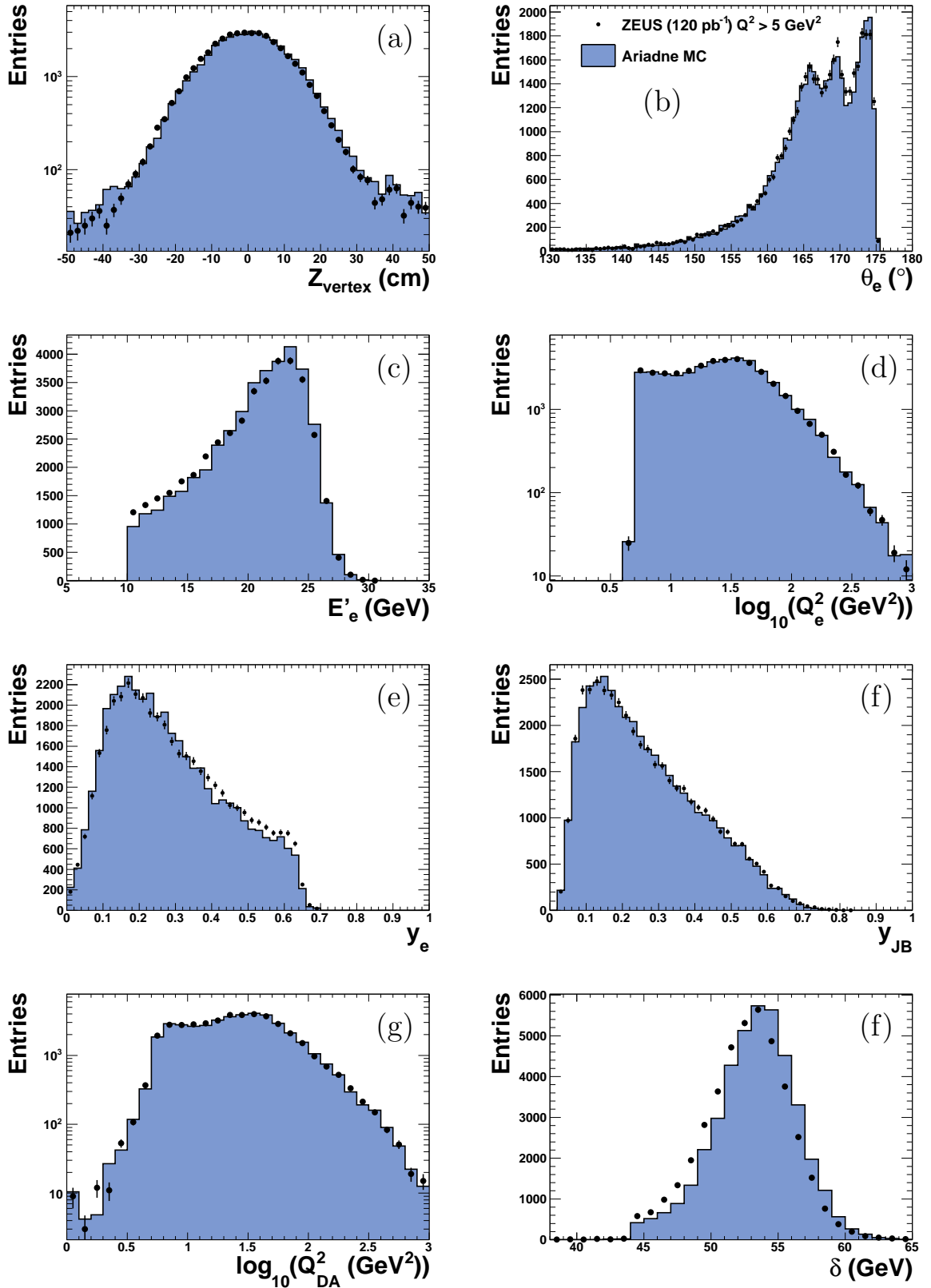


Figure 6.1.: The event variables (a) Z_{vertex} , (b) θ_e , (c) E'_e , (d) $\log_{10} Q_e^2$, (e) y_e , (f) y_{JB} , (g) $\log_{10} Q_{DA}^2$ and δ . The data (dots) are compared to the inclusive **ARIADNE** MC (histograms).

6.3. Strange-particle reconstruction

This analysis used charged tracks measured in the CTD that were assigned either to the primary or to a secondary vertex. The tracks were required to have transverse momenta $p_T > 0.15$ GeV and pseudorapidity in the laboratory frame $|\eta| < 1.75$, restricting the study to a region where the CTD track acceptance and resolution were high. Candidates for long-lived neutral strange hadrons decaying to two charged particles were identified by selecting pairs of oppositely charged tracks, fitted to a displaced secondary vertex (see Sec. 5.1.3). The events were required to have at least one such candidate.

6.3.1. K_S^0 meson candidate selection

The K_S^0 mesons were identified by their charged decay mode, $K_S^0 \rightarrow \pi^+\pi^-$. Both tracks were assigned the mass of the charged pion and the invariant mass, $M(\pi^+\pi^-)$, of each track pair was calculated. Additional requirements to select K_S^0 were imposed:

- $M(e^+e^-) > 50$ MeV, where the electron mass was assigned to each track, to eliminate tracks from photon conversions;
- $M(p\pi) > 1121$ MeV, where the proton mass was assigned to the track with higher momentum, to eliminate Λ contamination in the K_S^0 signal;
- $\cos \theta_{XY} > 0.98$, where θ_{XY} is defined as the angle between the momentum vector of the K_S^0 candidate and the vector defined by the primary interaction vertex and the K_S^0 decay vertex in the X - Y plane;
- $483 < M(\pi^+\pi^-) < 513$ MeV;
- $|\eta(K_S^0)| < 1.6$.

The invariant-mass spectrum of the K_S^0 candidates is shown in Fig. 6.2. The data were fitted using the sum of a linear background and a “modified” Gaussian function [76] given by:

$$g^{\text{mod}}(x) \propto \exp \left[-0.5 \cdot x^{1+1/(1+0.5 \cdot x)} \right], \quad (6.6)$$

where $x = |(M - M_0)/\sigma|$. The fit yielded $N = 257930 \pm 740$ candidates.

6.3.2. Λ candidate selection

The Λ candidates were reconstructed by their charged decay mode to $p\pi^-$. The decay proton has a larger momentum than the pion, provided the Λ momentum is greater than 0.3 GeV. This condition is fulfilled for all reconstructed Λ baryons originating from $\Lambda_c^+ \rightarrow \Lambda\pi^+$ decays after the selection cuts described in Sec. 6.4.3 were applied. Hence the track with the larger momentum was assigned the mass of the proton, while the other was assigned the mass of the charged pion. Additional requirements to select Λ were imposed:

- $M(e^+e^-) > 50$ MeV;

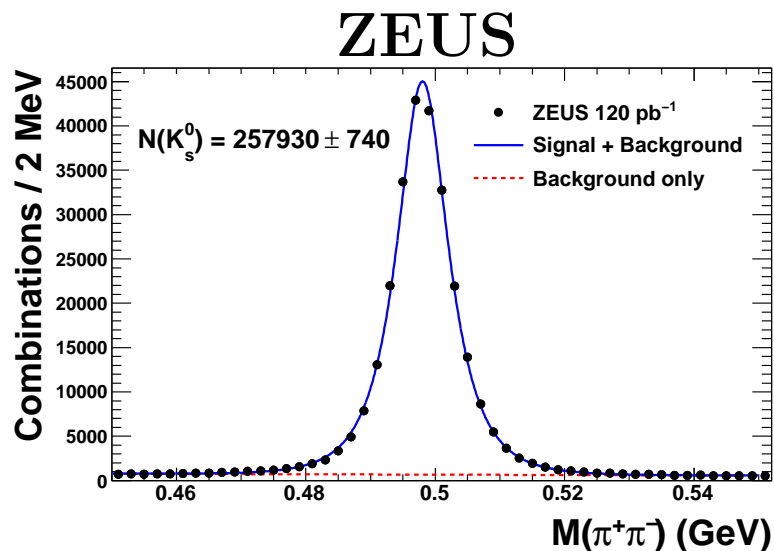


Figure 6.2.: Mass distribution of the secondary vertex candidates in the K_S^0 sample. The statistical uncertainties are in general smaller than the point size. For illustration the data have been fitted using the sum of a “modified” Gaussian function and a linear background.

- $M(\pi^+\pi^-) < 483$ MeV, where the charged pion mass was assigned to both tracks, to remove K_S^0 contamination in the Λ signal;
- $\cos\theta_{XY} > 0.98$;
- $1112 < M(p\pi) < 1121$ MeV;
- $|\eta(\Lambda)| < 1.6$.

Fig. 6.3 shows the invariant-mass spectra of Λ and $\bar{\Lambda}$ candidates. The fits yielded $N = 17010 \pm 200$ Λ candidates and $N = 15510 \pm 190$ $\bar{\Lambda}$ candidates. Distributions of the reconstructed proper lifetime and kinematic properties for these particles based on the same data sample were found to be described by the inclusive ARIADNE MC [4].

6.4. Reconstruction of charmed hadrons

The production of D^+ and Λ_c^+ hadrons was measured in the range of transverse momentum $0 < p_T(D^+, \Lambda_c^+) < 10$ GeV and pseudorapidity $|\eta(D^+, \Lambda_c^+)| < 1.6$. Strange-hadron candidates were combined with a further track measured in the CTD which was assigned to the primary interaction vertex.

The combinatorial background was significantly reduced by requiring:

$$\frac{p_T(D^+)}{E_T^{\theta > 10^\circ}} > 0.1 \text{ and } \frac{p_T(\Lambda_c^+)}{E_T^{\theta > 10^\circ}} > 0.12, \quad (6.7)$$

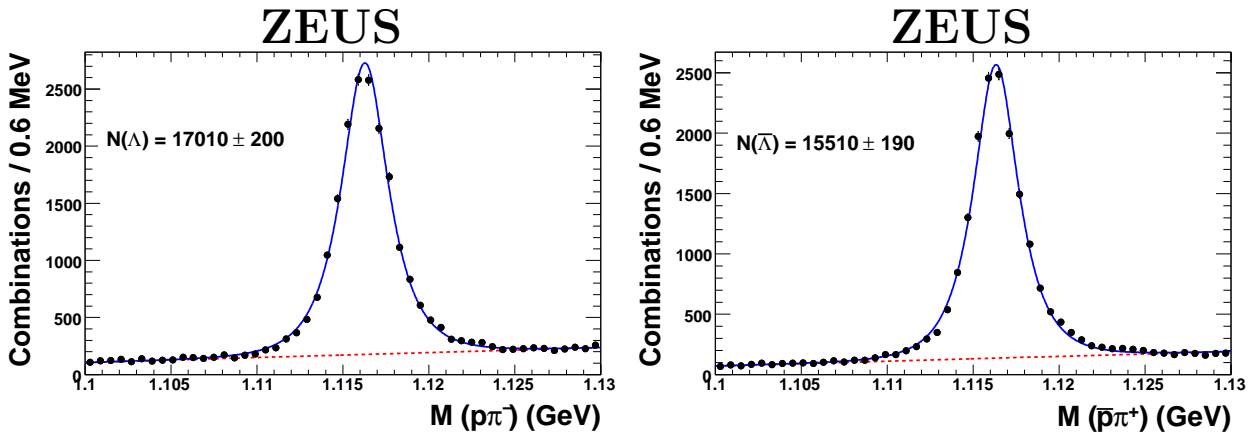


Figure 6.3.: Mass distributions of the secondary vertex candidates in the Λ (left) and $\bar{\Lambda}$ (right) samples. The statistical uncertainties are mostly smaller than the point size. For illustration the data have been fitted using the sum of a “modified” Gaussian function and a linear background.

where the transverse energy $E_T^{\theta > 10^\circ}$ was evaluated as $E_T^{\theta > 10^\circ} = \sum_{i, \theta_i > 10^\circ} (E_i \sin \theta_i)$. The sum runs over all energy deposits in the CAL with a polar angle θ above 10° . A cone in the forward direction was excluded because the description of the proton remnant by the Monte Carlo is insufficient. The details of the reconstruction of the three different decay channels are given in the next subsections.

6.4.1. Reconstruction of the decay $D^+ \rightarrow K_S^0 \pi^+$

The D^+ mesons were reconstructed from the decay channel $D^+ \rightarrow K_S^0 \pi^+$. In each event, D^+ candidates were formed from combinations of K_S^0 candidates reconstructed as described in Section 6.3 with further tracks assumed to be pions. The pion candidates were required to have $p_T(\pi^+)/E_T^{\theta > 10^\circ} > 0.04$. Only pion candidates with $dE/dx < 1.5$ mips were considered. This cut removed low momentum kaons and protons. Further reduction of the combinatorial background was achieved by cutting on the angle between the pion in the D^+ rest frame and the D^+ flight direction, $\theta^*(\pi^+)$. Different cuts depending on $p_T(D^+)$ were used because the background combinations more and more tend to higher values of $\cos \theta^*$ for increasing $p_T(D^+)$. The following requirements were imposed to ensure optimal background suppression:

- $\cos \theta^*(\pi^+) < 0.9$ for $0.0 < p_T(D^+) < 1.5$ GeV;
- $\cos \theta^*(\pi^+) < 0.8$ for $1.5 < p_T(D^+) < 3.0$ GeV;
- $\cos \theta^*(\pi^+) < 0.6$ for $3.0 < p_T(D^+) < 10.0$ GeV.

The selection criteria for D^+ mesons were tuned to provide the best possible acceptance for the signal and at the same time the best possible rejection of the background. The RAPGAP MC was used to simulate the signal while $K_S^0 \pi^+$ combinations from the data

excluding the mass range $1.82 < M(K_S^0\pi^+) < 1.92$ GeV, i.e. outside the region of the D^+ signal, were used to model the background.

Signal extraction procedure

The $K_S^0\pi^+$ invariant-mass distribution was fitted with the sum of contributions from the signal, the non-resonant background and a reflection caused by $D_s^+ \rightarrow K_S^0 K^+$ decays. The signal was described by a Gaussian function defined as:

$$g(\sigma, M_0; M) = \frac{1}{\sqrt{2\pi}\sigma} \exp \frac{-(M - M_0)^2}{2\sigma^2}, \quad (6.8)$$

where M_0 and σ are the resonance mass and width, respectively. For the background a sum of Chebyshev polynomials up to the second order was used:

$$b(A, B, C; y(M)) = A \cdot (1 + B \cdot y + C \cdot (2y^2 - 1)), \quad (6.9)$$

where $y(M) = (2M - M_{\max} - M_{\min}) / (M_{\max} - M_{\min})$ and $M_{\max}(M_{\min}) = 2.1(1.6)$ GeV is the upper (lower) limit of the range where the fit was performed.

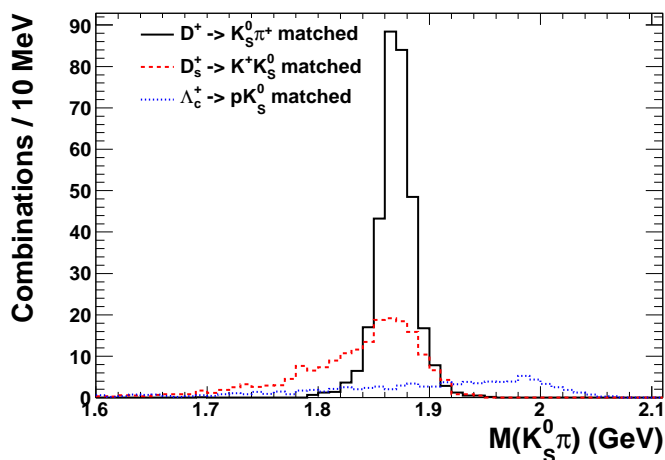


Figure 6.4.: Invariant-mass spectra of reconstructed candidates matched to $D^+ \rightarrow K_S^0\pi^+$, $D_s^+ \rightarrow K_S^0 K^+$ and $\Lambda_c^+ \rightarrow p K_S^0$ decays on generator level. The histograms were obtained from the RAPGAP MC and normalised to an integrated luminosity of 120.4 pb^{-1} .

Reflections are structures in the $K_S^0\pi^+$ invariant-mass distribution close to the D^+ mass caused by decays of other hadrons. The influence of reflections caused by the decays $D_s^+ \rightarrow K_S^0 K^+$ and $\Lambda_c^+ \rightarrow p K_S^0$ is illustrated in Fig. 6.4. The invariant-mass spectra for the signal and possible reflections are compared. Candidates after the full selection as

described above matched¹ to $D^+ \rightarrow K_S^0 \pi^+$, $D_s^+ \rightarrow K_S^0 K^+$ and $\Lambda_c^+ \rightarrow p K_S^0$ decays on generator level are shown. The distribution of matched $\Lambda_c^+ \rightarrow p K_S^0$ decays is almost flat in the signal region. On the other hand, the invariant-mass spectrum of matched $D_s^+ \rightarrow K^+ K_S^0$ decays shows a clear maximum at the D^+ mass. Hence this contribution needs to be considered in the signal extraction procedure. The invariant-mass distribution of reconstructed candidates matched to $D_s^+ \rightarrow K_S^0 K^+$ decays on generator level is referred to as $r(M)$ in the following.

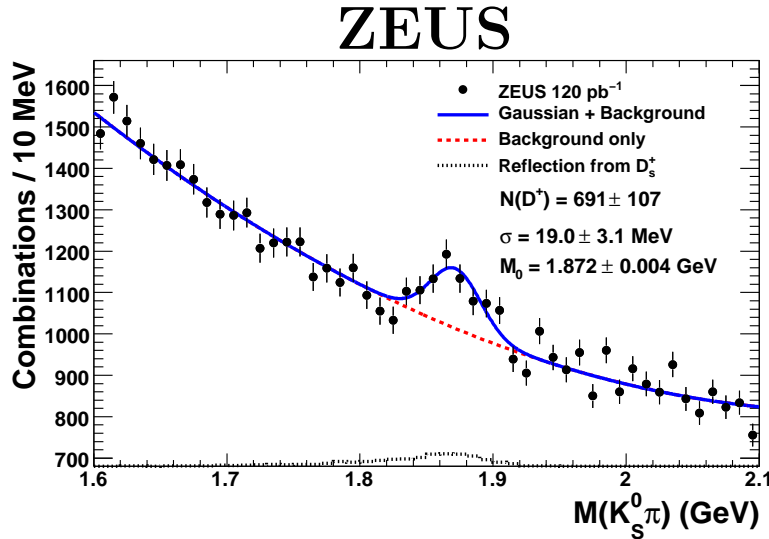


Figure 6.5.: The $M(K_S^0 \pi^+)$ distribution (dots) for D^+ candidates. The reflection caused by the decay $D_s^+ \rightarrow K_S^0 K^+$ has been subtracted as described in the text. The solid curve represents a fit to the sum of a Gaussian signal and a background function, while the background contribution alone is given by the dashed curve. The dotted histogram shows the reflection scaled as described in the text with an offset of 680 to position it at the bottom of the figure.

The normalisation of $r(M)$ with respect to the Gaussian signal assumed for $D^+ \rightarrow K_S^0 \pi^+$ decays is based on previously measured fragmentation fractions f [72] and branching ratios \mathcal{B} [143] and the detector acceptances for both decay channels. For this purpose, the invariant-mass distribution of the reflection was normalised to unity and then multiplied by the expected ratio of D_s^+ to D^+ mesons:

$$R = \frac{f(c \rightarrow D_s^+) \cdot \mathcal{B}(D_s^+ \rightarrow K_S^0 K^+ \rightarrow \pi^+ \pi^- K^+)}{f(c \rightarrow D^+) \cdot \mathcal{B}(D^+ \rightarrow K_S^0 \pi^+ \rightarrow \pi^+ \pi^- \pi^+)} \cdot \frac{\mathcal{A}(D_s^+)}{\mathcal{A}(D^+)} = 0.44 \pm 0.10, \quad (6.10)$$

where $\mathcal{A}(D_s^+)$ and $\mathcal{A}(D^+)$ are the reconstruction acceptances for D_s^+ and D^+ mesons, respectively, as obtained from the Monte Carlo simulation. The resulting fitting function

¹Details of the matching procedure are explained in Appendix A (taken from [4]). The efficiency of the matching procedure was generally above 99%.

is given by:

$$F(A, B, C, D, \sigma, M_0; M) = b(A, B, C; y(M)) + D \cdot [r(M) + g(\sigma, M_0; M)], \quad (6.11)$$

where the parameters A , B , C , D , σ and M_0 were determined by the fit.

Figure 6.5 shows the invariant-mass spectrum for the D^+ candidates after the reflection was subtracted using the fit, resulting in a 20% reduction in the number of D^+ mesons. A clear signal is visible. The fit yielded a D^+ mass of 1872 ± 4 MeV, in agreement with the PDG value [143]. The width of the signal was 19.0 ± 3.1 MeV, reflecting the detector resolution. The number of D^+ mesons yielded by the fit was $N(D^+) = 691 \pm 107$.

In order to extract the D^+ -meson yields in bins of some observable, the signals in all analysis bins of a given quantity were fitted simultaneously, fixing the ratios of the widths in the bins to the Monte Carlo prediction. All other parameters including the masses were left free for all bins in the simultaneous fit.

The signal in the region $0 < p_T(D^+) < 1.5$ GeV that was not accessible in previous measurements is shown in Fig. 6.6. A signal of 3.3 standard deviations is visible at the nominal D^+ mass.

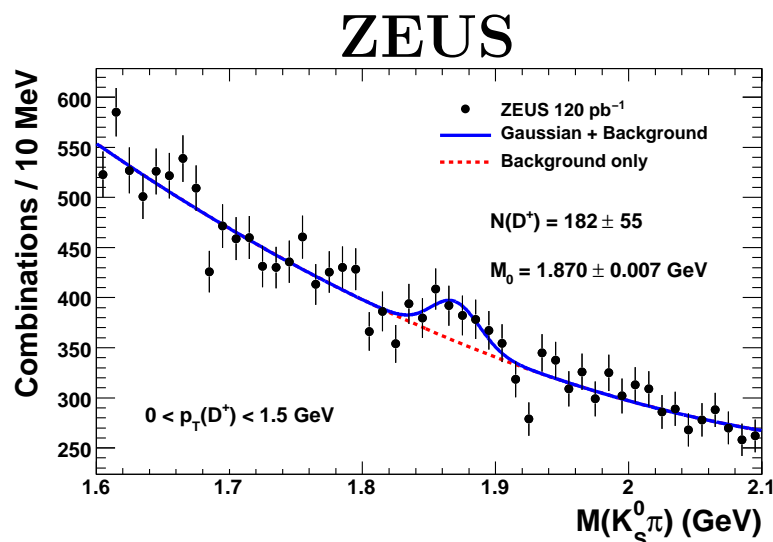


Figure 6.6.: The $M(K_S^0\pi^+)$ distribution (dots) for D^+ candidates in the region $0 < p_T(D^+) < 1.5$ GeV. The reflection caused by the decay $D_s^+ \rightarrow K_S^0 K^+$ has been subtracted as described in the text. The solid curve represents a fit to the sum of a Gaussian signal and a background function, while the background contribution alone is given by the dashed curve.

Control distributions for D^+ variables and Monte Carlo reweighting

To verify the acceptance corrections extracted using the RAPGAP MC samples, differential distributions for different D^+ and event properties are compared at detector level in Fig. 6.7. The numbers of candidates in the data were obtained using the fit procedure

described above. Each entry in the histograms corresponds to a D^+ candidate. The distributions obtained using the D^+ Monte Carlo were area normalised to the data. To obtain the shown histograms for the Monte Carlo, the distributions for the individual data taking periods were scaled to the corresponding integrated luminosities measured for the data before they were added.

In general, the Monte Carlo describes the data reasonably well. To improve the agreement further, the RAPGAP Monte Carlo was reweighted to reproduce the $p_T(D^+)$ distributions observed in the data. The same weights were also applied to the D_s^+ and Λ_c^+ samples. A comparison of the weighted Monte Carlo to the data is shown in Fig. 6.8. The weighting in $p_T(D^+)$ also improved the description of $E_T^{\theta > 10^\circ}$ by the RAPGAP MC.

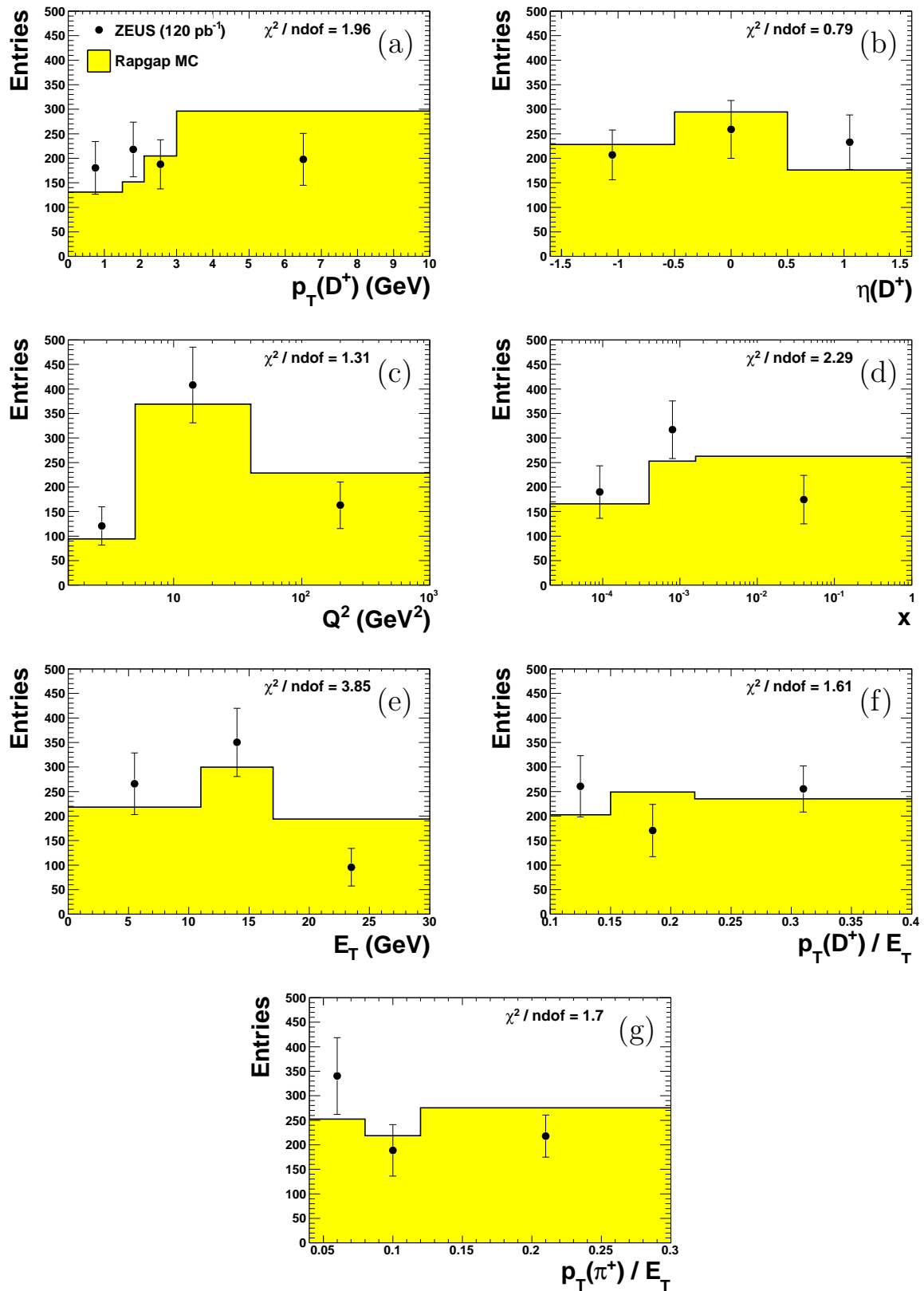


Figure 6.7.: Number of D^+ candidates in the data (dots) in bins of (a) $p_T(D^+)$, (b) $\eta(D^+)$, (c) Q^2 , (d) x , (e) $E_T^{\theta > 10^\circ}$, (f) $p_T(D^+) / E_T^{\theta > 10^\circ}$ and (g) $p_T(\pi^+) / E_T^{\theta > 10^\circ}$. The distributions obtained from the RAPGAP MC (yellow area) were normalised to the data.

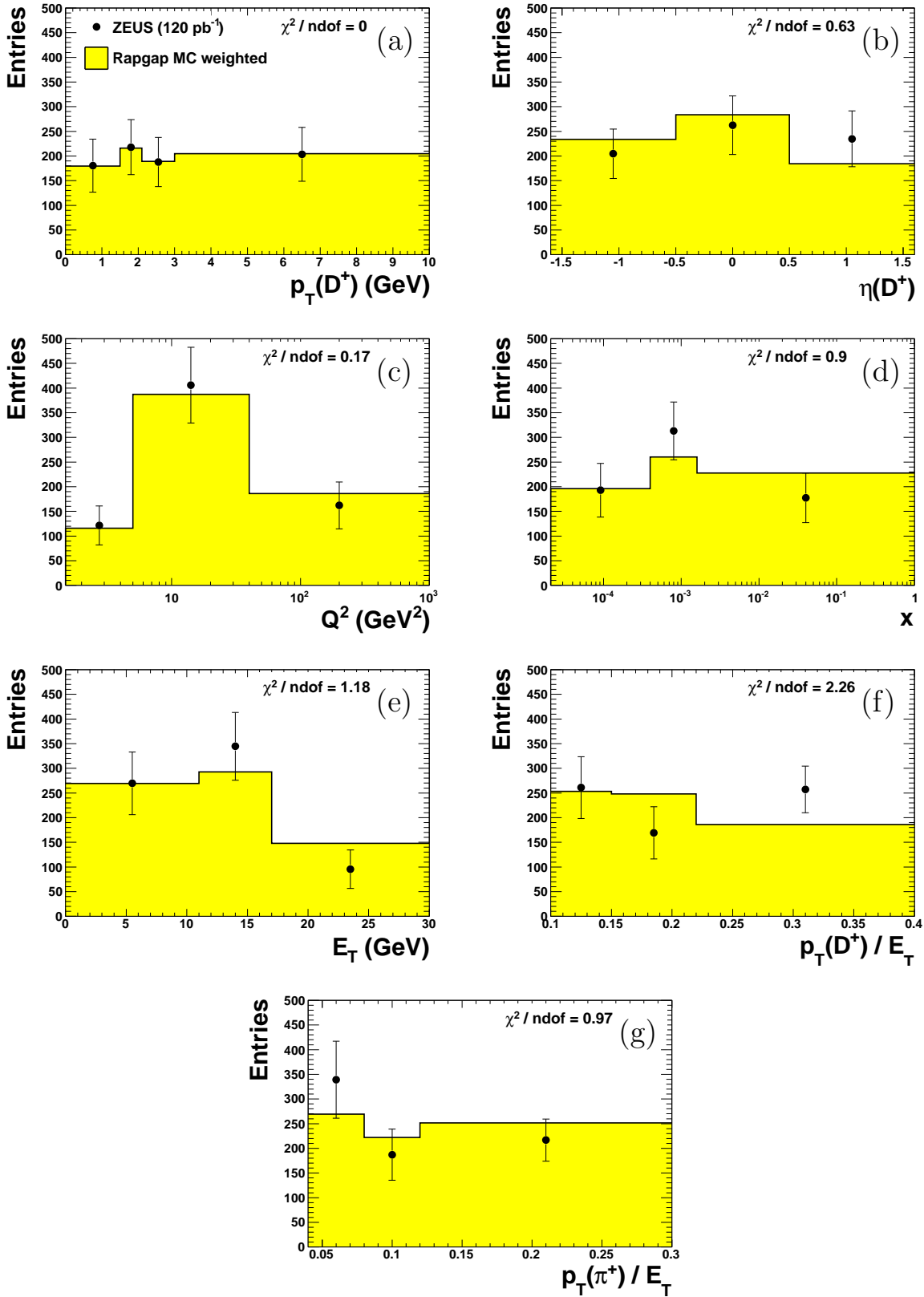


Figure 6.8.: Number of D^+ candidates in the data (dots) in bins of (a) $p_T(D^+)$, (b) $\eta(D^+)$, (c) Q^2 , (d) x , (e) $E_T^{\theta > 10^\circ}$, (f) $p_T(D^+) / E_T^{\theta > 10^\circ}$ and (g) $p_T(\pi^+) / E_T^{\theta > 10^\circ}$. The distributions obtained from the weighted RAPGAP MC (yellow area) were normalised to the data.

6.4.2. Reconstruction of the decay $\Lambda_c^+ \rightarrow pK_S^0$

The Λ_c^+ baryons were reconstructed from the decay channel $\Lambda_c^+ \rightarrow pK_S^0$. In each event, Λ_c^+ candidates were formed from combinations of K_S^0 candidates reconstructed as described in Section 6.3 with proton candidates. The proton-candidate selection used the energy-loss measurement in the CTD. Tracks fitted to the primary vertex with more than 40 hits were considered. The proton band was parametrised separately for positive and negative tracks from an examination of dE/dx as a function of the momentum [4]. The proton selection was checked by studying proton-candidate tracks from Λ decays. To remove the region where the proton band completely overlaps the pion band, the proton momentum was required to be less than 1.5 GeV and a cut on $dE/dx > 1.2$ mips was applied. The proton selection is illustrated in Fig. 6.9. Due to the proton selection described above, reflections from $D^+ \rightarrow K_S^0\pi^+$ and $D_s^+ \rightarrow K_S^0K^+$ decays are suppressed.

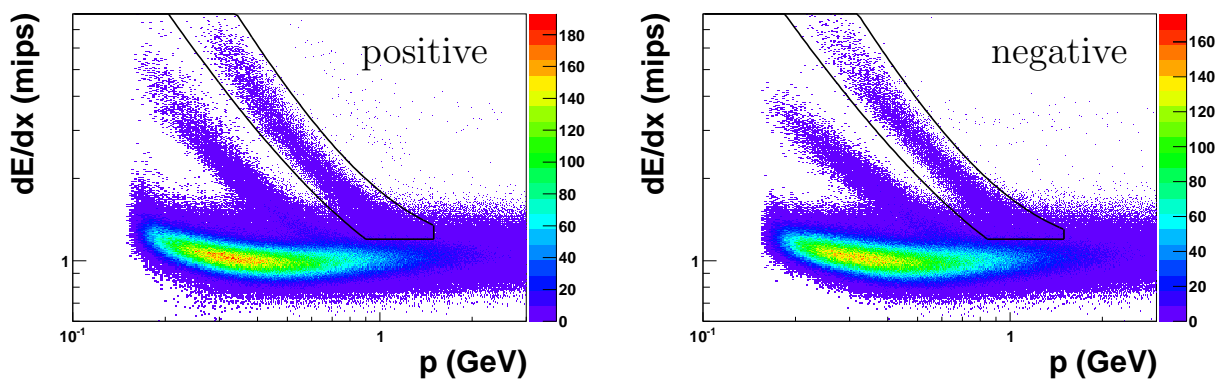


Figure 6.9.: The measured energy loss of charged particles as a function of the momentum for positive (left) and negative (right) tracks. The cuts to select proton candidates are shown by black lines.

As a result of the cut on the proton momentum, there was no acceptance for Λ_c^+ baryons at very high $p_T(\Lambda_c^+)$. Hence the measurement of the cross section for this decay channel was restricted to the region $0 < p_T(\Lambda_c^+) < 6$ GeV.

Figure 6.10 shows the $M(pK_S^0)$ distribution for the Λ_c^+ candidates. A clear signal is seen at the nominal value of the Λ_c^+ mass [143]. The mass distribution was fitted to the sum of a Gaussian function describing the signal and the function defined in Eq. 6.9 to describe the non-resonant background. The number of reconstructed Λ_c^+ baryons yielded by the fit was $N(\Lambda_c^+) = 79 \pm 25$.

6.4.3. Reconstruction of the decay $\Lambda_c^+ \rightarrow \Lambda\pi^+$

The Λ_c^+ baryons were also reconstructed from the decay channel $\Lambda_c^+ \rightarrow \Lambda\pi^+$. In each event, Λ_c^+ candidates were formed from combinations of Λ candidates as described in Section 6.3, with further tracks assumed to be pions. The pion candidates were required to have $p_T(\pi^+)/E_T^{\theta > 10^\circ} > 0.05$. Only pion candidates with $dE/dx < 1.5$ mips were considered. To suppress combinatorial background further, the cut $\cos\theta^*(\pi^+) < 0.8$ was

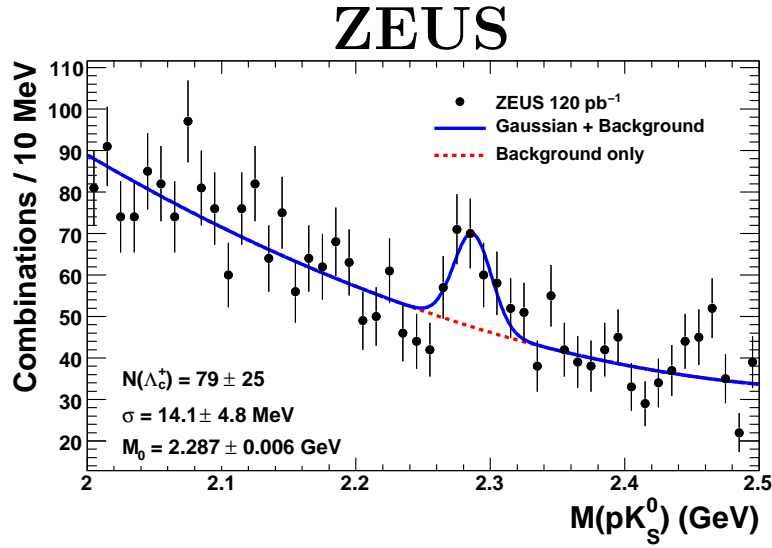


Figure 6.10.: The $M(pK_S^0)$ distribution (dots) for Λ_c^+ candidates in the region $0 < p_T(\Lambda_c^+) < 6$ GeV. The solid curve represents a fit to the sum of a Gaussian signal and a background function, while the background contribution alone is given by the dashed curve.

imposed, where $\theta^*(\pi^+)$ is the angle between the pion in the Λ_c^+ rest frame and the Λ_c^+ flight direction. This cut was applied since, in contrast to the signal, the background distribution peaks at $\cos\theta^*(\pi^+) \approx 1$.

Figure 6.11 shows the $M(\Lambda\pi)$ distribution for the Λ_c^+ candidates. Wrong-charge combinations in the data sample are also shown. For wrong-charge combinations, the sum of the charges of the proton from the Λ candidate and the further track is equal to zero. The distribution of wrong-charge combinations was multiplied by a factor 0.91 to normalise to the right-charge combinations in the region outside the peak. The data were fitted to the sum of a Gaussian function describing the signal and the background function defined in Eq. 6.9. The number of reconstructed Λ_c^+ baryons obtained from the fit was $N(\Lambda_c^+) = 84 \pm 34$.

The signal-to-background ratio for both studied Λ_c^+ decay channels is similar. Figure 6.12 shows the invariant-mass spectrum containing both $\Lambda_c^+ \rightarrow pK_S^0$ and $\Lambda_c^+ \rightarrow \Lambda\pi^+$ candidates. The fit yielded $N(\Lambda_c^+) = 146 \pm 33$ candidates. This combined peak was not used to extract any cross sections or fragmentation fractions.

6.5. Cross sections and acceptance corrections

For a given observable, Y , the differential cross section in a bin i was determined using:

$$\left(\frac{d\sigma}{dY}\right)_i = \frac{N_i(D^+)}{\mathcal{A}_i \cdot \mathcal{L} \cdot \mathcal{B} \cdot \Delta Y_i},$$

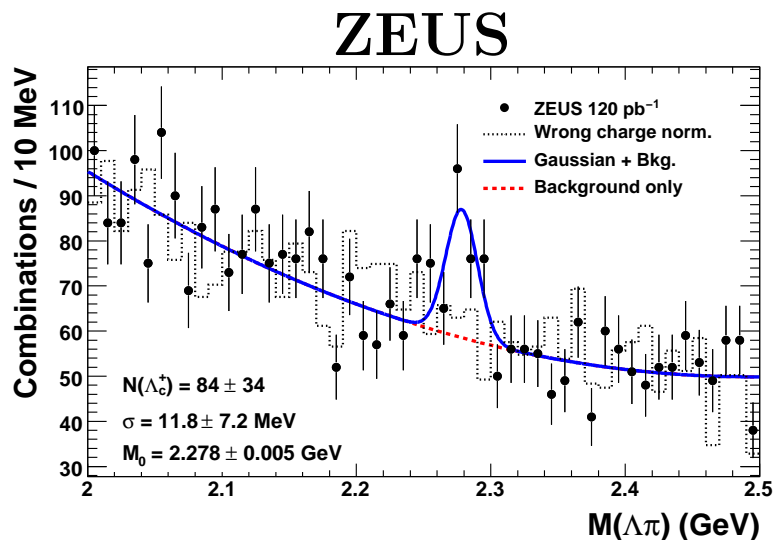


Figure 6.11.: The $M(\Lambda\pi^+)$ distribution (dots) for Λ_c^+ candidates. The solid curve represents a fit to the sum of a Gaussian signal and a background function, while the background contribution alone is given by the dashed curve. The dotted histogram shows the distribution of wrong-charge combinations normalised to the right-charge combinations in the region outside the peak.

where $N_i(D^+)$ is the number of reconstructed D^+ mesons in bin i having size ΔY_i . The reconstruction acceptance, \mathcal{A}_i , takes into account migrations, efficiencies and QED radiative effects for the i^{th} bin, \mathcal{L} is the integrated luminosity and \mathcal{B} is the branching ratio [143] for the decay channel used in the reconstruction. The total visible production cross sections were determined using:

$$\sigma = \frac{N(D^+, \Lambda_c^+)}{\mathcal{A} \cdot \mathcal{L} \cdot \mathcal{B}},$$

where $N(D^+, \Lambda_c^+)$ and \mathcal{A} were determined for the whole kinematic range of the measurement.

The reconstruction acceptance is defined as the fraction of D^+ or Λ_c^+ hadrons in the kinematic region of the measurement which is reconstructed by the detector. All acceptances were obtained from the RAPGAP Monte Carlo separately for each data taking period. The overall acceptance was calculated as the luminosity weighted average of the values for the individual data taking periods:

$$\mathcal{A} = \frac{N_{96/97}^{\text{det}}}{N_{96/96}^{\text{gen}}} \cdot \frac{\mathcal{L}_{96/97}}{\mathcal{L}} + \frac{N_{98/99}^{\text{det}}}{N_{98/99}^{\text{gen}}} \cdot \frac{\mathcal{L}_{98/99}}{\mathcal{L}} + \frac{N_{99/00}^{\text{det}}}{N_{99/00}^{\text{gen}}} \cdot \frac{\mathcal{L}_{99/00}}{\mathcal{L}}, \quad (6.12)$$

where N^{gen} is the number of generated D^+ or Λ_c^+ hadrons in the kinematic region of the measurement and N^{det} is the number of reconstructed candidates after all selection cuts on detector level.

To calculate cross sections using a single number for the integrated luminosity, the accep-

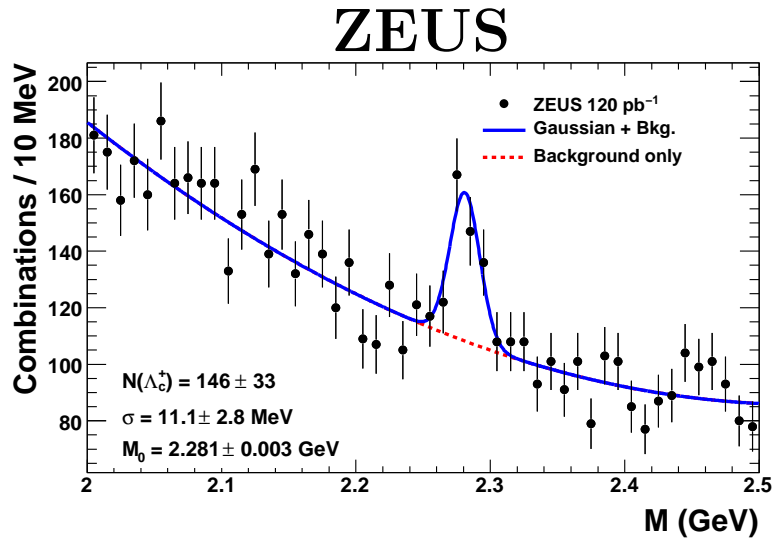


Figure 6.12.: The invariant mass distribution (dots) for $\Lambda_c^+ \rightarrow pK_S^0$ and $\Lambda_c^+ \rightarrow \Lambda\pi^+$ candidates. The solid curve represents a fit to the sum of a Gaussian signal and a background function, while the background contribution alone is given by the dashed curve.

tance contained the prescale factors of the DIS01 slot. This was achieved applying the prescale factors to N^{det} , but not to N^{gen} .

The D^+ reconstruction capability of the detector is illustrated in Fig. 6.13 where only events passing the trigger and box cuts on detector level were considered for N^{gen} . In this way the effect of the DIS01 prescales was removed from the acceptance values. Even in the region $p_T(D^+) < 1.5$ GeV the acceptance is about 6%. At high values of $p_T(D^+)$, the acceptance decreased again because some K_S^0 particles decayed inside the CTD.

The b -quark contribution, predicted by the MC simulation, was subtracted from all measured cross sections. The RAPGAP prediction for beauty production was multiplied by two, in agreement with previous ZEUS measurements of beauty production in DIS [83, 84]. The subtraction of the b -quark contribution reduced the measured cross sections by 2–3% for the D^+ and about 1% for the Λ_c^+ .

There is no sizable acceptance for charmed hadrons in the transverse-momentum range $0 < p_T(D^+, \Lambda_c^+) < 0.5$ GeV. Hence an extrapolation using the reference Monte Carlo was performed when the cross sections were extracted. For example, the extrapolation accounts for 6% of the D^+ production in the full kinematic range of the measurement and for 11% of the D^+ production in the restricted range $0 < p_T(D^+) < 1.5$ GeV.

In the Monte Carlo simulation, the Λ_c^+ baryons were assumed to be unpolarised. Due to the limited statistical precision, the measurements described in this chapter are not sensitive to the Λ_c^+ polarisation.

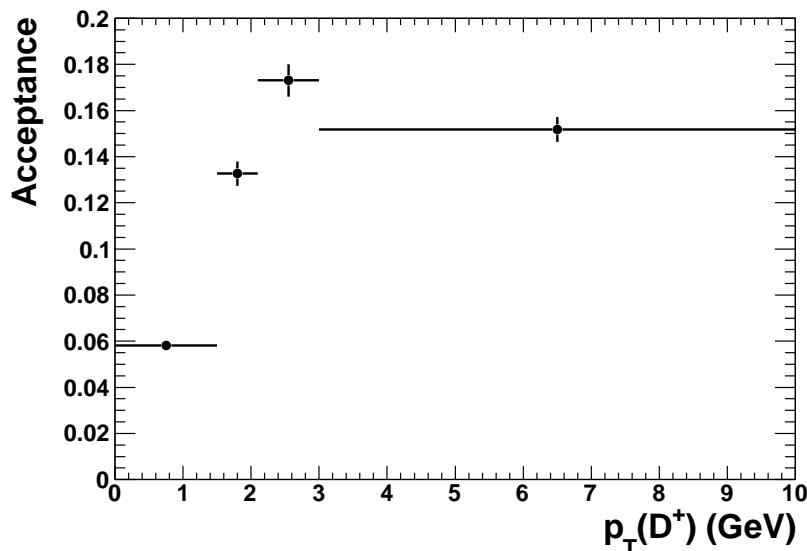


Figure 6.13.: D^+ reconstruction acceptance for events passing the trigger.

6.6. Systematic uncertainties

The systematic uncertainties of the measured cross sections and fragmentation fractions were determined by changing the analysis procedure and repeating all calculations. In the measurement of the differential and total cross sections, the following groups of systematic uncertainty sources were considered. The effects on the total cross sections are shown in parentheses (D^+ ; $\Lambda_c^+ \rightarrow pK_S^0$; $\Lambda_c^+ \rightarrow \Lambda\pi^+$):

- $\{\delta_1\}$ event and DIS selection ($+4\%$, $+1\%$, $+8\%$; -3% , -2% , -4%). The following cut variations were applied to data and MC simultaneously:
 - the cut on y_{JB} was changed to $y_{JB} > 0.03$;
 - the cut on the scattered electron energy E'_e was changed to $E'_e > 11$ GeV;
 - the cuts on δ were changed by $+2$ GeV;
 - the cut on $|Z_{\text{vertex}}|$ was changed to $|Z_{\text{vertex}}| < 45$ cm;
 - additionally, a box cut of 26×14 cm² was used for all electron candidates without an SRTD requirement;
- $\{\delta_2\}$ Q^2 and x reconstruction ($<1\%$; -3% ; -6%). The double-angle method was used for the reconstruction of Q^2 and x instead of the electron method;
- $\{\delta_3\}$ energy scale ($\pm 2\%$; $+3\%$, $+2\%$; -4% , -4%). To account for the uncertainty of the absolute CAL energy scale, the energy of the scattered electron was raised and lowered by 1% and $E_T^{\theta > 10^\circ}$ was raised and lowered by 2%. These variations were only applied to the MC;

- $\{\delta_4\}$ model dependence of the acceptance corrections:
 - the process $cg \rightarrow cg$ was included in the RAPGAP MC sample (+5%; +3%; +9%);
 - the MC samples were not reweighted in $p_T(D^+, D_s^+, \Lambda_c^+)$ (−17%; −6%; −21%);
- $\{\delta_5\}$ uncertainty of the beauty subtraction ($^{+1\%}_{-3\%}$; $\pm 1\%$; $< 1\%$). This was determined by varying the subtracted b -quark contributions by a factor 2;
- $\{\delta_6\}$ uncertainty of the signal extraction procedure ($^{+12\%}_{-9\%}$; $^{+14\%}_{-5\%}$; $^{+24\%}_{-8\%}$):
 - the fit was repeated changing the invariant mass window of 1.6 – 2.1 GeV by ± 50 MeV on both sides for $D^+ \rightarrow K_S^0 \pi^+$ decays. Similarly, the considered invariant mass region of 2.0 – 2.5 GeV was changed by ± 50 MeV for $\Lambda_c^+ \rightarrow p K_S^0$ decays and by ± 30 MeV for the channel $\Lambda_c^+ \rightarrow \Lambda \pi^+$;
 - the choice of the background function was assigned an uncertainty of $\pm 5\%$. This value was estimated by comparing the fit results obtained using different choices for the background function, such as polynomials of different orders or exponential functions;
 - for differential cross sections, the assumed Gaussian width ratios were varied by $\pm 10\%$;
- $\{\delta_7\}$ uncertainty in the luminosity measurement of $\pm 2.0\%$.

The following uncertainty was considered only for the decays $D^+ \rightarrow K_S^0 \pi^+$ and $\Lambda_c^+ \rightarrow K_S^0 p$:

- $\{\delta_8\}$ K_S^0 reconstruction (+2%; +1%; −). Since the MC signal had a narrower width than observed in the data, the invariant-mass window for the K_S^0 candidate selection was reduced to $0.486 < M(\pi^+ \pi^-) < 0.510$ GeV in the MC only.

The following source of uncertainty was considered only for the decay $D^+ \rightarrow K_S^0 \pi^+$:

- $\{\delta_9\}$ uncertainty of the reflection subtraction ($\pm 5\%$; −; −). The normalisation of the D_s^+ reflection was changed by the uncertainty of R (see Eq. 6.10) due to the uncertainties of the fragmentation fractions and branching ratios used in the calculation.

The following source of uncertainty was considered only for the decay $\Lambda_c^+ \rightarrow K_S^0 p$:

- $\{\delta_{10}\}$ proton reconstruction (−; −14%; −). The following checks were performed:
 - the number of hits required for the proton candidates was lowered to 32;
 - the uncertainty of the dE/dx simulation for low-momentum protons was evaluated changing the parametrisation of the proton band [4];
 - the cut on the energy loss was lowered to $dE/dx > 1.15$ mips.

The following source of uncertainty was considered only for the decay $\Lambda_c^+ \rightarrow \Lambda\pi^+$:

- $\{\delta_{11}\}$ Λ reconstruction ($-$; $-$; $+4\%$). Since the MC signals had a narrower width than observed in the data, the invariant-mass window for the Λ candidate selection was reduced to $1.113 < M(p\pi) < 1.120$ GeV in the MC only.

The dominant contribution to the systematic uncertainty of the total visible D^+ cross section was obtained when the RAPGAP MC was not reweighted in $p_T(D^+)$. This variation was included since the shape of the $p_T(D^+)$ distribution before the reweighting (see Fig. 6.7) is not significantly excluded by the data.

Contributions from the different systematic uncertainties were calculated and added in quadrature separately for positive and negative variations. These estimates were made in each bin in which the differential cross sections were measured. Uncertainties due to those on the luminosity measurement and branching ratios were only included in the measured D^+ and Λ_c^+ total cross sections. For differential cross sections, these uncertainties are not included.

As an additional check, the dE/dx efficiency for pions and protons was verified directly in the data using K_S^0 and Λ decays. For the $D^+ \rightarrow K_S^0\pi^+$ decay channel, the effect of the dE/dx cut on the pion candidate tracks was very small and the result changed only marginally when the cut was released.

6.7. NLO QCD predictions for D^+ production

NLO QCD predictions for the measured D^+ production cross sections were obtained using the HVQDIS program. The FFNS variant of the ZEUS-S NLO QCD fit [144] to structure function data was used as the parametrisation of the proton parton density functions. In this fit, $\alpha_s(M_Z)$ was set to 0.118 and the pole mass of the charm quark was set to 1.5 GeV; the same mass was used in the HVQDIS calculation. The renormalisation and factorisation scales were set to $\mu_R = \mu_F = \sqrt{Q^2 + 4m_c^2}$. The charm fragmentation to the D^+ meson was modelled using the Peterson function (see Sec. 2.6.2) with the Peterson parameter, ϵ , set to 0.079 [79]. For the hadronisation fraction, $f(c \rightarrow D^+)$, the value $0.216_{-0.029}^{+0.021}$ was used [72].

The HVQDIS predictions for the production of D^+ mesons are affected by the theoretical uncertainties listed below. The uncertainty on the total cross section is given in parentheses:

- the ZEUS PDF uncertainties were propagated from the experimental uncertainties of the fitted data ($+5.3\%$);
- the charm quark mass was changed consistently in the PDF fit and in HVQDIS by ± 0.15 GeV ($+15.2\%$);
- the renormalisation scale was varied by a factor 2 ($+19.7\%$);
- the factorisation scale was changed by a factor 2 independently of the renormalisation scale ($+13.1\%$);

6. Measurement of D^+ and Λ_c^+ production

- the ϵ parameter of the Peterson fragmentation function was changed to 0.01 and 0.1 [79, 81]. This modification affects the shapes of the p_T , Q^2 and x distributions (+0.1% / -0.4%).

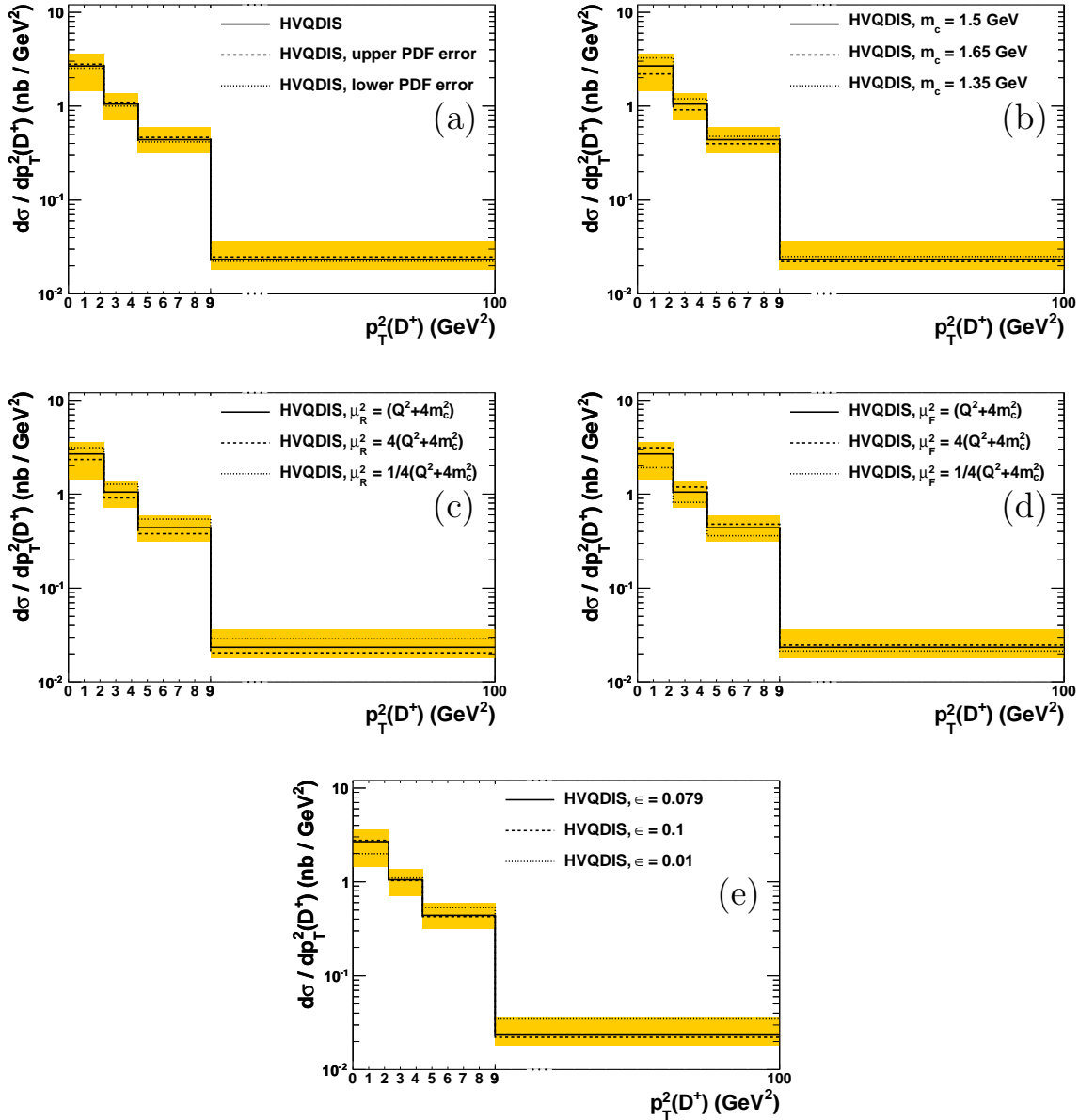


Figure 6.14.: Uncertainties of the HVQDIS NLO QCD prediction due to the (a) PDF uncertainty, (b) charm mass, (c) renormalisation scale, (d) factorisation scale and (e) Peterson parameter as a function of $p_T^2(D^+)$. Details on the individual variations are given in the text. The prediction for the default parameters is shown by black lines. The variations are shown by dashed and dotted lines. The total uncertainty of the prediction is given by the yellow bands.

The effect of the individual uncertainties as a function of $p_T^2(D^+)$ is shown in Fig. 6.14. The largest uncertainties are caused by the renormalisation and factorisation scales. At low values of $p_T^2(D^+)$, the charm mass causes a similar uncertainty. The variation of the Peterson parameter is important at the lowest and highest values of $p_T^2(D^+)$.

6.8. Cross sections and extraction of $f(c \rightarrow \Lambda_c^+)$

Charm hadron production cross sections were measured using the reconstructed D^+ and Λ_c^+ signals in the kinematic range $0 < p_T(D^+, \Lambda_c^+) < 10$ GeV, $|\eta(D^+, \Lambda_c^+)| < 1.6$, $1.5 < Q^2 < 1000$ GeV² and $0.02 < y < 0.7$. The average cross sections obtained from the two different running periods ($\sqrt{s} = 300$ and 318 GeV) are expressed in terms of cross sections at $\sqrt{s} = 318$ GeV. This involves a typical correction of +1% determined using HVQDIS. In addition to the statistical and systematic uncertainties, a third set of uncertainties is quoted for the measured cross sections and charm fragmentation fractions, due to the propagation of the relevant branching-ratio uncertainties.

6.8.1. D^+ cross sections

The following total visible cross section for D^+ mesons was measured:

$$\sigma(D^+) = 25.7 \pm 4.1 \text{ (stat.) } {}_{-5.2}^{+3.8} \text{ (syst.) } \pm 0.8 \text{ (br.) nb.}$$

The corresponding prediction from HVQDIS is $\sigma(D^+) = 12.7 {}_{-4.1}^{+3.8}$ nb. The measured and predicted cross sections are in agreement to better than two standard deviations.

The differential cross sections as functions of $p_T^2(D^+)$, $\eta(D^+)$, x and Q^2 are shown in Fig. 6.15 and given in Tab. 6.7. The bins in $p_T^2(D^+)$ correspond to the bins in $p_T(D^+)$ shown in Figs. 6.7, 6.8 and 6.13. The corresponding signal peaks are shown in Appendix B. The cross sections in Q^2 and x fall by about three orders of magnitude, while the cross section in $p_T^2(D^+)$ falls by about two orders of magnitude in the measured region. There is no significant dependence of the cross section on $\eta(D^+)$. The HVQDIS predictions describe the shape of all measured differential cross sections reasonably well. The differential cross section in $p_T^2(D^+)$ is compared to a previous ZEUS result [72] for $p_T^2(D^+) > 9$ GeV². The two measurements are in good agreement.

At low values of $p_T^2(D^+)$, the data tend to lie above the HVQDIS prediction. However, no significant deviation is observed. In the bins $0 < p_T^2(D^+) < 2.25$ GeV² and $2.25 < p_T^2(D^+) < 4.41$ GeV², the ratios of the data to the NLO QCD prediction are 1.3 and 1.6 standard deviations above unity, respectively. The agreement between the data and QCD predictions might improve in the future in this region if corrections obtained using threshold resummation (see Fig. 2.10) become available.

To allow a direct comparison to a recent measurement of D^+ production by the ZEUS collaboration using a lifetime tag [71], the cross section was extracted for the kinematic region defined by $1.5 < p_T(D^+) < 15$ GeV, $|\eta(D^+)| < 1.6$, $5.0 < Q^2 < 1000$ GeV² and $0.02 < y < 0.7$. The measurements using different decay channels and different techniques were found to be consistent. More details are given in Appendix C.

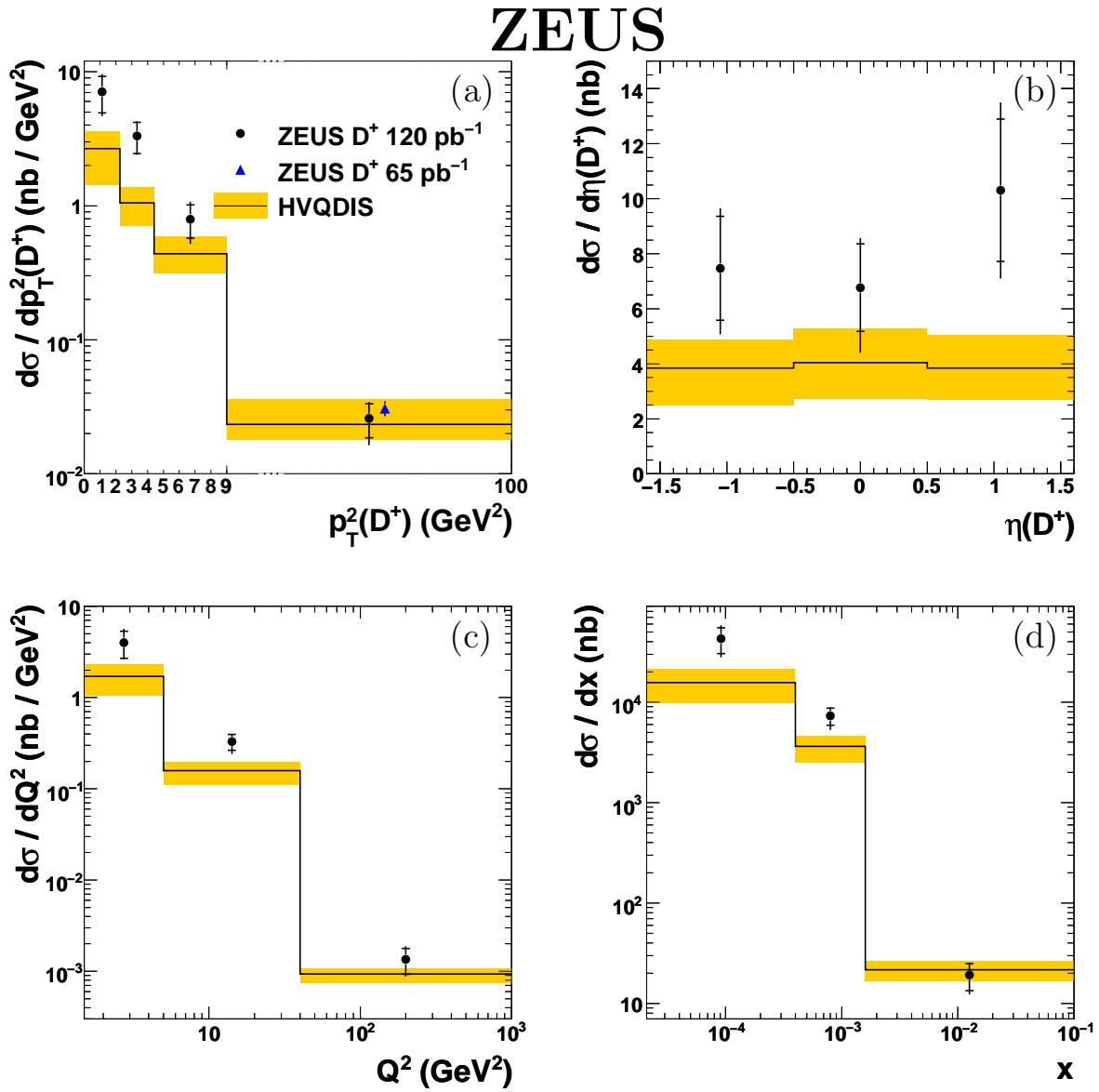


Figure 6.15.: Differential D^+ cross sections as a function of (a) $p_T^2(D^+)$, (b) $\eta(D^+)$, (c) Q^2 and (d) x compared to the NLO QCD calculation of HVQDIS. The measured cross sections are shown as dots and the triangle represents a previous ZEUS result [72]. The X -axis in (a) is broken. The inner error bars show the statistical uncertainties and the outer error bars show the statistical and systematic uncertainties added in quadrature. The band shows the estimated theoretical uncertainty of the HVQDIS calculation.

$p_T^2(D^+)$ bin (GeV ²)	$d\sigma/dp_T^2(D^+)$ (nb/GeV ²)	Δ_{stat} (nb/GeV ²)	Δ_{syst} (nb/GeV ²)	
0, 2.25	7.1	± 2.1	+1.3	-1.1
2.25, 4.41	3.3	± 0.9	+0.4	-0.3
4.41, 9.0	0.80	± 0.22	+0.17	-0.16
9.0, 100.0	0.026	± 0.007	+0.004	-0.006
$\eta(D^+)$ bin	$d\sigma/d\eta(D^+)$ (nb)	Δ_{stat} (nb)	Δ_{syst} (nb)	
-1.6, -0.5	7.5	± 1.9	+1.1	-1.5
-0.5, 0.5	6.8	± 1.6	+0.9	-1.8
0.5, 1.6	10.3	± 2.6	+1.9	-1.9
Q^2 bin (GeV ²)	$d\sigma/dQ^2$ (nb/GeV ²)	Δ_{stat} (nb/GeV ²)	Δ_{syst} (nb/GeV ²)	
1.5, 5.0	4.0	± 1.3	+1.0	-0.5
5.0, 40.0	0.33	± 0.06	+0.03	-0.06
40.0, 1000.0	0.0013	± 0.0004	+0.0003	-0.0002
x bin	$d\sigma/dx$ (nb)	Δ_{stat} (nb)	Δ_{syst} (nb)	
0.000021, 0.0004	43000	± 12000	+9000	-8000
0.0004, 0.0016	7300	± 1400	+800	-1400
0.0016, 0.1	19.2	± 5.7	+2.8	-3.7

Table 6.7.: Measured D^+ cross sections as a function of $p_T^2(D^+)$, $\eta(D^+)$, Q^2 and x for $1.5 < Q^2 < 1000$ GeV², $0.02 < y < 0.7$, $0 < p_T(D^+) < 10$ GeV and $|\eta(D^+)| < 1.6$. The statistical and systematic uncertainties are shown separately. The cross sections have further uncertainties of 3% from the $D^+ \rightarrow K_S^0 \pi^+ \rightarrow \pi^+ \pi^- \pi^+$ branching ratio, and 2% from the uncertainty in the luminosity measurement.

6.8.2. Λ_c^+ cross sections and fragmentation fractions

The following Λ_c^+ cross sections were measured:

- using the decay channel $\Lambda_c^+ \rightarrow pK_S^0$ in the restricted range $0 < p_T(\Lambda_c^+) < 6$ GeV:

$$\sigma(\Lambda_c^+) = 14.9 \pm 4.9 \text{ (stat.) } {}^{+2.2}_{-2.6} \text{ (syst.) } \pm 3.9 \text{ (br.) nb;} \quad (6.13)$$

- using the decay channel $\Lambda_c^+ \rightarrow \Lambda\pi^+$:

$$\sigma(\Lambda_c^+) = 14.0 \pm 5.8 \text{ (stat.) } {}^{+3.8}_{-3.3} \text{ (syst.) } \pm 3.7 \text{ (br.) nb.} \quad (6.14)$$

To compare and combine both measurements, the value obtained for the decay channel $\Lambda_c^+ \rightarrow pK_S^0$ was multiplied by 1.01 ± 0.01 to extrapolate to the full kinematic region considered in this analysis. The cross sections obtained using different decay channels are in good agreement. To extract the Λ_c^+ fragmentation fraction, the measurements were combined taking into account all systematic uncertainties and their correlations:

$$\sigma_{\text{combined}}(\Lambda_c^+) = 14.7 \pm 3.8 \text{ (stat.) } {}^{+2.1}_{-2.2} \text{ (syst.) } \pm 3.9 \text{ (br.) nb.} \quad (6.15)$$

The individual systematic uncertainties were either assumed to be fully correlated ($\delta_1 - \delta_5, \delta_7$) or fully uncorrelated ($\delta_6, \delta_8 - \delta_{11}$) between the two measurements. The uncertainty of the branching ratio was treated as partially correlated since both branching ratios, $\mathcal{B}(\Lambda_c^+ \rightarrow pK_S^0)$ and $\mathcal{B}(\Lambda_c^+ \rightarrow \Lambda\pi^+)$, were measured relative to the decay mode $\Lambda_c^+ \rightarrow pK^-\pi^+$ [143].

The fragmentation fraction $f(c \rightarrow \Lambda_c^+)$ can be calculated using the D^+ cross section:

$$f(c \rightarrow \Lambda_c^+) = \frac{\sigma(\Lambda_c^+)}{\sigma(D^+)} \cdot f(c \rightarrow D^+). \quad (6.16)$$

In a previous ZEUS publication [72] $f(c \rightarrow D^+)$ was defined as:

$$f(c \rightarrow D^+) = \frac{\sigma^0(D^+)}{\sigma^0(D^+) + \sigma^0(D^0) + \sigma^0(D_s^+)} \cdot [1 - 1.14 \cdot f(c \rightarrow \Lambda_c^+)], \quad (6.17)$$

where $\sigma^0(D^+)$, $\sigma^0(D^0)$ and $\sigma^0(D_s^+)$ are the cross sections for $p_T(D) > 3$ GeV. The factor 1.14 takes into account the production of charm-strange baryons [72]. For D^+ and D^0 mesons the equivalent cross sections (as described elsewhere [76]) were used. Combining Eqs. 6.16 and 6.17 yields:

$$f(c \rightarrow \Lambda_c^+) = \frac{\sigma(\Lambda_c^+) \cdot \sigma^0(D^+)}{\sigma(D^+) \cdot (\sigma^0(D^+) + \sigma^0(D^0) + \sigma^0(D_s^+)) + 1.14 \sigma(\Lambda_c^+) \cdot \sigma^0(D^+)} \quad (6.18)$$

Since the cross sections $\sigma(D^+)$ and $\sigma(\Lambda_c^+)$ were measured down to $p_T(D^+, \Lambda_c^+) = 0$ GeV, no treatment of the different transverse momentum distributions for D^+ and Λ_c^+ hadrons

	$f(c \rightarrow \Lambda_c^+)$
ZEUS (DIS)	0.117 ± 0.033 (stat.) $^{+0.026}_{-0.022}$ (syst.) ± 0.027 (br.)
ZEUS (γp) [76]	0.144 ± 0.022 (stat.) $^{+0.013}_{-0.022}$ (syst.) $^{+0.037}_{-0.025}$ (br.)
combined e^+e^- data	0.076 ± 0.007 (stat. \oplus syst.) $^{+0.027}_{-0.016}$ (br.)

Table 6.8.: The fraction of c quarks hadronising to a Λ_c^+ baryon, $f(c \rightarrow \Lambda_c^+)$.

was necessary. The measured value:

$$f(c \rightarrow \Lambda_c^+) = 0.117 \pm 0.033 \text{ (stat.) } ^{+0.026}_{-0.022} \text{ (syst.) } \pm 0.027 \text{ (br.)}, \quad (6.19)$$

is compared to previous measurements in Table 6.8. The result is consistent with a previous ZEUS measurement in the photoproduction regime [76] and with the e^+e^- average value. This comparison is visualised in Fig. 6.16 [145]. The correlated part of the branching ratio uncertainty is not shown in the figure.

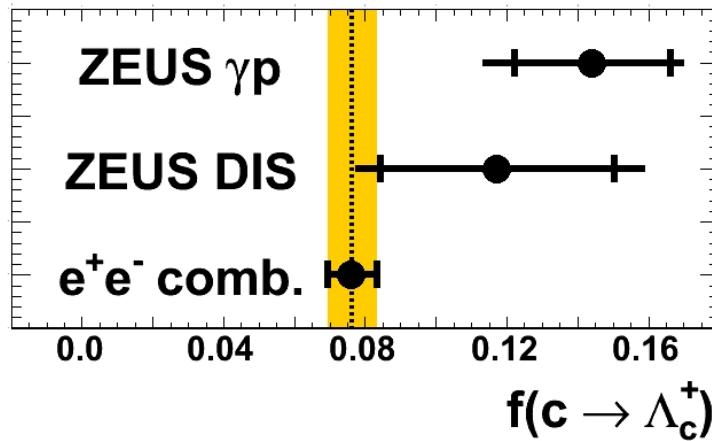


Figure 6.16.: $f \rightarrow \Lambda_c^+$ from different measurements. The correlated part of the branching ratio uncertainty is not shown.

The extraction of the fragmentation fraction for any charmed meson or baryon requires the measurement of all charmed ground state hadrons with sizable production cross sections. No measurement of Λ_c^+ production in DIS was available in the past. Hence assumptions on $f(c \rightarrow \Lambda_c^+)$ had to be used when the fragmentation fractions for D mesons were calculated resulting in additional systematic uncertainties. The measurement of $f(c \rightarrow \Lambda_c^+)$ presented here allows to recalculate the fragmentation fractions using previous measurements of D meson production. This will improve extractions of $F_2^{c\bar{c}}$ from visible D^{*+} cross sections which rely on $f(c \rightarrow D^{*+})$.

6.9. Conclusions

Open-charm production in ep collisions at HERA has been measured in deep inelastic scattering for the first time at HERA using the three decay channels $D^+ \rightarrow K_S^0 \pi^+$, $\Lambda_c^+ \rightarrow p \bar{K}_S^0$ and $\Lambda_c^+ \rightarrow \Lambda \pi^+$. The presence of a neutral strange hadron in the final state allowed the measurement to be extended to very low transverse momenta of the reconstructed charmed hadrons.

The total visible and differential cross sections for D^+ production are in reasonable agreement with NLO QCD predictions. The region $p_T(D) < 1.5$ GeV was studied for the first time in ep interactions. This is particularly important since the extraction of $F_2^{c\bar{c}}$ using visible cross sections for D meson production requires an extrapolation to the full range in $p_T(D)$. This extrapolation is usually performed using the same NLO QCD prediction which was tested in the presented analysis. The agreement of the data and QCD predictions at low $p_T(D^+)$ might be improved in the future using threshold resummation. At higher values of $p_T(D^+)$, the measured cross sections are in good agreement with previous results.

The fragmentation fraction $f(c \rightarrow \Lambda_c^+)$ has been measured for the first time at HERA in deep inelastic scattering. The result obtained from a combination of two decay channels is consistent with a previous measurement performed in the photoproduction regime and with the average e^+e^- value. The measurement of $f(c \rightarrow \Lambda_c^+)$ also improves the knowledge of the fragmentation fractions for other charmed hadrons.

The data collected during the HERA I period are particularly suited for the analysis presented in this chapter. The DIS electron can not be fully reconstructed in the region $Q^2 < 5$ GeV² for the HERA II data. The events where $p_T(D^+)$ is small tend to low values of Q^2 . Additionally, the resolution for K_S^0 and Λ particles and the proton efficiency are better than for the HERA II detector configuration since charged particles passed through less material before entering the CTD.

7. Measurement of $F_2^{b\bar{b}}$ and $F_2^{c\bar{c}}$ using lifetime information

In this chapter a measurement of charm and beauty quark production based on lifetime information is presented. The MVD allowed the reconstruction of secondary vertices from charm and beauty hadron decays. The mass and decay-length significance of inclusive secondary vertices were used to extract the charm content and beauty content in events with a jet. The analysis used the full HERA II data sample recorded between 2004 and 2007.

First, an overview of the analysed data and Monte Carlo samples is given. The event selection and the extraction of the charm and beauty signals are discussed in the following sections. Cross sections for jet production in charm and beauty events are compared to QCD predictions. Double differential cross sections in x and Q^2 were used to extract the charm and beauty contributions to the proton structure function F_2 . The measured $F_2^{c\bar{c}}$ and $F_2^{b\bar{b}}$ values are compared to previous measurements and predictions from perturbative QCD.

To extract $F_2^{c\bar{c}}$, the cut on the transverse energy of the jets used as reference axes for the reconstruction of secondary vertices was reduced. Hence the measurement of charm production is described in a separate section.

The measured cross sections for jet production in beauty events and the extracted $F_2^{b\bar{b}}$ values were first shown publicly at the DIS 2010 [146] and ICHEP 2010 [147] conferences, respectively.

7.1. Data samples and Monte Carlo sets

The data set collected during the HERA II period and the Monte Carlo samples used to extract the charm and beauty content in the data are described in detail in the following.

7.1.1. Data samples

Data collected during the HERA II period were analysed. Events were preselected using the EVTAK and MVDTAKE routines. The first selects events if the data quality of the CTD, CAL, trigger chain and luminosity measurement was good while the latter required that the MVD was in a good state during data taking. The luminosities of the individual data taking periods after the EVTAK and MVDTAKE selections are summarised in Tab. 7.1.

The events collected before March 2004 were not considered since the inclusive DIS triggers were not fully available for that period. The whole analysed data sample corresponds to

an integrated luminosity of $354 \pm 7 \text{ pb}^{-1}$. This number was used for the calculation of all cross sections presented in the following.

Year	Interaction	\sqrt{s} (GeV)	\mathcal{L} (pb^{-1})	$\sigma_{\text{syst.}}$ (%)
2004	e^+p	318	30.48	3.5
2005	e^-p	318	133.69	1.8
2006	e^-p	318	52.69	1.8
2006/2007	e^+p	318	137.29	1.8
Total			354.15	2.0

Table 7.1.: Data samples collected with the ZEUS detector between 2004 and 2007. Events recorded before March 2004 were not considered in the analysis.

7.1.2. Monte Carlo samples

To model properties of light quark events, flavour inclusive samples generated using the ARIADNE MC program were used. An overview of the samples is given in Tab 7.2. All events were generated for $Q^2 > 4 \text{ GeV}^2$. As shown in the table, the integrated luminosities of the ARIADNE samples are similar to those of the data.

Period	Interaction	Events	\mathcal{L} (pb^{-1})
2004	e^+p	10234955	32.0
2005	e^-p	42938144	134.3
2006	e^-p	17478901	54.7
2006/2007	e^+p	45188338	141.4

Table 7.2.: ARIADNE Monte Carlo samples used for the HERA II data taking period.

Since different trigger configurations were used during the data taking for a single period, dedicated subsamples were generated for each relevant trigger configuration. Detailed information on the subsamples for each individual trigger configuration are given in Appendix D. The event numbers and luminosities given in the tables in this section are summarising all subsamples for a given data taking period.

Charm and beauty events were generated using the RAPGAP MC program. The CTEQ5L parametrisation was used for the proton PDFs. To account for the migration of low Q^2 events into the kinematic range of the measurement, the charm and beauty samples were generated for $Q^2 > 1.5 \text{ GeV}^2$ and $Q^2 > 1 \text{ GeV}^2$, respectively. The charm quark mass was set to 1.5 GeV and the beauty quark mass to 4.75 GeV.

Tab. 7.3 shows the samples where charm quarks were produced by the BGF process. In the region $Q^2 < 4 \text{ GeV}^2$, the integrated luminosities of the charm MC samples are similar to those of the data. At higher values of Q^2 , the integrated luminosity is several times

Period	Interaction	minimal Q^2 (GeV ²)	Events	\mathcal{L} (pb ⁻¹)
2004	e^+p	1.5	1953344	32.0
2004	e^+p	4.0	3459940	97.8
2004	e^+p	16.0	1820000	157.6
2005	e^-p	1.5	8999815	147.4
2005	e^-p	4.0	9959951	281.7
2005	e^-p	8.0	6000000	280.9
2005	e^-p	16.0	3200000	276.9
2005	e^-p	50.0	1400000	422.0
2006	e^-p	1.5	3325059	54.5
2006	e^-p	4.0	5857146	165.2
2006	e^-p	16.0	3200000	58.9
2006/2007	e^+p	1.5	8657663	141.9
2006/2007	e^+p	4.0	17551483	496.7

Table 7.3.: Monte Carlo samples for charm quark production by the BGF process.

larger than that of the data. These samples were used to obtain the central values of the measured cross sections.

To estimate the systematic uncertainty caused by the model dependence of the Monte Carlo simulation, additional RAPGAP samples were generated where charm was produced by the excitation process $cg \rightarrow cg$. An overview of the samples is given in Tab. 7.4.

Period	Interaction	minimal Q^2 (GeV ²)	Events	\mathcal{L} (pb ⁻¹)
2004	e^+p	1.5	863745	32.6
2004	e^+p	4.0	1209949	97.8
2005	e^-p	1.5	3902159	147.4
2005	e^-p	4.0	3485060	282.4
2006	e^-p	1.5	1457645	54.9
2006	e^-p	4.0	2048089	165.2
2006/2007	e^+p	1.5	13199925	498.1

Table 7.4.: Monte Carlo samples for charm quark production by the process $cg \rightarrow cg$.

The beauty MC samples used for the analysis described in this chapter are shown in Tab. 7.5. Beauty quarks were produced by the BGF process. The integrated luminosities of the Monte Carlo samples for beauty quark production are 16 – 18 times larger than those of the data.

Period	Interaction	Events	\mathcal{L} (pb $^{-1}$)
2004	e^+p	840000	925.4
2005	e^-p	1919946	2115.1
2006	e^-p	828275	912.6
2006/2007	e^+p	2339942	2577.9

Table 7.5.: RAPGAP beauty MC samples used for the HERA II data taking period. All samples were generated in the region $Q^2 > 1$ GeV 2 .

7.2. Event selection

Compared to the HERA I period, the online and offline selections for NC DIS events needed to be adjusted to cope with the increased luminosity, different background conditions and a changed detector geometry. Especially the beam hole in the RCAL was widened to install additional focusing magnets for the electron beam inside the detector. Larger box cuts had to be used and thus events with Q^2 values below 5 GeV 2 could not be reconstructed any more.

7.2.1. Online event selection

In this section the trigger chain used to select inclusive DIS events online is explained in detail. The requirements imposed at each trigger level are given.

First level trigger

As for the HERA I data taking period, the FLT slots could be vetoed by signals from the C5, Veto Wall, SRTD or CTD detectors. A logical or of nine slots was used to select events at the first trigger level. The following requirements were imposed by the different slots:

- **FLT28:** A good track, $FisoE$ or $BisoE$, and a total transverse energy in the CAL of greater than 18 GeV;
- **FLT30:** $RisoE$ and an EMC energy deposit of greater than 4 GeV in the RCAL;
- **FLT40:** EMC energy in the CAL greater than 20 GeV;
- **FLT41:** Transverse energy in the CAL greater than 30 GeV;
- **FLT43:** Transverse energy in the CAL greater than 15 GeV and a good track;
- **FLT44:** A good track and more than 4.8 GeV EMC energy in the BCAL or more than 3.4 GeV EMC energy in the RCAL;
- **FLT46:** A good track, $RisoE3q$ and an EMC energy in the RCAL greater than 2 GeV;

- **FLT47:** Total energy in the CAL greater than 4 GeV, *RisoE3q* and an EMC energy in the RCAL greater than 2 GeV;
- **FLT62:** Multiple isolated EMC energy deposits.

Here *R/B/FisoE* refers to an isolated EMC energy deposit (*isoE*) in the RCAL, BCAL or FACL, respectively. To calculate *RisoE3q*, one of the four RCAL quadrants which suffered from background caused by off-momentum electrons was excluded.

Second level trigger

Events had to be accepted by the SLT SPP01 slot. The following conditions were applied:

- the event had to be accepted at the first trigger level by a logical or of the FLT28, FLT30, FLT40, FLT41, FLT43, FLT44, FTL46, FLT47 and FLT62 slots;
- $\delta_{\text{SLT}} > 30$ GeV, where δ_{SLT} was calculated using the nominal interaction point;
- a logical or of the following requirements:
 - EMC energy deposit in the RCAL greater than 2.5 GeV;
 - EMC energy deposit in the BCAL greater than 2.5 GeV;
 - EMC energy deposit in the FCAL greater than 10 GeV;
 - HAC energy in the FCAL greater than 10 GeV;
- an SLT electron with an energy of $E'_e > 5$ GeV.

No tracking requirements were imposed at the second trigger level.

Third level trigger

Slots selecting inclusive NC DIS events were used at the third trigger level. For the 2004 e^+p and 2005 e^-p periods the SPP02 slot was used which imposed the following requirements:

- the event had to be accepted at the SLT by SPP01;
- an electron with an energy $E'_e > 4$ GeV had to be found;
- electrons in the RCAL were required to be outside a box centred around the beam pipe of 24×24 cm²;
- $30 < \delta_{\text{TLT}} < 100$ GeV, where δ_{TLT} was calculated using the reconstructed vertex.

For the 2006 e^-p and 2006/2007 e^-p periods, the SPP02 slot was replaced by the SPP09 slot with a slightly increased box cut of 30×30 cm². All other requirements were identical as before. To compensate for the larger box cut, two additional slots were used. The following requirements were imposed for the HPP31 slot:

- the event had to be accepted at the SLT by SPP01;
- an electron with an energy $E'_e > 7$ GeV had to be found;
- electrons in the RCAL were required to be outside a box centred around the beam pipe of 24×24 cm²;
- $\delta_{\text{TLT}} > 34$ GeV;
- $Q_{\text{TLT}}^2 > 6$ GeV²;
- at least one track had to be reconstructed in the CTD with $p_T > 200$ MeV.

Additionally, the HFL17 slot was used for the 2006 e^-p and 2006/2007 e^-p periods where at least two tracks reconstructed in the CTD were required. The other requirements were identical to the SPP02 slot.

7.2.2. NC DIS selection

To select NC DIS events, the following requirements were imposed offline:

- $44 < \delta < 65$ GeV, where δ was reconstructed from EFOs. More details on this cut are given in Sec. 6.2.2;
- a scattered electron had to be reconstructed by the SINISTRA finder with a probability greater than 0.9 and an energy $E'_e > 10$ GeV;
- the impact position of the electron on the face of the RCAL had to be outside the region 26×26 cm² centred on $X = Y = 0$;
- $5 < Q_{\text{DA}}^2 < 1000$ GeV²;
- $y_{\text{JB}} > 0.02$ and $y_e < 0.7$;
- a primary vertex position in the range $|Z_{\text{vertex}}| < 30$ cm.

For certain parts of the data collected during the 2006 e^-p and 2006/2007 e^+p periods, electron candidates reconstructed in the RCAL in the rectangle defined by $7.515 < X_e < 31.845$ cm and $7.90 < Y_e < 31.90$ cm were not considered. The RCAL efficiency was not correctly reproduced by the Monte Carlo for these candidates.

7.3. Signal determination

In this section the technique used to extract the beauty and charm contents in the data sample is discussed.

7.3.1. Secondary vertex reconstruction

The standard procedure to search for secondary vertices provided by the ZEUS reconstruction software is not suitable for all investigated event topologies. Hence different vertexing techniques dependent on the investigated final state need to be applied at the analysis level. The procedure to identify beauty and charm quark decays using inclusive secondary decay vertices is described in the following. It was originally developed to measure beauty production in the photoproduction region [148, 149] and was adopted for deep inelastic scattering here.

The first step to reconstruct secondary vertices was to select tracks to be used as input for the vertex fits. Jets reconstructed as described in Sec. 5.6 in the region $E_T^{\text{jet}} > 5 \text{ GeV}^1$ and $-1.6 < \eta^{\text{jet}} < 2.2$ were used as reference axes. Tracks were associated to the closest jet in the $\eta - \phi$ plane if:

$$\Delta R = \sqrt{(\Delta\eta)^2 + (\Delta\phi)^2} < 1, \quad (7.1)$$

where $\Delta\eta = \eta^{\text{track}} - \eta^{\text{jet}}$ and $\Delta\phi = \phi^{\text{track}} - \phi^{\text{jet}}$. Additionally, the tracks had to fulfil the following requirements:

- $p_T^{\text{track}} > 500 \text{ MeV}$;
- at least four hits in the MVD.

If at least two tracks passing these conditions were associated to a jet, a vertex was fit using the DAF (see Sec. 5.2.1) was performed. The beam spot constraint was not used to fit secondary vertices. For successful fits the algorithm returned the vertex position and its covariance matrix. To calculate the invariant mass of the secondary vertices, m_{vtx} , the charged pion mass was assumed for all tracks.

After all secondary vertices were reconstructed in an event, the remaining tracks not associated to any secondary vertex were used to fit a new primary vertex. The beam spot was used as a constraint for this *reduced primary vertex*.

The procedure described above was not optimised to reconstruct the exact heavy hadron decay vertices. An example are cascade decays of B mesons into D mesons where the obtained secondary vertices are neither identical to the B decay vertices nor to the D decay vertices.

The following requirements were imposed to select secondary vertices:

- $\chi^2/n_{\text{dof}} < 6$, where n_{dof} is the number of degrees of freedom in the vertex fit. This cut ensured a reasonable quality of the secondary vertex fit;
- a distance between the beam spot and the secondary vertex in the $X - Y$ plane of less than 1 cm. This requirement suppressed backgrounds caused by photon conversions and hadronic interactions in the beam pipe or detector material, and strange hadron decays.

¹For a dedicated measurement of charm production this requirement was later lowered to 4.2 GeV (see Sec. 7.5).

7. Measurement of $F_2^{b\bar{b}}$ and $F_2^{c\bar{c}}$ using lifetime information

- a secondary vertex mass in the range $1 < m_{\text{vtx}} < 6$ GeV. At low masses, there is a significant contribution from K_S^0 and Λ decays. Hence the region $m_{\text{vtx}} < 1$ GeV was excluded. On the other hand, no beauty or charm signals were found in the region $m_{\text{vtx}} > 6$ GeV;
- a secondary vertex position in the range $|Z_{\text{sec. vertex}}| < 30$ cm.

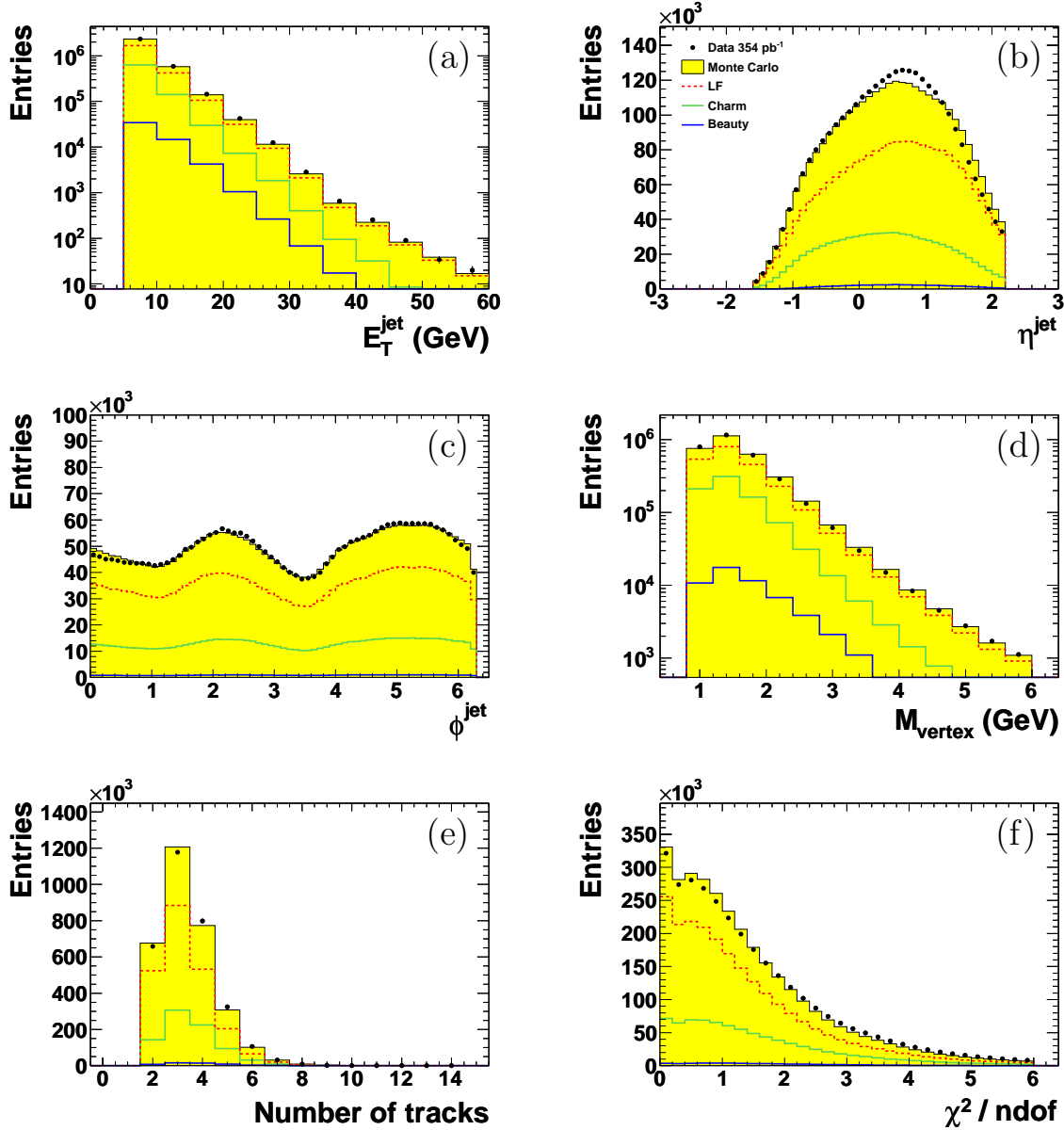


Figure 7.1.: The jet and vertex variables (a) E_T^{jet} , (b) η^{jet} , (c) ϕ^{jet} , (d) m_{vtx} , (e) secondary vertex multiplicity and (f) χ^2/ndof . The data (dots) are compared to the sum of all MC samples (yellow area). The individual MC samples are shown as solid lines.

After all selection cuts as described above, the data sample contained 3.1×10^6 secondary vertex candidates. Fig 7.1 shows control plots of secondary vertex properties and of variables describing the associated jets. The contributions of the MC samples for beauty, charm and light flavour events are shown separately and combined. The individual contributions were scaled using the result of the signal extraction procedure (see Sec. 7.3.3). The ARIADNE MC was reweighted in E_T^{jet} (see Sec. 7.3.4). The η^{jet} distribution predicted by the ARIADNE MC differs somewhat from the data. All other observed distributions are reasonably well described by the Monte Carlo simulation.

7.3.2. Decay length and significance

As mentioned before, beauty and charmed hadron decays were separated from the background caused by light flavour events using lifetime information. First, the decay length of each secondary vertex was calculated in the $X - Y$ plane. The decay length was calculated as the distance between the beam spot and the secondary vertex. It was shown that almost identical distributions were obtained if the beam spot constrained reduced primary vertex was used instead of the beam spot [149]. The beam spot position was corrected for the beam tilt at the Z position of the reduced primary vertex for every event. The sign of the decay length was obtained using the axis of the associated jet. If the two-dimensional vector pointing from the beam spot to the secondary vertex, \vec{L} , was located in the same hemisphere as the two-dimensional jet axis, \vec{j} , i.e. the scalar product $\vec{L} \cdot \vec{j}$ was positive, a positive sign was assigned to the decay length. Otherwise the sign of the decay length was negative.

Additionally, the decay length was projected onto the axis of the associated jet as illustrated in Fig 7.2. This was done to avoid a dip around zero in the decay-length distribution (see Fig. 7.3). The calculation of the projected decay length, L_{XY} , can be summarised as follows:

$$L_{XY} = \vec{L} \cdot \frac{\vec{j}}{|\vec{j}|} = \begin{pmatrix} X_{\text{vtx}} - X_{\text{bsp}} \\ Y_{\text{vtx}} - Y_{\text{bsp}} \end{pmatrix} \cdot \frac{\vec{j}}{|\vec{j}|}, \quad (7.2)$$

where X_{vtx} (X_{bsp}) and Y_{vtx} (Y_{bsp}) are the X and Y positions of the secondary vertex (beam spot). The projected decay lengths for beauty, charm and light quark MC events are shown in Fig 7.3. The distribution for light quarks is almost symmetrical around

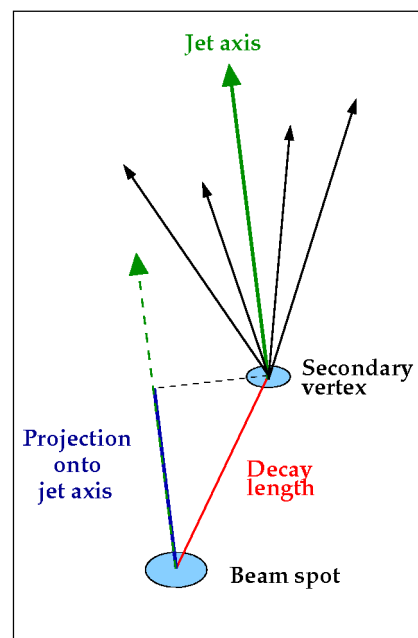


Figure 7.2.: Illustration of the decay length and its projection on the jet axis.

$X = 0$ while the beauty and charm distributions have more entries for positive decay lengths.

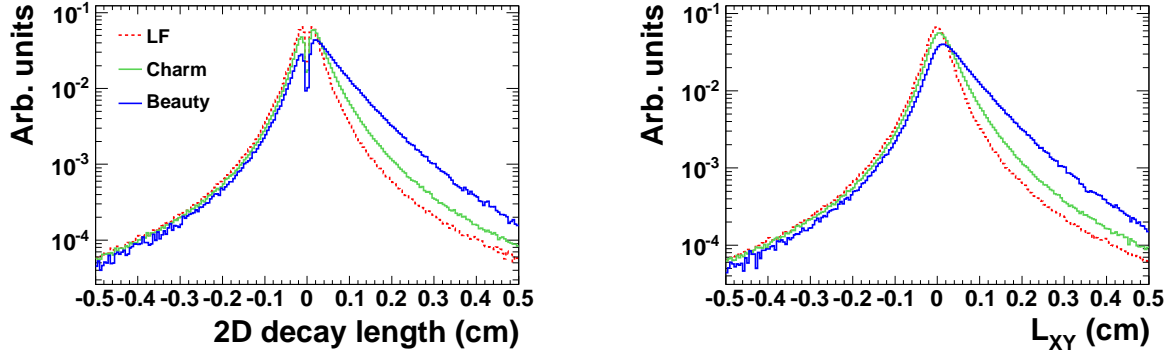


Figure 7.3.: Comparison of the decay length (left) to the projected decay length (right) distributions for beauty (line), charm (dashed line) and light quark (dotted line) MC events. All distributions were normalised to unity.

The uncertainty of the projected decay length is given by:

$$\sigma(L_{XY}) = \sqrt{\hat{j} \cdot (C_{\text{bsp}} + C_{\text{vtx}}) \cdot \hat{j}}, \quad (7.3)$$

where $\hat{j} = \vec{j}/|\vec{j}|$ is the normalised jet momentum vector and C_{bsp} and C_{vtx} are the covariance matrices of the beam spot and secondary vertex, respectively. The covariance matrix of the secondary vertex was provided by the vertex fit and describes the uncertainties of the different coordinates of the secondary vertex and their correlations. The diagonal elements of C_{bsp} are given by the squared measured beam spot widths in the X and Y directions (see Sec. 5.2.1) while all other elements are zero. The *decay-length significance* was defined as the projected decay length divided by its error:

$$S = \frac{L_{XY}}{\sigma(L_{XY})}. \quad (7.4)$$

The decay-length significance for MC events is shown in Fig. 7.4. The asymmetries for the charm and beauty distributions are even stronger compared to the projected decay-length distributions.

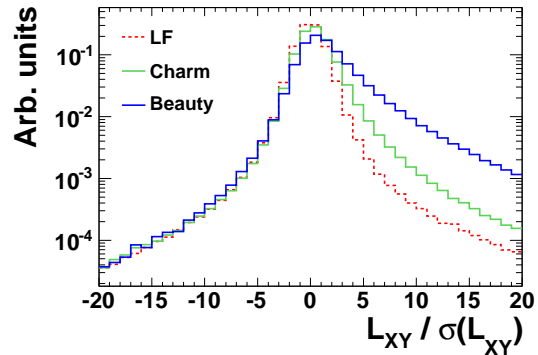


Figure 7.4.: Decay-length significance distributions for beauty (line), charm (dashed line) and light quark (dotted line) MC events. All distributions were normalised to unity.

7.3.3. Extraction of the charm and beauty fractions

Two quantities were used to extract the beauty and charm quark contributions to the data sample. The heavy flavour contribution was enhanced using the decay-length significance explained above. The invariant mass of the secondary vertices was used as an additional constraint. To illustrate the benefit of using a combination of the decay-length significance and the vertex mass, Fig 7.5 shows the decay-length significance for all selected secondary vertices and for the restricted mass range $2 < m_{\text{vtx}} < 6$ GeV. An almost pure beauty sample was obtained for secondary vertices in the range $2 < m_{\text{vtx}} < 6$ GeV and $S \gtrsim 8$.

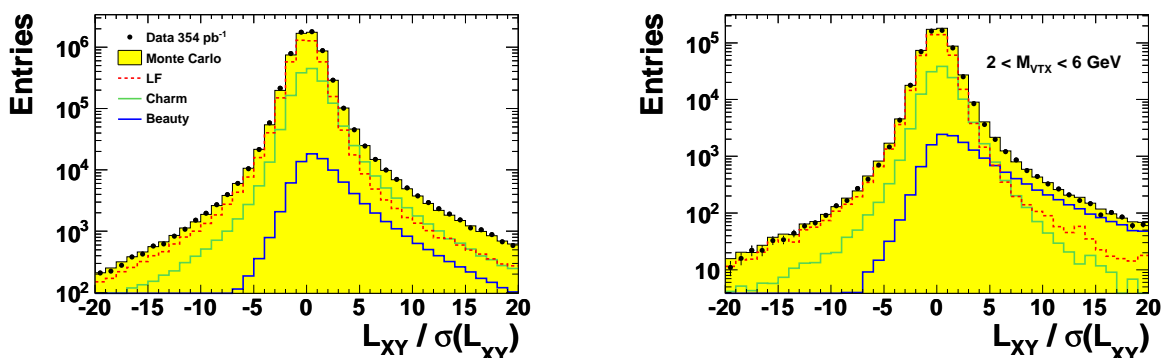


Figure 7.5.: Decay-length significance for all vertex candidates (left) and for the restricted region $2 < m_{\text{vtx}} < 6$ GeV (right). The data (dots) are compared to the sum of all MC samples (yellow area) and to the individual contributions separately (lines). The MC samples were scaled using the fit result (see text).

The negative part ($S < 0$) of the significance distribution, S^- , which was caused by the finite resolution of the detector was accordingly mirrored onto and subtracted from the positive side ($S > 0$) of the significance distribution, S^+ . In this way the contribution from light quarks is minimised since its decay-length significance distribution is largely symmetric around zero. Additionally, possible systematic effects arising from differences in the tails of the unmirrored decay-length distribution between the data and the Monte Carlo are reduced. The mirrored and subtracted decay-length distributions, $S^+ - S^-$, for all selected secondary vertices and for the restricted mass range $2 < m_{\text{vtx}} < 6$ GeV are shown in Fig. 7.6. As expected, the light quark contribution is drastically reduced. To extract the beauty, charm and light quark contents in the data, the mirrored significance distributions were split into three bins of the vertex mass. The following binning was used for the vertex mass:

$$\begin{aligned}
 &1 < m_{\text{vtx}} < 1.4 \text{ GeV}, \\
 &1.4 < m_{\text{vtx}} < 2.0 \text{ GeV and} \\
 &2.0 < m_{\text{vtx}} < 6.0 \text{ GeV.}
 \end{aligned}$$

A χ^2 fit of the Monte Carlo templates to the data was performed simultaneously in

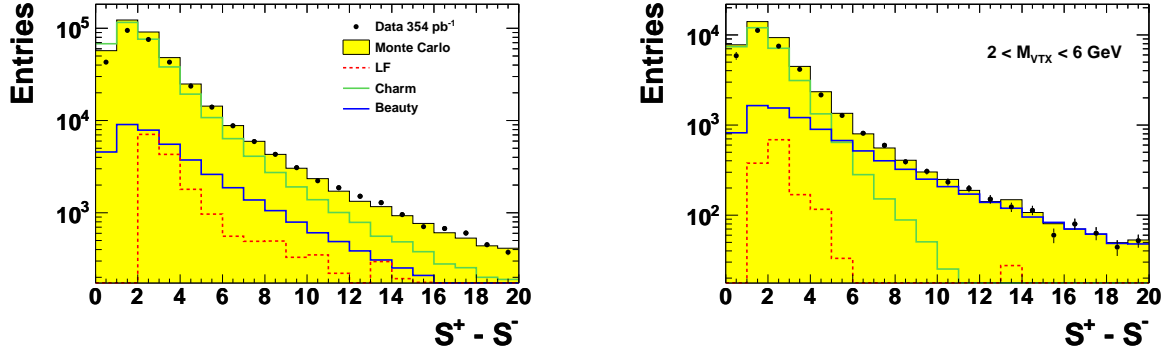


Figure 7.6.: Mirrored decay-length significance for all vertex candidates (left) and for the restricted region $2 < m_{\text{vtx}} < 6$ GeV (right). The data (dots) are compared to the sum of all MC samples (yellow area) and to the individual contributions separately (lines). The MC samples were scaled using the fit result (see text).

the three bins of m_{vtx} . All MC distributions were scaled to the integrated luminosity of the data before the fit. The overall normalisation of the MC was constrained using the unmirrored decay-length significance distributions. The following fit function was minimised:

$$\chi^2 = \sum_i \frac{(N_i^{\text{data}} - k_b N_i^b - k_c N_i^c - k_{\text{lf}} N_i^{\text{lf}})^2}{(\sigma_i^{\text{data}})^2 + (k_b \cdot \sigma_i^b)^2 + (k_c \cdot \sigma_i^c)^2 + (k_{\text{lf}} \cdot \sigma_i^{\text{lf}})^2} + \frac{(N_{\text{tot}}^{\text{data}} - k_b \cdot N_{\text{tot}}^b - k_c \cdot N_{\text{tot}}^c - k_{\text{lf}} \cdot N_{\text{tot}}^{\text{lf}})^2}{(\sigma_{\text{tot}}^{\text{data}})^2 + (k_b \cdot \sigma_{\text{tot}}^b)^2 + (k_c \cdot \sigma_{\text{tot}}^c)^2 + (k_{\text{lf}} \cdot \sigma_{\text{tot}}^{\text{lf}})^2}, \quad (7.5)$$

where the sum runs over all bins i of the three fitted $S^+ - S^-$ distributions. N_i^{data} , N_i^b , N_i^c and N_i^{lf} are the entries in a given bin i of the $S^+ - S^-$ distributions, and $N_{\text{tot}}^{\text{data}}$, N_{tot}^b , N_{tot}^c and $N_{\text{tot}}^{\text{lf}}$ are the numbers of selected vertices in the unmirrored distributions. σ_i^{data} , σ_i^b , σ_i^c and σ_i^{lf} are the statistical uncertainties for a given bin i of the $S^+ - S^-$ distributions, and $\sigma_{\text{tot}}^{\text{data}}$, σ_{tot}^b , σ_{tot}^c and $\sigma_{\text{tot}}^{\text{lf}}$ are the statistical uncertainties of the numbers of selected vertices in the unmirrored distributions. The fit yielded the so-called k -factors, k_b , k_c and k_{lf} for the beauty, charm and light flavour samples. These values give the scaling factors for the individual MC contributions to obtain the best description of the data.

The following k -factors were obtained for the full kinematic region of the measurement given by $5 < Q^2 < 1000$ GeV², $0.02 < y < 0.7$, $E_T^{\text{jet}} > 5$ GeV and $-1.6 < \eta^{\text{jet}} < 2.2$:

$$\begin{aligned} k_{\text{lf}} &= 0.889 \pm 0.005 \\ k_c &= 1.273 \pm 0.020 \\ k_b &= 1.470 \pm 0.050 \end{aligned}$$

The quoted uncertainties are the statistical errors provided by the fit. The quality of the fit was reasonable ($\chi^2/\text{ndof} = 1.41$). The fit result is illustrated in Fig. 7.7 where $S^+ - S^-$

is shown in three bins of the invariant mass. The first two mass bins corresponding to the region $1 < m_{\text{vtx}} < 2$ GeV are dominated by charm events. In the third mass bin a very pure beauty signal is visible at high values of the decay-length significance. The light flavour contribution is mostly constrained by the unmirrored distributions.

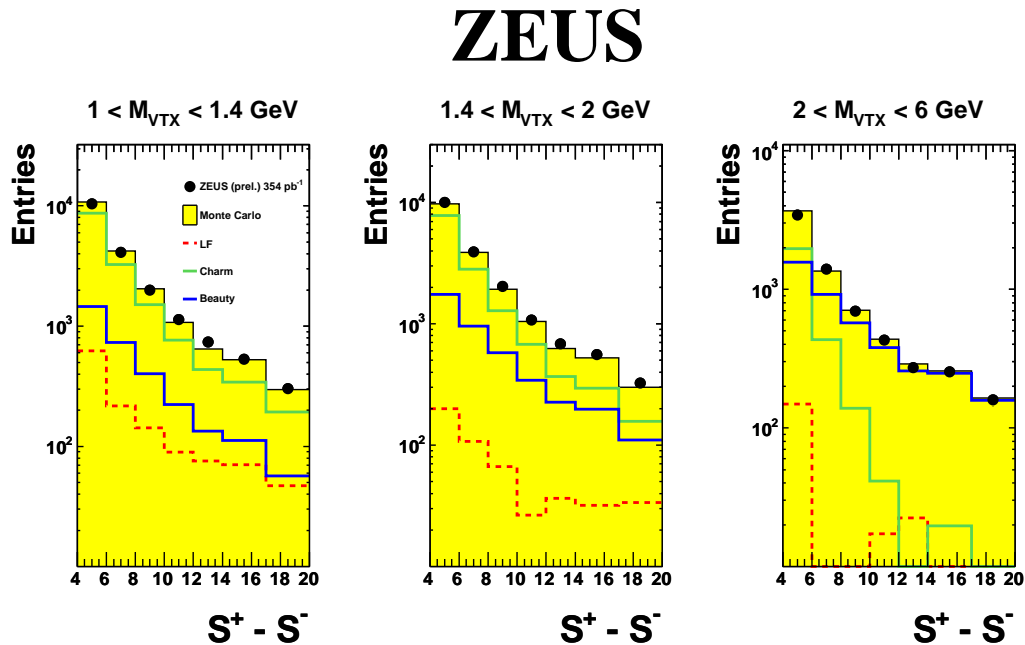


Figure 7.7.: Mirrored decay-length significance in three bins of the invariant mass. The data (dots) are compared to the sum of all MC samples (yellow area) and to the individual contributions separately (lines). The MC samples were scaled using the fit result (see text).

The region where the mirrored decay-length significance was small, $S^+ - S^- < 4$, was excluded from the fit. As visible already in Fig. 7.6, the decay-length significance is not described in this region by the Monte Carlo simulation. If the region of small decay-length significances was not excluded from the fit, unphysical results were obtained. For example, in Fig. 7.8 the differential cross sections for jet production in charm and beauty events are shown as a function of ϕ^{jet} . Details on the cross section calculation are given below in Sec. 7.4.1. The full range $0 < S^+ - S^- < 20$ was used in the fit. The cross sections are expected to be flat, but the measurements significantly disagree from this assumption. The differential cross sections as a function of ϕ^{jet} were also extracted in bins of η^{jet} to check if the effect is localised in some region of the detector. However, no dependence of the ϕ^{jet} distribution on η^{jet} was found. On the other hand, the cross sections in ϕ^{jet} extracted using the restricted range $S^+ - S^- > 4$ are consistent with the flat expectation (see Fig. 7.9).

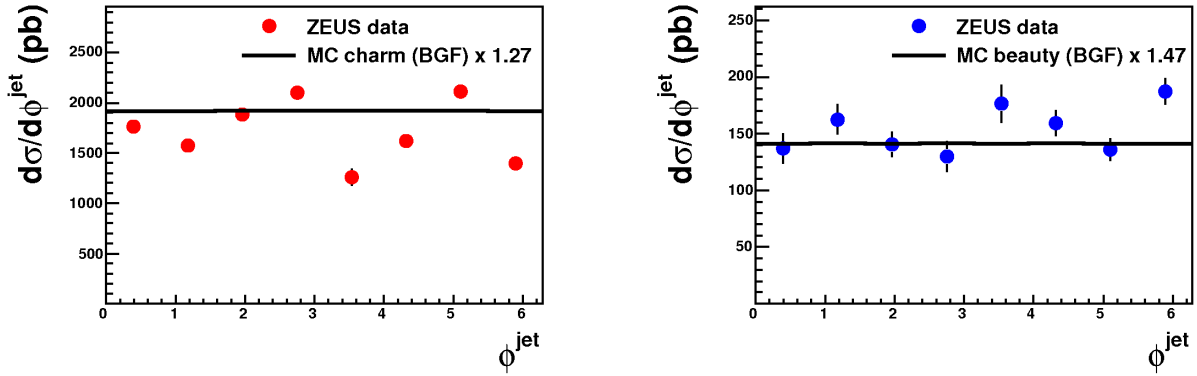


Figure 7.8.: Cross sections for jet production in charm (left) and beauty (right) DIS events. The cross sections were extracted using the full range $0 < S^+ - S^- < 20$.

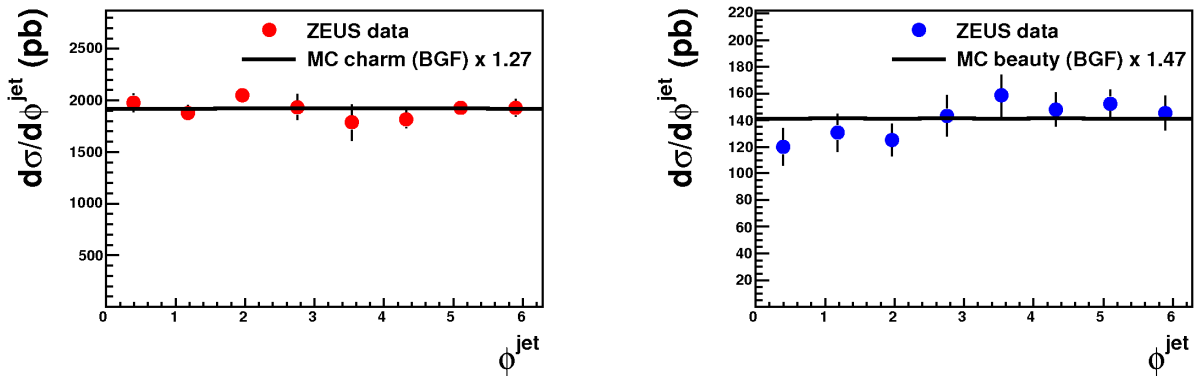


Figure 7.9.: Cross sections for jet production in charm (left) and beauty (right) DIS events. The cross sections were extracted using the restricted range $4 < S^+ - S^- < 20$.

7.3.4. Corrections

To obtain a good overall description of the data by the Monte Carlo simulation, several corrections had to be applied. These corrections are explained in the following.

Decay length smearing

The default decay-length significance distribution before corrections is not fully described by the Monte Carlo. This difference was corrected for by smearing the MC. The same empirical smearing function as described in the following was applied to all MC samples. The smearing procedure consisted of three components:

- for 5% of all vertices the projected decay length was smeared by a Gaussian of the width $1.8 \cdot \sigma(L_{XY})$;
- for 1% of all vertices the projected decay length was smeared by a Gaussian of the width $2.3 \cdot \sigma(L_{XY})$;

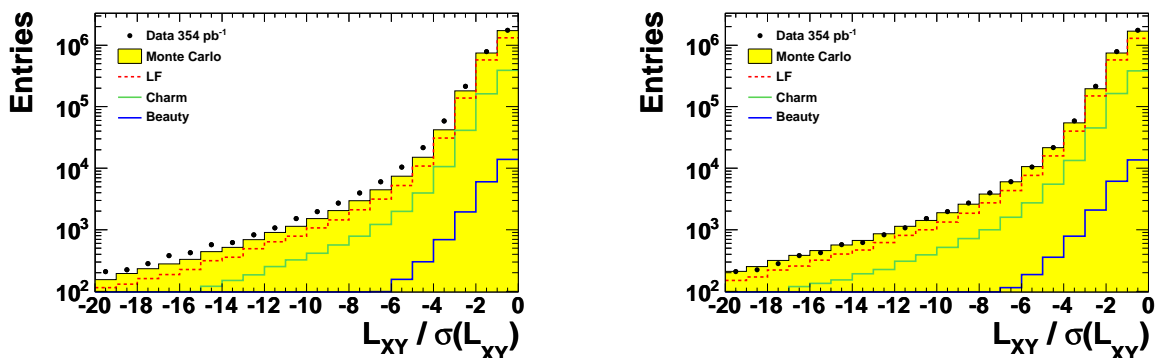


Figure 7.10.: Negative part of the decay-length significance for all vertex candidates before (left) and after (right) the smearing was applied. The data (dots) are compared to the sum of all MC samples (yellow area) and to the individual contributions separately (lines). The MC samples were scaled using the fit result (see text).

- if $0.1 \cdot \sigma(L_{XY}) < R_1$, where R_1 is a random number uniformly distributed in the range $]0, 1]$ and $\sigma(L_{XY})$ is given in cm, the decay length was modified by the following function to adjust the extreme tails:

$$L_{XY,\text{smearred}} = L_{XY} + \frac{R_2}{|R_2|} \cdot \frac{\ln(1 - |R_2|)}{-5.0}, \quad (7.6)$$

where R_2 is a random number uniformly distributed in the range $] -1, 1]$.

The smearing can be tested using the negative part ($S < 0$) of the decay-length significance distribution. As visible in Fig. 7.10, good agreement of data and Monte Carlo was achieved once the smearing was applied. The effect of the decay-length smearing on the measured beauty and charm cross sections is small. This is expected since the effect of the smearing mostly cancels when the significance distributions are mirrored.

Reweighting of the ARIADNE MC in E_T^{jet}

In the Q^2 range considered in this analysis, the ADRIADNE MC program overestimates the production of jets at very high E_T^{jet} . This effect was corrected for by reweighting the ARIADNE MC samples in E_T^{jet} . The change in the measured beauty and charm cross sections is marginal since the contribution of the affected region $E_T^{\text{jet}} \gtrsim 30$ GeV to the total cross section is very small. Fig 7.11 shows the E_T^{jet} distribution for all secondary vertices before and after the reweighting was applied.

Reweighting of the RAPGAP MC in Q^2

The measured Q^2 distributions for beauty and charm quark production fall more steeply than predicted by the RAPGAP MC program. The ratio of the measured cross sections to

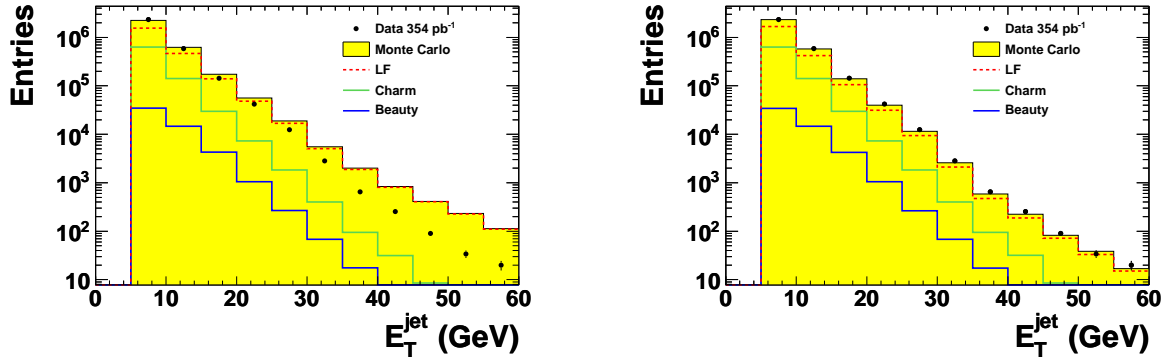


Figure 7.11.: Transverse energy of the jets associated to all secondary vertices before (left) and after (right) the reweighting was applied. The data (dots) are compared to the sum of all MC samples (yellow area) and to the individual contributions separately (lines). The MC samples were scaled using the fit result (see text).

the predictions obtained using the RAPGAP MC are shown in Fig. 7.12.

The RAPGAP MC samples for beauty and charm quark production were reweighted in Q^2 to ensure that the acceptance corrections were reasonable. To avoid statistical fluctuations, smooth functions instead of discrete values for the cross section ratios in bins were used to determine the weight for each event. The weighting function used for beauty events was parameterised as:

$$w_b(Q^2) = e^{-0.599-0.00389 \cdot Q^2} + 0.631. \quad (7.7)$$

The corresponding function used for charm events is given by:

$$w_c(Q^2) = e^{-0.486-0.0158 \cdot Q^2} + 0.781. \quad (7.8)$$

Both weighting functions are shown in Fig. 7.12. The systematic uncertainty caused by this procedure was estimated changing the correction by $\pm 50\%$ (see Sec. 7.4.2).

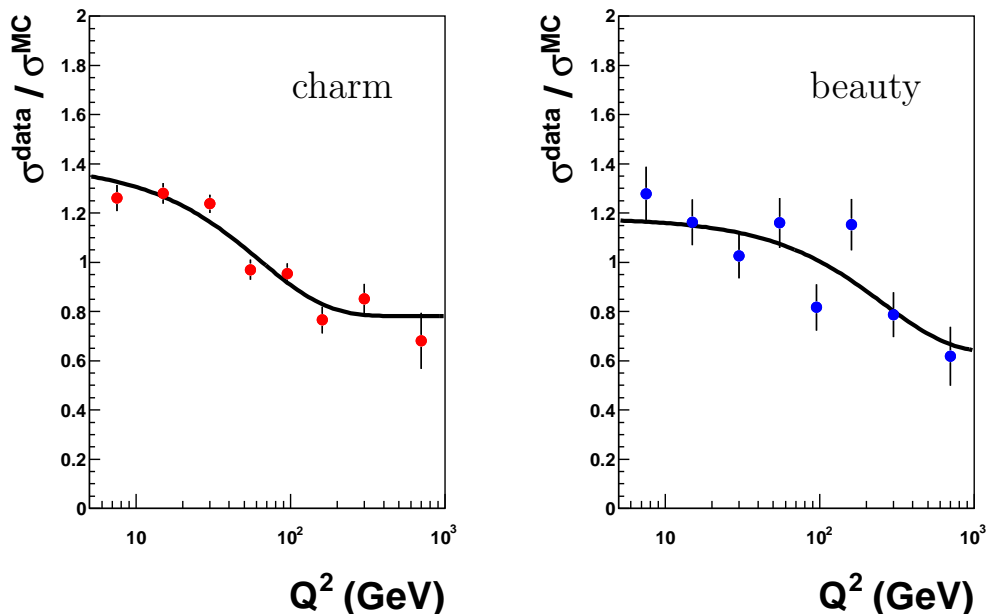


Figure 7.12.: Ratio of the measured cross sections, σ^{data} , to the cross sections predicted by the RAPGAP MC program, σ^{MC} , for charm (left) and beauty (right). Both distributions were normalised to the number of bins. The weighting functions w_c and w_b to correct the RAPGAP MC are shown as black lines.

7.3.5. Control distributions

To validate the RAPGAP MC samples for beauty and charm production, control distributions for regions with a high purity of the beauty or charm signals are shown here.

For beauty a high purity was obtained for high masses and decay-length significances of the secondary vertices. Hence control plots for DIS, jet and secondary vertex variables in the range $2 < m_{\text{vtx}} < 6$ GeV and $S^+ - S^- > 8$ are shown in Figs. 7.13 and 7.14. Good agreement is observed for all distributions.

Charm enriched control plots for the region $1 < m_{\text{vtx}} < 2$ GeV and $S^+ - S^- > 4$ are shown in Figs. 7.15 and 7.16. In general, the agreement between data and MC is good. The small excess in the vertex mass distribution at $m_{\text{vtx}} \approx 1.5$ GeV is mostly caused by a too small branching ratio for the decay $D^+ \rightarrow K^- \pi^+ \pi^+$ used by the RAPGAP MC program. The effect of this disagreement on the beauty and charm cross sections is small compared to the systematic uncertainties of the measurement [150].

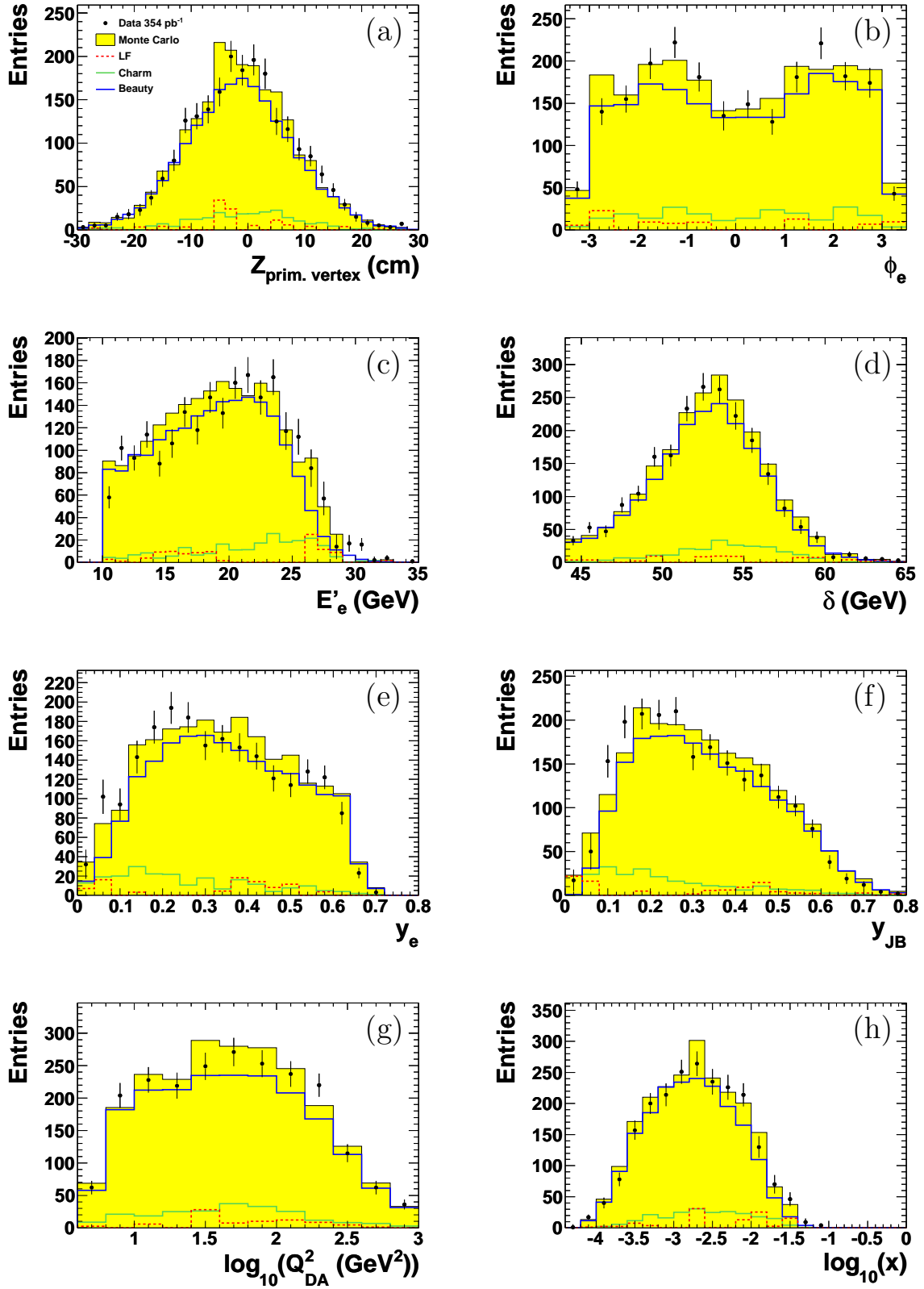


Figure 7.13.: The event variables (a) Z_{vertex} , (b) ϕ_e , (c) E'_e , (d) δ , (e) y_e , (f) y_{JB} , (g) $\log_{10} Q_{DA}^2$ and (h) $\log_{10}(x_{DA})$ for the beauty enriched region. The data (dots) are compared to the sum of all MC samples (yellow area). The individual MC samples are shown as solid lines.

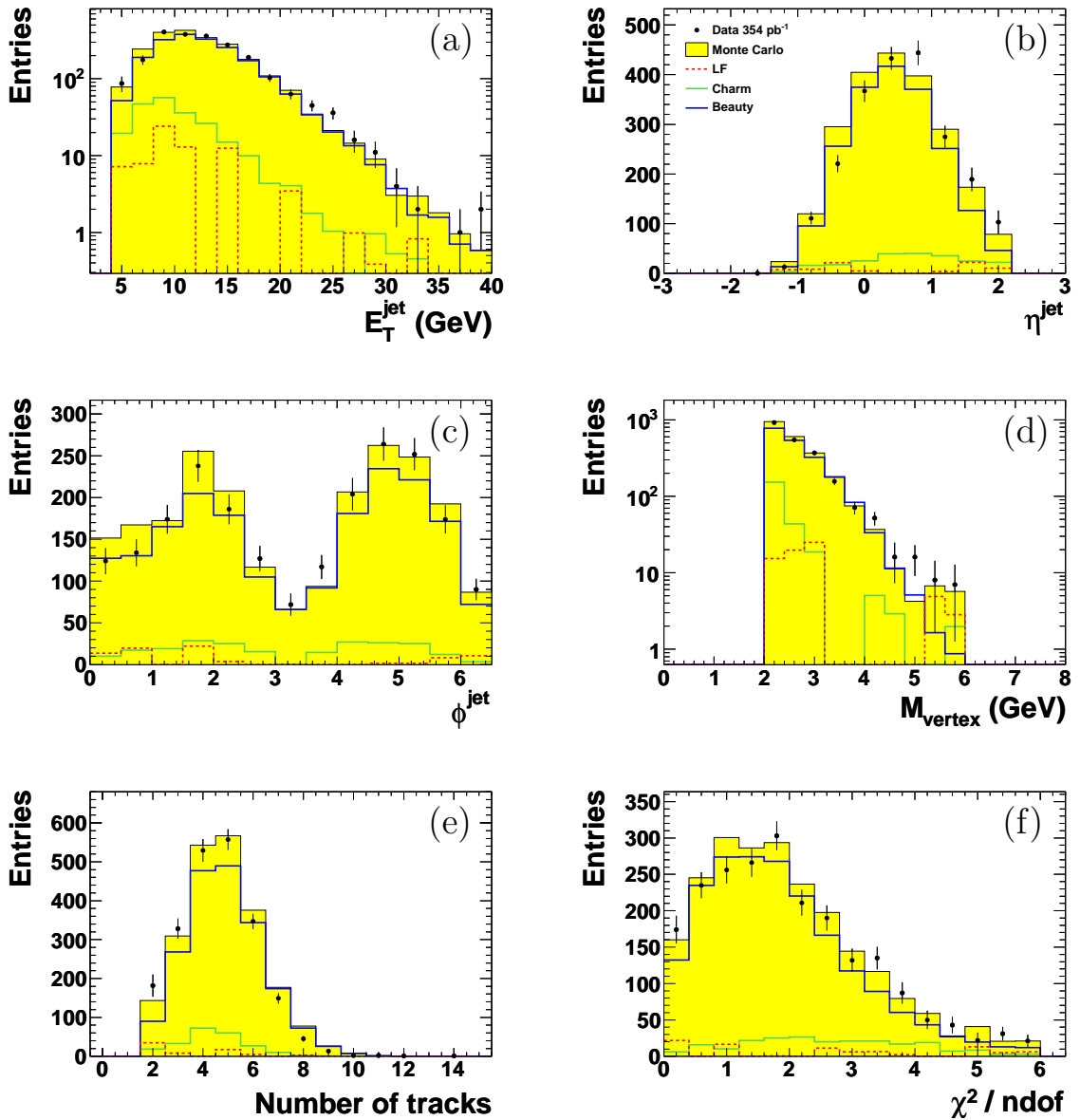


Figure 7.14.: The jet and vertex variables (a) E_T^{jet} , (b) η^{jet} , (c) ϕ^{jet} , (d) m_{vtx} , (e) secondary vertex multiplicity and (f) χ^2/ndof for the beauty enriched region. The data (dots) are compared to the sum of all MC samples (yellow area). The individual MC samples are shown as solid lines.

7. Measurement of $F_2^{b\bar{b}}$ and $F_2^{c\bar{c}}$ using lifetime information

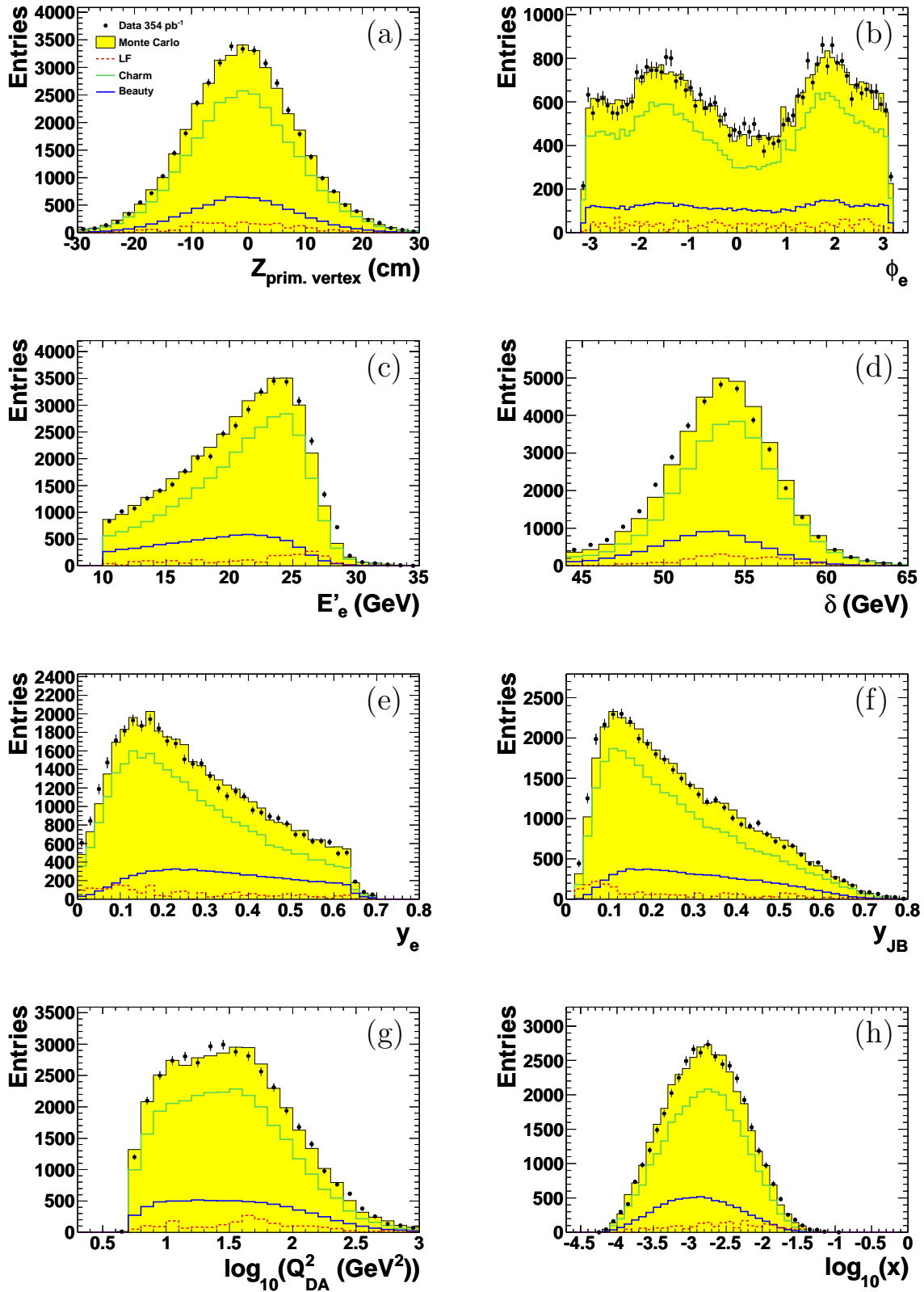


Figure 7.15.: The event variables (a) Z_{vertex} , (b) ϕ_e , (c) E'_e , (d) δ , (e) y_e , (f) y_{JB} , (g) $\log_{10} Q^2_{DA}$ and (h) $\log_{10}(x_{DA})$ for the charm enriched region. The data (dots) are compared to the sum of all MC samples (yellow area). The individual MC samples are shown as solid lines.

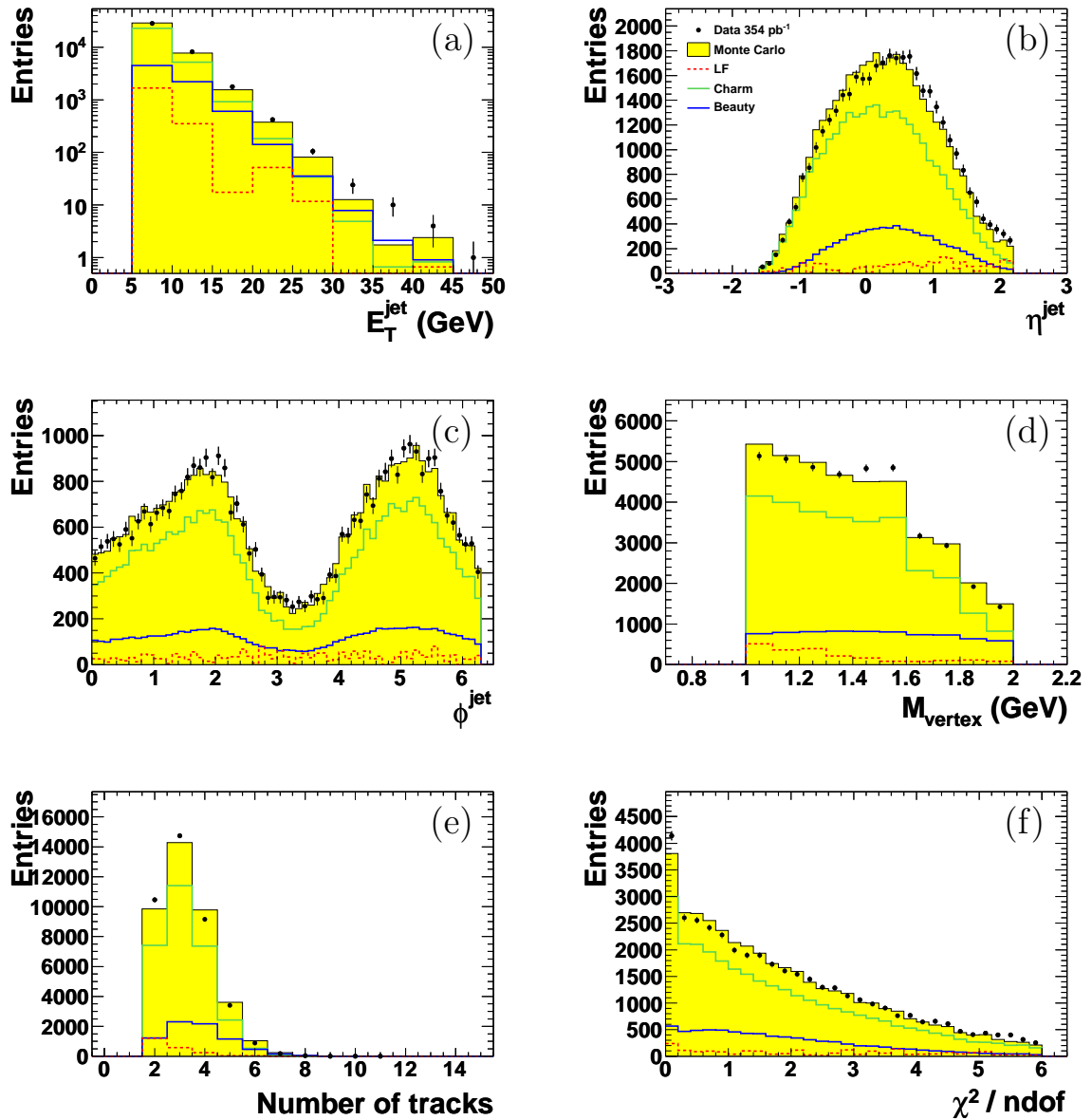


Figure 7.16.: The jet and vertex variables (a) E_T^{jet} , (b) η^{jet} , (c) ϕ^{jet} , (d) m_{vtx} , (e) secondary vertex multiplicity and (f) χ^2/ndof for the charm enriched region. The data (dots) are compared to the sum of all MC samples (yellow area). The individual MC samples are shown as solid lines.

7.4. Measurement of beauty production and extraction of $F_2^{b\bar{b}}$

The analysis presented in this chapter was performed in two steps. The procedure described so far was optimised to measure beauty quark production. The results of the beauty measurement are given in the following. In the second step, the cut on E_T^{jet} was reduced to improve the kinematic acceptance for charm quarks. This is described in Sec. 7.5.

7.4.1. Cross sections

In the following, the definition of the cross section is described. Differential cross sections for jet production in beauty events were measured. The differential cross section in a bin i of a given observable Y is given by:

$$\left(\frac{d\sigma}{dY}\right)_i = \frac{N_i^{\text{rec,data}}}{\mathcal{A}_i \cdot \mathcal{L} \cdot \Delta Y_i}, \quad (7.9)$$

where $N_i^{\text{rec,data}}$ is the number of jets reconstructed in beauty events in bin i having size ΔY_i and \mathcal{L} is the integrated luminosity of the investigated data sample. The acceptance for bin i can be written as:

$$\mathcal{A}_i = \frac{N_i^{\text{rec,MC}}}{N_i^{\text{true}}}, \quad (7.10)$$

where $N_i^{\text{rec,MC}}$ is the number of jets reconstructed in beauty events in bin i using the Monte Carlo and N_i^{true} is the number of jets on hadron level found in the beauty MC. The latter was determined running the same jet reconstruction algorithm as used for the data on all final-state particles from the generator output. Weakly decaying B and D hadrons were treated as stable particles and were decayed only after the application of the jet algorithm. In this way well defined jet directions were obtained even for B and D mesons almost at rest which decay isotropically.

The relation between $N_i^{\text{rec,data}}$ and $N_i^{\text{rec,MC}}$ was determined from the fit:

$$N_i^{\text{rec,data}} = k_{b,i} \cdot N_i^{\text{rec,MC}}, \quad (7.11)$$

where $k_{b,i}$ is the k-factor for the beauty MC obtained for bin i . Finally, Eqs. 7.9, 7.10 and 7.11 can be combined to:

$$\left(\frac{d\sigma}{dY}\right)_i = \frac{k_{b,i} \cdot N_i^{\text{true}}}{\mathcal{L} \cdot \Delta Y_i}. \quad (7.12)$$

The kinematic region of the measurement is given by:

$$\begin{aligned} E_T^{\text{jet}} &> 5 \text{ GeV}, \\ -1.6 &< \eta^{\text{jet}} < 2.2, \end{aligned}$$

$$0.02 < y < 0.7 \text{ and} \\ 5 < Q^2 < 1000 \text{ GeV}^2.$$

Due to their large masses, even beauty hadrons with very low transverse momenta fulfil the condition $E_T^{\text{jet}} > 5 \text{ GeV}$. Hence the measurement of beauty production presented here is sensitive in the threshold region. The lower cut on η^{jet} was imposed since there is no beauty signal in the backward direction. The cut $\eta^{\text{jet}} < 2.2$ was necessary since the MVD hit efficiency was not yet correctly simulated in the very forward direction by the version of the detector simulation used for the analysis presented in this chapter.

7.4.2. Systematic uncertainties

The systematic uncertainties of the measurements presented in this chapter were obtained by changing the selection or signal extraction procedure and repeating the determination of the cross sections. The following groups of systematic uncertainty sources were investigated. The effects on the cross sections for the full kinematic region are given in parentheses:

- $\{\delta_1\}$ event and DIS selection ($\pm 1\%$). The following cut variations were applied to data and MC simultaneously:
 - the cut on y_{JB} was changed by ± 0.01 ;
 - the cut on E'_e was changed by $\pm 1 \text{ GeV}$;
 - the cut on δ was changed by $\pm 2 \text{ GeV}$;
- $\{\delta_2\}$ tracking simulation ($+8\%$). It was shown using pions from K_S^0 decays that the ratio of the track reconstruction efficiencies for the data and the Monte Carlo simulation is flat for $p_T^{\text{track}} > 300 \text{ MeV}$ [151]. A constant difference independent of p_T^{track} between the tracking efficiencies for data and Monte Carlo was not yet excluded. It was assumed that the efficiency of the track reconstruction was overestimated by maximally 2% in the detector simulation. To estimate the effect of this assumption, the following changes were applied to the MC for every track with a probability of 2%:
 - if the track was associated to a secondary vertex fitted using more than two tracks, the vertex multiplicity was reduced by the factor $(N - 1)/N$ and the vertex significance was reduced by the factor $\sqrt{(N - 1)/N}$;
 - if the track was associated to a secondary vertex consisting of only two tracks, the vertex was dropped.

These modifications intend to simulate a 2% difference in the tracking efficiency between the data and the Monte Carlo simulation.

- $\{\delta_3\}$ decay length smearing (-1%). To estimate the uncertainty of the decay length smearing procedure, the cross sections were extracted before the smearing was applied;

- $\{\delta_4\}$ uncertainty of the signal extraction procedure ($^{+2\%}_{-1\%}$). The $S^+ - S^-$ interval used in the signal extraction fit was changed from $[4, 20]$ to $[3, 20]$ and $[5, 20]$;
- $\{\delta_5\}$ calorimeter energy scale ($^{+2\%}_{-1\%}$). The transverse energy of all jets was raised and lowered by 3% as suggested by dedicated studies [152]. These variations were only applied to the MC;
- $\{\delta_6\}$ FLT efficiency (+2%). At the first trigger level, events were vetoed using CTD information. This so-called *track veto* rejected events where only a small fraction of the reconstructed tracks were assigned to the primary vertex. Only an approximate track reconstruction was available at the FLT. It is known that the efficiency of the track-veto condition is underestimated by the MC simulation. To evaluate the systematic uncertainty due to the simulation of the track-veto efficiency, it was estimated that the difference in the track veto efficiency between the data and the MC was maximally 5%. The FLT30 slot was not using the track-veto condition. Hence all events in the MC were weighted by 0.95 if they were not accepted by the FLT30 slot to estimate the systematic uncertainty of the measured cross sections.
- $\{\delta_7\}$ Q^2 reweighting ($\pm 3\%$). The RAPGAP MC samples to simulate beauty events were reweighted in Q^2 as described in Sec. 7.3.4. To estimate the systematic uncertainty caused by this correction, the applied weighting was varied by $\pm 50\%$;
- $\{\delta_8\}$ model dependence of the acceptance corrections ($< 1\%$). To account for a possible discrepancy of the η^{jet} distribution between the data and the beauty MC (see Fig. 7.14 (b)), the beauty MC samples obtained using the RAPGAP program were reweighted in η^{jet} to reproduce the shape of the measured differential cross section;
- $\{\delta_9\}$ uncertainty in the luminosity measurement of $\pm 2.0\%$.

The contributions from the different systematic uncertainties were calculated and added in quadrature separately for positive and negative variations. The same estimates were made in each bin in which differential cross sections were measured.

The dominant contribution to the total systematic uncertainty is given by the uncertainty of the tracking efficiency. To improve this, a better understanding of the HERA II tracking is needed. Efforts are ongoing within the ZEUS collaboration to improve the knowledge of the tracking efficiency.

Non-BGF processes such as $bg \rightarrow bg$ simulated using the RAPGAP program were investigated. The inclusion of these processes worsened the description of the data significantly. Hence it was decided not to use non-BGF samples to study the model dependence of the acceptance corrections.

As an additional check, the binning of the input distributions to the fit in $S^+ - S^-$ was varied. The resulting cross section changed only marginally.

7.4.3. NLO QCD predictions from HVQDIS

Calculation of visible cross sections

NLO QCD predictions for visible cross sections and for $F_2^{b\bar{b}}$ were obtained using the HVQDIS program. The HVQDIS program provides the four-momenta of the final state particles of the hard interaction, i.e. the four-momenta of two heavy quarks and eventually a gluon. The first step to obtain visible cross sections that can be compared to the data was to run the KTCLUS algorithm in the same mode as used for the cross section measurement on the final state partons. The obtained parton level cross sections need to be transformed to the hadron level accordingly. The hadronisation correction was obtained using the RAPGAP Monte Carlo: $C_{\text{had}} = \sigma_{\text{had}}/\sigma_{\text{part}}$, where σ_{had} and σ_{part} are the visible cross sections on hadron and parton level, respectively.

The predictions from the HVQDIS program are given at the QED born level with a running electromagnetic coupling constant α . Hence a correction for QED radiative effects was necessary before the HVQDIS predictions were compared to the data. The correction was obtained according to: $C_{\text{rad}} = \sigma_{\text{rad}}/\sigma_{\text{born}}$, where σ_{rad} is the cross section predicted by RAPGAP including full QED corrections using the default samples and σ_{born} is the cross section obtained using a dedicated RAPGAP sample where QED corrections were switched off except for the running of α . Both cross sections, σ_{rad} and σ_{had} , were obtained at the hadron level.

In conclusion, any differential cross section predicted by HVQDIS, $\left(\frac{d\sigma^{\text{HVQDIS}}}{dY}\right)_i$, was corrected for hadronisation and QED effects in the following way:

$$\left(\frac{d\sigma^{\text{HVQDIS,corr}}}{dY}\right)_i = C_{\text{had}} \cdot C_{\text{rad}} \cdot \left(\frac{d\sigma^{\text{HVQDIS}}}{dY}\right)_i. \quad (7.13)$$

The obtained values for C_{had} and C_{rad} are shown in Tabs. 7.6 and 7.7. Both corrections are small in most bins.

Parameters

Three different HVQDIS predictions for jet production in beauty events were obtained for different choices of the renormalisation and factorisation scales, and for different proton PDFs. The different settings are summarised in the following:

- The proton parton density functions were taken from the FFNS variant of the ZEUS-S NLO QCD fit. As in the PDF fit, the value of $\alpha_s(M_Z)$ was set to 0.118 and the pole mass of the beauty quark was set to 4.75 GeV. The renormalisation and factorisation scales were both set to $\mu_R = \mu_F = \frac{1}{2}\sqrt{Q^2 + p_T^2 + m_b^2}$, where p_T is the average transverse momentum of the two b quarks in the Breit frame². The same scales were chosen in a recent measurement by the ZEUS collaboration [84].
- The second variant of the HVQDIS predictions is identical to the first one except that the renormalisation and factorisation scales were set to $\mu_R = \mu_F = \sqrt{Q^2 + 4m_b^2}$.

²The Breit frame is defined as the frame in which the exchanged boson is completely spacelike.

- Predictions were also obtained using the ABKM NLO PDFs for the proton. The pole mass of the beauty quark was set to 4.5 GeV in the PDF fit and in the HVQDIS calculation. The values of $\alpha_s(\mu_R^2)$ were provided by LHAPDF to ensure that the same function was used as in the PDF fit. The renormalisation and factorisation scales were both set to $\mu_R = \mu_F = \frac{1}{2}\sqrt{Q^2 + 4m_b^2}$.

HVQDIS was slightly modified to obtain the NLO QCD predictions using the ABKM NLO PDFs. The diagram shown in Fig. 7.17 needs to be added to HVQDIS when the ABKM FFNS scheme is used. The loop in the gluon line consists of a heavy quark pair. To consider this missing diagram, the value of $\alpha_s(\mu_R^2)$ in the LO contribution to the cross section needs to be multiplied by the following correction factor [153]:

$$C = 1 + \beta_{0Q} \cdot \log\left(\frac{\mu_R^2}{m_Q^2}\right) \cdot \frac{\alpha_s}{4\pi}, \quad (7.14)$$

where $\beta_{0Q} = -\frac{4}{3}T_F = -\frac{2}{3}$. Since this correction was considered in the PDF fit, it also needs to be applied in the HVQDIS calculation to obtain a self-consistent prediction. The effect of the modification is typically only 1–2% in the investigated kinematic region.

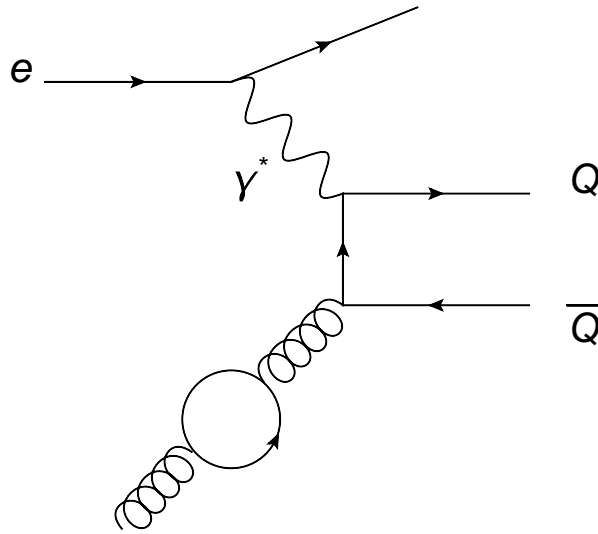


Figure 7.17.: Diagram missing in the HVQDIS when used in the ABKM scheme. The loop in the gluon propagator consists of a heavy quark pair.

The uncertainties of the NLO QCD predictions using the ZEUS-S PDFs were estimated by independently varying μ_R and μ_F by a factor of $\frac{1}{2}$ and 2. The beauty quark mass was changed to 4.5 and 5.0 GeV. Additionally, the experimental uncertainties of the data used in the PDF fit were propagated to the predicted cross sections. These contributions result in total uncertainties of 10–20%.

As an example, Fig 7.18 shows the effect of the individual variations performed to estimate the uncertainties of the HVQDIS prediction obtained using $\mu_R = \mu_F = \sqrt{Q^2 + p_T^2 + m_b^2}$

as a function of Q^2 . The same distributions as functions of E_T^{jet} , η^{jet} and x , and for $\mu_R = \mu_F = \sqrt{Q^2 + 4m_b^2}$ are shown in Appendix G.

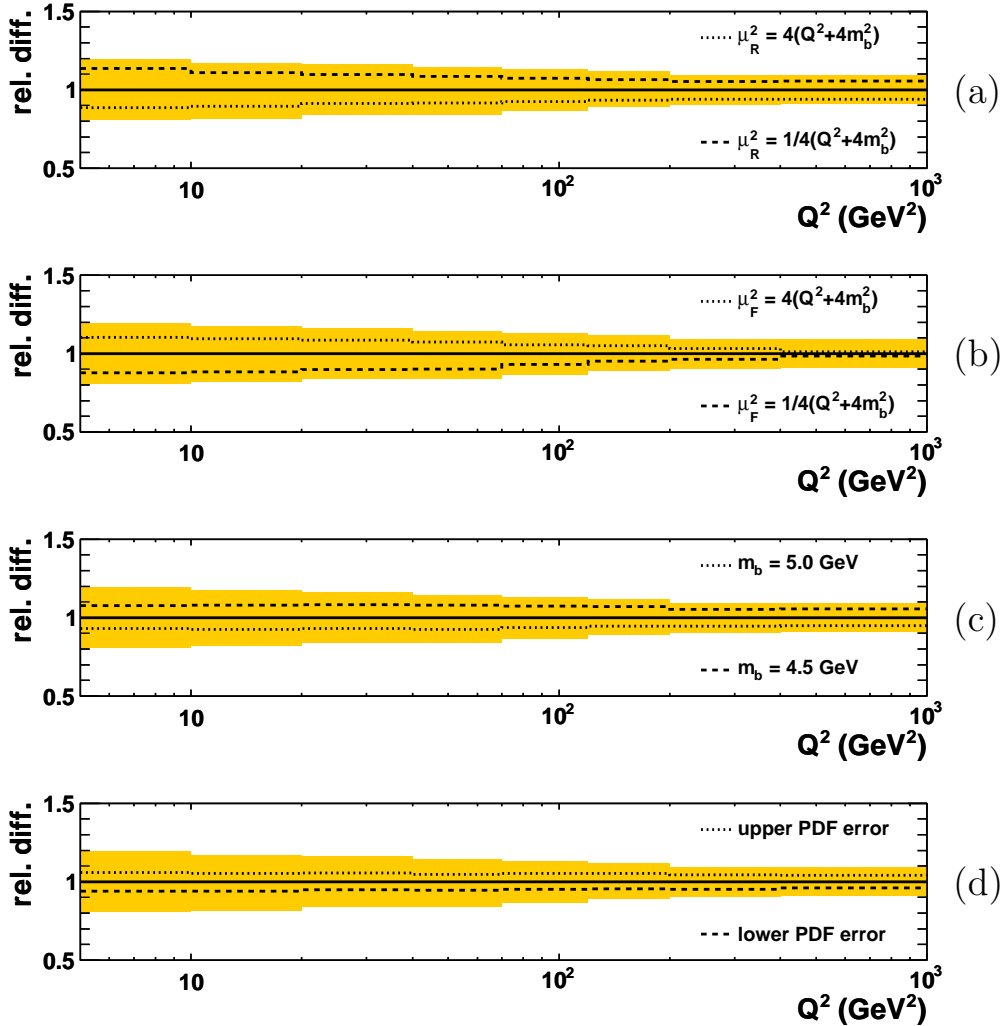


Figure 7.18.: Ratio of the systematic variations of the HVQDIS NLO QCD predictions using $\mu_R = \mu_F = \sqrt{Q^2 + p_T^2 + m_b^2}$ to the central value (lines) as a function of Q^2 . The effects due to the (a) renormalisation scale variation, (b) factorisation scale variation, (c) mass variation and (d) PDF uncertainties are shown separately. The sum all all systematic uncertainties is shown by the yellow band.

7.4.4. Results

Single differential cross sections were measured as functions of E_T^{jet} , η^{jet} , Q^2 and x . Some examples for the fitted mirrored significance distributions in bins of the invariant mass are shown in Appendix E. The results are given in Tab. 7.6 and compared to the NLO QCD predictions from HVQDIS using $\mu_R = \mu_F = \sqrt{Q^2 + p_T^2 + m_b^2}$ in Figs. 7.19, 7.20, 7.21 and 7.22. The cross sections in E_T^{jet} , Q^2 and x fall by about three orders of magnitude in the

measured region while the cross section in η^{jet} varies only by about a factor three.

The measured cross sections are generally about 30% larger than the predictions from HVQDIS. The shapes of the measured cross sections are reasonably well described by HVQDIS. However, the measured distributions in Q^2 and x are somewhat steeper than the HVQDIS prediction.

The same measured single differential cross sections are compared to the HVQDIS predictions calculated setting the renormalisation and factorisation scales to $\mu_R = \mu_F = \sqrt{Q^2 + m_b^2}$ in Figs. 7.23, 7.24, 7.25 and 7.26. The data are compared to predictions obtained using the ZEUS-S and ABKM NLO PDFs for the proton.

The differences between the predictions for the different proton PDFs are mostly very small. The largest deviation of about 10% is visible at high values of Q^2 . This is expected since the gluon densities in both PDF sets are similar in the relevant ranges in x and Q^2 . The different functional form for the renormalisation and factorisation scales, $\mu_R = \mu_F = \sqrt{Q^2 + m_b^2}$, improves the description of the measured η^{jet} distribution significantly. Additionally, the normalisation of the predictions obtained using $\mu_R = \mu_F = \sqrt{Q^2 + m_b^2}$ is slightly better compared to those obtained using $\mu_R = \mu_F = \sqrt{Q^2 + p_T^2 + m_b^2}$.

The RAPGAP MC scaled by 1.6 describes the measured distributions in E_T^{jet} and η^{jet} well. As already discussed above, the Q^2 distribution predicted by RAPGAP before reweighting does not describe the data (see Sec. 7.3.4 for more details).

Double differential cross sections were measured as functions of x and Q^2 . The cross sections as a function of x for different ranges of Q^2 are listed in Tab. 7.7 and are shown in Figs. 7.27 and 7.28. The data points tend to lie above the HVQDIS prediction obtained using $\mu_R = \mu_F = \sqrt{Q^2 + p_T^2 + m_b^2}$ at low Q^2 and below the same HVQDIS prediction at high Q^2 as already seen for the single differential cross section in Q^2 . These double differential cross sections were used to extract $F_2^{b\bar{b}}$. The precision of the double differential cross sections is limited by the statistical uncertainties from the signal extraction fits.

7.4. Measurement of beauty production and extraction of $F_2^{b\bar{b}}$

E_T^{jet} bin (GeV)	$d\sigma/dE_T^{\text{jet}}$ (pb/GeV)	Δ_{stat} (pb/GeV)	Δ_{syst} (pb/GeV)		C_{had}	C_{rad}
5, 8	157.0	± 23.6	+53.0	-38.7	0.95	1.01
8, 11	79.9	± 5.4	+10.6	-8.2	1.08	0.98
11, 14	29.1	± 1.8	+2.7	-1.4	1.05	0.96
14, 17	11.4	± 0.8	+1.0	-0.5	1.04	0.95
17, 20	4.44	± 0.47	+0.64	-0.43	0.99	0.93
20, 25	1.86	± 0.24	+0.37	-0.29	0.93	0.89
25, 35	0.369	± 0.085	+0.074	-0.070	0.80	0.89
η^{jet} bin	$d\sigma/d\eta^{\text{jet}}$ (pb)	Δ_{stat} (pb)	Δ_{syst} (pb)		C_{had}	C_{rad}
-1.6, -0.8	97.7	± 29.3	+31.7	-12.1	0.96	0.98
-0.8, -0.5	251.9	± 30.1	+31.8	-10.7	0.98	0.98
-0.5, -0.2	212.3	± 23.2	+27.1	-10.9	0.93	0.99
-0.2, 0.1	304.2	± 21.9	+28.7	-14.4	0.91	0.99
0.1, 0.4	303.3	± 22.2	+30.2	-13.0	0.94	0.99
0.4, 0.7	358.6	± 23.6	+33.3	-22.4	1.01	0.99
0.7, 1.0	314.2	± 25.4	+31.0	-15.2	1.06	0.99
1.0, 1.3	304.1	± 29.5	+28.7	-12.4	1.07	0.99
1.3, 1.6	226.8	± 39.3	+22.4	-10.9	1.07	0.99
1.6, 2.2	173.5	± 57.4	+56.7	-34.8	1.07	0.98
Q^2 bin (GeV ²)	$d\sigma/dQ^2$ (pb/GeV ²)	Δ_{stat} (pb/GeV ²)	Δ_{syst} (pb/GeV ²)		C_{had}	C_{rad}
5, 10	47.9	± 4.1	+5.3	-2.2	1.01	0.99
10, 20	20.8	± 1.7	+1.9	-0.9	1.01	0.99
20, 40	8.27	± 0.73	+0.86	-0.36	0.99	0.99
40, 70	4.18	± 0.36	+0.36	-0.17	0.98	0.99
70, 120	1.28	± 0.15	+0.16	-0.03	0.98	0.98
120, 200	0.728	± 0.066	+0.063	-0.041	0.99	0.99
200, 400	0.146	± 0.017	+0.017	-0.05	0.99	0.99
400, 1000	0.0171	± 0.0033	+0.0016	-0.0028	1.01	0.95
x bin	$d\sigma/dx$ (pb)	Δ_{stat} (pb)	Δ_{syst} (pb)		C_{had}	C_{rad}
0.00008, 0.0002	720000	± 115000	+93000	-50000	1.09	0.99
0.0002, 0.0006	692000	± 45000	+68000	-33000	1.05	0.99
0.0006, 0.0016	238000	± 14000	+21000	-8000	0.99	0.99
0.0016, 0.005	54000	± 3400	+4900	-2600	0.95	0.99
0.005, 0.01	12000	± 1300	+1500	-700	0.93	1.00
0.01, 0.1	379	± 72	+57	-37	0.92	0.95

Table 7.6.: Measured cross sections for jet production in beauty events as a function of E_T^{jet} , η^{jet} , Q^2 and x for $5 < Q^2 < 1000$ GeV², $0.02 < y < 0.7$, $E_T^{\text{jet}} > 5$ GeV and $-1.6 < \eta^{\text{jet}} < 2.2$. The statistical and systematic uncertainties are shown separately. Additionally, the factors C_{had} and C_{rad} to correct the NLO QCD predictions for hadronisation and QED effects are listed.

ZEUS

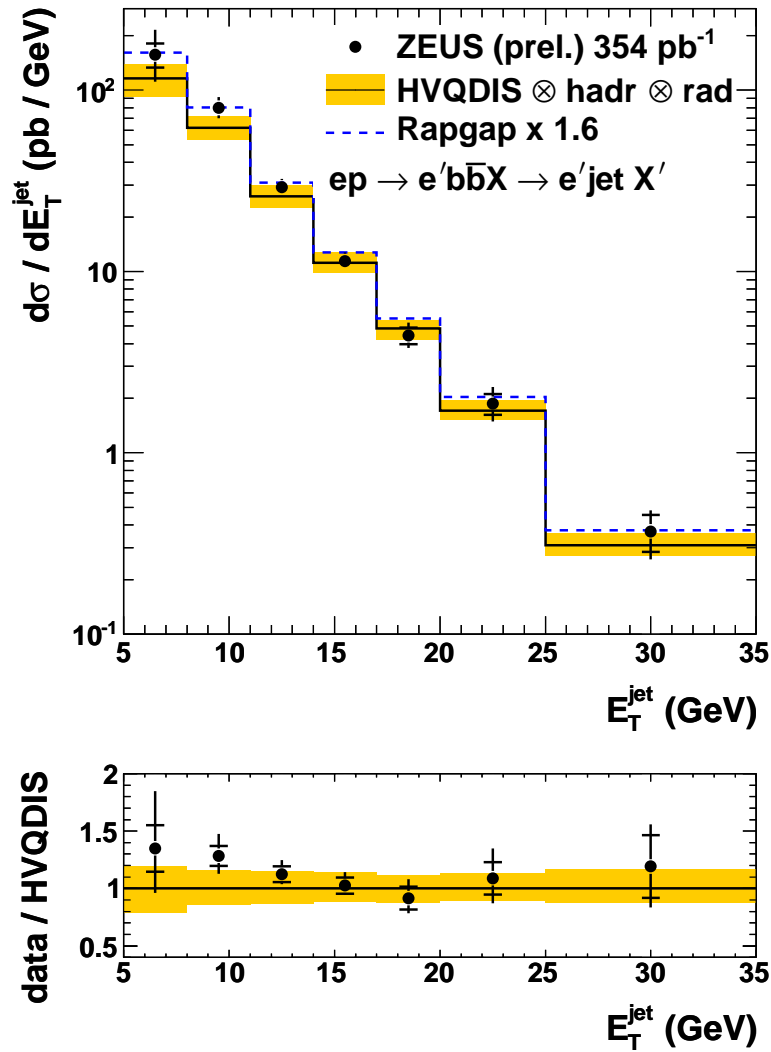


Figure 7.19.: Differential cross section for jet production in beauty events as a function of E_T^{jet} compared to the NLO QCD prediction of HVQDIS calculated using $\mu_R = \mu_F = \frac{1}{2}\sqrt{Q^2 + p_T^2 + m_b^2}$ and to the RAPGAP Monte Carlo scaled to the data.

ZEUS

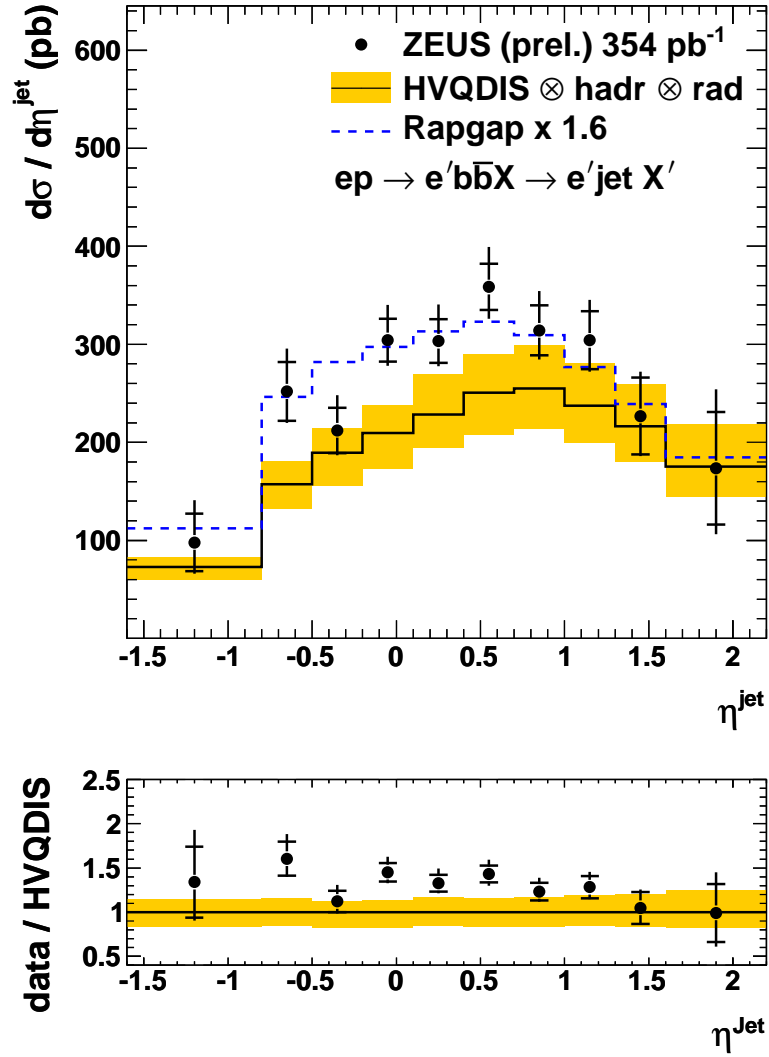


Figure 7.20.: Differential cross section for jet production in beauty events as a function of η^{jet} compared to the NLO QCD prediction of HVQDIS calculated using $\mu_R = \mu_F = \frac{1}{2}\sqrt{Q^2 + p_T^2 + m_b^2}$ and to the RAPGAP Monte Carlo scaled to the data.

ZEUS

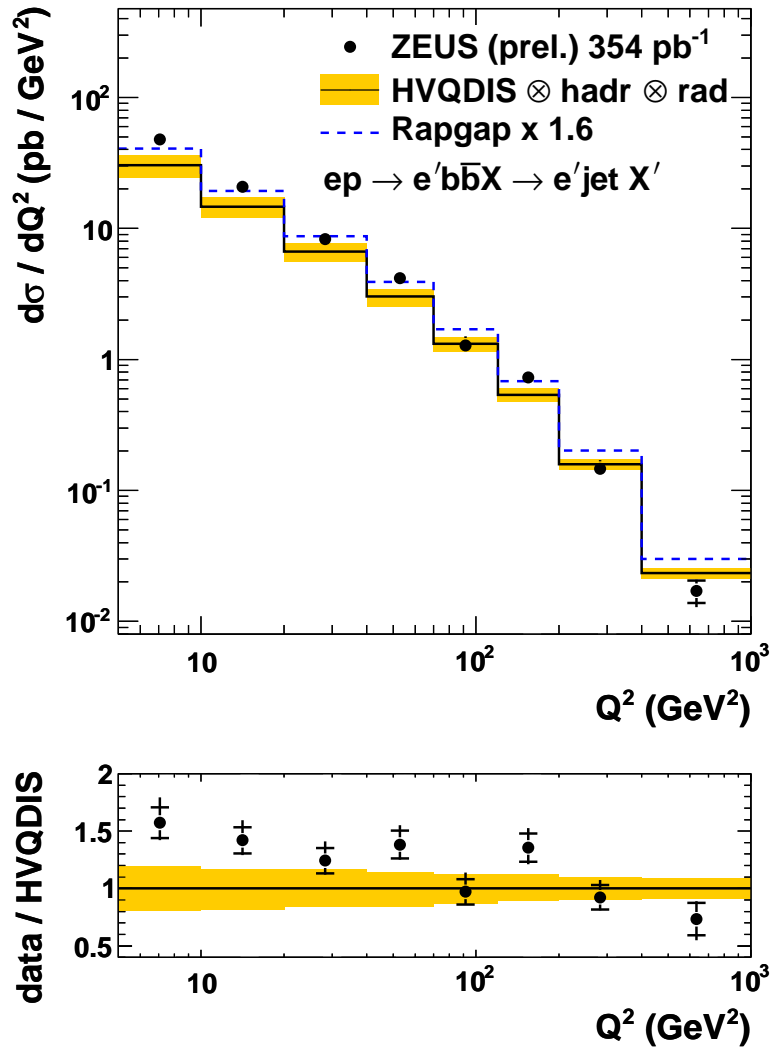


Figure 7.21.: Differential cross section for jet production in beauty events as a function of Q^2 compared to the NLO QCD prediction of HVQDIS calculated using $\mu_R = \mu_F = \frac{1}{2}\sqrt{Q^2 + p_T^2 + m_b^2}$ and to the RAPPAP Monte Carlo scaled to the data.

ZEUS

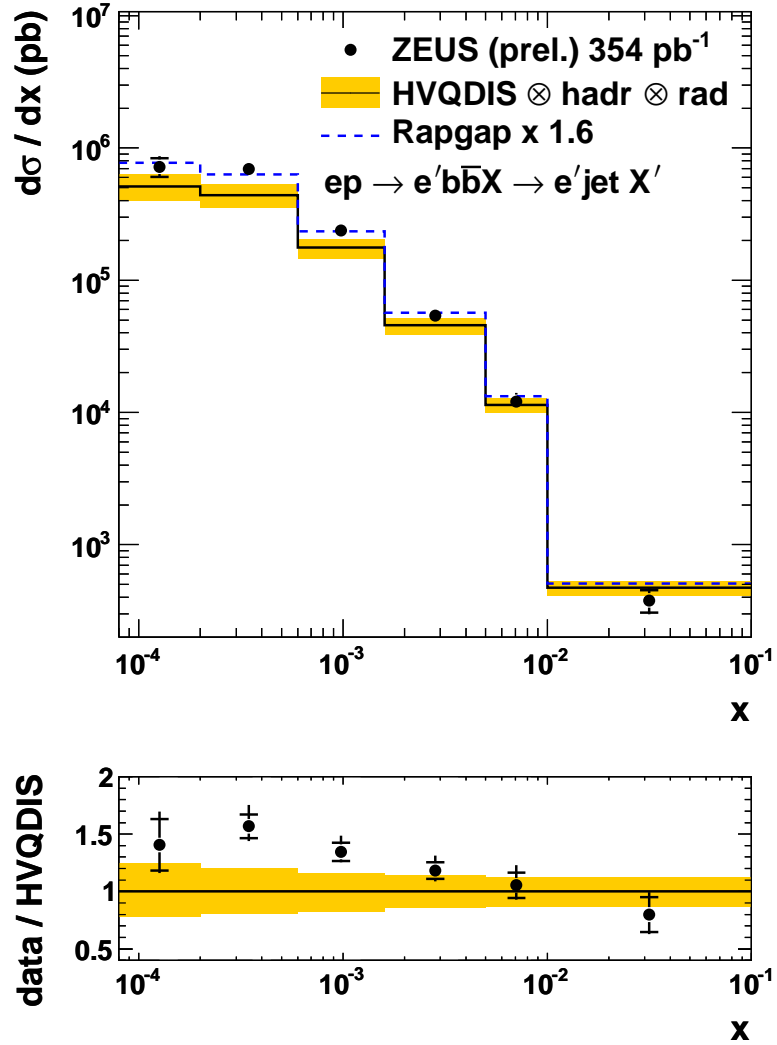


Figure 7.22.: Differential cross section for jet production in beauty events as a function of x compared to the NLO QCD prediction of HVQDIS calculated using $\mu_R = \mu_F = \frac{1}{2} \sqrt{Q^2 + p_T^2 + m_b^2}$ and to the RAPGAP Monte Carlo scaled to the data.

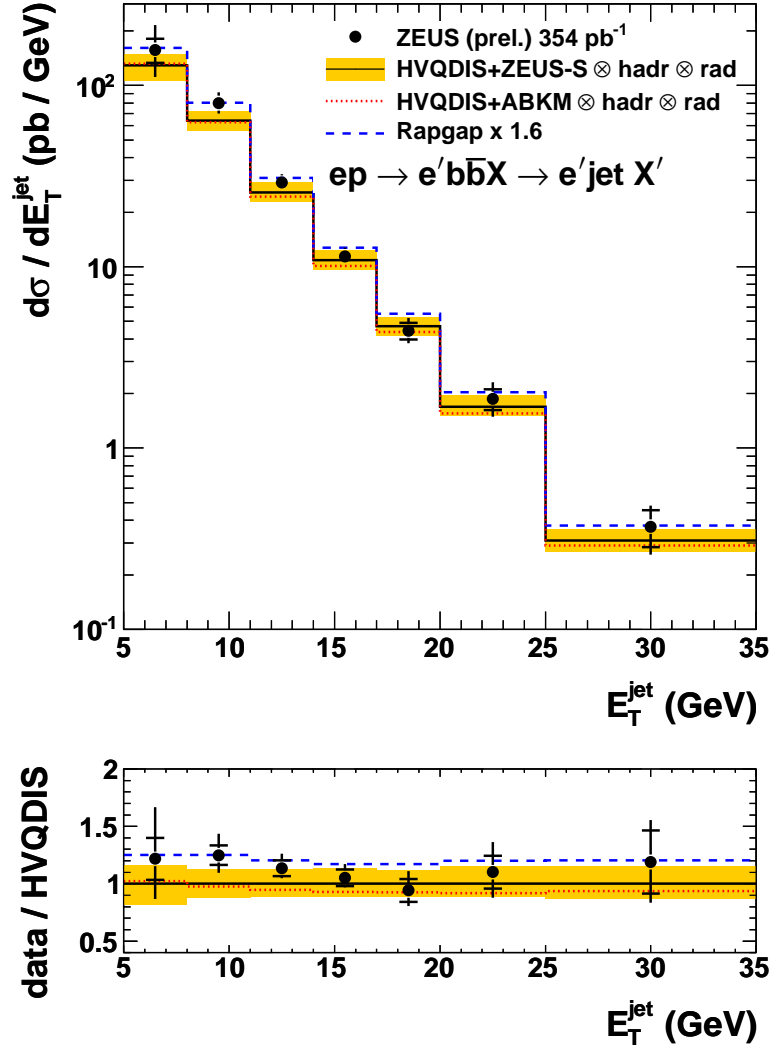


Figure 7.23.: Differential cross section for jet production in beauty events as a function of E_T^{jet} compared to the NLO QCD prediction of HVQDIS obtained using the ZEUS-S and ABKM NLO PDFs. The renormalisation and factorisation scales were set to $\mu_R = \mu_F = \sqrt{Q^2 + 4m_b^2}$. Additionally, the RAPGAP Monte Carlo scaled to the data is shown.

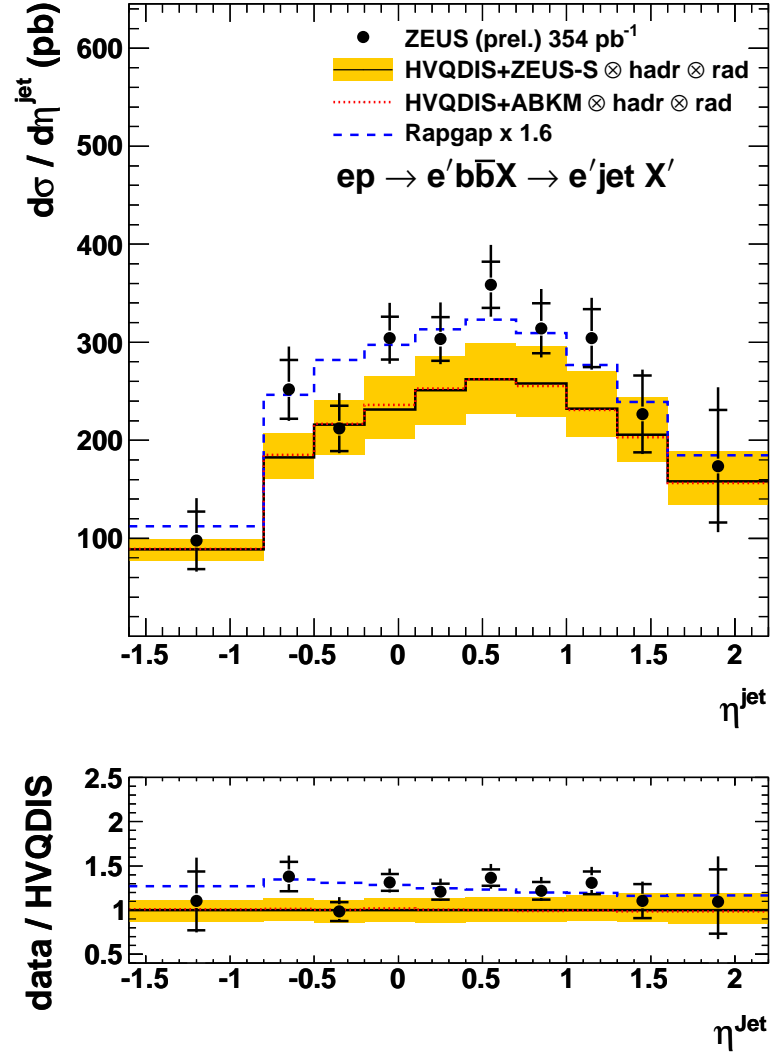


Figure 7.24.: Differential cross section for jet production in beauty events as a function of η^{jet} compared to the NLO QCD prediction of HVQDIS obtained using the ZEUS-S and ABKM NLO PDFs. The renormalisation and factorisation scales were set to $\mu_R = \mu_F = \sqrt{Q^2 + 4m_b^2}$. Additionally, the RAPPAP Monte Carlo scaled to the data is shown.

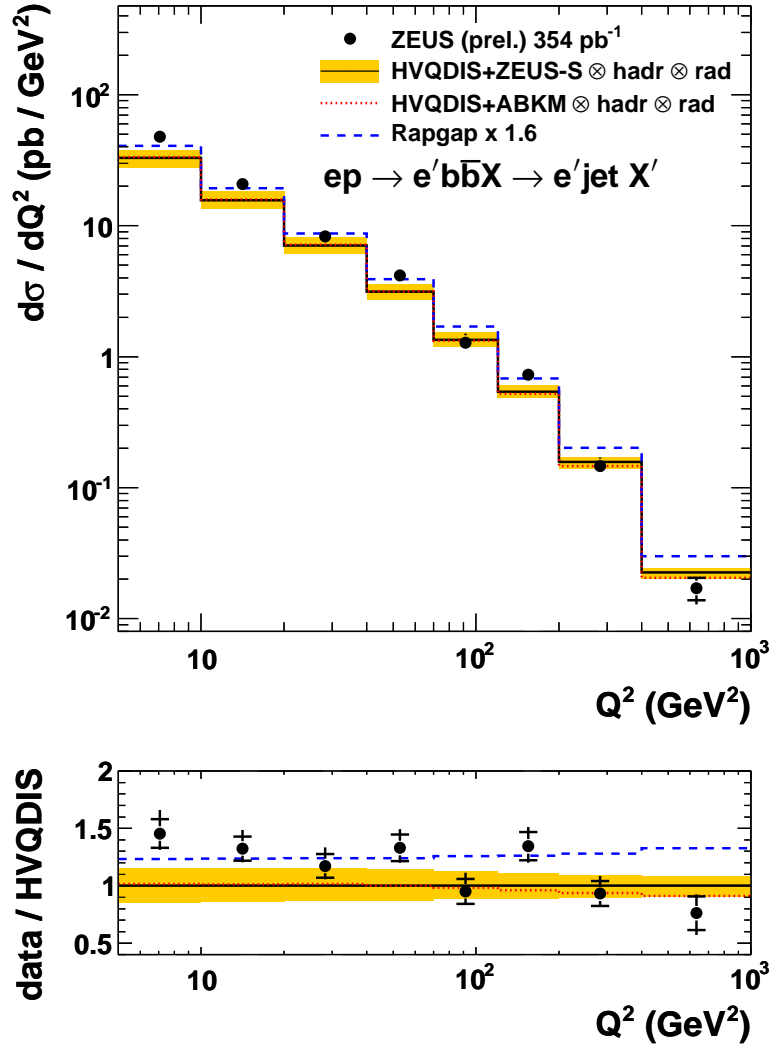


Figure 7.25.: Differential cross section for jet production in beauty events as a function of Q^2 compared to the NLO QCD prediction of HVQDIS obtained using the ZEUS-S and ABKM NLO PDFs. The renormalisation and factorisation scales were set to $\mu_R = \mu_F = \sqrt{Q^2 + 4m_b^2}$. Additionally, the RAPGAP Monte Carlo scaled to the data is shown.

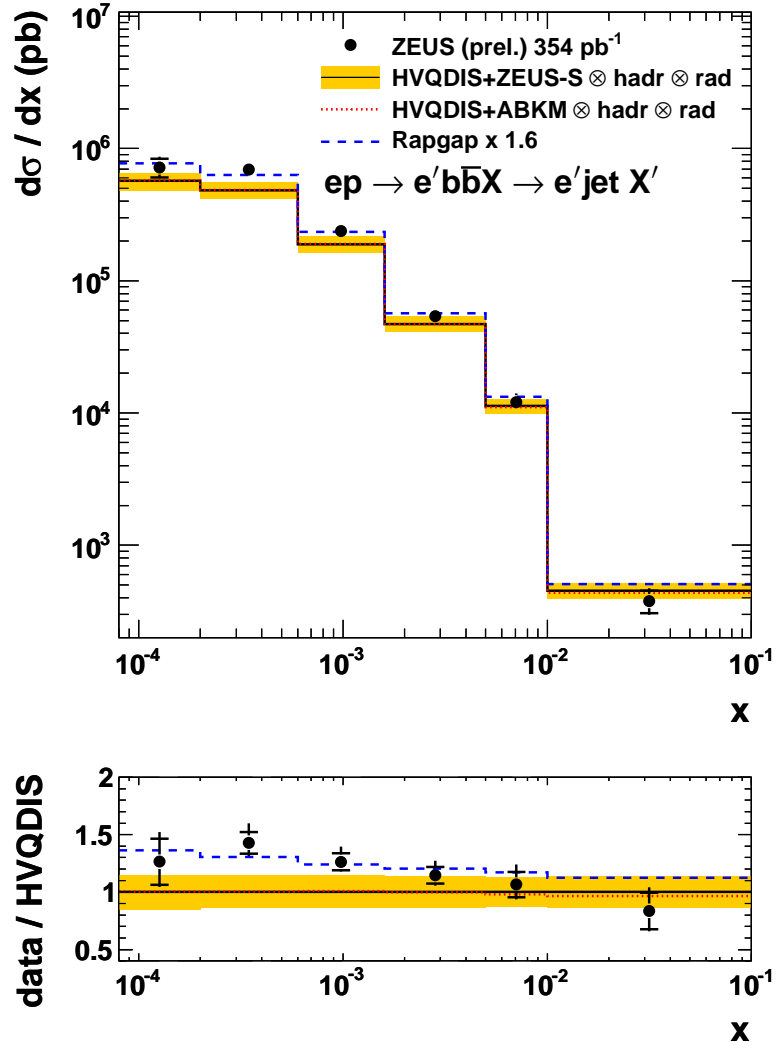


Figure 7.26.: Differential cross section for jet production in beauty events as a function of x compared to the NLO QCD prediction of HVQDIS obtained using the ZEUS-S and ABKM NLO PDFs. The renormalisation and factorisation scales were set to $\mu_R = \mu_F = \sqrt{Q^2 + 4m_b^2}$. Additionally, the RAPGAP Monte Carlo scaled to the data is shown.

7. Measurement of $F_2^{b\bar{b}}$ and $F_2^{c\bar{c}}$ using lifetime information

$\frac{5 < Q^2 < 20 \text{ GeV}^2}{x \text{ bin}}$	$d\sigma/dx$ (pb)	Δ_{stat} (pb)	Δ_{syst} (pb)	C_{had}	C_{rad}
0.00008, 0.0002	720000	± 115000	+93000 -50000	1.09	0.99
0.0002, 0.0003	873000	± 112000	+96000 -48000	1.07	0.98
0.0003, 0.0005	571000	± 57000	+57000 -28000	1.04	0.99
0.0005, 0.003	55100	± 5400	+5100 -3200	0.91	0.99
$\frac{20 < Q^2 < 60 \text{ GeV}^2}{x \text{ bin}}$	$d\sigma/dx$ (pb)	Δ_{stat} (pb)	Δ_{syst} (pb)	C_{had}	C_{rad}
0.0003, 0.0005	103000	± 27000	+16000 -12000	1.07	0.98
0.0005, 0.0012	147000	± 13000	+15000 -6000	1.05	0.99
0.0012, 0.002	75400	± 8100	+6700 -4800	1.00	1.00
0.002, 0.0035	27000	± 4200	+3000 -1400	0.94	1.01
0.0035, 0.01	4450	± 1690	+860 -610	0.81	0.99
$\frac{60 < Q^2 < 120 \text{ GeV}^2}{x \text{ bin}}$	$d\sigma/dx$ (pb)	Δ_{stat} (pb)	Δ_{syst} (pb)	C_{had}	C_{rad}
0.0008, 0.0018	30700	± 3800	+3000 -1700	1.03	0.98
0.0018, 0.003	24300	± 2900	+2300 -1700	1.02	0.99
0.003, 0.006	7340	± 1270	+1060 -290	0.98	0.98
$\frac{120 < Q^2 < 400 \text{ GeV}^2}{x \text{ bin}}$	$d\sigma/dx$ (pb)	Δ_{stat} (pb)	Δ_{syst} (pb)	C_{had}	C_{rad}
0.0016, 0.005	7600	± 940	+670 -640	1.01	0.99
0.005, 0.016	4320	± 340	+390 -200	0.99	1.02
0.016, 0.06	223	± 96	+51 -15	0.92	0.87
$\frac{400 < Q^2 < 1000 \text{ GeV}^2}{x \text{ bin}}$	$d\sigma/dx$ (pb)	Δ_{stat} (pb)	Δ_{syst} (pb)	C_{had}	C_{rad}
0.005, 0.02	378	± 87	+40 -45	1.01	0.95
0.02, 0.1	51.9	± 18.9	+5.1 -13.6	1.00	0.95

Table 7.7.: Measured cross sections for jet production in beauty events as a function of x for different ranges of Q^2 . The kinematic region is given by $0.02 < y < 0.7$, $E_T^{\text{jet}} > 5 \text{ GeV}$ and $-1.6 < \eta^{\text{jet}} < 2.2$. The statistical and systematic uncertainties are shown separately. Additionally, the factors C_{had} and C_{rad} to correct the NLO QCD predictions for hadronisation and QED effects are listed.

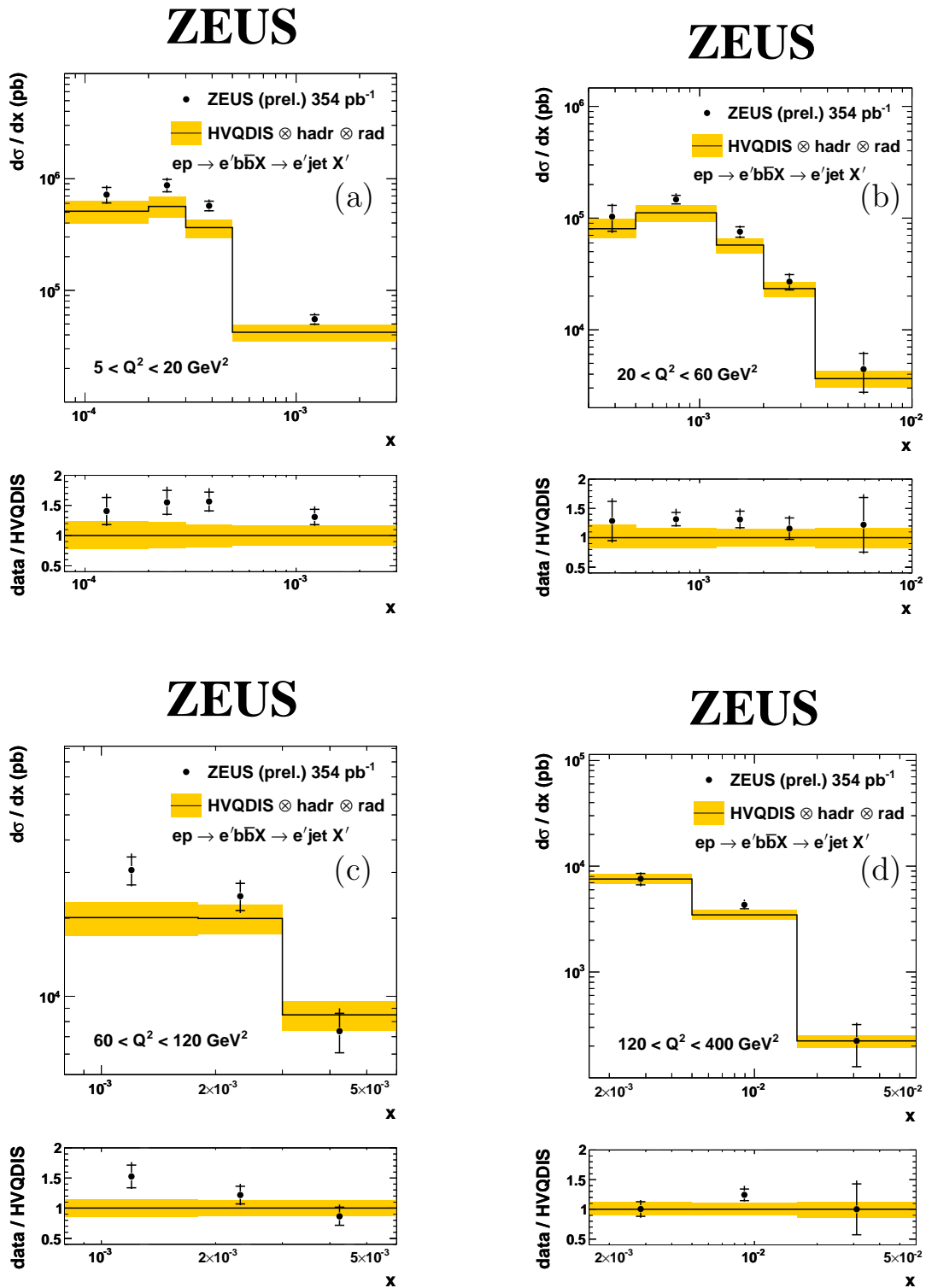


Figure 7.27.: Differential cross sections for jet production in beauty events as a function of x for (a) $5 < Q^2 < 20 \text{ GeV}^2$, (b) $20 < Q^2 < 60 \text{ GeV}^2$, (c) $60 < Q^2 < 120 \text{ GeV}^2$ and (d) $120 < Q^2 < 400 \text{ GeV}^2$ compared to the NLO QCD prediction of HVQDIS calculated using $\mu_R = \mu_F = \frac{1}{2}\sqrt{Q^2 + p_T^2 + m_b^2}$.

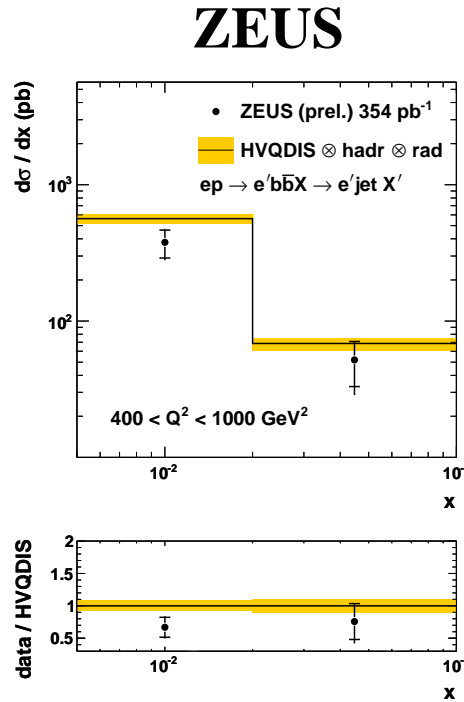


Figure 7.28.: Differential cross section for jet production in beauty events as a function of x for $400 < Q^2 < 1000 \text{ GeV}^2$ compared to the NLO QCD prediction of HVQDIS calculated using $\mu_R = \mu_F = \frac{1}{2} \sqrt{Q^2 + p_T^2 + m_b^2}$.

7.4.5. Extraction of $F_2^{b\bar{b}}$

To extract $F_2^{b\bar{b}}(x, Q^2)$ from the measured visible cross sections, an extrapolation from the measured range in E_T^{jet} and η^{jet} to the full phase space of beauty quark production at given values of x and Q^2 was performed. The extrapolation was based on NLO QCD predictions in the FFNS obtained using the HVQDIS program. The extrapolation for beauty was only moderate with extrapolation factors typically ranging from 1.3 to 1.0 decreasing with Q^2 . The factor was up to 1.7 at high values of x .

The measured values of $F_2^{b\bar{b}}$ were calculated using the following formula:

$$F_{2,\text{meas}}^{b\bar{b}}(x_i, Q_i^2) = \frac{\sigma_{\text{meas},i}}{\sigma_{\text{theo},i}} \cdot F_{2,\text{theo}}^{b\bar{b}}(x_i, Q_i^2), \quad (7.15)$$

where $\sigma_{\text{meas},i}$ is the measured visible cross section and $\sigma_{\text{theo},i}$ is the predicted cross section from HVQDIS in a bin i . The values x_i and Q_i^2 define the point in the x - Q^2 plane where $F_2^{b\bar{b}}$ is estimated. $F_{2,\text{theo}}^{b\bar{b}}$ was evaluated using the HVQDIS program.

The extraction of $F_2^{b\bar{b}}$ is illustrated in Fig. 7.29. The bins in Q^2 and x where $\sigma_{\text{meas},i}$ was obtained are shown by dashed lines. To extract $F_2^{b\bar{b}}$ at the same x values as were used for previous measurements (see Figs. 7.32 and 7.33), the values of x_i and Q_i^2 were not always chosen in the centre of the bins. This is equivalent to swimming the points after the extraction of $F_2^{b\bar{b}}$.

Since calculations of $F_2^{b\bar{b}}$ are usually given at the QED Born level, $\sigma_{\text{meas},i}$ was multiplied by

$1/C_{\text{rad}}$. To subtract the small contribution from $F_L^{b\bar{b}}$, the terms due to $F_L^{b\bar{b}}$ were switched off in HVQDIS when $F_{2,\text{theo}}^{b\bar{b}}$ was estimated. This correction changed the results by a few % at high y and was negligible at low y .

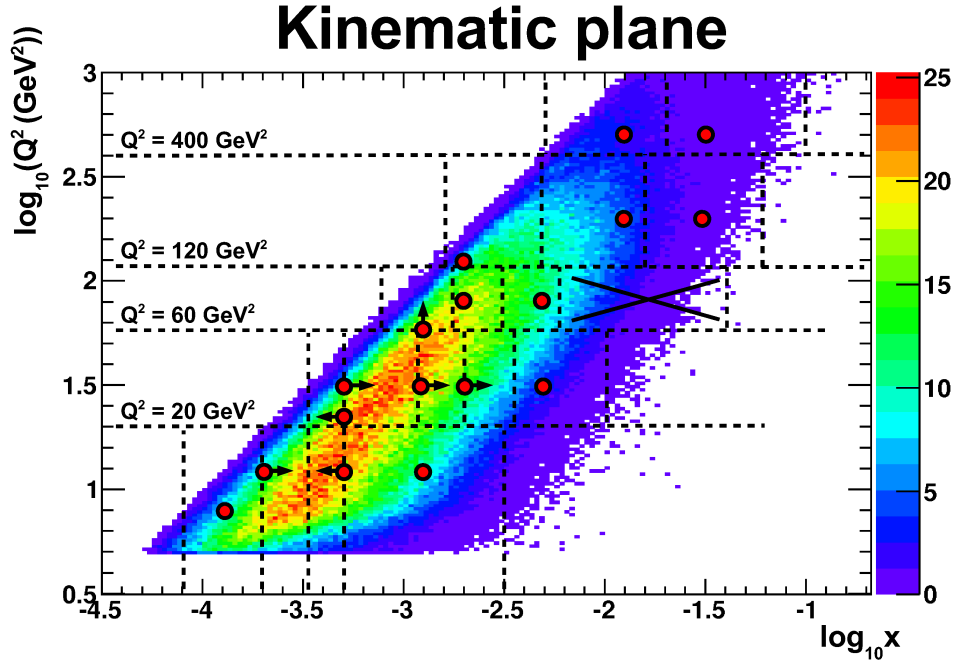


Figure 7.29.: Kinematic plane for the $F_2^{b\bar{b}}$ measurement. The bins where double differential cross sections were extracted are shown by dashed lines. The points show the values of x_i and Q_i where $F_2^{b\bar{b}}$ was extracted.

By default, the HVQDIS predictions obtained using $\mu_R = \mu_F = \sqrt{Q^2 + p_T^2 + m_b^2}$ were used to extract $F_2^{b\bar{b}}$. To estimate the uncertainty of the extrapolation procedure, the settings of the HVQDIS calculation were varied and $\sigma_{\text{theo},i}$ and $F_{2,\text{theo}}^{b\bar{b}}$ were recalculated. The resulting uncertainties for all variations were added in quadrature. The following parameter variations were considered:

- the ZEUS PDF uncertainties were propagated from the experimental uncertainties of the fitted data;
- the beauty quark mass was changed consistently in the PDF fit and in HVQDIS by ± 0.25 GeV;
- the renormalisation scale was varied by a factor 2;
- the factorisation scale was varied by a factor 2 independently of the renormalisation scale;
- the renormalisation and factorisation scales were set to $\mu_R = \mu_F = \sqrt{Q^2 + 4m_b^2}$.

7. Measurement of $F_2^{b\bar{b}}$ and $F_2^{c\bar{c}}$ using lifetime information

The extracted values of $F_2^{b\bar{b}}$ are given in Tab.7.8. The total uncertainties of the measurements were calculated from the statistical and systematic uncertainties of the measured cross sections, and of the extrapolation uncertainty, added in quadrature.

Q^2	x	$F_2^{b\bar{b}}$	$\delta_{\text{stat.}}$	$\delta_{\text{syst.}}$	$\delta_{\text{extrapol.}}$
8	0.00013	0.00549	± 0.00087	+0.00071 -0.00038	+0.00104 -0.00075
12	0.0002	0.00875	± 0.00113	+0.00096 -0.00048	+0.00148 -0.00095
12	0.0005	0.00633	± 0.00063	+0.00063 -0.00031	+0.00048 -0.00041
12	0.0013	0.00337	± 0.00033	+0.00031 -0.00019	+0.00015 -0.00013
22	0.0005	0.01107	± 0.00288	+0.00171 -0.00129	+0.00116 -0.00134
30	0.0005	0.01624	± 0.0014	+0.00165 -0.00069	+0.00197 -0.00133
30	0.0013	0.01097	± 0.00117	+0.00096 -0.00069	+0.00062 -0.00039
30	0.002	0.00785	± 0.00123	+0.00085 -0.00039	+0.00022 -0.00020
30	0.005	0.00473	± 0.0018	+0.00091 -0.00065	+0.00023 -0.00015
60	0.0013	0.02703	± 0.00333	+0.00265 -0.00151	+0.00177 -0.00169
80	0.002	0.02341	± 0.00282	+0.00219 -0.00161	+0.00089 -0.00102
80	0.005	0.01024	± 0.00177	+0.00148 -0.00041	+0.00025 -0.00028
130	0.002	0.02900	± 0.00357	+0.00252 -0.00241	+0.00157 -0.00166
200	0.013	0.01605	± 0.00127	+0.00140 -0.00072	+0.00035 -0.00056
200	0.032	0.00543	± 0.00233	+0.00141 -0.00042	+0.00017 -0.00013
500	0.013	0.01413	± 0.00327	+0.00154 -0.00174	+0.00022 -0.00036
500	0.032	0.00707	± 0.00257	+0.00071 -0.00191	+0.00014 -0.00003

Table 7.8.: Extracted values of $F_2^{b\bar{b}}$. The statistical and systematic uncertainties are shown separately. The uncertainty of the extrapolation to the full jet phase space is also shown.

Comparison to predictions and previous measurements

In Figs. 7.30 and 7.31 the extracted values of $F_2^{b\bar{b}}$ are shown as a function of x in bins of Q^2 . The measurements are compared to the HVQDIS+ZEUS-S and ABKM NNLO [33, 154] predictions which are both based on the FFNS. In Fig. 7.30 the renormalisation and factorisation scales for the HVQDIS calculation were set to $\mu_R = \mu_F = \frac{1}{2}\sqrt{Q^2 + p_T^2 + m_b^2}$ while in Fig. 7.31 both scales were set to $\mu_R = \mu_F = \sqrt{Q^2 + 4m_b^2}$.

The ABKM NNLO prediction gives the best description of the data in the studied kinematic region. Also the HVQDIS+ZEUS-S calculation based on the scales $\mu_R = \mu_F = \sqrt{Q^2 + 4m_b^2}$ gives a good description of the data. However, the HVQDIS+ZEUS-S prediction obtained using $\mu_R = \mu_F = \frac{1}{2}\sqrt{Q^2 + p_T^2 + m_b^2}$ underestimates the measured points at low values of Q^2 .

The results of the extraction are shown as a function of Q^2 for different values of x in Fig. 7.32 and are compared to previous ZEUS and H1 measurements (see Sec. 3.2 and Sec. 3.3). The measurement using inclusive secondary vertices represents the most precise determination of $F_2^{b\bar{b}}$ at HERA in a wide range of Q^2 . The data are all compatible within the uncertainties. Several QCD predictions based on the GM-VFNS and on the FFNS are compared to the measurements. The most important properties of the different calculations are compared in Tab. 7.9. The predictions from different theoretical approaches agree fairly well with each other. At low Q^2 and low x the HVQDIS+ZEUS-S and CTEQ6.6 NLO predictions are somewhat lower than the data. In this region the largest influence from mass effects is expected. All predictions are able to reproduce the measured values at higher Q^2 .

PDF	Order	Scheme	μ_F^2	μ_R^2	m_b (GeV)	$\alpha_s(M_Z)$
MSTW08 NLO	α_s^2	GM-VFNS		Q^2	4.75	0.1202
MSTW08 NNLO	appr. α_s^3	GM-VFNS		Q^2	4.75	0.1171
CTEQ6.6 NLO	α_s, α_s^2	GM-VFNS	Q^2	$Q^2 + 4m_b^2$	4.75	0.1180
GJR08 NLO	α_s^2	FFNS		m_b^2	4.2	0.1145
ABKM NNLO	appr. α_s^3	FFNS		$Q^2 + 4m_b^2$	4.5	0.1129
ZEUS-S+HVQDIS	α_s^2	FFNS	$\frac{1}{4}(Q^2 + p_T^2 + m_b^2)$		4.75	0.1180

Table 7.9.: PDF schemes and parameters of the calculations shown in Fig. 7.32.

In Fig. 7.33 the same data are compared to a new variant of the ABKM NNLO prediction which uses the $\overline{\text{MS}}$ mass [155] instead of the pole mass. This prediction gives a good description of the data in the entire range of the measurement.

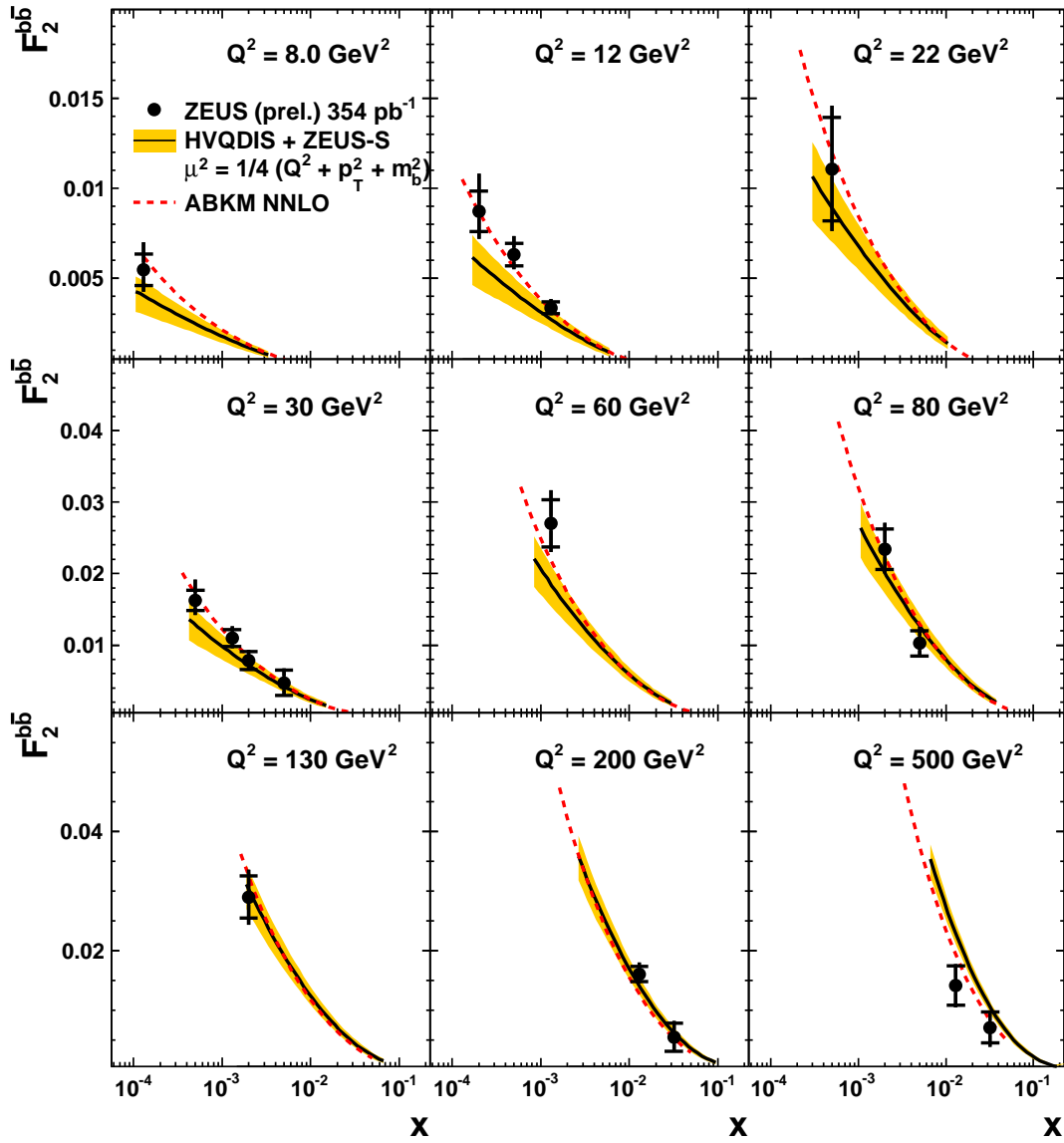


Figure 7.30.: $F_2^{b\bar{b}}$ as a function of x for different values of Q^2 . The measurement is compared to FFNS predictions.

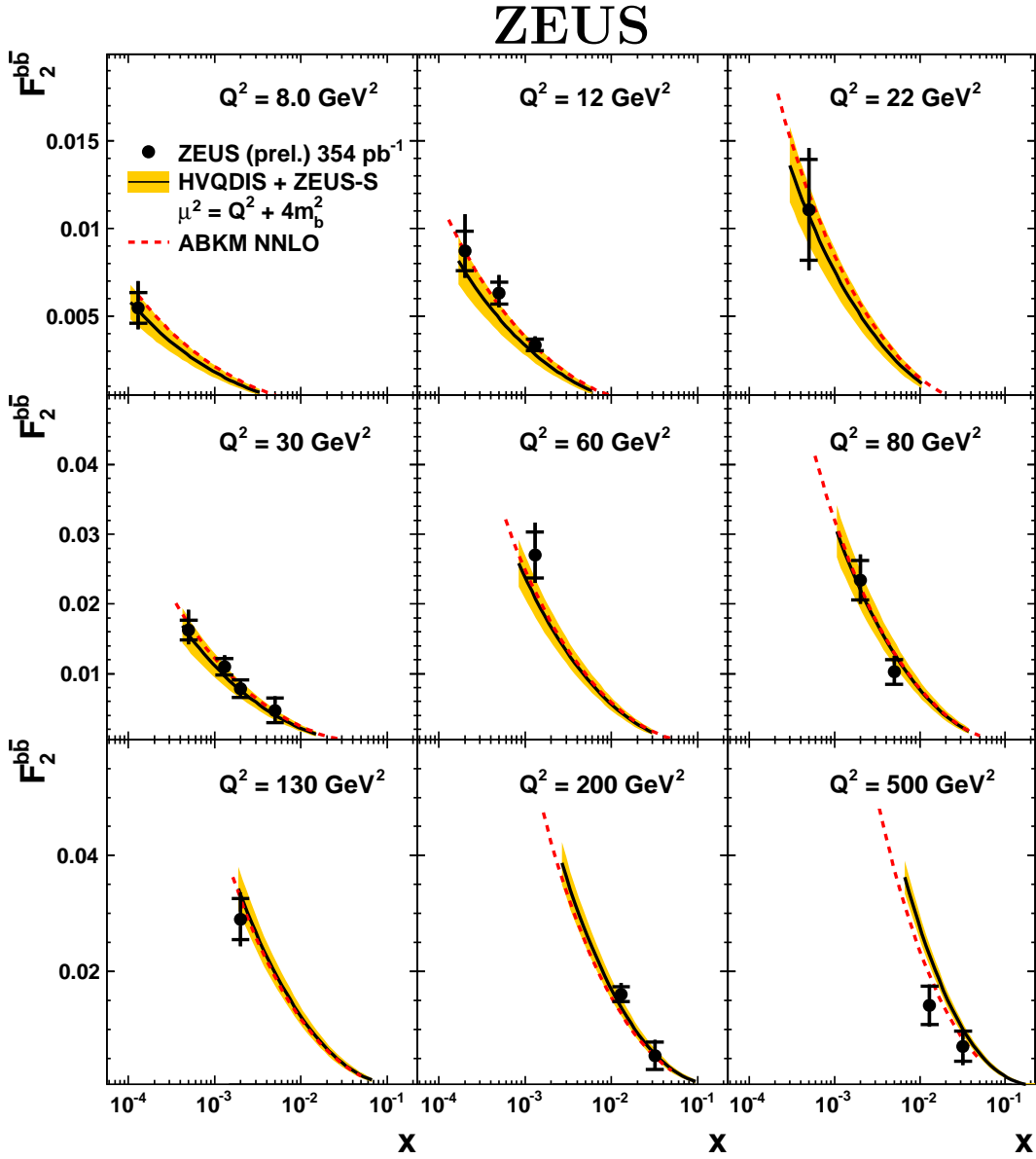


Figure 7.31.: $F_2^{b\bar{b}}$ as a function of x for different values of Q^2 . The measurement is compared to FFNS predictions.

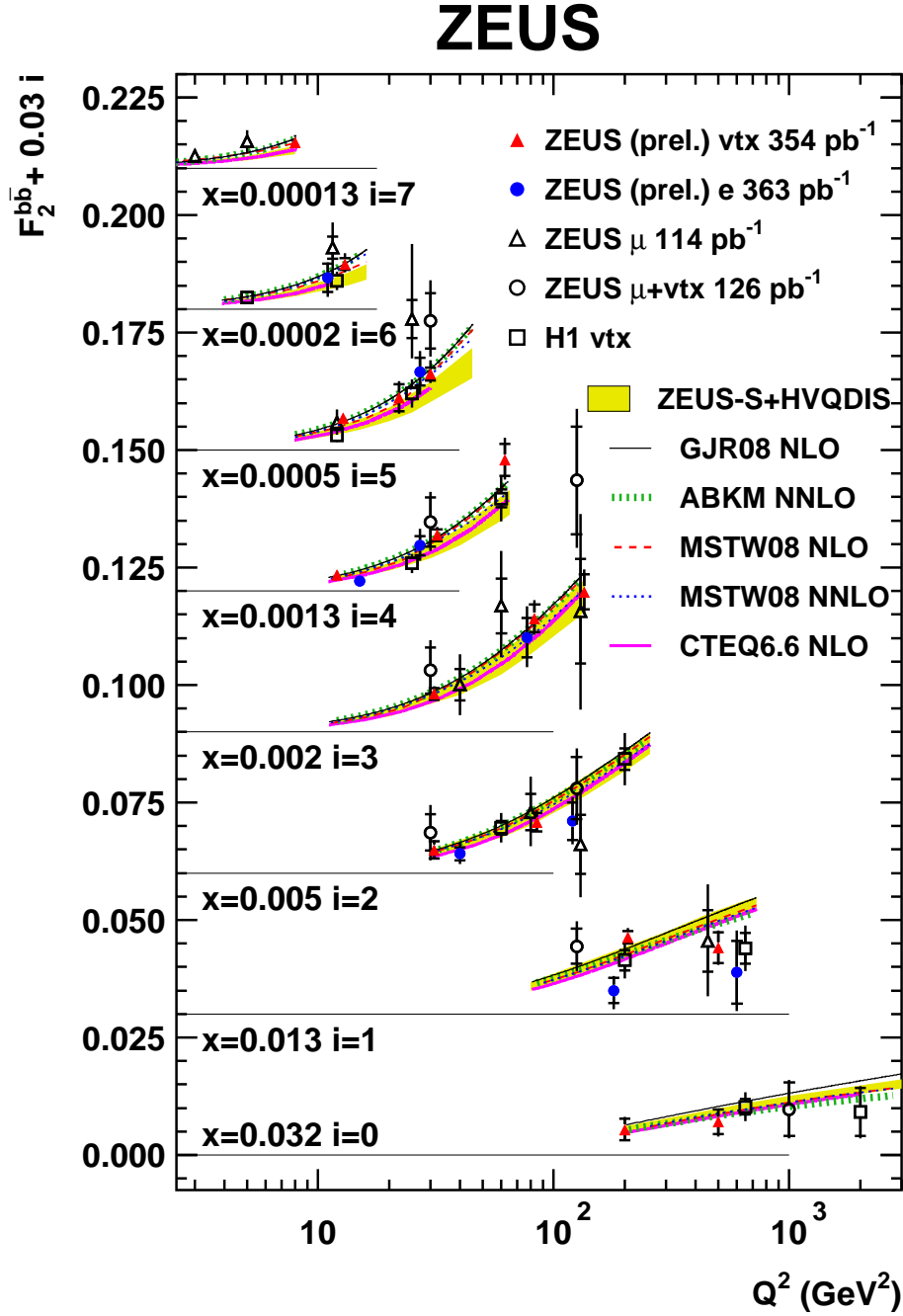


Figure 7.32.: $F_2^{b\bar{b}}$ as a function of Q^2 . The measurements described in this chapter are labelled “ZEUS (prel.) vtx 354 pb⁻¹”. Different measurements (see Sec. 3.2 and Sec. 3.3) are compared to QCD predictions.

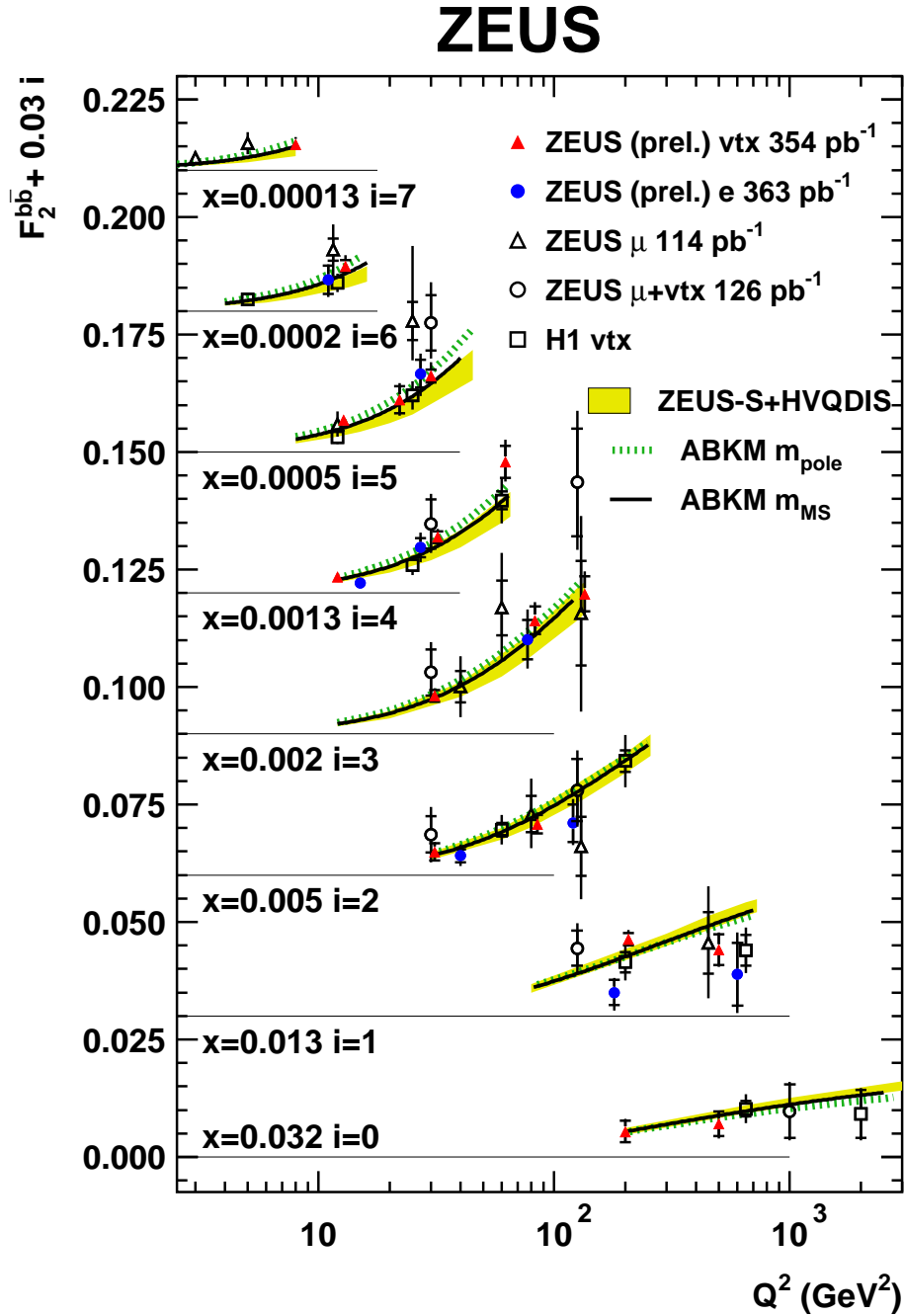


Figure 7.33.: $F_2^{b\bar{b}}$ as a function of Q^2 . The measurements described in this chapter are labelled “ZEUS (prel.) vtx 354 pb⁻¹”. Different measurements (see Sec. 3.2 and Sec. 3.3) are compared to QCD predictions.

7.5. Measurement of charm production and extraction of $F_2^{c\bar{c}}$ in an extended kinematic region

In this section an extension of the analysis to measure cross sections for jet production in charm events and to extract $F_2^{c\bar{c}}$ is described. In contrast to beauty, the cut on E_T^{jet} removes a large fraction of the produced charm quarks at low values of Q^2 . This results in large extrapolation factors and hence large extrapolation uncertainties for $F_2^{c\bar{c}}$. Hence the cut on E_T^{jet} was lowered to 4.2 GeV. Thus the kinematic region of the charm measurement is given by:

$$\begin{aligned} E_T^{\text{jet}} &> 4.2 \text{ GeV}, \\ -1.6 &< \eta^{\text{jet}} < 2.2, \\ 0.02 &< y < 0.7 \text{ and} \\ 5 &< Q^2 < 1000 \text{ GeV}^2. \end{aligned}$$

Apart from the change of the kinematic range of the measurement, the jet cross sections in charm events were extracted in exactly the same way as described above for beauty. Control distributions for the extended kinematic region are shown in Appendix F. The distributions are similar to those shown in Sec. 7.3.5 for $E_T^{\text{jet}} > 5 \text{ GeV}$.

7.5.1. Systematic uncertainties

The same sources of systematic uncertainty as studied for the beauty analysis were investigated (see Sec. 7.4.2). The effects on the cross sections for the full kinematic region are given in parentheses:

- $\{\delta_1\}$ event and DIS selection (${}_{-2\%}^{+1\%}$);
- $\{\delta_2\}$ tracking simulation (+5%);
- $\{\delta_3\}$ decay length smearing (+2%);
- $\{\delta_4\}$ uncertainty of the signal extraction procedure (${}_{-2\%}^{+3\%}$);
- $\{\delta_5\}$ calorimeter energy scale (${}_{-3\%}^{+2\%}$);
- $\{\delta_6\}$ FLT efficiency (+1%);
- $\{\delta_7\}$ Q^2 reweighting. ($\pm 2\%$);
- $\{\delta_8\}$ model dependence of the acceptance corrections (+7%). In contrast to the beauty measurement, the model dependence of the acceptance corrections was estimated including the process $cg \rightarrow cg$ in the reference Monte Carlo;
- $\{\delta_9\}$ uncertainty in the luminosity measurement of $\pm 2.0\%$.

Two additional sources of uncertainty were considered for charm:

- $\{\delta_{10}\}$ Electromagnetic energy scale ($< 1\%$). The energy of the scattered electron was raised and lowered by 1%;
- $\{\delta_{11}\}$ Asymmetry of the light flavour (LF) contribution ($\pm 2\%$). The asymmetry of the LF templates in the fit was varied by $\pm 30\%$ to take into account the uncertainties of the simulation of secondary interactions in the detector material, and of the K_S^0 and Λ cross sections. This effect was negligible for beauty. However, the asymmetry of the decay-length significance distribution for light quark events is much stronger in the range of m_{vtx} dominated by charm events (see Fig. 7.7) compared to the region dominated by beauty events. Hence the uncertainty of the asymmetry of the light flavour templates has an impact on the measured cross sections for charm.

The contributions from the different systematic uncertainties were calculated and added in quadrature separately for positive and negative variations. The same estimates were made in each bin in which differential cross sections were measured.

7.5.2. NLO QCD predictions from HVQDIS

The calculation of NLO QCD predictions for jet production in charm events using HVQDIS was performed in the same way as for beauty (see Sec. 7.4.3). The charm quark mass was set to 1.5 GeV. Only two variants of the HVQDIS predictions were obtained. In both cases, the renormalisation and factorisation scales were set to $\mu_R = \mu_F = \sqrt{Q^2 + 4m_c^2}$. Predictions were obtained using the ZEUS-S PDFs and using the ABKM NLO PDFs for the proton.

The uncertainties of the HVQDIS predictions using the ZEUS-S PDFs were estimated by changing the charm quark mass to 1.3 and 1.7 GeV. The renormalisation and factorisation scales were independently varied by a factor of $\frac{1}{2}$ and 2. Additionally, the experimental uncertainties of the data used in the PDF fit were propagated to the predicted cross sections. These contributions result in total uncertainties of 10 – 50%. Compared to beauty, the uncertainties are larger at low Q^2 and low x due to the smaller charm quark mass. The individual contributions to the uncertainties of the HVQDIS predictions as functions of E_T^{jet} , η^{jet} , Q^2 and x are shown in Appendix G.

The values of the correction factors C_{had} and C_{rad} obtained for charm are listed in Tabs. 7.10 and 7.11.

7.5.3. Results

Single differential cross sections for jet production in charm events were measured as functions of E_T^{jet} , η^{jet} , Q^2 and x . The measured cross sections and their uncertainties are listed in Tab. 7.10 and compared to the NLO QCD prediction from HVQDIS in Figs. 7.34, 7.35, 7.36 and 7.37. The binning was chosen similar to that of the beauty measurement. The size of the lowest bin in E_T^{jet} was increased and the lowest bin in η^{jet} was split into two bins.

The measured cross sections are typically 30% larger than the predictions from HVQDIS. On the other hand, the shapes of all differential cross sections are well described by NLO

QCD. Hence no problems are expected when the HVQDIS predictions are used for the extrapolation in E_T^{jet} and η^{jet} to extract $F_2^{c\bar{c}}$.

The data are also compared to the cross sections predicted by the RAPGAP program. The RAPGAP MC prediction multiplied by 1.4 describes the measured cross sections as functions of E_T^{jet} , η^{jet} and x well. As for beauty, the Q^2 distribution is not reproduced by the RAPGAP program.

The forward direction, $1.6 < \eta^{\text{jet}} < 2.2$, is especially interesting because charm production has not been measured before in this region at HERA. The cross section in the forward direction is well described by the NLO QCD prediction obtained using HVQDIS. Hence the validity of the extrapolation to the forward direction to extract $F_2^{c\bar{c}}$ using other measurements, e.g. from D^{*+} production, is confirmed.

Double differential cross sections were measured as functions of x and Q^2 . The cross sections as a function of x for different ranges of Q^2 are listed in Tab.7.11 and are shown in Figs. 7.38 and 7.39. Compared to the beauty analysis, one bin in x was added in the range $60 < Q^2 < 120 \text{ GeV}^2$. All cross sections are reasonably well described by the NLO QCD predictions from HVQDIS. Except at very high values of Q^2 , the precision of the measurement is limited by systematic uncertainties.

7.5. Measurement of charm production and extraction of F_2^{cc} in an extended kinematic region

E_T^{jet} bin (GeV)	$d\sigma/dE_T^{\text{jet}}$ (pb/GeV)	Δ_{stat} (pb/GeV)	Δ_{syst} (pb/GeV)		C_{had}	C_{rad}
4.2, 8	3560	± 120	+320	-220	1.06	0.98
8, 11	718	± 21	+76	-72	1.05	0.97
11, 14	206	± 10	+47	-27	1.03	0.96
14, 17	81.4	± 5.5	+13.7	-14.7	0.99	0.93
17, 20	34.0	± 3.7	+6.3	-7.1	0.96	0.93
20, 25	11.5	± 2.3	+2.3	-2.1	0.95	0.85
25, 35	1.44	± 0.97	+0.29	-0.26	0.86	0.88
η^{jet} bin	$d\sigma/d\eta^{\text{jet}}$ (pb)	Δ_{stat} (pb)	Δ_{syst} (pb)		C_{had}	C_{rad}
-1.6, -1.1	2090	± 260	+280	-290	0.89	0.99
-1.1, -0.8	3800	± 220	+370	-520	0.97	0.98
-0.8, -0.5	4660	± 210	+500	-460	1.02	0.98
-0.5, -0.2	5740	± 210	+710	-190	1.05	0.98
-0.2, 0.1	5850	± 220	+610	-360	1.07	0.98
0.1, 0.4	6270	± 230	+740	-270	1.10	0.98
0.4, 0.7	6020	± 230	+810	-330	1.11	0.98
0.7, 1.0	6010	± 250	+520	-480	1.10	0.98
1.0, 1.3	5150	± 290	+550	-640	1.09	0.98
1.3, 1.6	4380	± 380	+510	-860	1.07	0.97
1.6, 2.2	4350	± 560	+580	-1390	1.13	0.97
Q^2 bin (GeV ²)	$d\sigma/dQ^2$ (pb/GeV ²)	Δ_{stat} (pb/GeV ²)	Δ_{syst} (pb/GeV ²)		C_{had}	C_{rad}
5, 10	890	± 37	+94	-64	1.15	0.98
10, 20	474	± 15	+43	-37	1.08	0.99
20, 40	207	± 6	+19	-13	1.01	0.98
40, 70	67.1	± 2.7	+5.8	-3.3	1.00	0.97
70, 120	21.5	± 1.0	+3.5	-1.0	1.00	0.97
120, 200	6.54	± 0.44	+0.48	-0.57	1.01	0.96
200, 400	1.75	± 0.13	+0.11	-0.20	1.01	0.95
400, 1000	0.187	± 0.030	+0.046	-0.022	1.02	0.87
x bin	$d\sigma/dx$ (pb)	Δ_{stat} (pb)	Δ_{syst} (pb)		C_{had}	C_{rad}
0.00008, 0.0002	12200000	± 900000	+1900000	-2500000	1.19	0.96
0.0002, 0.0006	11000000	± 400000	+1200000	-400000	1.20	0.98
0.0006, 0.0016	5210000	± 140000	+470000	-430000	1.09	0.99
0.0016, 0.005	1220000	± 30000	+100000	-48000	0.97	0.99
0.005, 0.01	248000	± 13000	+33000	-22000	0.91	1.00
0.01, 0.1	9940	± 770	+1040	-1170	0.88	0.88

Table 7.10.: Measured cross sections for jet production in charm events as a function of E_T^{jet} , η^{jet} , Q^2 and x for $5 < Q^2 < 1000$ GeV², $0.02 < y < 0.7$, $E_T^{\text{jet}} > 4.2$ GeV and $-1.6 < \eta^{\text{jet}} < 2.2$. The statistical and systematic uncertainties are shown separately. Additionally, the factors C_{had} and C_{rad} to correct the NLO QCD predictions for hadronisation and QED effects are listed.

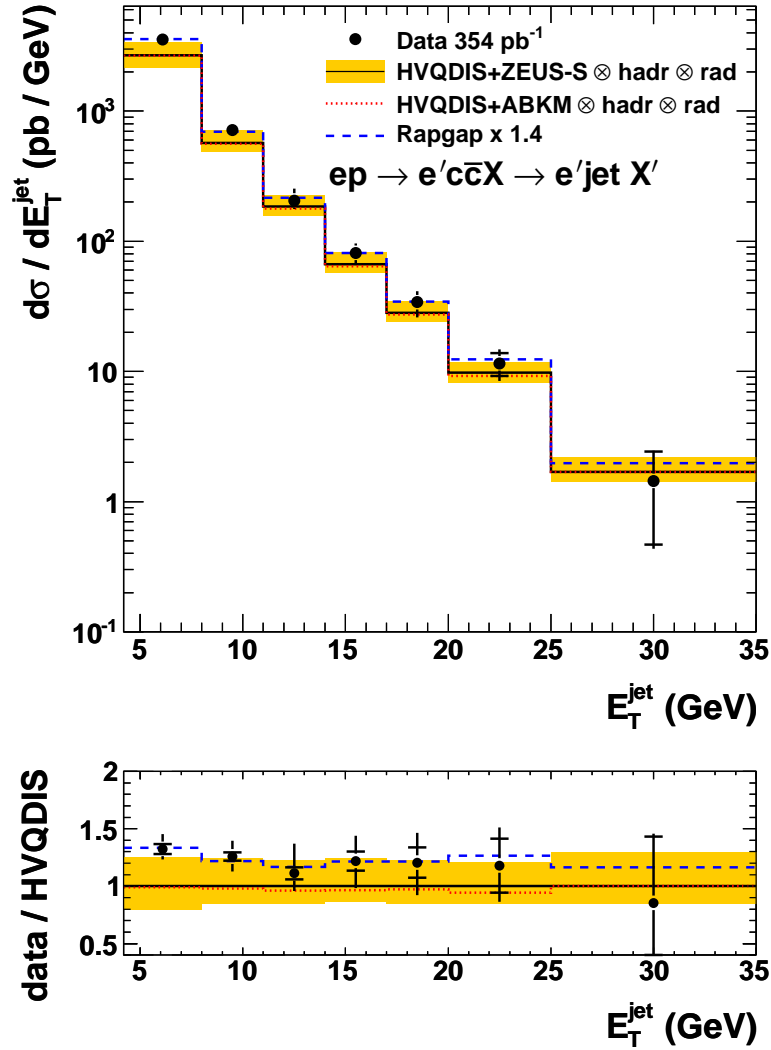


Figure 7.34.: Differential cross section for jet production in charm events as a function of E_T^{jet} compared to the NLO QCD prediction of HVQDIS obtained using the ZEUS-S and ABKM NLO PDFs. The renormalisation and factorisation scales were set to $\mu_R = \mu_F = \sqrt{Q^2 + 4m_c^2}$. Additionally, the RAPGAP Monte Carlo scaled to the data is shown.

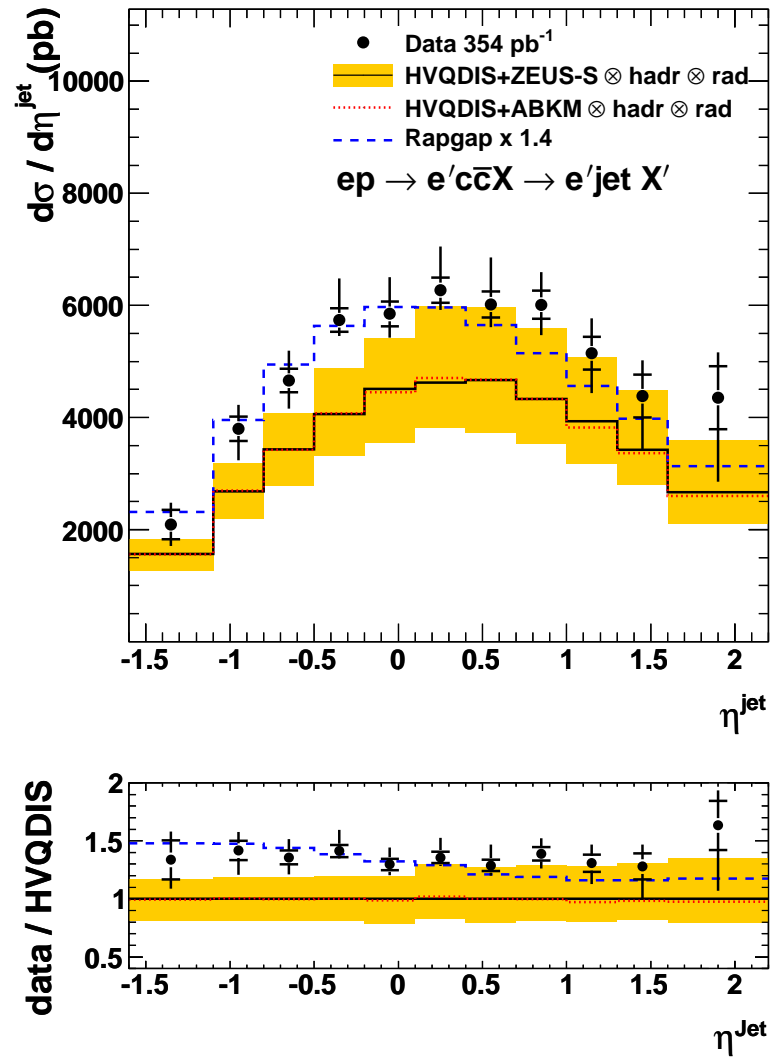


Figure 7.35.: Differential cross section for jet production in charm events as a function of η^{jet} compared to the NLO QCD prediction of HVQDIS obtained using the ZEUS-S and ABKM NLO PDFs. The renormalisation and factorisation scales were set to $\mu_R = \mu_F = \sqrt{Q^2 + 4m_c^2}$. Additionally, the RAPGAP Monte Carlo scaled to the data is shown.

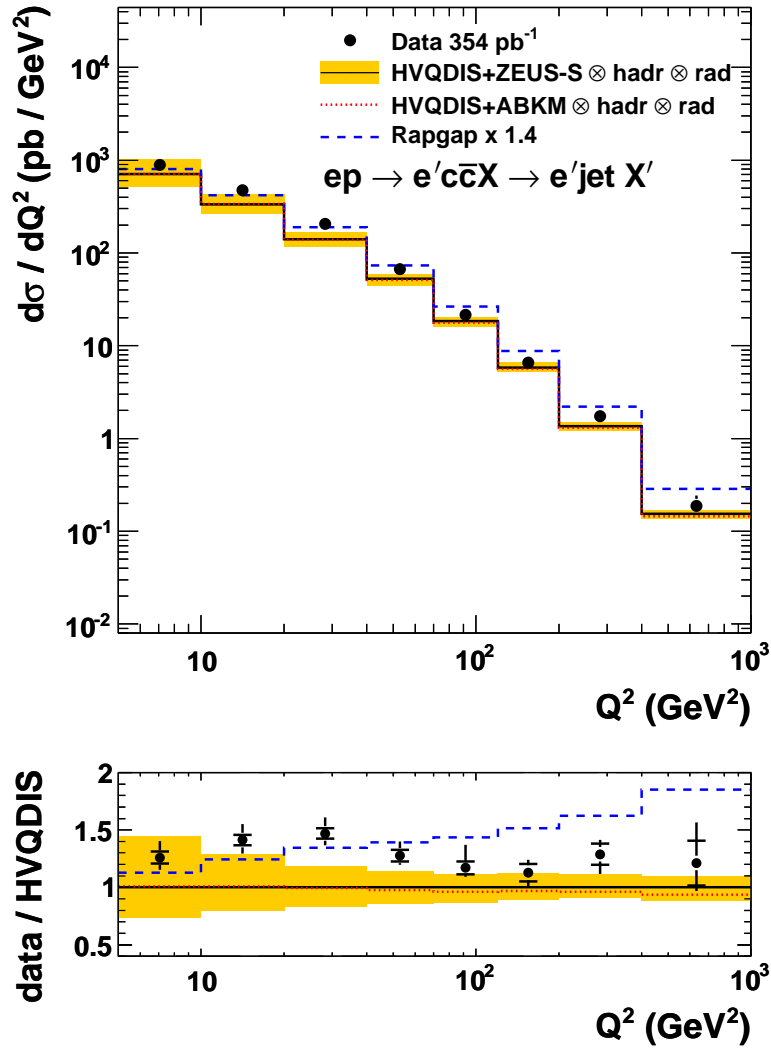


Figure 7.36.: Differential cross section for jet production in charm events as a function of Q^2 compared to the NLO QCD prediction of HVQDIS obtained using the ZEUS-S and ABKM NLO PDFs. The renormalisation and factorisation scales were set to $\mu_R = \mu_F = \sqrt{Q^2 + 4m_c^2}$. Additionally, the RAPGAP Monte Carlo scaled to the data is shown.

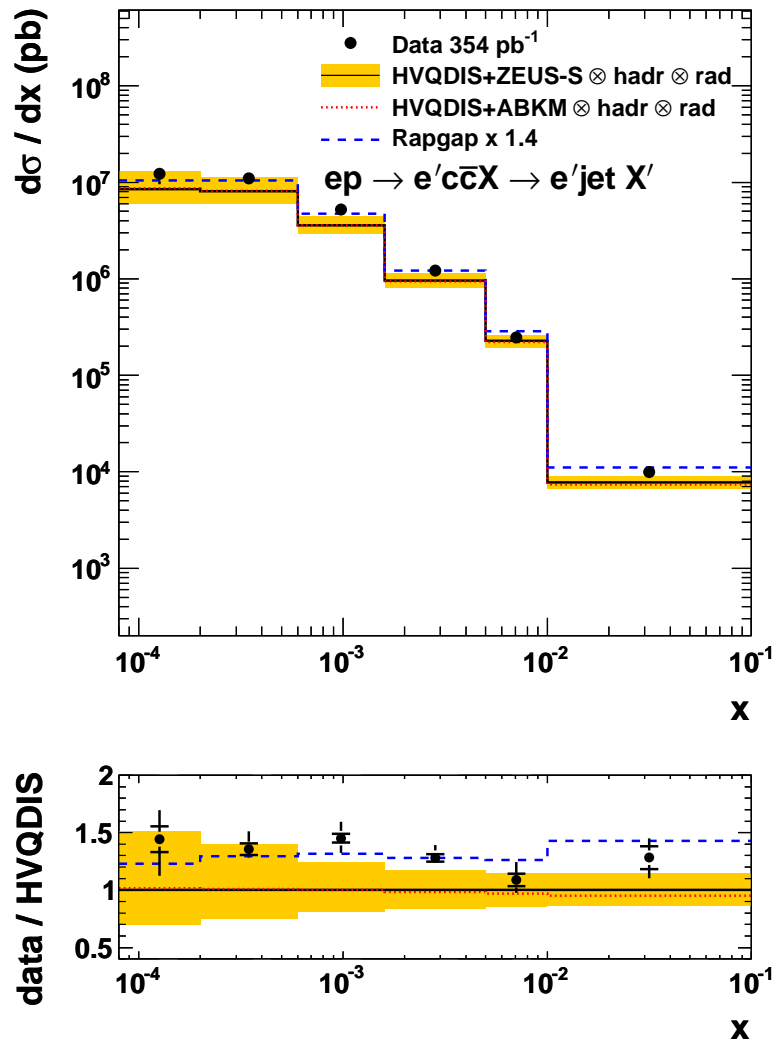


Figure 7.37.: Differential cross section for jet production in charm events as a function of x compared to the NLO QCD prediction of HVQDIS obtained using the ZEUS-S and ABKM NLO PDFs. The renormalisation and factorisation scales were set to $\mu_R = \mu_F = \sqrt{Q^2 + 4m_c^2}$. Additionally, the RAPGAP Monte Carlo scaled to the data is shown.

7. Measurement of $F_2^{b\bar{b}}$ and $F_2^{c\bar{c}}$ using lifetime information

$5 < Q^2 < 20 \text{ GeV}^2$ x bin	$d\sigma/dx$ (pb)	Δ_{stat} (pb)	Δ_{syst} (pb)	C_{had}	C_{rad}
0.0008, 0.0002	12200000	± 900000	+1900000 -2500000	1.19	0.96
0.0002, 0.0003	14200000	± 1000000	+1700000 -1100000	1.21	0.98
0.0003, 0.0005	8870000	± 520000	+1210000 -370000	1.23	0.98
0.0005, 0.003	1670000	± 60000	+150000 -150000	1.07	1.00
$20 < Q^2 < 60 \text{ GeV}^2$ x bin	$d\sigma/dx$ (pb)	Δ_{stat} (pb)	Δ_{syst} (pb)	C_{had}	C_{rad}
0.0003, 0.0005	1450000	± 220000	+170000 -70000	1.13	0.97
0.0005, 0.0012	2760000	± 110000	+260000 -350000	1.09	0.97
0.0012, 0.002	1470000	± 70000	+140000 -120000	1.05	0.98
0.002, 0.0035	637000	± 33000	+65000 -27000	1.01	0.99
0.0035, 0.01	175000	± 13000	+31000 -16000	0.91	0.99
$60 < Q^2 < 120 \text{ GeV}^2$ x bin	$d\sigma/dx$ (pb)	Δ_{stat} (pb)	Δ_{syst} (pb)	C_{had}	C_{rad}
0.0008, 0.0018	280000	± 33000	+43000 -24000	1.07	0.97
0.0018, 0.003	281000	± 23000	+74000 -8000	1.03	0.99
0.003, 0.006	139000	± 8000	+14000 -7000	1.01	0.98
0.006, 0.04	13900	± 1400	+4200 -1000	0.93	0.93
$120 < Q^2 < 400 \text{ GeV}^2$ x bin	$d\sigma/dx$ (pb)	Δ_{stat} (pb)	Δ_{syst} (pb)	C_{had}	C_{rad}
0.0016, 0.005	103000	± 7000	+7000 -6000	1.05	0.97
0.005, 0.016	35000	± 2300	+2400 -3700	1.01	1.00
0.016, 0.06	3930	± 760	+460 -1200	0.96	0.80
$400 < Q^2 < 1000 \text{ GeV}^2$ x bin	$d\sigma/dx$ (pb)	Δ_{stat} (pb)	Δ_{syst} (pb)	C_{had}	C_{rad}
0.005, 0.02	5010	± 770	+410 -670	1.02	0.88
0.02, 0.1	470	± 191	+38 -63	1.01	0.84

Table 7.11.: Measured cross sections for jet production in charm events as a function of x for different ranges of Q^2 . The kinematic region is given by $0.02 < y < 0.7$, $E_T^{\text{jet}} > 4.2 \text{ GeV}$ and $-1.6 < \eta^{\text{jet}} < 2.2$. The statistical and systematic uncertainties are shown separately. Additionally, the factors C_{had} and C_{rad} to correct the NLO QCD predictions for hadronisation and QED effects are listed.

7.5. Measurement of charm production and extraction of $F_2^{c\bar{c}}$ in an extended kinematic region

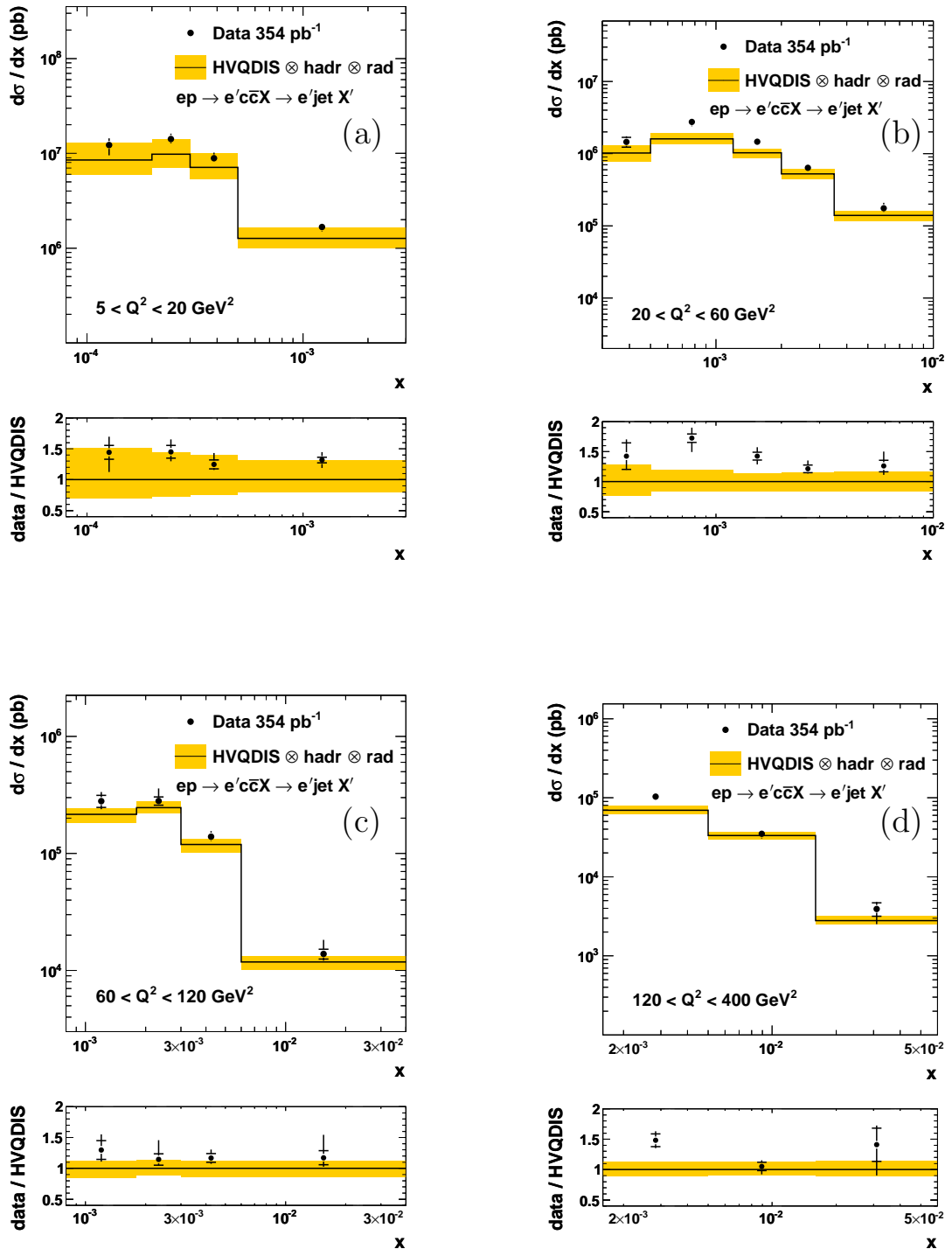


Figure 7.38.: Differential cross sections for jet production in charm events as a function of x for (a) $5 < Q^2 < 20 \text{ GeV}^2$, (b) $20 < Q^2 < 60 \text{ GeV}^2$, (c) $60 < Q^2 < 120 \text{ GeV}^2$ and (d) $120 < Q^2 < 400 \text{ GeV}^2$ compared to the NLO QCD prediction of HVQDIS.

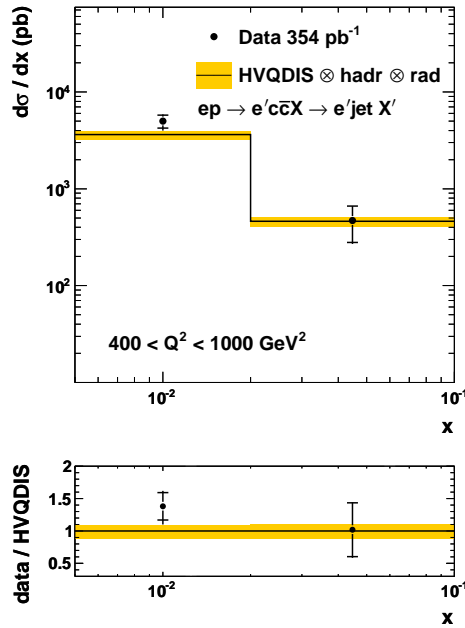


Figure 7.39.: Differential cross section for jet production in charm events as a function of x for $400 < Q^2 < 1000 \text{ GeV}^2$ compared to the NLO QCD prediction of HVQDIS.

7.5.4. Extraction of $F_2^{c\bar{c}}$

The same procedure as described in 7.4.5 was used to extract $F_2^{c\bar{c}}(x, Q^2)$ from the measured visible cross sections for jet production in charm events. The HVQDIS predictions obtained using $\mu_R = \mu_F = \sqrt{Q^2 + 4m_c^2}$ were used to extract $F_2^{c\bar{c}}$. To estimate the uncertainty of the extrapolation procedure, the settings of the HVQDIS calculation were varied and $\sigma_{\text{theo},i}$ and $F_{2,\text{theo}}^{c\bar{c}}$ were recalculated. The resulting uncertainties for all variations were added in quadrature. The following parameter variations were performed:

- the ZEUS PDF uncertainties were propagated from the experimental uncertainties of the fitted data;
- the charm quark mass was changed consistently in the PDF fit and in HVQDIS by $\pm 0.2 \text{ GeV}$;
- the renormalisation scale was varied by a factor 2;
- the factorisation scale was varied by a factor 2 independently of the renormalisation scale;

Since the observed η^{jet} distribution is well described by the HVQDIS prediction using $\mu_R = \mu_F = \sqrt{Q^2 + 4m_b^2}$ (see Fig. 7.35), the functional form of the renormalisation and

factorisations scales was not considered as a source of uncertainty for the extrapolation procedure.

The extracted values and their uncertainties are listed in 7.12. The extrapolation factors were typically about 4 in the region $5 < Q^2 < 20 \text{ GeV}^2$ and about 2 in the region $20 < Q^2 < 60 \text{ GeV}^2$. Hence the extrapolation uncertainties are large compared to the experimental uncertainties at low Q^2 and low x . At larger values of Q^2 the extrapolation was small.

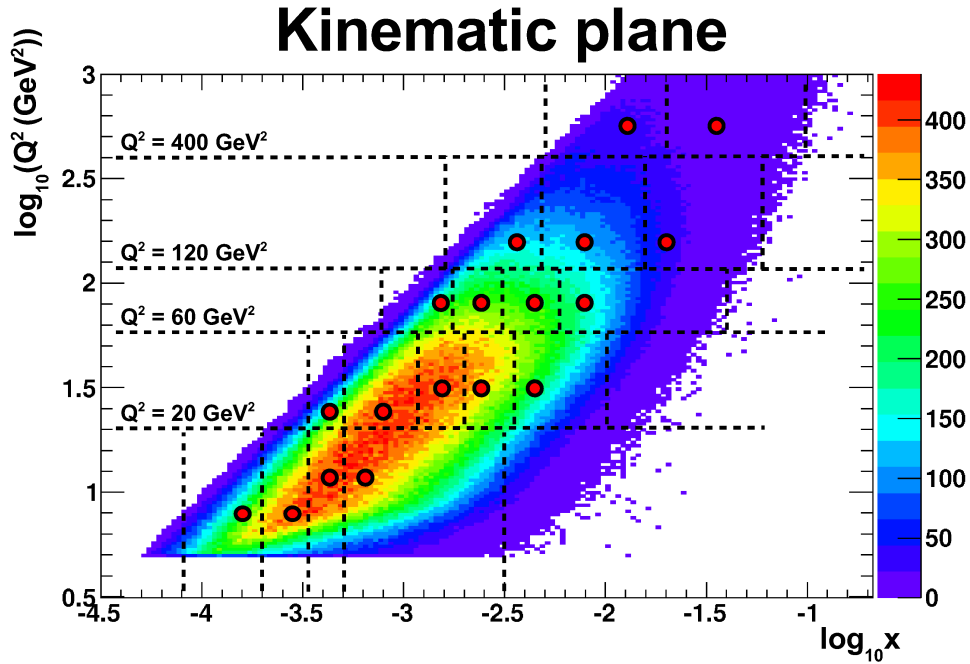


Figure 7.40.: Kinematic plane for the $F_2^{c\bar{c}}$ measurement. The bins where double differential cross sections were extracted are shown by dashed lines. The points show the values of x_i and Q_i where $F_2^{c\bar{c}}$ was extracted.

The binning used for the measurement of double differential cross sections in x and Q^2 and the points in the $x - Q^2$ plane where $F_2^{c\bar{c}}$ was extracted are shown in Fig. 7.40. In Fig. 7.41 the extracted values are shown as a function of x for different values of Q^2 . The data are compared to the HVQDIS+ZEUS-S and ABKM NNLO predictions. Both predictions are consistent with the measurement within the uncertainties. However, the normalisation at low Q^2 is better reproduced by the ABKM NNLO prediction.

The measured $F_2^{c\bar{c}}$ values are compared to the average of previous $F_2^{c\bar{c}}$ measurements at HERA (see Sec. 3.1.1) and to the HERAPDF1.0 prediction in Fig. 7.42. For this purpose some of the measured values were swum in Q^2 using the ABKM NNLO prediction. Additionally, a recent preliminary measurement of D^+ production by the ZEUS collaboration [156] using the data collected between 2005 and 2007 is shown. All measurements are consistent within the uncertainties. The measurement using inclusive secondary ver-

7. Measurement of $F_2^{b\bar{b}}$ and $F_2^{c\bar{c}}$ using lifetime information

tices is especially competitive at high Q^2 . The $F_2^{c\bar{c}}$ values measured from D^+ mesons, the H1 and ZEUS combination, the secondary vertex measurement and the HERAPDF1.0 expectation are based on independent data sets.

Q^2	x	$F_2^{c\bar{c}}$	$\delta_{\text{stat.}}$	$\delta_{\text{syst.}}$	$\delta_{\text{extrapol.}}$
6.5	0.00015	0.2389	± 0.0184	+0.0388 -0.0513	+0.0492 -0.0631
6.5	0.00028	0.2002	± 0.0142	+0.0243 -0.0159	+0.0371 -0.0426
12	0.00043	0.2519	± 0.0148	+0.0348 -0.0107	+0.0372 -0.0560
12	0.00065	0.2409	± 0.0082	+0.0220 -0.0224	+0.0117 -0.0534
25	0.00043	0.4709	± 0.0725	+0.0581 -0.0218	+0.0805 -0.0755
25	0.0008	0.4603	± 0.0188	+0.0445 -0.0601	+0.0339 -0.0505
30	0.0016	0.3247	± 0.0152	+0.0306 -0.028	+0.0179 -0.0170
30	0.0025	0.2315	± 0.012	+0.0239 -0.0097	+0.0060 -0.0108
30	0.0045	0.1842	± 0.0139	+0.0326 -0.0166	+0.0040 -0.0049
80	0.0016	0.451	± 0.053	+0.0724 -0.0406	+0.0337 -0.0213
80	0.0025	0.328	± 0.0265	+0.0869 -0.0098	+0.0078 -0.0175
80	0.0045	0.2536	± 0.0154	+0.0257 -0.0134	+0.0072 -0.0042
80	0.008	0.1865	± 0.0182	+0.0604 -0.015	+0.0064
160	0.0035	0.4448	± 0.031	+0.0332 -0.0251	+0.0094 -0.0154
160	0.008	0.2018	± 0.0131	+0.0140 -0.0214	+0.0023 -0.0057
160	0.02	0.1421	± 0.0275	+0.0206 -0.0535	+0.0014 -0.0024
600	0.013	0.2428	± 0.0371	+0.0224 -0.0370	+0.0149 -0.0020
600	0.035	0.0748	± 0.0304	+0.0072 -0.0119	+0.0020

Table 7.12.: Extracted values of $F_2^{c\bar{c}}$. The statistical and systematic uncertainties are shown separately. The uncertainty of the extrapolation to the full jet phase space is also shown.

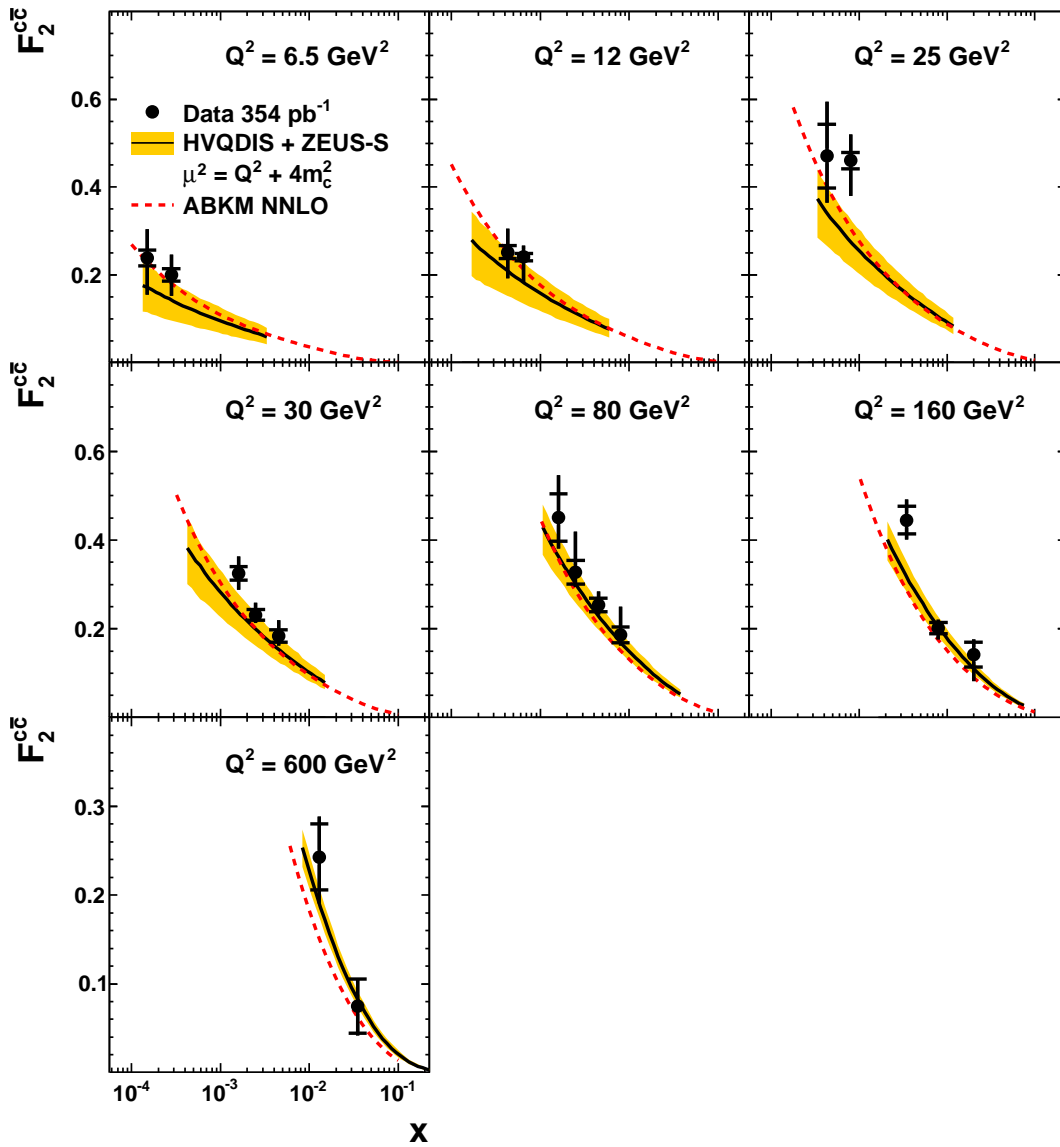


Figure 7.41.: $F_2^{c\bar{c}}$ as a function of x for different values of Q^2 . The measurement is compared to FFNS predictions.

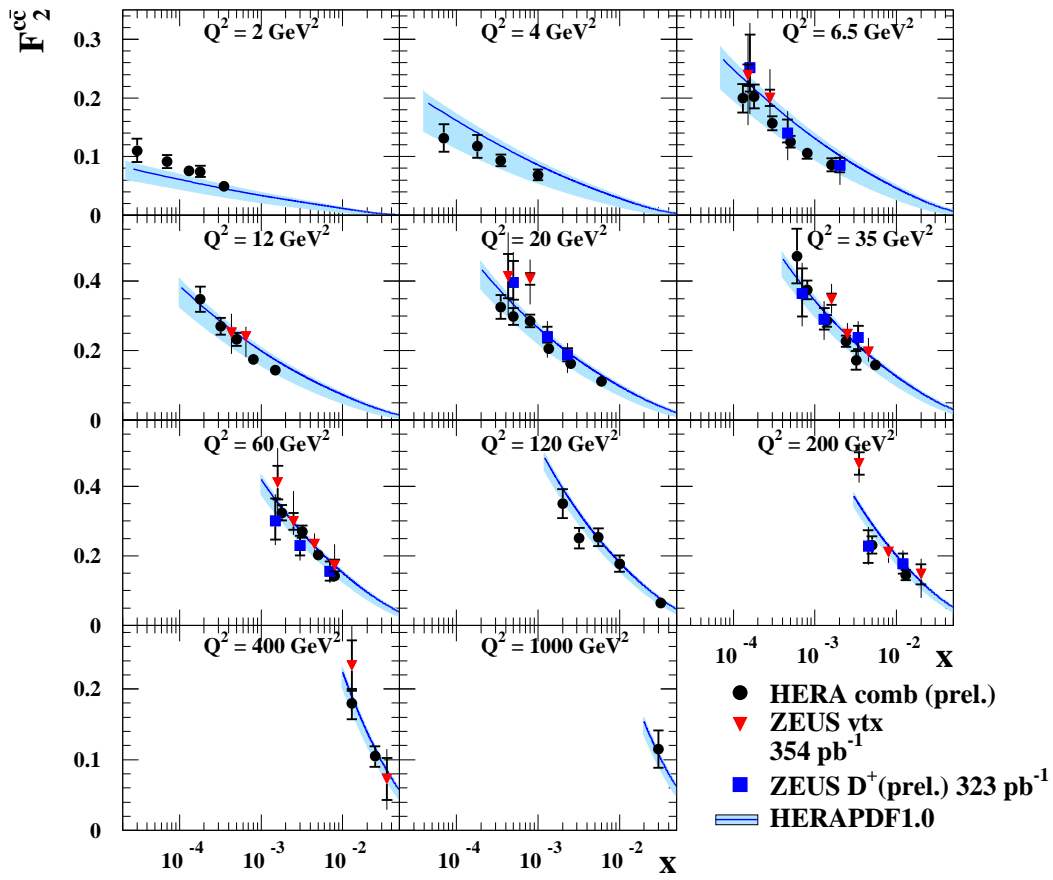


Figure 7.42.: $F_2^{c\bar{c}}$ as a function of Q^2 . Different measurements are compared to the HERAPDF1.0 prediction.

7.6. Conclusions and outlook

Cross sections for jet production in charm and beauty events were measured using the full data set collected using the ZEUS detector between 2004 and 2007 corresponding to an integrated luminosity of 354 pb^{-1} .

Compared to previous analyses at ZEUS, the measurement was not restricted to any particular final state. The micro vertex detector allowed the identification of charmed and beauty hadron decays using lifetime information. Jets were used as reference axes to reconstruct secondary vertices. For this purpose, tracks close to a jet in the $\eta - \phi$ plane were used as input to a vertex fit. The charm and beauty contents in events with a jet were obtained using the invariant mass and decay-length significance of secondary decay vertices. This was achieved fitting MC templates for beauty, charm and light quark events to the mirrored significance distributions in three bins of the invariant mass.

Single differential cross sections for jet production in beauty events were measured as functions of E_T^{jet} , η^{jet} , Q^2 and x in the range $E_T^{\text{jet}} > 5 \text{ GeV}$, $-1.6 < \eta^{\text{jet}} < 2.2$, $0.02 < y < 0.7$ and $5 < Q^2 < 1000 \text{ GeV}^2$. The cross sections are a factor 1.6 higher than Monte Carlo predictions based on LO matrix elements and DGLAP parton showers. On the other hand, the shape of all distributions except for Q^2 are well reproduced by the MC. NLO QCD predictions obtained using the HVQDIS program give a reasonable description of the shapes of the measured cross sections, but are generally about 30% lower than the data.

Several variations of the input parameters used for the HVQDIS calculations were investigated. The influence of the choice of the PDF parametrisation (ZEUS-S or ABKM NLO) on the cross sections predicted by HVQDIS is rather small. In contrast, sizable differences in the η^{jet} distribution were observed when the functional form of the renormalisation and factorisation scales was changed.

The contribution from open beauty production to the inclusive structure function F_2 was extracted from double differential cross sections in x and Q^2 . This required an extrapolation from the measured range in E_T^{jet} and η^{jet} to the full phase space of beauty quark production at given values of x and Q^2 . The extrapolation uncertainty estimated using the HVQDIS program was smaller than the experimental uncertainties since the required extrapolation was only moderate. The obtained results represent the most precise determination of $F_2^{b\bar{b}}$ at the ZEUS experiment. The measurement is in good agreement with previous results from the H1 and ZEUS collaborations. The results are consistent with predictions from perturbative QCD. Especially at low Q^2 , NNLO predictions give a better description than NLO calculations. The data are sensitive to details of the QCD predictions like scale choices.

The cut on E_T^{jet} was lowered to 4.2 GeV to extract cross sections for jet production in charm events. The shapes of single differential cross sections are well described by NLO QCD predictions. As for beauty the normalisation of the central NLO QCD predictions is about 30% below the measured cross sections. The LO+PS MC multiplied by a factor 1.4 gives a good description of the observed E_T^{jet} , η^{jet} and x distributions.

Despite the lowered cut on E_T^{jet} the extrapolation needed to extract $F_2^{c\bar{c}}$ is still sizable at low Q^2 resulting in larger extrapolation uncertainties. The precision of the extracted $F_2^{c\bar{c}}$

points is especially competitive at high Q^2 where the uncertainty due to the extrapolation is small. The obtained results are in good agreement with previous measurements and NLO QCD predictions.

Future improvements

One of the dominant sources of uncertainty is caused by the simulation of the tracking efficiency. Once the tracking efficiency is extracted directly from the data, the Monte Carlo can be corrected before the secondary vertex fit is applied. This will allow to reduce the related systematic uncertainty substantially.

The technique used for the analysis described in this chapter was optimised to measure beauty production. The threshold region is included in the measurement due to the relatively low cut on E_T^{jet} . Extensions of the kinematic region of the measurement are possible. For example, the region $Q^2 > 1000 \text{ GeV}^2$ could be included. This would require the usage of a different algorithm to reconstruct the scattered electron because the SINISTRA finder is not suited to reconstruct electrons in the FCAL. On the other hand, improved simulations of the FMVD efficiency will allow to extend the measurement to the very forward direction, i.e. $\eta^{\text{jet}} > 2.2$, in the future.

Additional improvements are possible for charm production. To reduce the necessary extrapolation at low Q^2 , the cut on E_T^{jet} could be reduced even further. Also events where no jets were reconstructed could be added to the analysis. In this case a different reference axis is needed to reconstruct secondary decay vertices. One possibility is the so-called pseudo thrust [157]. The relevant modifications to the vertex reconstruction algorithm have already been implemented. First tests of this extension are promising [158].

Finally, the results obtained using inclusive secondary vertices at ZEUS can be combined with measurements based on other techniques from the H1 and ZEUS collaborations. Since several measurements of $F_2^{b\bar{b}}$ with complementary systematic uncertainties are available, this will improve the precision in the entire range of Q^2 and x . In case of $F_2^{c\bar{c}}$, the secondary vertex measurement is expected to contribute mostly at high Q^2 where the measurements of D^{*+} production have large statistical uncertainties.

Relevance of the measurements presented in this chapter

The measurements of jet production in beauty and charm events described in this chapter provide a stringent test of perturbative QCD.

Mass effects are important in a large part of the kinematic region for beauty production accessible at HERA. Hence especially the measurement of beauty production can be used to test various aspects of the treatment of heavy quark production in QCD predictions.

The measured $F_2^{b\bar{b}}$ and $F_2^{c\bar{c}}$ values provide an independent check of the gluon density in the proton. A good understanding of the gluon density is crucial to provide precise predictions for many physics processes at the LHC. For example, the production of top quarks and Higgs bosons at the LHC is dominated by gluon-gluon fusion.

Alternatively, the results presented here combined with other measurements of heavy quark production at HERA can be included in future PDF fits.

8. First test beam measurements with the EUDET pixel telescope

Within the EUDET consortium a high resolution pixel beam telescope was developed. The telescope consists of up to six planes of Monolithic Active Pixel Sensors and is equipped with a flexible data acquisition environment. After an introduction, the hardware and software of the telescope is described in the following sections. Finally, results from test beam measurements in 2007 and 2008 to characterise a prototype of the pixel beam telescope are given.

8.1. Introduction

A linear electron-positron collider is the next large-scale international project in high energy physics. At the moment the *International Linear Collider* (ILC) [6] and *Compact Linear Collider* (CLIC) [7] concepts are being investigated. While the ILC will have a centre-of-mass energy between 500 GeV and 1 TeV, CLIC will reach beam energies of 1.5 TeV. The EUDET project [159], which was supported by the EU in the 6th Framework Programme (FP6), aimed to provide infrastructure for the R&D of detector technologies towards the international linear collider¹. Within the EUDET project the JRA1 activity worked on the improvement of test beam infrastructure. For this purpose, a high resolution pixel telescope was developed. The design goals included a high position resolution ($\sigma < 3.0 \mu\text{m}$) and readout rate of 1 kHz. Additionally, the telescope can be operated in a 1.2 T solenoid magnet (PCMAG) [161].

The construction of the telescope was performed in two steps. In June 2007, the so-called demonstrator telescope [162] was installed for the first time using an analog readout. After the first successful operation at the electron beam at DESY, the demonstrator was transported to CERN and its performance was studied using 180 GeV hadrons at the SPS. After the first successful integration of a Device Under Test (DUT) in September 2007 [163], the demonstrator telescope has been used by various groups [164] and was improved continuously. More data processing was moved to the sensors in the fully digital final telescope [165], which was assembled during the summer 2009.

In this chapter results from the first tests to characterise the demonstrator telescope in 2007 are described. Additionally, measurements to test improvements of the telescope in 2008 are reviewed.

¹For an overview of current test beam activities by the linear collider detector community, see [160].

8.2. The demonstrator telescope

The EUDET pixel telescope is being used to test very different detector prototypes in beams of high-energy particles. Additionally, the telescope has to cope with the very different beam conditions at the DESY II synchrotron (electrons in the energy range between 1 and 6 GeV), at the CERN PS (hadrons, electrons or muons of momentum up to 15 GeV) and at the CERN SPS (hadrons, electrons or muons of up to 400 GeV).

Up to three sensors mounted in aluminium boxes are located at both sides of the *device under test* (DUT). The telescope sensors are kept at a constant temperature using a cooling device [166]. Water is usually used as coolant. A trigger system consisting of four scintillators attached to photomultiplier tubes can be used to trigger on particles passing the telescope.

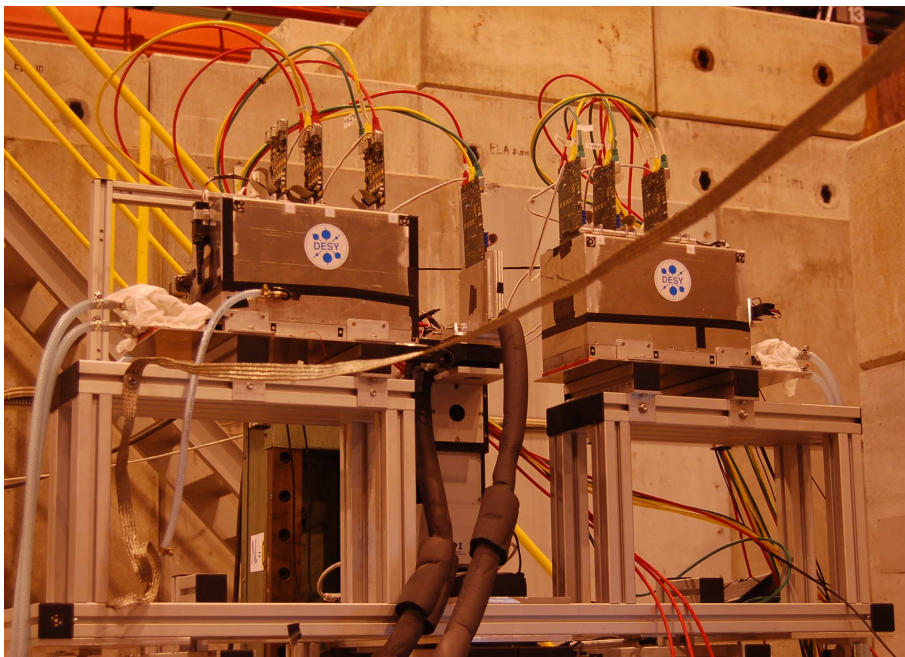


Figure 8.1.: The demonstrator telescope installed at the CERN SPS. A DUT is installed between the two sensor boxes.

A photo of the EUDET pixel telescope installed at the H6 beam line at the CERN SPS in September 2008 is shown in Fig. 8.1. A DUT is visible between the two sensor boxes. The telescope sensors and the data acquisition system (DAQ) are described in the following subsections.

8.2.1. The sensor

At the time when the EUDET pixel telescope was designed, Monolithic Active Pixel Sensors (MAPS) were the only available linear collider vertex-detector technology developed in Europe which could provide sensors of the size ($\approx 2 \text{ cm}^2$) and intrinsic resolution required for the final telescope.

Principle of monolithic active pixel sensors

The schematic cross section of a MAPS device is shown in Fig. 8.2. The charge collecting element of the sensor is an n -well diode on p -type epitaxial silicon. The lightly-doped epitaxial layer (about 10^{15} atoms/cm³) is grown on a highly-doped p^{++} substrate ($10^{18} - 10^{19}$ atoms/cm³). The readout circuit is integrated in a p -well (about 10^{18} atoms/cm³) on top of the epitaxial layer. The p^{++} substrate is typically made of low quality silicon where the recombination time is comparably short. Hence only a small fraction of the charge created in the substrate is expected to contribute to the signals seen by the collection electrodes.

Ionising particles passing through the sensor produce electron-hole pairs. The electrons in the epitaxial layer diffuse towards the charge-collecting n -well diode on a timescale of typically a few tens of nanoseconds. The large difference of about three orders of magnitude between the doping levels of the epitaxial layer compared to the p -well and the substrate creates potential barriers at the boundaries which act as mirrors for the signal electrons. Thus a 100% fill factor, i.e. the full pixel area is sensitive for particle detection, is achieved. The collected charge is directly converted into an electric signal at the pixel level.

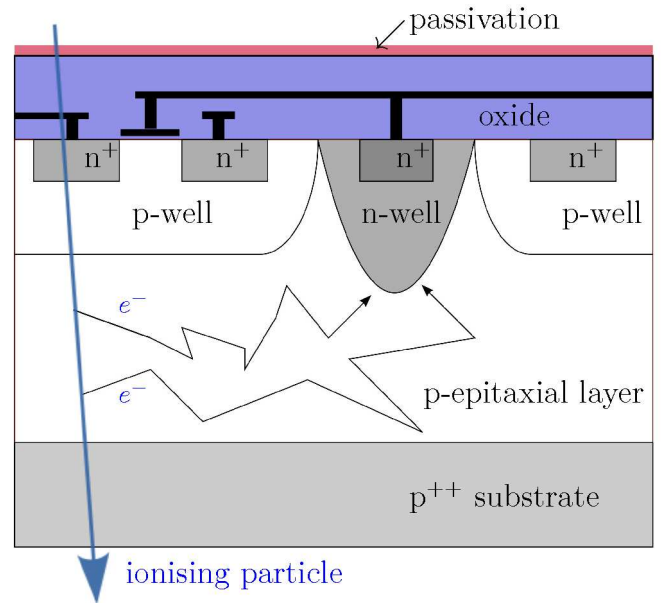


Figure 8.2.: Principle of operation of a MAPS.

The MimoTEL sensor

The MimoTEL² sensor [169], used for the demonstrator telescope, was developed by the CNRS-IHPC institute in Strasbourg, France. It is a Monolithic Active Pixel Sensor produced in the AMS 0.35 OPTO process.

Sensors with a thickness of the epitaxial layer of 14 or 20 μm are available. In total, the sensor is 680 μm thick. Four sub-arrays of 64×256 pixels are read in parallel. With a pixel pitch of $30 \times 30 \mu\text{m}^2$ this results in a sensor size of $7.7 \times 7.7 \text{ cm}^2$.

Each pixel of the MimoTEL sensor contains a simple readout circuit [169, 170, 171] which is shown in Fig. 8.3. This readout circuit contains only two transistors, half of a source follower and a readout selection switch. The charge is collected via the n -well diode. The collected charge is loaded into the parasitic capacity of the pixel. The voltage drop in this capacity is measured. A second, forward-biased diode is used to reset the pixel signal and

²The MimoTEL sensor is also referred to as Mimosa 17.

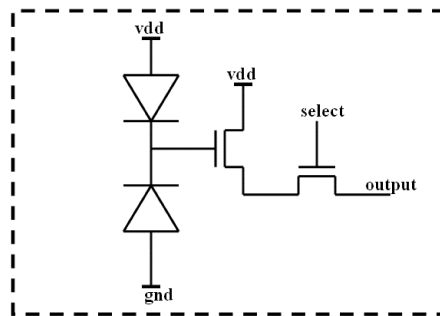


Figure 8.3.: Pixel circuit of the MimoTEL sensor. The charge-collecting n -well diode is visible in the bottom left of the figure.

to compensate for leakage current. Generated signal charge remains in the pixel for several readout cycles since the reset mechanism is slow compared to the readout frequency. The pixel signals from two or three successive frames are read to perform *correlated double sampling* (CDS) during the data analysis. In this way double counting of the pixel signals is avoided.

The signal information from each pixel is serialised by one circuit per sub-array with a readout frequency of up to 25 MHz. This results in a full frame readout time of 800 μ s. The frame readout time is equal to the signal integration window.

8.2.2. The DAQ system

The DAQ system can be summarised as follows: All data from the sensors is transferred via frontend boards to an intermediate readout and data reduction board called EU-DRB (EUDET Data Reduction Board) [172]. The EU-DRB board allows the first steps of the data processing online to be performed. Two I/O busses are supported: For the telescope the VME64x bus is used to allow high speed data transfer and synchronous operation with other devices while an USB2.0 interface is foreseen for standalone testing. A mother/daughter board scheme has been followed to maximise the flexibility. All computing and memory elements are located on the motherboard while the sensor specific components have been implemented on removable and interchangeable daughter cards. The two following modes of operation were used for the measurements using the demonstrator telescope described in this chapter:

- **Transparent mode (RAW):** All pixel signals are transferred without further data processing. This mode is important for debugging and for the characterisation of the telescope sensors itself.
- **Zero suppressed mode (ZS):** The CDS is performed online and only the signals and addresses of pixels above a certain user-defined threshold are transferred. This mode is intended for data taking at higher rates keeping the output files reasonably small.

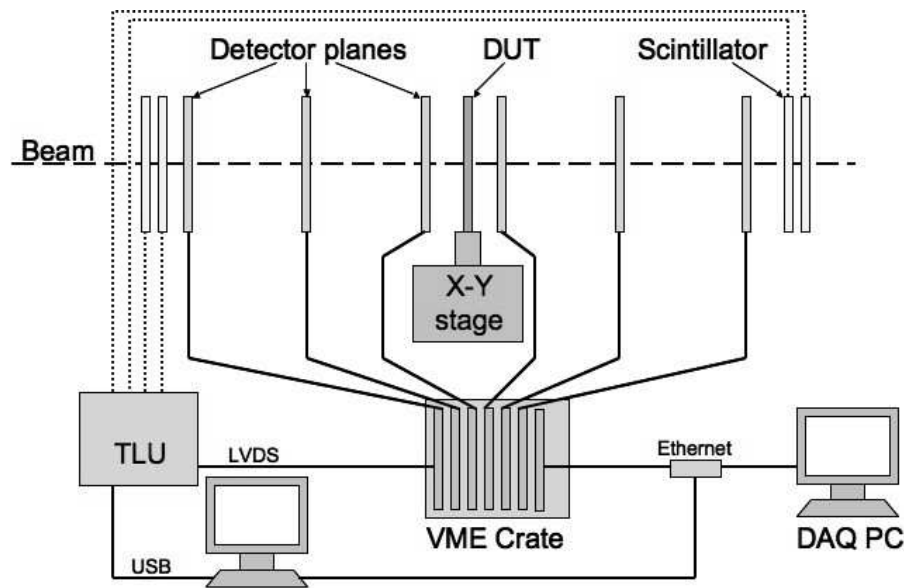


Figure 8.4.: The DAQ system of the EUDET pixel telescope.

The sampling frequency of the EUDRB boards was set to 10 MHz during the data taking in 2007 and 2008. The output of the EUDRB boards is collected by an MVME6100 single board computer, which is located in the same VME64x crate. Finally, the data are sent to the main DAQ PC using gigabit ethernet. This computer can also collect the information from the DUT.

Another important component of the DAQ system is the Trigger Logic Unit (TLU) [173]. It can generate any coincidence or anticoincidence of four trigger scintillators. Six LVDS and two TTL interfaces are provided. Furthermore, the TLU generates event numbers and time stamps. It is connected by USB2.0 to a control PC running the Linux operating system that is in turn connected to the main DAQ PC through gigabit ethernet. The advantages of the TLU are that it allows to change the trigger configuration from the control room and that can be used to provide a centrally distributed trigger for the telescope and several DUTs.

Fig. 8.4 shows the DAQ system of the EUDET pixel telescope as described above.

A custom DAQ system named EUDAQ has been implemented in C++ [174]. Several producer tasks communicate with a global run control using sockets. These producer tasks connect to the hardware of the beam telescope, to the TLU and eventually to the DUT. Data from all producers is sent to the central data collector and can be monitored by several processes. An online monitor, based on the ROOT framework, shows online data quality monitoring histograms [175] and a process to collect log messages is available. EUDAQ runs on MacOS, Linux and Windows using cygwin.

8.2.3. User integration

Different scenarios for the integration of the DUT in the DAQ system of the EUDET pixel telescope are possible:

- **Integration at hardware level:** In this case the user has to provide a hardware interface able to read out the telescope sensors and the DUT. This approach is supported by the EUDRB boards, but is only feasible for some dedicated DUTs.
- **Integration at DAQ software level:** The user provides their own DAQ hardware to read out the DUT, but the data are treated by a common DAQ software. In the case that the EUDAQ is used as the common DAQ system, a producer to read out the DUT needs to be implemented.
- **Integration at trigger level:** This default scenario was chosen by most users so far, because it is easy to implement and relatively safe. Different hardware and software are used for the telescope and the DUT. The synchronisation is done using the trigger, busy and reset logic provided by the TLU. To protect against slippage of event numbers between the telescope and the DUT, the event numbers provided by the TLU can be read by the DUT.
- **Integration at data level:** Both, the DUT and the telescope use their own dedicated DAQ hardware and software. The data streams are combined offline by inter process communication. In this scenario the synchronisation and the configuration during the start-up might be difficult.

8.3. The EU Telescope software

For the offline reconstruction of track positions in the DUT the software package EU Telescope [176] has been developed, which is implemented as a set of Marlin processors [177]. This design allows to integrate the DUT data at different steps of the analysis chain. Furthermore, the package can be executed on the Grid to allow a fast processing of large datasets.

Fig. 8.5 summarises the structure of the offline analysis package. Each step in the analysis procedure is implemented in a separate Marlin processor. It is possible to run each processor separately or to execute the whole analysis chain by a single command. In the first step the data is converted from the native format used by the EUDAQ software to the LCIO format. Afterwards a pedestal correction is applied and clusters are searched for. It is possible to improve the reconstructed cluster positions using the η algorithm. Clusters are accordingly transformed into hits in the telescope frame of reference. Details about the configuration of the telescope, e.g. the distances between the telescope sensors or their layout, are stored using the geometry description toolkit, GEAR. The alignment procedure is based on the Millepede II [178] package and uses full tracks in a simultaneous fit to derive the alignment parameters. Finally, tracks are fitted using the hits after the alignment constants have been applied. The result of the track fit can be saved in a ROOT file if needed by the user of the telescope.

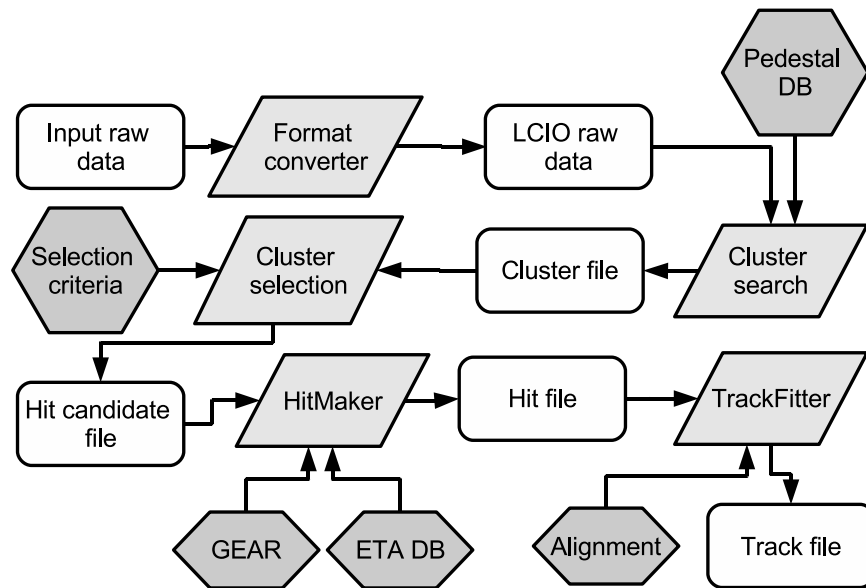


Figure 8.5.: Schematic overview of the offline analysis package EUTelescope.

During the work for this thesis, the alignment processor mentioned above was developed. Details on the algorithm are given in Sec. 8.5. Additionally, a processor to reconstruct straight line-tracks was implemented.

8.4. Signal extraction

In this section the extraction of clusters in the demonstrator telescope sensors is described. First, the noise and pedestal are calculated. After the rejection of hot pixels, clusters are reconstructed. Finally, the calculation of the cluster positions from the measured pixel signals is discussed.

8.4.1. Pedestal and noise

The *raw signal* observed by a pixel is given by the sum of the signal, which is the convolution of the physical charge signal and of the random noise, and the so-called *pedestal*. The pedestal for a pixel is given by the mean raw signal without input charge. The noise is calculated as the root mean square of the deviations between the individual raw signals and the pedestal value. Both, the pedestal and the noise, were calculated from events recorded without beam in the RAW mode using a random trigger. Typically, these calibration runs consisted of 300 events and were collected every 6 hours. Additionally, the measured pixel signals were corrected for common-mode shifts. A gain calibration was not performed.

8.4.2. Cluster reconstruction

In the following, the reconstruction of clusters from the signals measured by the individual pixels is described. A cluster is a group of pixels having a signal above a certain threshold. To obtain the results shown in this chapter, so-called *fixed-frame clustering* methods were applied. In this case, the cluster search starts from so-called *seed pixels*. A simple cut on the signal-to-noise ratio (S/N) is applied to select seed pixels. The list of all accepted seed pixels is sorted according to the signal size in decreasing order. A rectangular cluster candidate is formed around each seed pixel. The size of the cluster candidate is typically 3×3 pixels. A second cut is applied on the signal-to-noise ratio for the entire cluster candidate, ($S_{\text{cluster}}/N_{\text{cluster}}$). The signal, S_{cluster} , and noise value, N_{cluster} , for a cluster candidate are given by:

$$S_{\text{cluster}} = \sum_i S_i \quad \text{and} \quad N_{\text{cluster}} = \sqrt{\sum_i N_i}, \quad (8.1)$$

where the sums run over all pixels in the cluster candidate and S_i and N_i are the signals and noise values measured for pixel i , respectively. If the cluster is accepted, all pixels in the cluster are flagged and not used for other clusters any more. This step is repeated for all seed pixels.

The procedure described above does not allow to reconstruct clusters of even-numbered size, e.g. clusters of 2×2 or 4×4 pixels.

8.4.3. Cluster position

The first step to determine the position of a reconstructed cluster is to evaluate the *centre-of-gravity* (CoG) of the signal distribution. In one dimension the cluster position is given by:

$$X_{\text{cluster}} = \frac{\sum_i S_i \cdot X_i}{\sum_i S_i}, \quad (8.2)$$

where the sums run over all pixels in the cluster. The X_i and S_i are the positions and signals of the pixel i , respectively. The cluster position in the Y direction is calculated in the same way³.

The resolution can be improved using a non-linear correction of the cluster positions referred to as *η function* [179]. The η function correction is based on the assumption that the probability to find the cluster centre is flat over the pixel surface. It is calculated using experimental data. Sufficient samples of reconstructed clusters are needed for each detector plane. The η function is obtained in the following way:

- The signed distance between the centre of the seed pixel of a cluster and the CoG is filled into a binned histogram from $-1/2 \cdot P$ to $+1/2 \cdot P$, where P is the readout pitch.

³The coordinate system used by the EU Telescope software is a right-handed Cartesian system. The Z axis is pointing in the direction of the beam.

- The obtained histogram is integrated.
- Finally, the integrated histogram is normalised and shifted by $1/2 \cdot P$. This results in the η function shown in Fig. 8.6 used to correct the cluster positions obtained from the CoG.

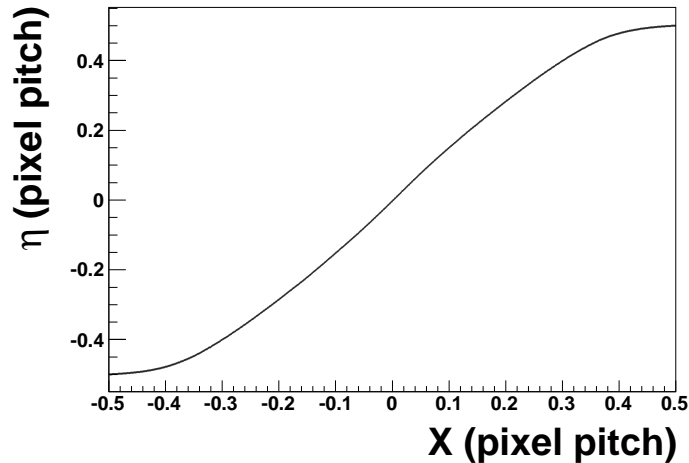


Figure 8.6.: The η function.

The η function corrections are applied independently for the X and Y coordinates. To illustrate the effect of the η correction, Fig. 8.7 shows typical distributions of the cluster positions relative to the pixel centre. Before the η correction is applied, the distribution peak at the pixel centre. The corrected distributions for the X and Y directions are flat.

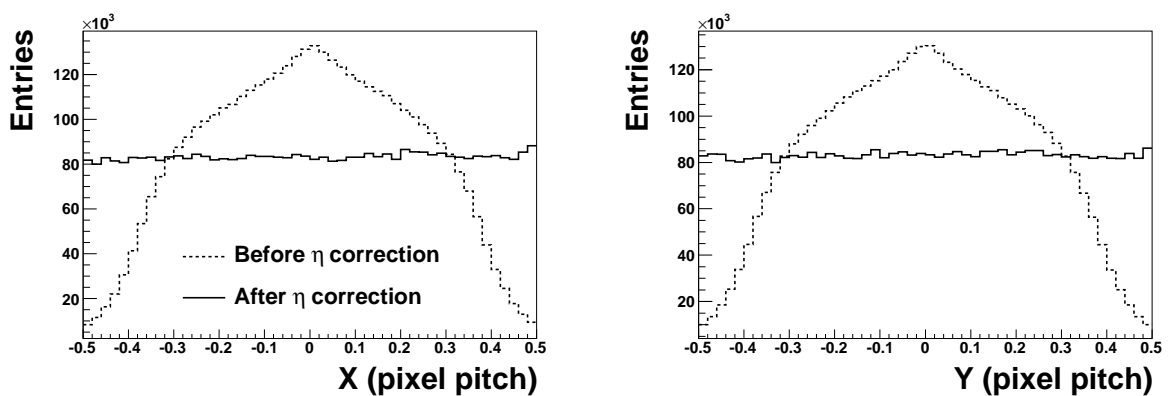


Figure 8.7.: Positions of reconstructed clusters relative to the pixel centre in the X (left) and Y (right) directions before and after the application of the η correction.

The η function corrections improved the spatial resolution of the MimoTEL sensors by about 20% for events collected in the RAW mode.

8.5. Alignment

The aim of the alignment procedure described in the following is to determine the displacement of the telescope sensors with respect to their nominal positions. An alignment processor based on the Millepede II package was developed. Full-length tracks are used to estimate the alignment parameters.

8.5.1. Alignment parameters

The parameters which occur in the alignment procedure are grouped into two classes:

- **Local parameters:** These parameters are only present in a subset of the data. For the alignment of the demonstrator telescope the local parameters are given by the parameters describing individual tracks. The following linear track model is used:

$$X(Z) = a_1 + a_2 \cdot Z \quad \text{and} \quad Y(Z) = b_1 + b_2 \cdot Z, \quad (8.3)$$

where each track is described by the four local parameters a_1 , a_2 , b_1 and b_2 . Hence the total number of local parameters is given by:

$$N_{\text{local}} = 4 \times \text{Number of tracks.} \quad (8.4)$$

- **Global parameters:** The global parameters are given by the shifts and rotations of the telescope sensors. In general, the displacement of a sensor with respect to its nominal position is described by three shifts in the directions of the X , Y and Z axes and by three rotations around these axes.

The tracks observed in the demonstrator telescope are almost parallel to the Z axis. Hence shifts in this direction and rotations around the X and Y axes are not well constrained by the alignment. Thus these parameters are usually fixed in the alignment fit⁴ and the number of global parameters is given by:

$$N_{\text{global}} = 3 \times \text{Number of sensors.} \quad (8.5)$$

The number of global parameters for a beam telescope is small (≈ 20). On the other hand, the number of local parameters can become very large since the telescope needs to be aligned for data samples containing hundreds of thousands of tracks. Millepede II solves the linear least squares problem with a simultaneous fit of all global and local parameters, irrespectively of the number of local parameters.

⁴If the hits measured in the DUT are included in the alignment fit, the rotations around the X and Y axes can be treated as free parameters for the DUT. This is for example important to perform measurements using a rotated DUT.

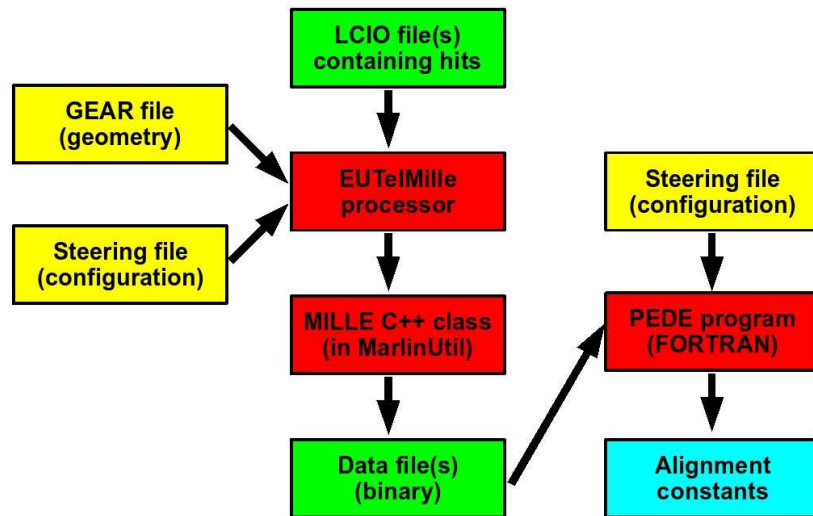


Figure 8.8.: Overview of the alignment procedure.

8.5.2. Implementation of the alignment procedure

A schematic overview of the alignment procedure is given in Fig. 8.8. Starting point of the alignment is an LCIO file containing information about the positions of the reconstructed clusters. A steering file contains the parameters for the EUTelMille processor, e.g. which preselection should be applied to find track candidates. The nominal positions of the telescope sensors are provided by GEAR.

The Millepede II package consists of two components. The C++ class Mille can be called from user code to write a binary file. This binary file is read by the PeDe program which performs the fit to determine the alignment constants.

The Marlin processor EUTelMille loops over all desired events and finds track candidates using a linear track model. The mean values of the residual distributions observed in the individual sensors before the alignment are used to calculate the starting values for the shifts in the X and Y directions. The starting values for the other parameters are set to zero.

If events with more than one track have to be used for the alignment, cuts on the residual distributions before the alignment can be applied to reduce the combinatorial background. This is possible since physical tracks are visible as peaks in the residual distributions even before the alignment.

The EUTelMille processor uses the class Mille to write a binary file as described above. The following information is stored for every hit associated to a track candidate:

- numbers and labels of the local and global parameters describing the track;
- derivatives of the track parametrisation with respect to the relevant global and local

parameters (the shifts and rotations of the sensor where the hit was reconstructed and the parameters of the associated track);

- residual of the hit;
- standard deviation of the measurement, i.e. resolution of the sensor plane.

Pede was written in Fortran and performs the least squares minimisation to derive the alignment constants. A further steering file is needed to control the execution of the Pede program. This steering file contains for example the starting values of the alignment constants. The Pede steering file can be generated automatically by the EUTelMille processor. Additionally, the EUTelMille processor can execute the Pede program directly. Hence the entire alignment procedure can be steered like a normal Marlin processor.

8.5.3. Alignment of the demonstrator telescope

As described above, three global parameters are usually considered for each telescope sensor: two shifts in the directions perpendicular to the beam and a rotation around the beam axis. Typically, the sensors are shifted by up to a few hundred μm in the directions perpendicular to the beam and rotated a few mrad around the beam direction. The global parameters for the first and last sensor in the beam direction are fixed in the alignment fit.

Additionally, the alignment can be used to monitor the mechanical stability of test beam experiments. For this purpose the time dependence of the alignment constants is studied. As an example, Fig. 8.9 shows typical time dependences of two alignment constants. All alignment parameters were constant in time for the data described in this chapter. This demonstrates the good mechanical stability of the telescope.

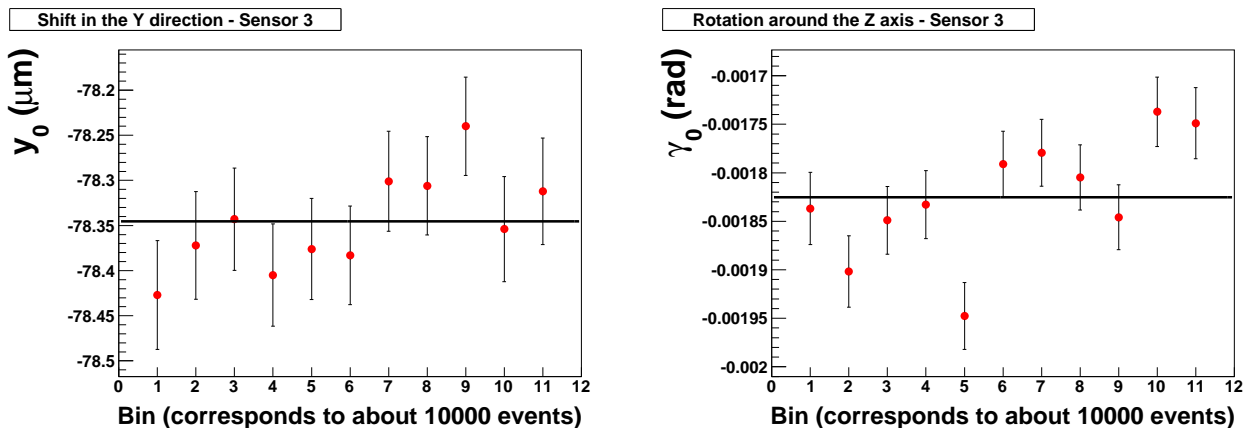


Figure 8.9.: Time dependence of the shift in the Y direction (left) and of the rotation around the beam direction (right) of a sensor during a test beam measurement. The data shown in the figure were collected during a time period of 28 h. Each point corresponds to about 10000 tracks.

8.6. Laboratory tests

To test the sensors, readout electronics and cooling of the telescope, measurements using low-energy X-rays emitted by an ^{55}Fe radioactive source and studies of the temperature dependence of the observed noise were performed. The presented results are not intended to provide a full characterisation of the MimoTEL sensor but were obtained as a part of the commissioning procedure of the demonstrator telescope.

All results in this section were obtained using a readout frequency of 10 MHz. The sensor was mounted in a small aluminium box. Its temperature was controlled using the same cooling device as was used for the telescope during test beam measurements. In the aluminium box the temperature of the sensor was similar to that of the coolant.

8.6.1. Calibration with low-energy X-rays

A MimoTEL sensor with an epitaxial layer thickness of $20\ \mu\text{m}$ was illuminated with low-energy X-rays from an ^{55}Fe radioactive source. This source emits photons at an energy of 5.90 keV with a probability of 24.4% and photons at an energy of 6.49 keV with a probability of 2.86% [66]. The absorption lengths for these photons in silicon are $27.0\ \mu\text{m}$ and $35.4\ \mu\text{m}$, respectively. Hence signals caused by the photoelectric effect are generated from the entire depth of the epitaxial layer.

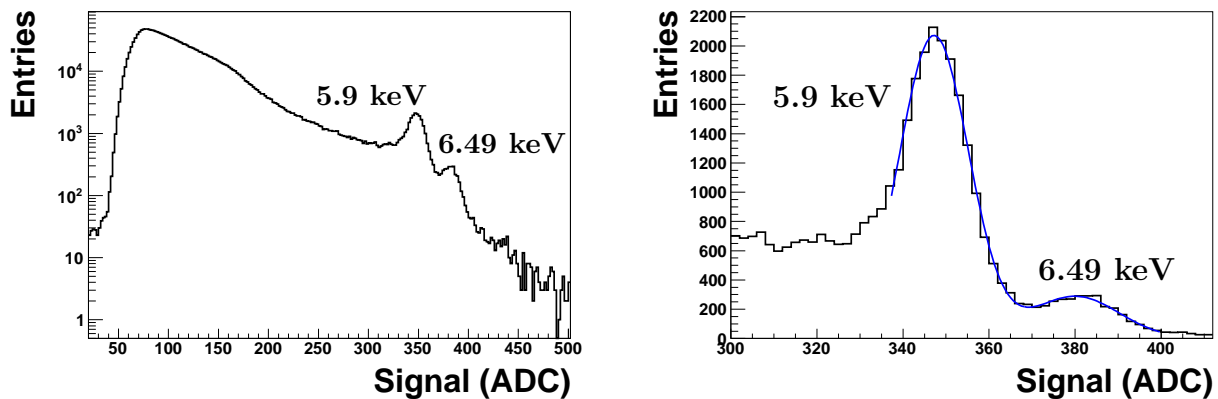


Figure 8.10.: ^{55}Fe seed pixel spectrum observed in a MimoTEL sensor at $T = 4^\circ\text{C}$ in logarithmic (left) and linear (right) scale. The peaks caused by the emission lines at 5.9 keV and at 6.49 keV are clearly visible. The data were fitted to the sum of two Gaussian peaks as shown by the blue line in the right figure.

The charge created by most absorbed photons in a MAPS device spreads among several neighbouring pixels. However, a small fraction of the photons interacts in the shallow depletion region around the charge collecting diode where the electric field is non-zero. In this case the generated charge is rapidly collected by a single pixel. Photons of 5.90 keV and of 6.49 keV generate on average 1640 and 1804 electrons, respectively. Thus photons whose charges are absorbed by a single pixel cause two characteristic peaks in the single

pixel signal distribution. The positions of these peaks can be used to determine the e/ADC conversion factor.

As an example, Fig. 8.10 shows the ^{55}Fe spectrum measured at a temperature⁵ of $T = 4^\circ\text{C}$. The signal in the seed pixel of reconstructed 3×3 clusters is shown in ADC counts. To optimise the selection for clusters where the entire photon energy is measured by a single pixel, the cuts $S/N > 15$ for the seed pixels and $S/N > 2$ for whole clusters were applied. For most clusters the charge collected by the seed pixel is incomplete. This causes the broad peak which dominates the spectrum. On the right end of the spectrum, the two peaks caused by the discrete emission lines at 5.9 keV and at 6.49 keV are clearly visible. The positions of both peaks were determined simultaneously by fitting the sum of two Gaussians to the data. No background contribution was included in the fit.

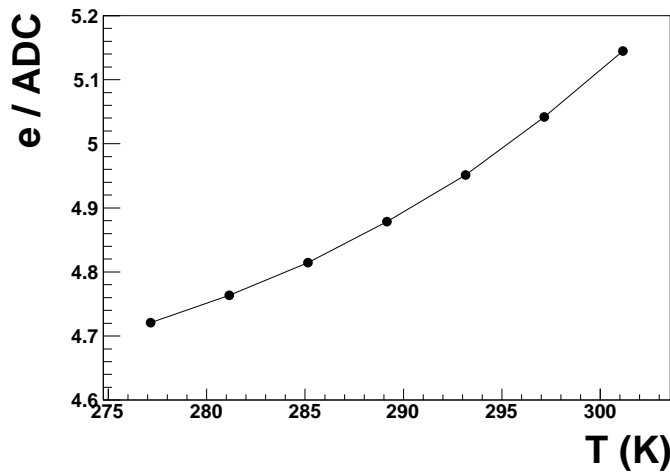


Figure 8.11.: Conversion factor e/ADC measured at different temperatures.

The same measurement was performed at several temperatures in the range $4 < T < 28^\circ\text{C}$. The conversion factor from ADC counts measured by the EUDET DAQ system to electrons in the MimoTEL sensor, e/ADC , was calculated for each temperature. Only the peak caused by 5.9 keV photons was used for this purpose. The result is shown in Fig. 8.11. A dependence of the conversion factor on the temperature is clearly visible. The result of this measurement is used in the next subsection.

8.6.2. Temperature dependence of the noise

The pedestal and noise distributions measured using the same MimoTEL sensor as investigated in Sec. 8.6.1 are shown in Fig. 8.12 for a temperature of $T = 4^\circ\text{C}$. The mean of the pedestal distribution is very close to zero since the pixels are self-biased. The noise distribution has a mean value of 3.0 ADC counts with an RMS of 0.3 ADC counts.

⁵All temperatures given are the temperatures of the cooling water.

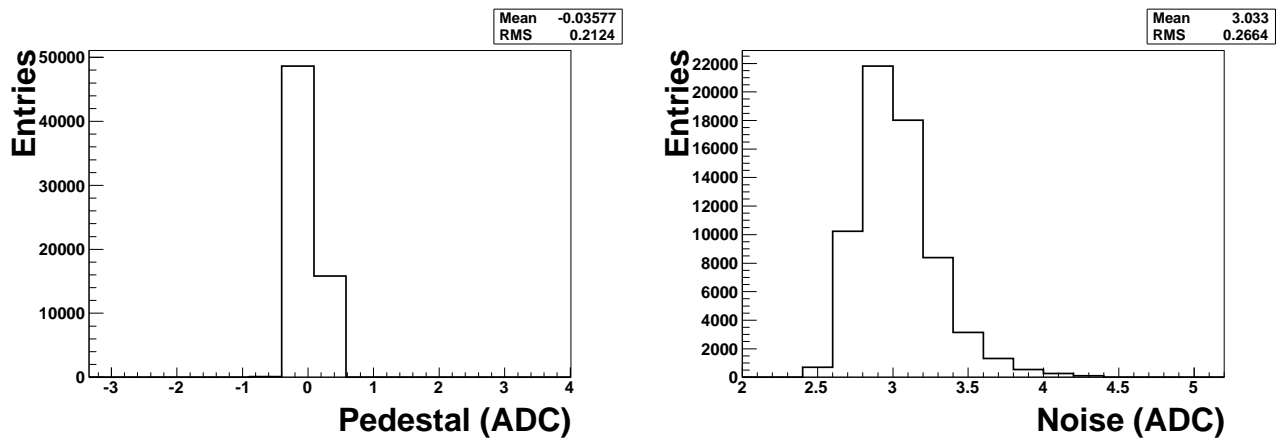


Figure 8.12.: Pedestal (left) and noise (right) distributions for a MIMO TEL sensor measured at $T = 4^\circ\text{C}$ in ADC counts.

The noise was measured at different temperatures in the range $4 < T < 28^\circ\text{C}$. The *equivalent noise charge* (ENC), which describes the noise in terms of the charge pulse at the pixel needed to create the same output, is shown in Fig. 8.13 as a function of the temperature. The ENC was calculated from the measured noise values in ADC counts using the e/ADC conversion factors shown in Fig. 8.11. The uncertainties shown in the figure were calculated from the RMS values of the observed noise distributions.

At $T = 4^\circ\text{C}$, the ENC measured in the small aluminium box is compared to the value obtained when the same sensor was mounted in the mechanics used during test beam measurements. The ENC is larger in the latter case suggesting that the temperature of the sensor is somewhat higher in the telescope mechanics for the same temperature of the coolant. A moderate dependence of the ENC on the temperature in the investigated region is observed.

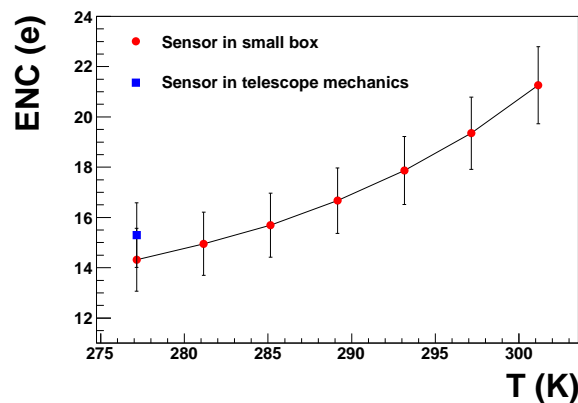


Figure 8.13.: ENC measured as a function of the temperature. The dots show the results measured for a single sensor in a small aluminium box. The square shows the measurement for the same sensor mounted in the telescope mechanics.

8.7. First test beam measurements in 2007

The demonstrator telescope was commissioned during summer 2007. The performance of the demonstrator was first investigated during a campaign of test beam measurements at DESY and CERN. In parallel to the analysis of the data, substantial parts of the reconstruction software EUTelescope were developed (see Sec. 8.3). The computing-intensive steps of the analysis were performed on the Grid.

The zero suppressed mode (see Sec. 8.2.2) was not yet working properly during the test beam measurements in 2007. Hence the results presented in this section were all obtained using data collected in the RAW mode. However, important tests were performed and led to successful data taking in the ZS mode in 2008 as described in Sec. 8.8. In the RAW mode the data taking was limited to a rate of about 3 Hz due to the large size of the uncompressed events.

8.7.1. Analysed data samples

DESY II

The demonstrator telescope was tested in August 2007 using an electron beam from the DESY II synchrotron [180]. Since the mechanics of the telescope were not available at the time of the measurements, a provisional setup was used as shown in Fig 8.14. Five aluminium boxes similar to that used for laboratory measurements were connected. In this configuration the individual telescope sensors were mounted in a distance of 2.5 cm in the beam direction. The first sensor in the beam direction had an epitaxial layer of 14 μm . All other MimoTEL sensors had epitaxial layers with a thickness of 20 μm . Measurements were performed at two beam energies, 3 GeV and 6 GeV. About 100000 events were collected at both beam energies.

CERN SPS

In September 2007, data was collected at the H8 beamline located at the CERN SPS. A beam of hadrons at an energy of 180 GeV was used. The MimoTEL sensors were mounted in the mechanics shown in Fig. 8.1. The first box contained three MimoTEL sensors with thin (14 μm) epitaxial layers. Only two sensors were installed in the second box since only five EUDRB boards were available. The sensors in the second box had 20 μm thick



Figure 8.14.: Mechanics used for the test beam measurements at DESY in August 2007.

epitaxial layers. The sensors were positioned at a distance of 10 cm inside the boxes. The distance between the last sensor in the first box and the first sensor in the second box was 34 cm. An overview of the setup is shown in Fig. 8.15.

About 100000 events were collected with high particle multiplicity. On average 40 hits were reconstructed in each sensor plane. This sample was used to investigate the response of the MimoTEL sensors to minimum ionising particles. Additionally, a sample of about 6000 events with low multiplicity (about 3.5 hits per plane) was taken. The latter is especially suited for alignment and resolution studies.

During the data taking, the telescope was operated using only moderate cooling, keeping the sensors at a constant temperature between 20 and 22°C.

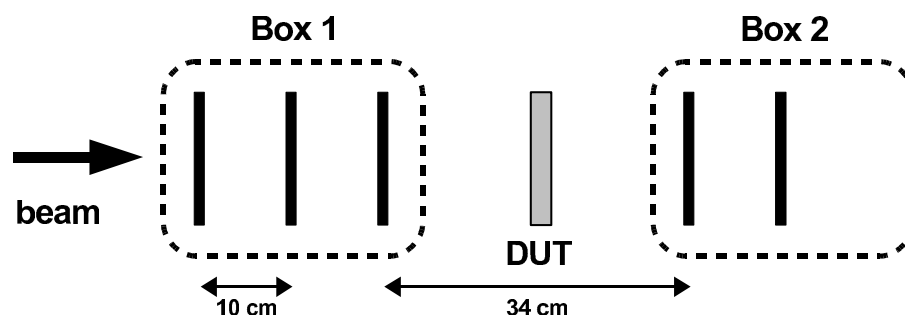


Figure 8.15.: Schematic overview of the setup used during the test beam measurements at CERN in September 2007.

8.7.2. Cluster selection

Clusters were reconstructed as described in Sec. 8.4.2. The following requirements were imposed to select clusters:

- $S/N > 5$ for seed pixels. This cut was increased to $S/N > 6$ for the first sensor in the direction of the beam;
- less than 100 seeds per sensor plane;
- $S/N > 4$ for clusters of 3×3 pixels.

The same selection was applied to all data collected in 2007. The positions of reconstructed clusters in the middle sensor, i.e. in the third sensor in the beam direction, are shown in Fig 8.16. For the sample recorded at DESY, where the track multiplicity was low, the trigger window is clearly visible. The profile of the beam is visible for the data collected at CERN since the track multiplicity was high.

8.7.3. Sensor characterisation with MIPs

First, the response of the MimoTEL sensors to minimal ionising particles was investigated. The results shown here were obtained using the data collected at CERN. The S/N values

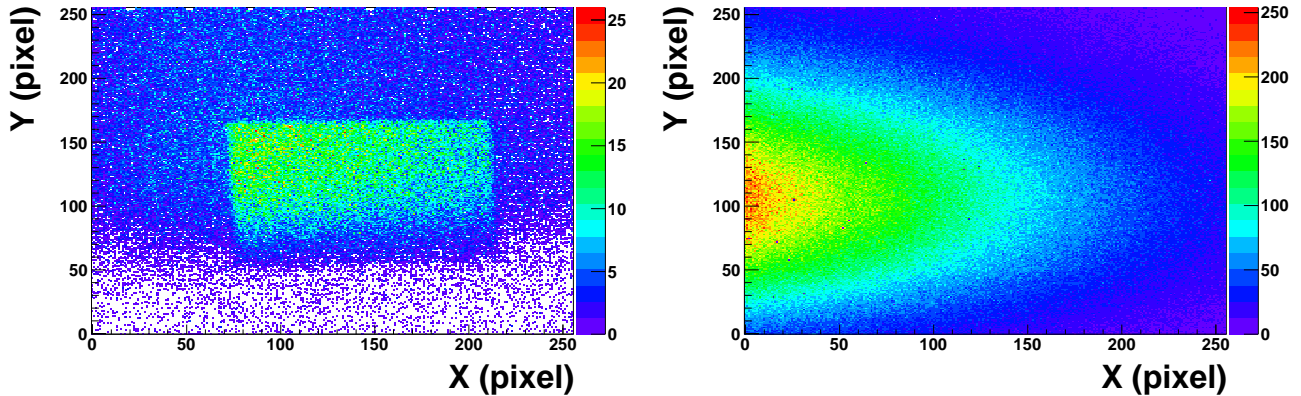


Figure 8.16.: Positions of reconstructed clusters in the middle sensor for the data taken at DESY (left) and CERN (right). The trigger window is visible for the data collected at DESY.

for seed pixels, for clusters of 3×3 pixels and for clusters formed from the four pixels with the highest signals observed in a sensor with an epitaxial layer of $14 \mu\text{m}$ are shown in Fig. 8.17. The convolution of a Landau curve and a Gaussian distribution was used to fit all histograms. The same distributions for a sensor with an epitaxial layer of $20 \mu\text{m}$ are shown in Fig. 8.18. The signals observed in all sensors are summarised in Tab. 8.1.

Sensor	Epi thickness	Seed pixel		3×3 cluster		Four pixel cluster	
		(e)	S/N	(e)	S/N	(e)	S/N
0	$14 \mu\text{m}$	234	11.8	650	10.8	518	13.5
1		229	11.5	640	10.6	511	13.2
2		235	12.1	646	11.1	521	13.8
3	$20 \mu\text{m}$	236	10.4	751	10.8	559	12.6
4		230	12.0	732	12.8	544	14.7

Table 8.1.: Signals in electrons and signal-to-noise ratios for seed pixels, 3×3 clusters and four pixel clusters in the individual planes measured with the setup used at CERN in September 2007.

For both types of sensors the same amount of charge is collected in the seed pixels. The sensor 3 shows a lower signal-to-noise ratio compared to the other sensors. This is caused by the fact that sensor 3 has a 20% larger mean single pixel noise, which was introduced by the acquisition and sampling electronics that were used and not by the sensor itself. In the sensors with thicker epitaxial layers more charge is collected in clusters of 3×3 pixels. This indicates a greater signal production but also a larger charge spread in these sensors compared to the sensors with a $14 \mu\text{m}$ epitaxial layer. For both sensor types the mean cluster size is around 8 pixels if a threshold of 2.5 times the pixel noise is applied [181].

Different properties of the charge collection are observed for the sensors with $14 \mu\text{m}$ and $20 \mu\text{m}$ thick epitaxial layers. The thickness of the epitaxial layer is the only known

difference between the two variants of the sensor. The size of the depletion zone is small compared to the size of the epitaxial layer for the MimoTEL sensor and the charge is mostly transported by diffusion. This could explain the different behaviour of the MimoTEL sensors depending on the epitaxial layer thickness.

The signal-to-noise ratios for seed pixels and clusters were improved by up to 20% in later test beams due to improved cooling of the MimoTEL sensors.

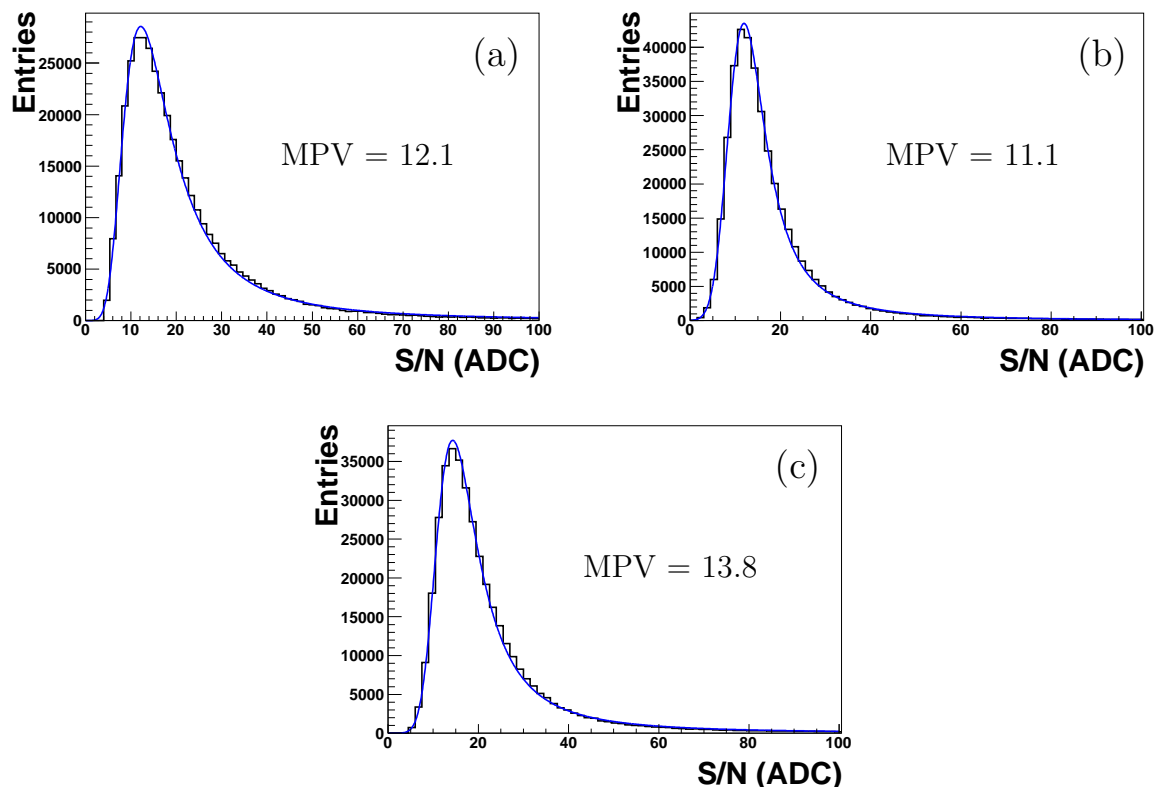


Figure 8.17.: S/N for (a) seed pixels, (b) 3×3 clusters and (c) clusters of four pixels with the highest signals observed in a sensor with thin ($14 \mu\text{m}$) epitaxial layer. The data have been fitted using the convolution of a Landau curve and a Gaussian function. The most probable values (MPV) of the Landau curves are given in the figures.

8.7.4. Track reconstruction

Track candidates were formed using loose cuts on the distances between hits in neighbouring sensors in the $X - Y$ plane. This preselection is very effective to remove ambiguities, i.e. hits associated to more than one track candidate, since the tracks are almost parallel in the investigated data samples. Least squares fits [182] were used to reconstruct straight-line tracks (see Eq. 8.3). The fits for the X and Y directions were performed separately.

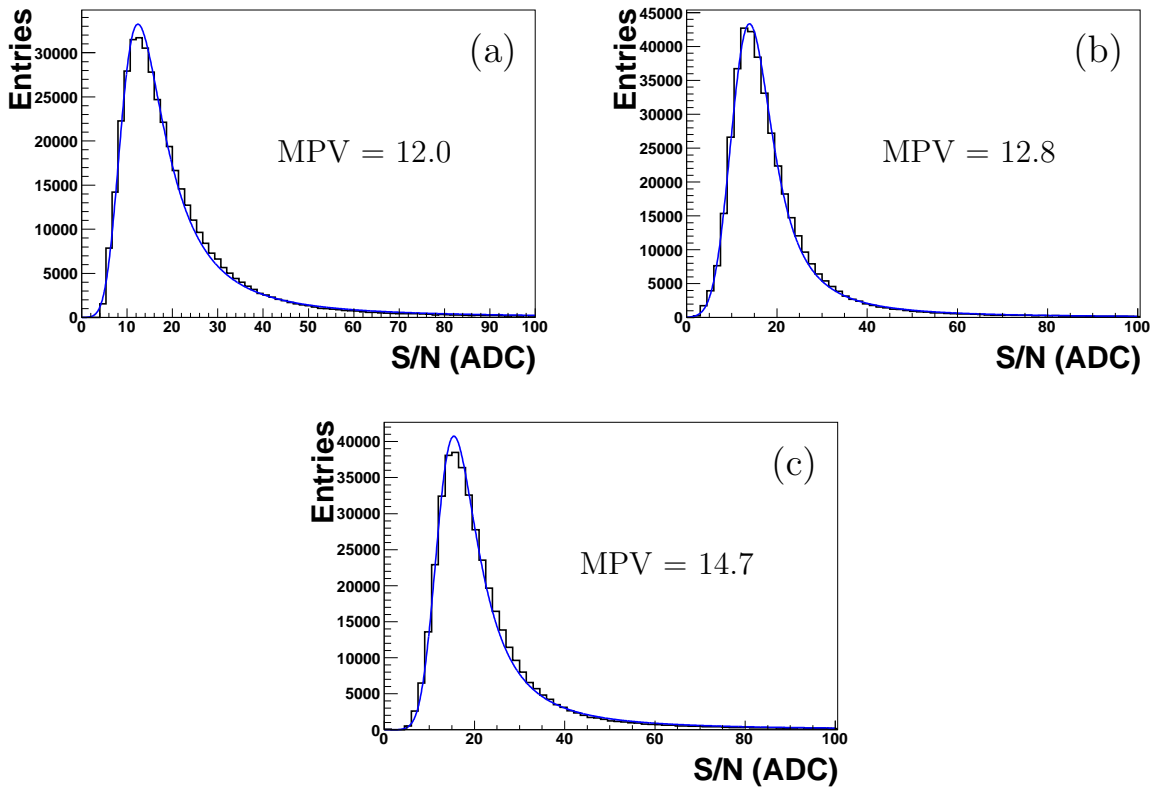


Figure 8.18.: S/N for (a) seed pixels, (b) 3×3 clusters and (c) clusters of four pixels with the highest signals observed in a sensor with an epitaxial layer thickness of $20 \mu\text{m}$. The data have been fitted using the convolution of a Landau curve and a Gaussian function. The most probable values (MPV) of the Landau curves are given in the figures.

Tracks were selected if the results from the fits fulfilled the following requirements:

$$\chi_X^2 = \sum_i \frac{(X_{\text{pred}}^i - X_{\text{meas}}^i)^2}{\sigma^2} < 20 \quad \text{and} \quad \chi_Y^2 = \sum_i \frac{(Y_{\text{pred}}^i - Y_{\text{meas}}^i)^2}{\sigma^2} < 20, \quad (8.6)$$

where the sums run over all telescope sensors. X_{pred}^i and Y_{pred}^i are the positions of the fitted tracks in sensor i and X_{meas}^i and Y_{meas}^i are the positions of the hits measured in sensor i . The resolution, σ , was set to $3.0 \mu\text{m}$. These requirements removed the remaining ambiguities.

A histogram of the differences between the measured hits and the predicted positions from the track fits is called *residual* distribution. As an example, Fig. 8.19 shows the residuals observed in the middle sensor plane for the data taken using a beam of 6 GeV electrons at DESY. Gaussian distributions were fitted to the observed residual distributions in the X and Y directions.

The residual distributions can be used to estimate the precision of the telescope alignment. For a perfectly aligned telescope the mean values of the Gaussians should vanish. The

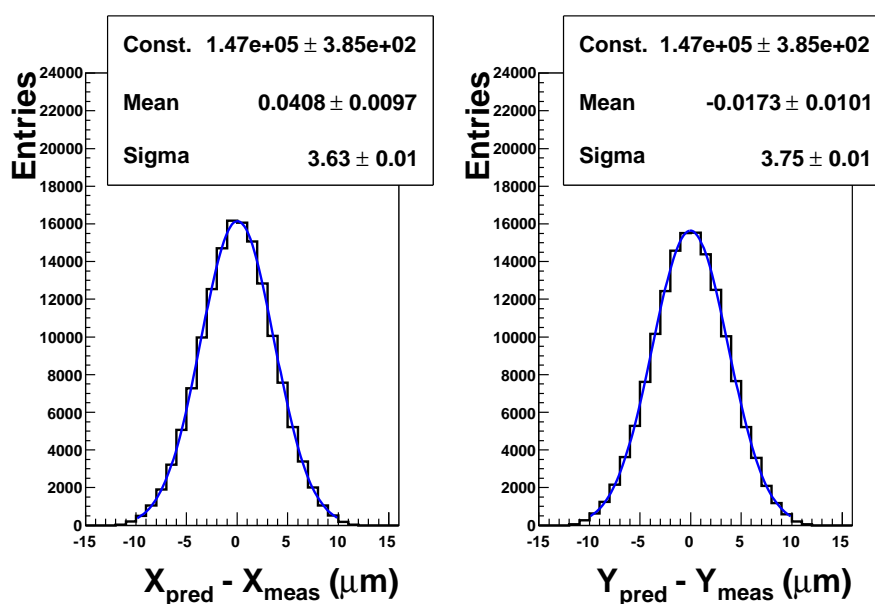


Figure 8.19.: Residuals observed in the middle telescope sensor using the data collected at DESY at a beam energy of 6 GeV.

mean values observed in the individual telescope sensors are shown in Tab. 8.2. The results demonstrate that the alignment of the telescope is possible with sufficient precision for the intended applications.

Sensor	Mean X (μm)	Mean Y (μm)
0	-0.002 ± 0.008	-0.005 ± 0.008
1	-0.023 ± 0.008	0.042 ± 0.008
2	0.041 ± 0.010	0.017 ± 0.010
3	-0.023 ± 0.008	-0.024 ± 0.008
4	-0.022 ± 0.008	-0.002 ± 0.008

Table 8.2.: Mean values of the residual distributions for tracks fitted after the alignment. These values were obtained using a beam of 6 GeV electrons at the DESY II test beam facility.

8.7.5. Resolution studies

CERN data

The easiest way to measure the resolution of a DUT in a beam telescope is to use particles of sufficient energy that multiple scattering can be neglected. For the EUDET demonstrator telescope equipped with MimoTEL sensors, this condition is fulfilled for the hadron beams in the SPS. In this case the squared width of the track residuals observed in the

DUT, σ_{observed} , is given by:

$$\sigma_{\text{observed}}^2 = \sigma_{\text{DUT}}^2 + \sigma_{\text{telescope}}^2, \quad (8.7)$$

where σ_{DUT} is the resolution of the DUT and $\sigma_{\text{telescope}}$ is the uncertainty of the track position in the DUT predicted by the telescope. If the telescope is constructed using identical sensors, this can be expressed as:

$$\sigma_{\text{observed}}^2 = \sigma_{\text{DUT}}^2 + k \cdot \sigma_{\text{MimoTEL}}^2, \quad (8.8)$$

where σ_{MimoTEL} is the resolution of the MimoTEL sensor and k is referred to as the *geometrical factor* of the telescope. Assuming that the DUT is located at $Z = 0$, the geometrical factor can be calculated as:

$$k = \frac{\sum_{i=1}^n Z_i^2}{n \cdot \sum_{i=1}^n Z_i^2 - (\sum_{i=1}^n Z_i)^2}, \quad (8.9)$$

where n is the number of telescope sensors and the Z_i are the positions of the telescope sensors in the beam direction. For a telescope configuration which is symmetric in the Z direction, i.e. $Z_i = (-1) \cdot Z_{n-i+1}$, Eq. 8.9 simplifies to $k = 1/n$.

To measure the resolution of the MimoTEL sensor, one of the telescope planes was treated as DUT and excluded from the track fit. Since $\sigma_{\text{DUT}} = \sigma_{\text{MimoTEL}}$ in this case, the resolution of the MinoTel sensor can be directly obtained from the observed width in the DUT:

$$\sigma_{\text{MimoTEL}} = \sqrt{\frac{\sigma_{\text{observed}}^2}{(1+k)}}. \quad (8.10)$$

In Figs. 8.20 and 8.21 the observed residuals are shown when one sensor was excluded from the track fit and used as DUT. The spatial resolutions of the MimoTEL sensors extracted from these DUT residuals are listed in Tab. 8.3. Most measured resolutions are somewhat better than $3 \mu\text{m}$. The resolutions for the X direction are typically 3% more precise than those for the Y direction. The statistical precision of the resolution measurement is about 1%.

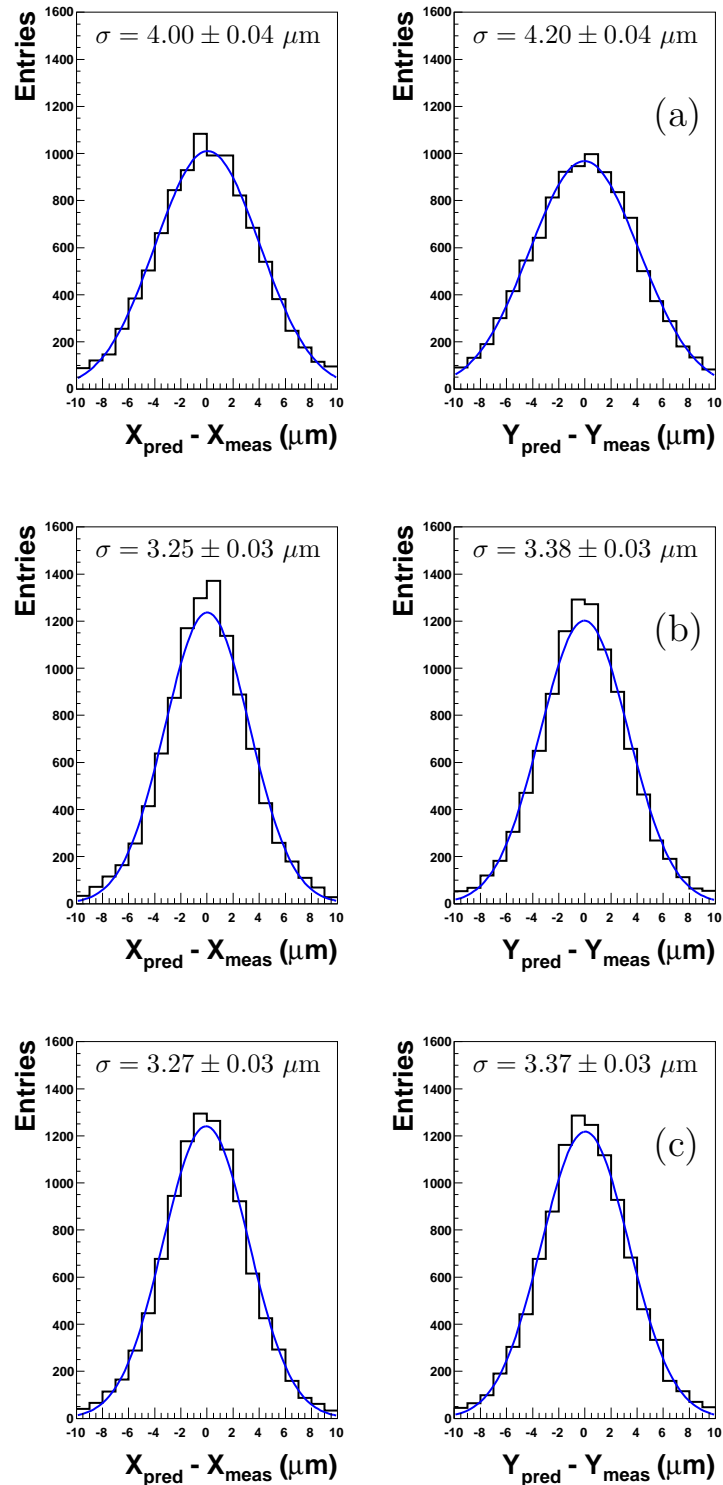


Figure 8.20.: Residuals observed in the DUT mode where (a) sensor 0, (b) sensor 1 and (c) sensor 2 was excluded from the track fit. The shown residuals were observed in the sensor used as DUT.

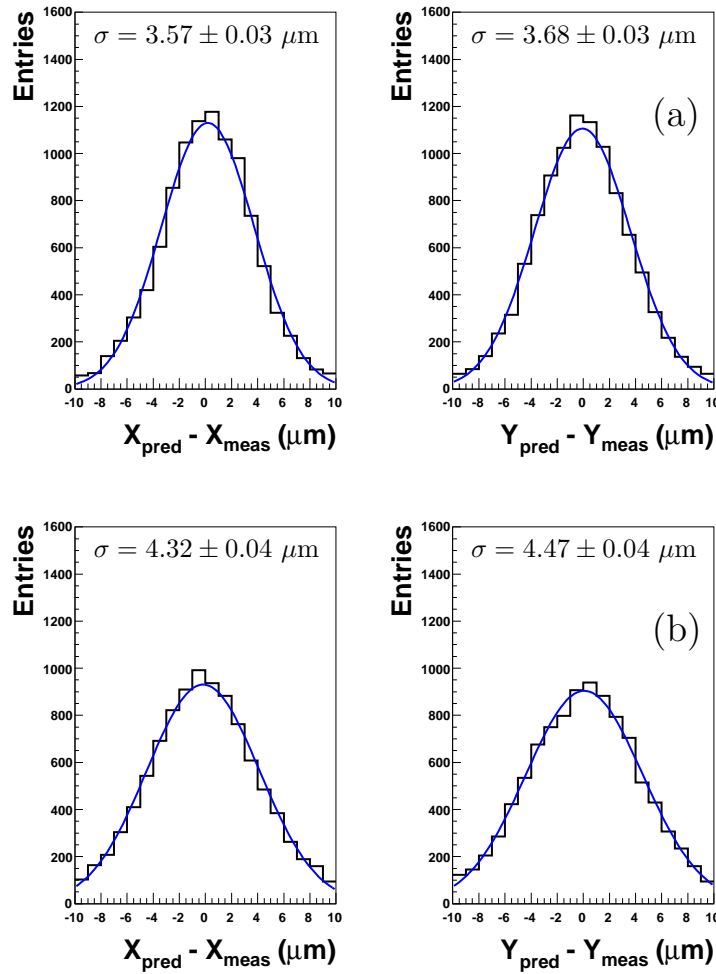


Figure 8.21.: Residuals observed in the DUT mode where (a) sensor 3 and (b) sensor 4 was excluded from the track fit. The shown residuals were observed in the sensor used as DUT.

Sensor	$\sigma_{\text{MimoTEL}}^X (\mu\text{m})$	$\sigma_{\text{MimoTEL}}^Y (\mu\text{m})$
0	2.89 ± 0.03	3.03 ± 0.03
1	2.67 ± 0.02	2.78 ± 0.02
2	2.87 ± 0.02	2.95 ± 0.02
3	2.79 ± 0.02	2.87 ± 0.03
4	2.81 ± 0.03	2.91 ± 0.03

Table 8.3.: Resolutions of the MimoTEL sensors in the X and Y directions extracted using the data collected at the CERN SPS.

DESY data

For the electron beams provided at the test beam facility located at the DESY II synchrotron, multiple scattering can not be neglected for the demonstrator telescope. In this case Eq. 8.7 needs to be modified to:

$$\sigma_{\text{observed}}^2 = \sigma_{\text{DUT}}^2 + \sigma_{\text{telescope}}^2 + \sigma_{\text{MS}}^2, \quad (8.11)$$

where σ_{MS} is the contribution to the observed width in the DUT caused by multiple scattering. It is however still possible to extract the resolution of the DUT if data are taken at different beam energies.

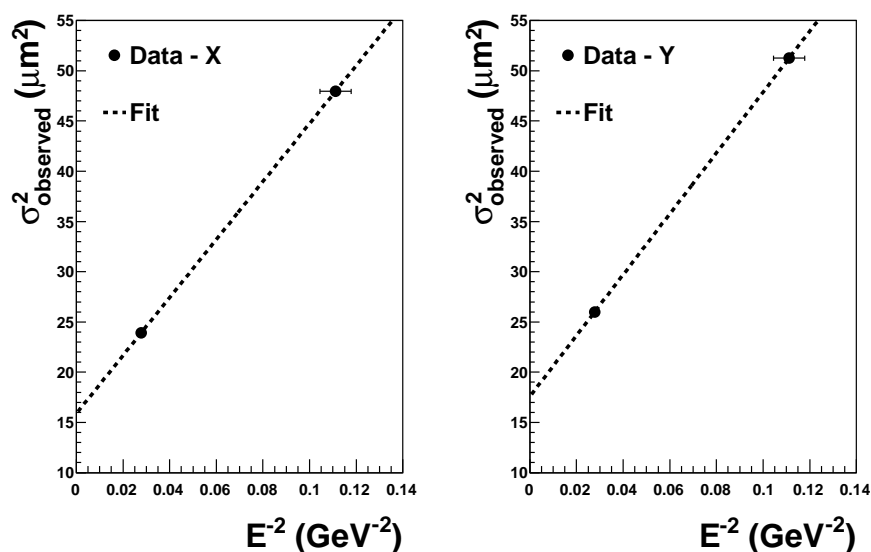


Figure 8.22.: Residual widths observed in the X (left) and Y (right) directions when the middle sensor was used as DUT as a function of $1/E^2$. The data were collected using electron beams of 3 GeV and 6 GeV.

In a medium, charged particles are deflected by many small-angle scatters which are mostly due to Coulomb scattering off nuclei. The angular distribution can be approximated by a Gaussian with a width of [66]:

$$\sigma_0 = \frac{13.6 \text{ MeV}}{\beta cp} z \sqrt{\frac{x}{X_0}} \left[1 + 0.038 \ln \left(\frac{x}{X_0} \right) \right], \quad (8.12)$$

where x/X_0 is the thickness of the medium in radiation lengths. This approximation is valid for the central 98% of the angular distribution. Since $\beta \approx 1$ and $E \approx cp$ for electrons with an energy of a few GeV, σ_{MS}^2 is proportional to $1/E^2$. Hence the observed width in the DUT without the contribution from multiple scattering can be obtained by an extrapolation to infinite energy. For this purpose, the observed width in the DUT

measured for different beam energies is plotted as a function of $1/E^2$. A straight line is fitted to the measured data points. The value of $\sigma_{\text{observed}}^2$ where the line crosses the Y axis gives $\sigma_{\text{DUT}}^2 + \sigma_{\text{telescope}}^2$ without the contribution from multiple scattering. Now the intrinsic resolution of the DUT can be extracted in the same way as described before using the k factor for the telescope geometry.

Fig. 8.22 shows the residual widths observed when the middle sensor was used as DUT as a function of $1/E^2$. The beam energy uncertainty is 3% [183]. A chi-square fit was performed to obtain the uncertainties of the extrapolation due to the statistical and beam energy uncertainties of the two data points for each direction.

In Tab. 8.4 the resolutions of the MimoTEL sensors obtained using the extrapolation to infinite energy are shown. The precision of the extrapolation method is much smaller compared to the direct extraction of the sensor resolution using the high-energy hadron beams available at the CERN SPS. The values are in good agreement with the results obtained from the CERN data (see Tab. 8.3). The quoted uncertainties are partially correlated due to the common uncertainty of the beam energy.

Sensor	$\sigma_{\text{MimoTEL}}^X$ (μm)	$\sigma_{\text{MimoTEL}}^Y$ (μm)
0	4.0 ± 1.2	4.1 ± 1.3
1	3.1 ± 0.6	3.2 ± 0.6
2	3.6 ± 0.9	3.8 ± 0.9
3	3.2 ± 0.6	3.3 ± 0.7
4	4.0 ± 1.3	4.2 ± 1.3

Table 8.4.: Resolutions of the MimoTEL sensors in the X and Y directions obtained using the data collected at DESY.

8.7.6. Sensor efficiency

In 2007 and 2008, the EUDRB boards used to read out the telescope sensors were operated in the so-called unsynchronised mode. In this mode, the clocks of the boards are not synchronised by any common signal. Hence tracks seen by some sensors were missed by other sensors due to the CDS calculation. Thus a calculation of the sensor efficiency is unfortunately not possible using the data analysed in this chapter.

8.8. Improvements in 2008

The demonstrator telescope was used by various detector R&D groups during the summer 2008. Measurements were performed at the T10 beamline located at the CERN PS and the CERN SPS using the H6 beamline. The performance of the demonstrator telescope during this campaign is described in the following.

8.8.1. Data taking in ZS mode

The zero suppression was fully operational in 2008. In this mode, the CDS is performed online by the EUDRB boards. A user-defined threshold could be defined for every pixel. Only the signals and addresses of the pixels passing the threshold were transferred to the MVME6100 and then to the DAQ PC. First, noise maps for all sensors were measured without beam using a random trigger. These noise maps were uploaded to the EUDRB boards. Only pixels with $S > C \cdot N$ were transferred, where the constant C was typically set to 2.0.

The data taking rate in the ZS mode was 60 Hz for operation with six MimoTEL sensors. Hence the telescope was 20 times faster in ZS mode compared to data taking in RAW mode.

8.8.2. Analysis of example data

To demonstrate the effect of the zero suppression on the telescope resolution, a sample of about 120000 events collected in August 2008 was analysed. During the data taking, a DEPFET [184] prototype was installed in the telescope. However, the information recorded by the this DUT was not considered in the following. The temperature of the cooling water was 12°C.

The reconstruction of clusters for the ZS data was performed in the same way as for the data collected in RAW mode using fixed frame clustering (see Sec. 8.4.2). The signals of clusters not passing threshold were set to zero. Clusters of 3×3 pixels were reconstructed. The following requirements were imposed offline to select clusters:

- $S/N > 5$ for seed pixels.
- less than 100 seeds per sensor plane;
- $S/N > 4$ for clusters of 3×3 pixels.

A different Marlin processor was used for the track fitting compared to the analysis of the 2007 data [185]. However, it was verified that both track reconstruction procedures give the same results if multiple scattering effects can be neglected.

The residuals observed in the third sensor in the beam direction, i.e. the innermost sensor in the first box, are shown in Fig. 8.23. The sensor where the residuals were measured was excluded from the fit. The distributions before and after the η function correction was applied are compared. As observed for the data collected in 2007, the resolution of the MimoTEL sensor in the X direction is a few % better than in the Y direction.

The same distributions were obtained for all six sensors of the telescope. In Fig. 8.24 the residual widths observed in all sensors are summarised. The measurements are compared to the expectations for different assumptions on the spatial resolutions of the MimoTEL sensors. Also in the ZS mode with a threshold of $S/N > 2$ for each pixel, the MimoTEL resolution is about 3 μm . This is expected since most pixels in 3×3 clusters have a higher signal-to-noise ratio than 2 and are hence accepted by the online zero suppression.

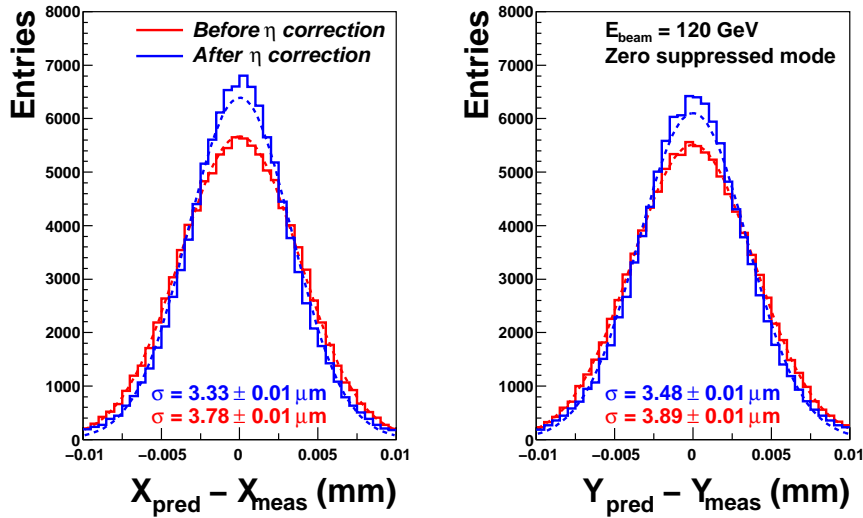


Figure 8.23.: Residuals observed in ZS mode for the X (left) and Y (right) directions. The distributions obtained before and after the η function correction are compared.

8.9. Conclusions and outlook

A pixel beam telescope was developed within the framework of the EUDET consortium. The demonstrator telescope consists of up to six MimoTEL sensors with an analogue readout. It was assembled in 2007 and first test beam measurements were performed in the same year. The demonstrator telescope was used by various detector R&D groups in 2007 and 2008. During this time, the telescope was continuously improved.

In parallel, a modular data analysis framework was developed. This thesis contributed to the alignment and tracking part of the reconstruction chain. The analysis software was used successfully to analyse the first data collected by the demonstrator telescope.

A single MimoTEL sensor was tested using an ^{55}Fe source. The ENC at 12°C is about 16 electrons. The response of the MimoTEL sensors to beams of minimum ionising particles was investigated. Despite the fact that only moderate cooling was possible, the intrinsic resolution of the MinoTEL sensor was found to be about $3 \mu\text{m}$. This can be translated into a telescope resolution of only $1.2 \mu\text{m}$ for the complete telescope of six planes.

Reliable data taking in the ZS mode was achieved in 2008. If a moderate threshold is chosen, the telescope precision is almost as good as in the RAW mode at an increased data taking rate.

In the meantime, the final telescope is available which uses the Mimosa 26 sensor. This chip consists of 1152 columns of 576 pixels. With a pitch of $18.4 \mu\text{m}$ the Mimosa 26 has an active area of $21.2 \times 10.6 \text{ cm}^2$, which is a factor of 3.8 larger than the MimoTEL of the demonstrator telescope. The Mimosa 26 sensor provides zero suppression and binary readout. For this purpose, the CDS calculation is performed on the sensor. A data taking rate of 1 kHz was reached using the EUDRB readout. On the other hand, the spatial

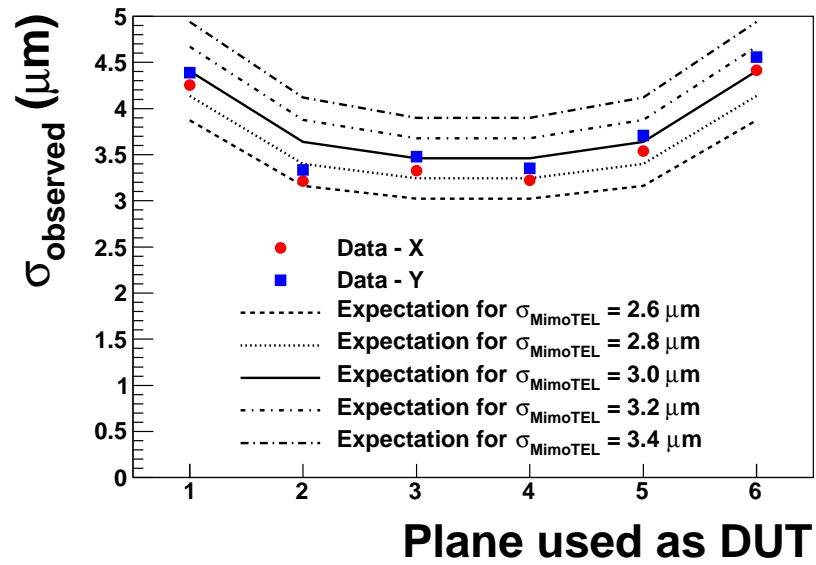


Figure 8.24.: Widths of the residuals observed in the sensor which was excluded from the track fit. The data are compared to the expectations for different assumptions on the intrinsic resolution of the MIMO TEL sensors.

resolution of the final telescope is somewhat less precise than that of the demonstrator.

A. Matching of charmed hadrons

Here the algorithm that was used to match tracks measured in the CTD with decay products of D^+ or Λ_c^+ hadrons on generator level is described. The matching procedure consists of two steps:

- The V0 particles originating from the investigated D^+ or Λ_c^+ decay channel on generator level were found. These true V0 particles were associated with a reconstructed V0 candidate if $\Delta R = \sqrt{(\phi_{true} - \phi_{reco})^2 + (\eta_{true} - \eta_{reco})^2} < 0.035$ and $\Delta p = p_{true} - p_{reco} < 0.2$ GeV.
- The true four vector of the additional pion or proton from the charmed hadron decay was compared to all reconstructed tracks in the event. For $\Delta R < 0.035$ and $\Delta p < 0.2$ GeV a track was matched with the true four vector.

Only if both criteria were fulfilled, the matching was successful. It is possible that several combinations were matched in a single event.

B. D^+ signals in bins of $p_T(D^+)$, $\eta(D^+)$, Q^2 and x

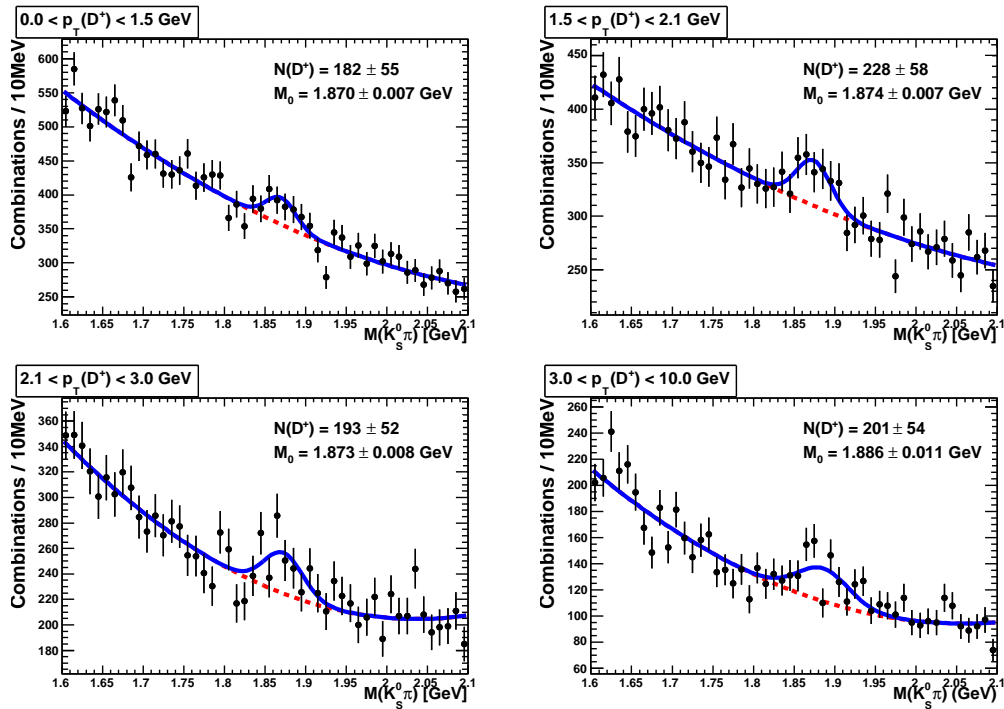


Figure B.1.: The $M(K_S^0\pi^+)$ distributions (dots) for D^+ candidates in bins of $p_T(D^+)$. The reflection caused by the decay $D_s^+ \rightarrow K_S^0 K^+$ has been subtracted. The solid curve represents a fit to the sum of a Gaussian signal and a background function, while the background contribution alone is given by the dashed curve. All bins were fitted simultaneously fixing the ratios of the signal widths to the Monte Carlo predictions.

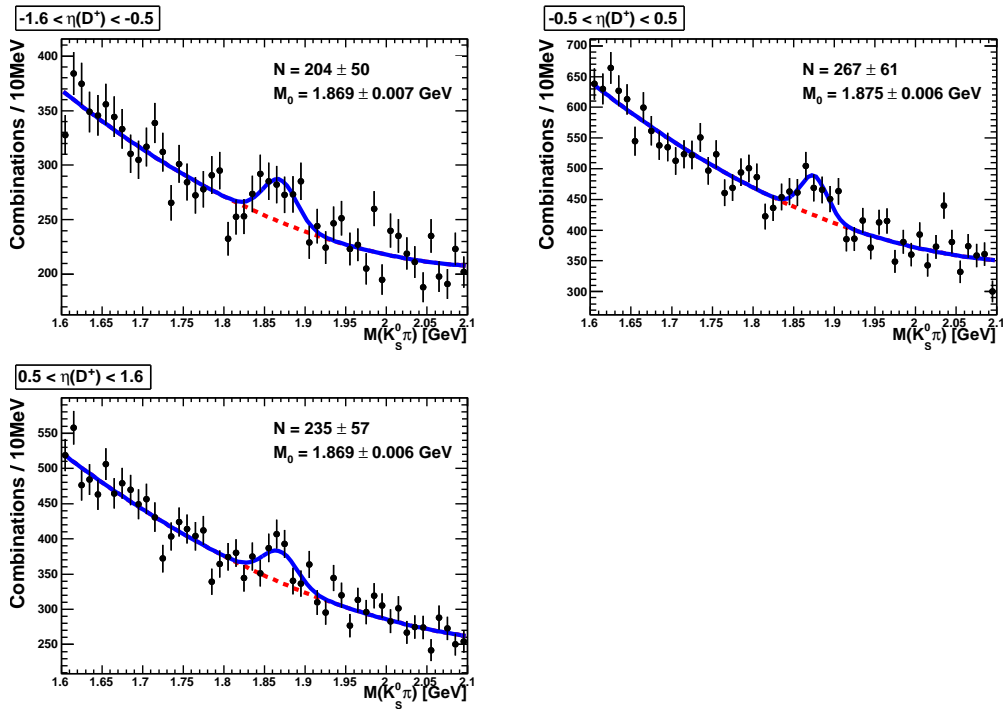


Figure B.2.: The $M(K_S^0 \pi^+)$ distributions (dots) for D^+ candidates in bins of $\eta(D^+)$. The reflection caused by the decay $D_s^+ \rightarrow K_S^0 K^+$ has been subtracted. The solid curve represents a fit to the sum of a Gaussian signal and a background function, while the background contribution alone is given by the dashed curve. All bins were fitted simultaneously fixing the ratios of the signal widths to the Monte Carlo predictions.

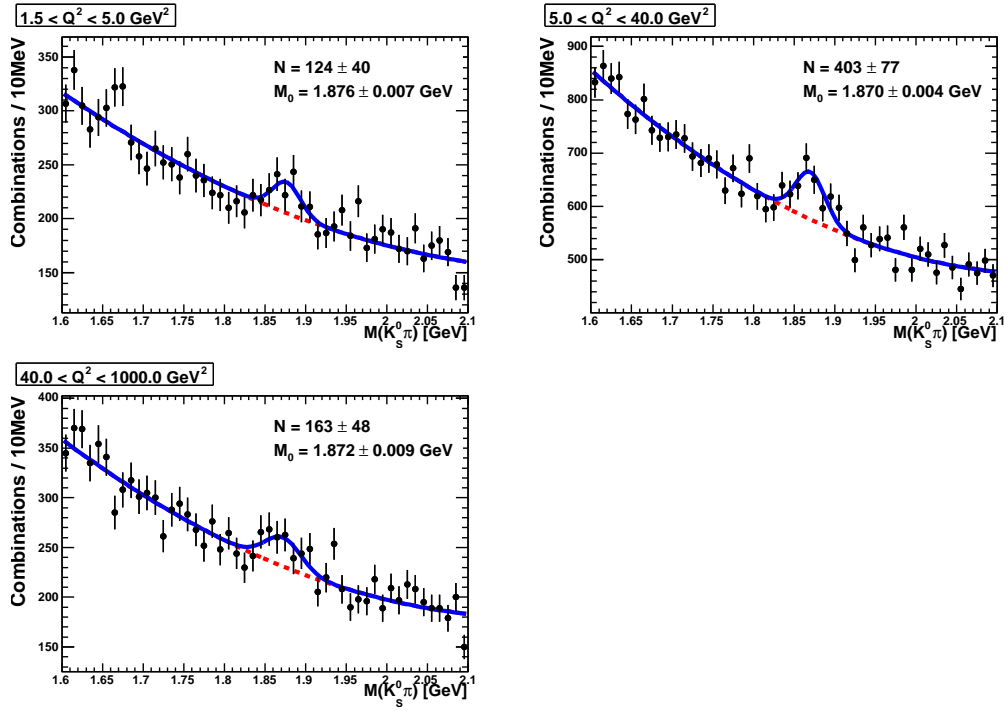


Figure B.3.: The $M(K_s^0\pi^+)$ distributions (dots) for D^+ candidates in bins of Q^2 . The reflection caused by the decay $D_s^+ \rightarrow K_s^0 K^+$ has been subtracted. The solid curve represents a fit to the sum of a Gaussian signal and a background function, while the background contribution alone is given by the dashed curve. All bins were fitted simultaneously fixing the ratios of the signal widths to the Monte Carlo predictions.

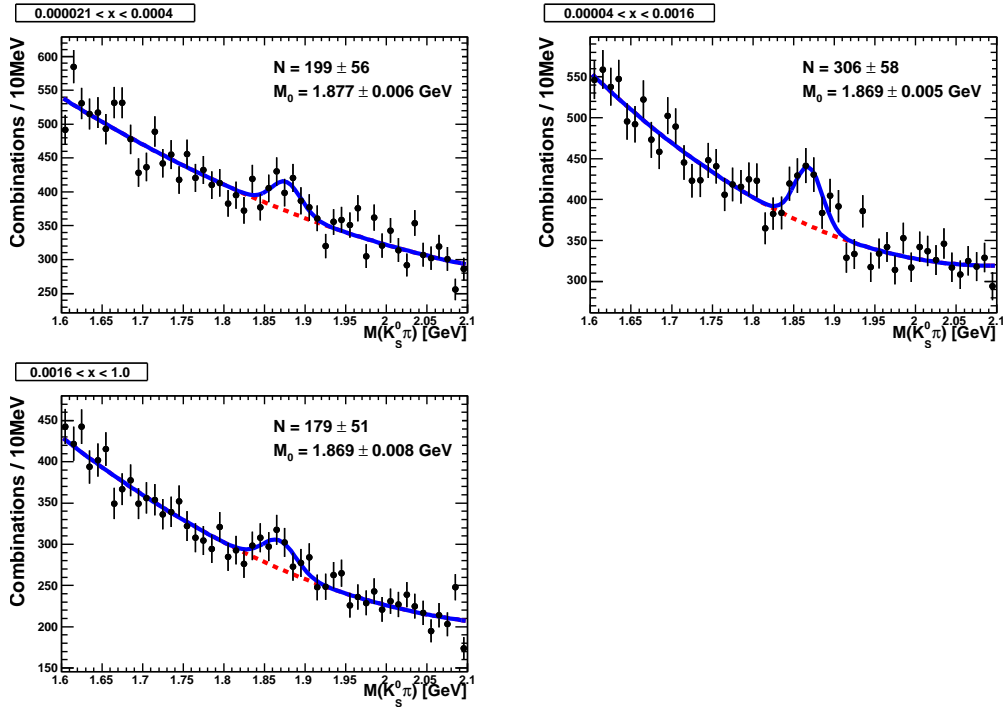


Figure B.4.: The $M(K_S^0\pi^+)$ distributions (dots) for D^+ candidates in bins of x . The reflection caused by the decay $D_s^+ \rightarrow K_S^0 K^+$ has been subtracted. The solid curve represents a fit to the sum of a Gaussian signal and a background function, while the background contribution alone is given by the dashed curve. All bins were fitted simultaneously fixing the ratios of the signal widths to the Monte Carlo predictions.

C. D^+ cross sections for $Q^2 > 5 \text{ GeV}^2$

As a cross check, the differential cross section for D^+ meson production as a function of $p_T^2(D^+)$ was extracted in the region $1.5 < p_T(D^+) < 15 \text{ GeV}$, $|\eta(D^+)| < 1.6$, $5.0 < Q^2 < 1000 \text{ GeV}^2$ and $0.02 < y < 0.7$. The extracted values are compared to a previous measurement [71] in Tab. C.1. No systematic uncertainties were calculated.

$p_T^2(D^+)$ bin	This measurement $d\sigma/dp_T^2(D^+)$ (GeV^2)	ZEUS 134 pb^{-1} [71] $d\sigma/dp_T^2(D^+)$ (GeV^2)
1.5, 2.1	1.83 ± 0.50 (stat.)	$0.80^{+0.23}_{-0.30}$ (stat. \oplus syst.)
2.1, 3.0	0.37 ± 0.13 (stat.)	$0.31^{+0.05}_{-0.06}$ (stat. \oplus syst.)
3.0, 15.0	0.016 ± 0.006 (stat.)	0.018 ± 0.001 (stat. \oplus syst.)

Table C.1.: Measured D^+ cross sections as a function of $p_T^2(D^+)$ for $5 < Q^2 < 1000 \text{ GeV}^2$, $0.02 < y < 0.7$, $1.5 < p_T(D^+) < 15 \text{ GeV}$ and $|\eta(D^+)| < 1.6$.

D. Detailed list of Monte Carlo samples for the HERA II period

The MC samples used to analyse the data collected between 2004 and 2007 are listed below in detail. The luminosities for all trigger configurations are given separately.

ARIADNE

Period	Interaction	Trigger configuration	Events	\mathcal{L} (pb ⁻¹)
2004	e^+p	pfap04	1539995	4.8
		pfhj04	4654975	14.6
		pfau04	2379990	7.4
		pfha04	1659995	5.2
2005	e^-p	efap05	8639943	27.0
		efha05	23399764	73.2
		efoc05	2539980	7.9
		efho05	8358457	26.2
2006	e^-p	efma06	3679940	11.5
		efhm06	13798961	43.2
2006/2007	e^+p	pfde06	18531771	58.0
		pfhd06	26656567	83.4

RAPGAP: charm production by the BGF process

Period	Interaction	min. Q^2 (GeV ²)	Trigger configuration	Events	\mathcal{L} (pb ⁻¹)
2004	e^+p	1.5	pfap04	294672	4.8
		1.5	pfhj04	881949	14.5
		1.5	pfau04	454593	7.4
		1.5	pfha04	322130	5.3
2004	e^+p	4.0	pfap04	519995	14.7
		4.0	pfhj04	1559950	44.1
		4.0	pfau04	800000	22.6
		4.0	pfha04	579995	16.4
2004	e^+p	16.0	pfap04	280000	24.2
		16.0	pfhj04	820000	71.0
		16.0	pfau04	420000	36.4
		16.0	pfha04	300000	26.0
2005	e^-p	1.5	efap05	1799975	29.5
		1.5	efha05	4919890	80.6
		1.5	efoc05	519990	8.5
		1.5	efho05	1759960	28.8
2005	e^-p	4.0	efap05	2000000	56.6
		4.0	efha05	5479971	155.0
		4.0	efoc05	560000	15.8
		4.0	efho05	1919980	54.3
2005	e^-p	8.0	efap05	1200000	56.2
		8.0	efha05	3280000	153.5
		8.0	efoc05	360000	16.9
		8.0	efho05	1160000	54.3
2005	e^-p	16.0	efap05	640000	55.4
		16.0	efha05	1760000	152.3
		16.0	efoc05	200000	17.3
		16.0	efho05	600000	51.9
2005	e^-p	50.0	efap05	280000	84.4
		50.0	efha05	760000	229.1
		50.0	efoc05	80000	24.1
		50.0	efho05	280000	84.4
2006	e^-p	1.5	efma06	697835	11.4
		1.5	efhm06	2627224	43.1
2006	e^-p	4.0	efma06	1239990	34.7
		4.0	efhm06	4617156	130.5
2006	e^-p	16.0	efma06	680000	58.9
		16.0	efhm06	2520000	218.1
2006/2007	e^+p	1.5	pfde06	3545289	58.1
2006/2007	e^+p	1.5	pfhd06	5112374	83.8
		4.0	pfde06	7152868	202.4
		4.0	pfhd06	10398615	294.3

RAPGAP: charm production by the process $cg \rightarrow cg$

Period	Interaction	min. Q^2 (GeV ²)	Trigger configuration	Events	\mathcal{L} (pb ⁻¹)
2004	e^+p	1.5	pfap04	129730	4.9
		1.5	pfhj04	390112	14.7
		1.5	pfau04	199296	7.5
		1.5	pfha04	144607	5.5
2004	e^+p	4.0	pfap04	182378	14.7
		4.0	pfhj04	545557	44.1
		4.0	pfau04	279566	22.6
		4.0	pfha04	202448	16.4
2005	e^-p	1.5	efap05	782328	29.5
		1.5	efha05	2133830	80.6
		1.5	efoc05	225873	8.5
		1.5	efho05	760128	28.8
2005	e^-p	4.0	efap05	698089	56.5
		4.0	efha05	1908267	154.8
		4.0	efoc05	209334	16.9
		4.0	efho05	669370	54.2
2006	e^-p	1.5	efma06	304881	11.6
2006	e^-p	1.5	efhm06	1152764	43.3
		4.0	efma06	428708	34.7
2006/2007	e^+p	4.0	efhm06	1619381	130.5
		1.5	pfde06	5399955	203.8
		1.5	pfhd06	7799970	294.3

RAPGAP: beauty production by the BGF process

Period	Interaction	Trigger configuration	Events	\mathcal{L} [pb ⁻¹]
2004	e^+p	pfap04	120000	132.2
		pfhj04	360000	396.6
		pfau04	220000	242.4
		pfha04	140000	154.2
2005	e^-p	efap05	380000	418.6
		efha05	1039951	1145.7
		efoc05	120000	132.2
		efho05	379995	418.6
2006	e^-p	efma06	177322	195.4
		efhm06	650953	717.2
2006/2007	e^+p	pfde06	959962	1057.6
		pfhd06	1379980	1520.3

E. Example beauty signals

The mirrored significance distributions in bins of the vertex mass are shown for several bins in Q^2 and η^{jet} .

Low Q^2

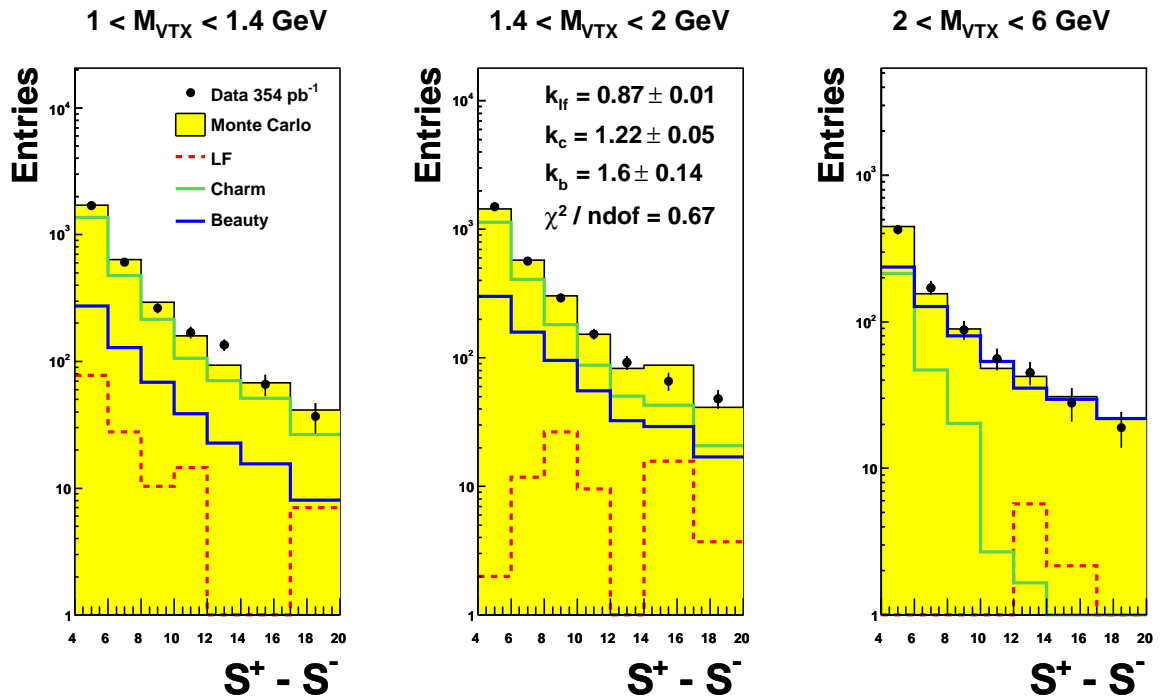


Figure E.1.: Mirrored decay-length significance in three bins of the invariant mass for $5 < Q^2 < 10 \text{ GeV}^2$. The data (dots) are compared to the sum of all MC samples (yellow area) and to the individual contributions separately (lines). The MC samples were scaled using the fit result.

Medium Q^2

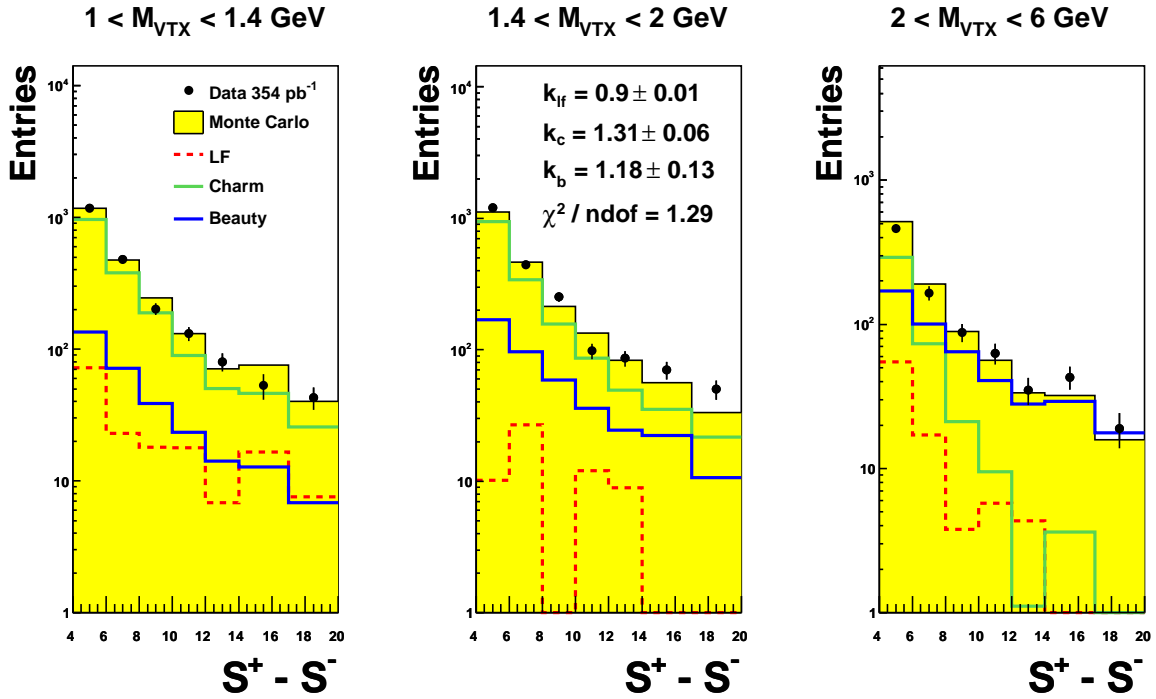


Figure E.2.: Mirrored decay-length significance in three bins of the invariant mass for $70 < Q^2 < 120 \text{ GeV}^2$. The data (dots) are compared to the sum of all MC samples (yellow area) and to the individual contributions separately (lines). The MC samples were scaled using the fit result.

High Q^2

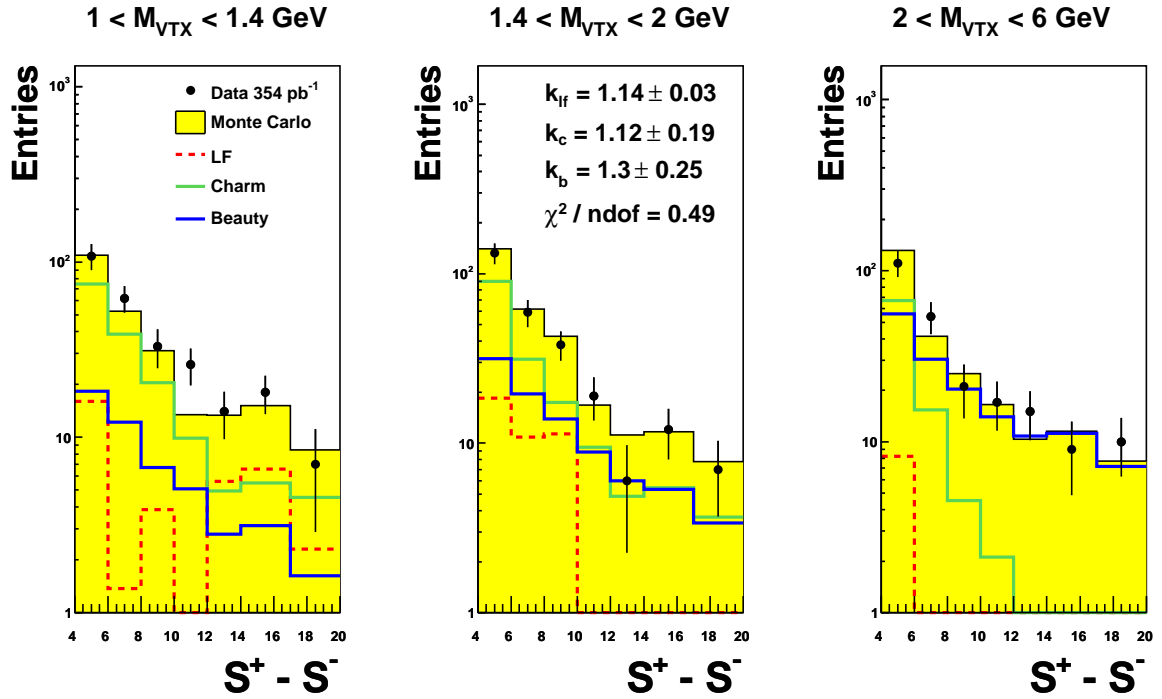


Figure E.3.: Mirrored decay-length significance in three bins of the invariant mass for $400 < Q^2 < 1000 \text{ GeV}^2$. The data (dots) are compared to the sum of all MC samples (yellow area) and to the individual contributions separately (lines). The MC samples were scaled using the fit result.

Backward direction

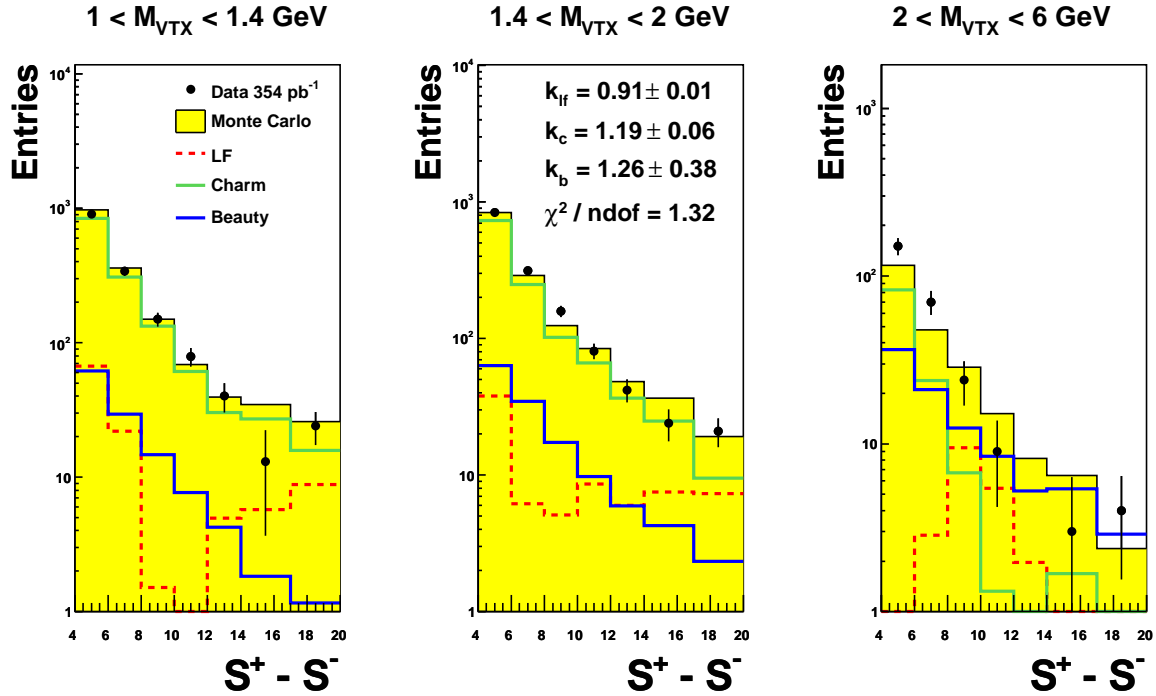


Figure E.4.: Mirrored decay-length significance in three bins of the invariant mass for $-1.6 < \eta^{\text{jet}} < -0.8$. The data (dots) are compared to the sum of all MC samples (yellow area) and to the individual contributions separately (lines). The MC samples were scaled using the fit result.

Central region

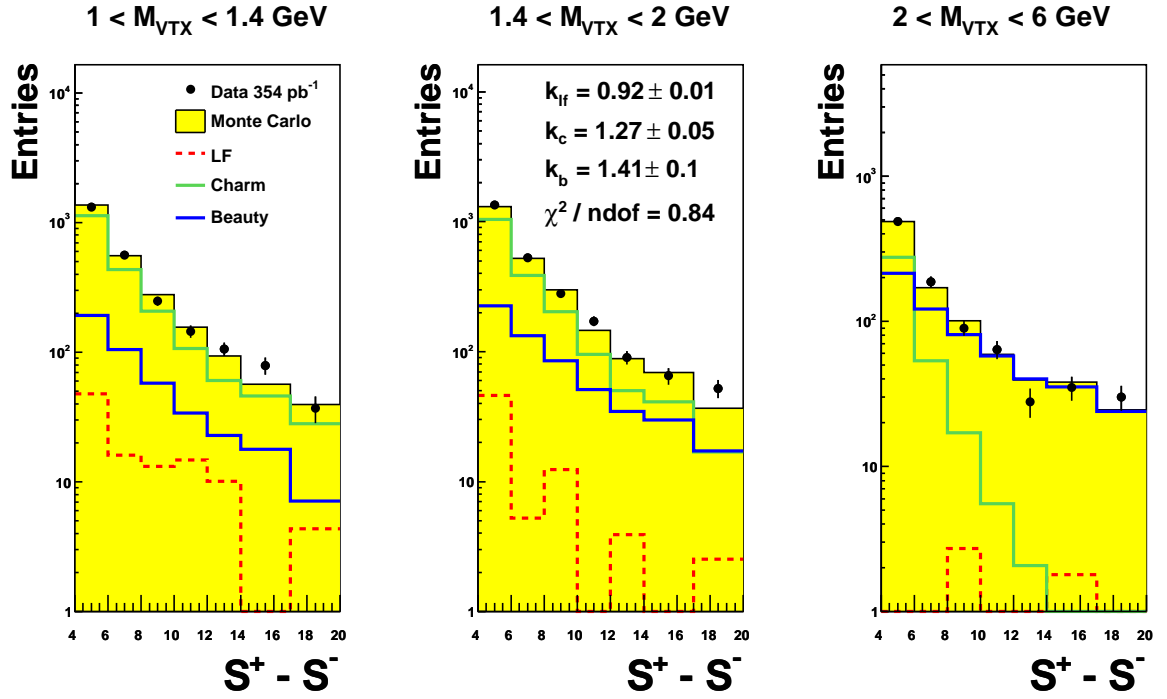


Figure E.5.: Mirrored decay-length significance in three bins of the invariant mass for $0.1 < \eta^{\text{jet}} < 0.4$. The data (dots) are compared to the sum of all MC samples (yellow area) and to the individual contributions separately (lines). The MC samples were scaled using the fit result.

Forward direction

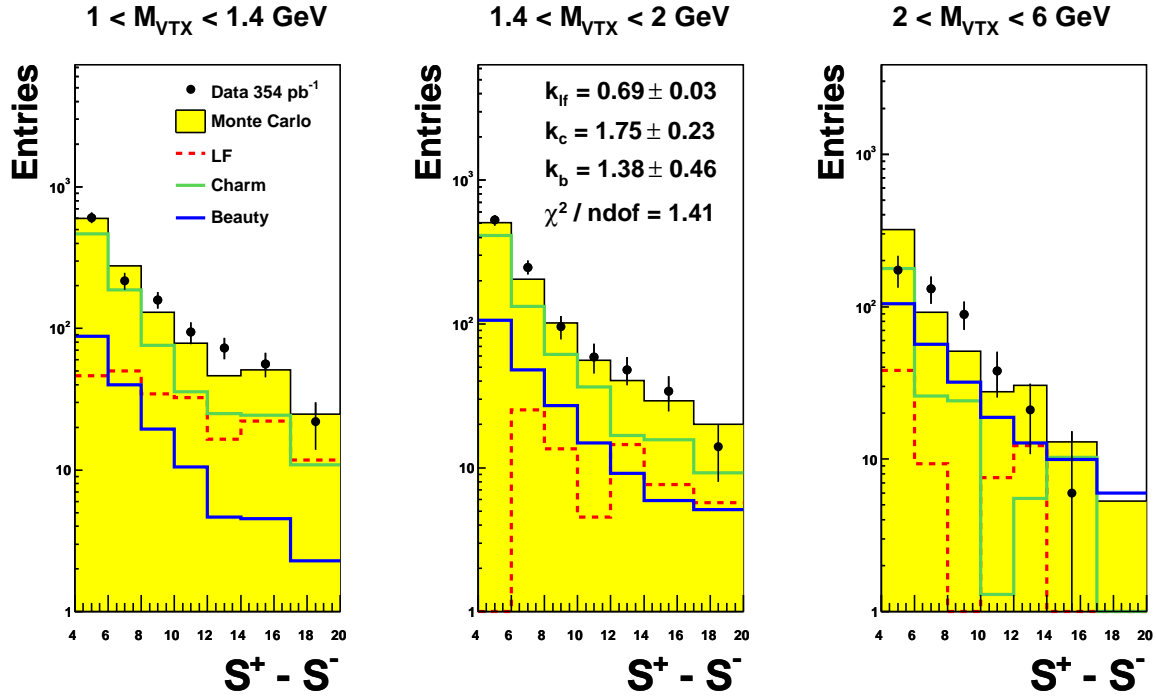


Figure E.6.: Mirrored decay-length significance in three bins of the invariant mass for $1.6 < \eta^{\text{jet}} < 2.2$. The data (dots) are compared to the sum of all MC samples (yellow area) and to the individual contributions separately (lines). The MC samples were scaled using the fit result.

F. Control distributions for $E_T^{\text{jet}} > 4.2 \text{ GeV}$

Control distributions for event, jet and vertex variables are shown on the following pages for the extended kinematic region $E_T^{\text{jet}} > 4.2 \text{ GeV}$, $-1.6 < \eta^{\text{jet}} < 2.2$, $0.02 < y < 0.7$ and $5 < Q^2 < 1000 \text{ GeV}^2$. The beauty enriched region is given by $2 < m_{\text{vtx}} < 6 \text{ GeV}$ and $S^+ - S^- > 8$. The charm enriched region is defined by $1 < m_{\text{vtx}} < 2 \text{ GeV}$ and $S^+ - S^- > 4$.

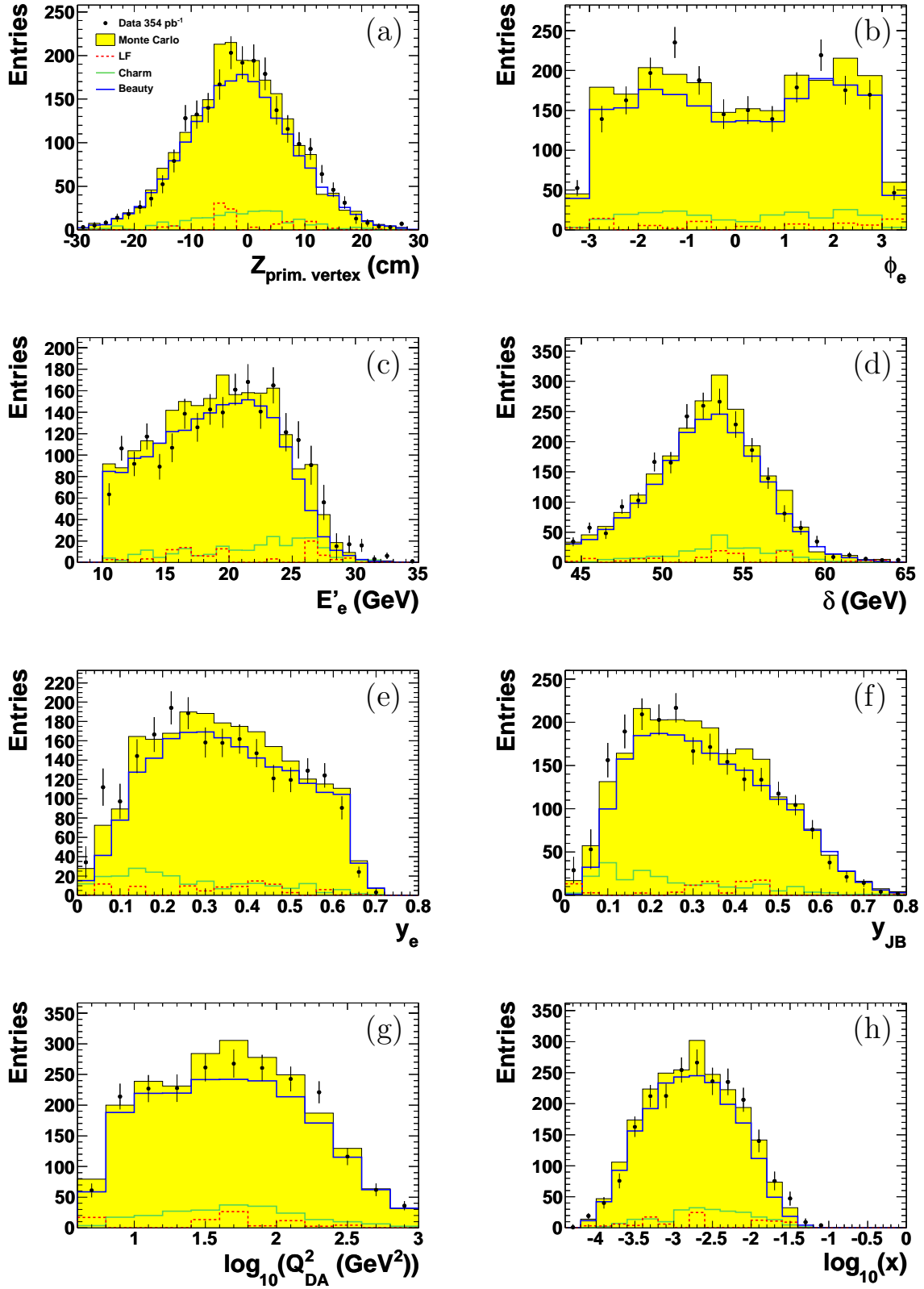


Figure F.1.: The event variables (a) Z_{vertex} , (b) ϕ_e , (c) E'_e , (d) δ , (e) y_e , (f) y_{JB} , (g) $\log_{10} Q_{DA}^2$ and (h) $\log_{10}(x_{DA})$ for the beauty enriched region. The data (dots) are compared to the sum of all MC samples (yellow area). The individual MC samples are shown as solid lines.

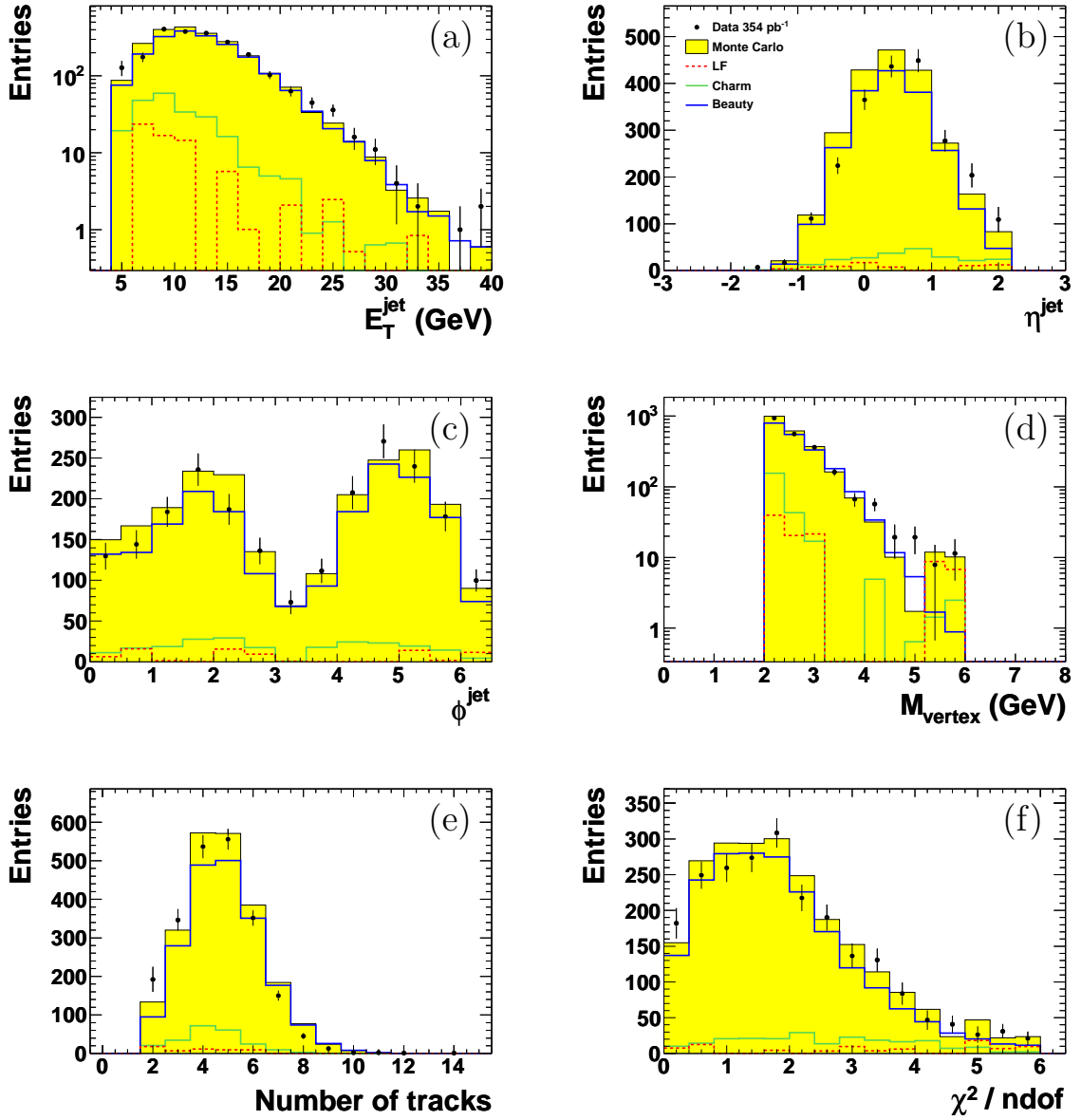


Figure F.2.: The jet and vertex variables (a) E_T^{jet} , (b) η^{jet} , (c) ϕ^{jet} , (d) m_{vtx} , (e) secondary vertex multiplicity and (f) χ^2/ndof for the beauty enriched region. The data (dots) are compared to the sum of all MC samples (yellow area). The individual MC samples are shown as solid lines.

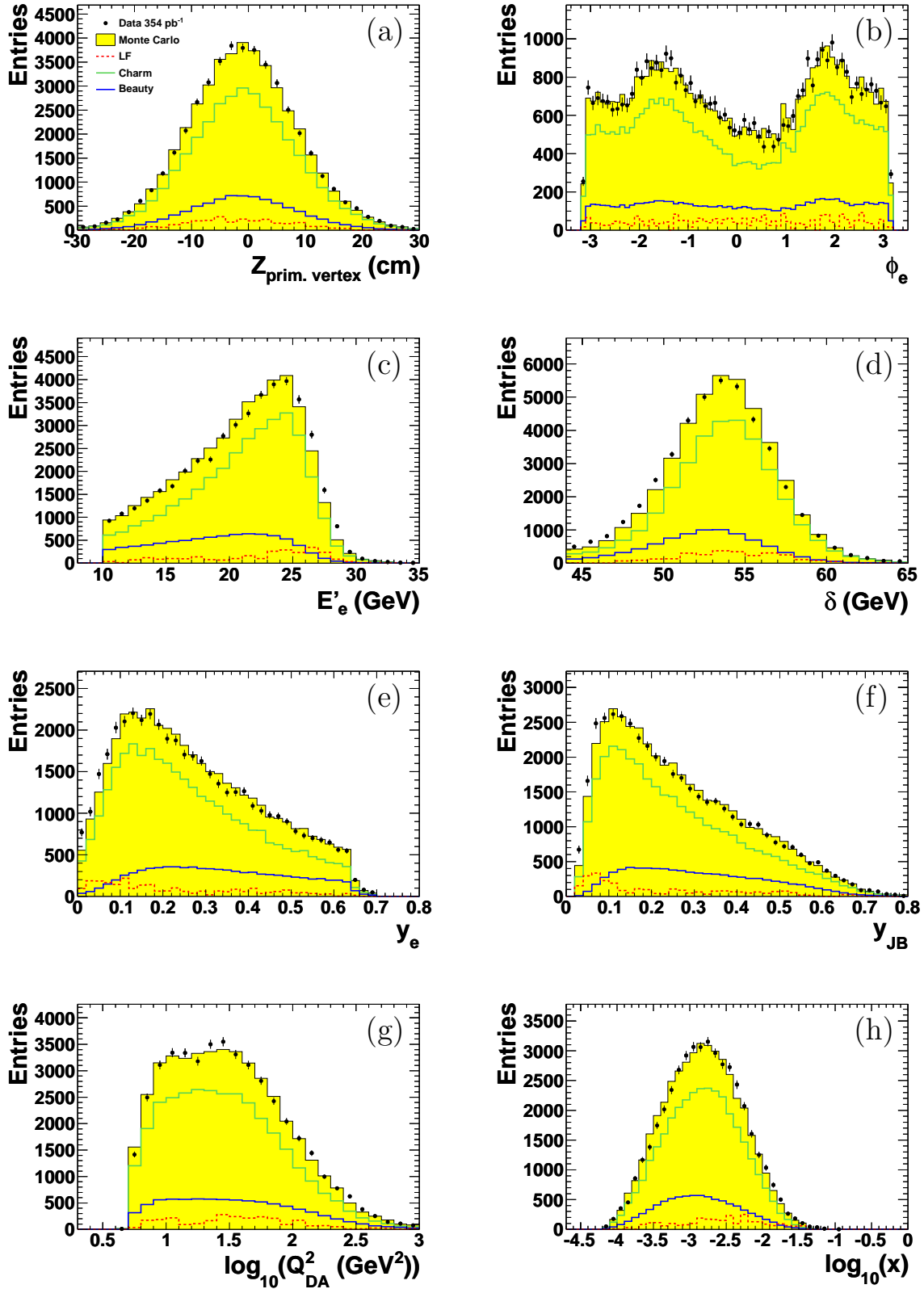


Figure F.3.: The event variables (a) Z_{vertex} , (b) ϕ_e , (c) E'_e , (d) δ , (e) y_e , (f) y_{JB} , (g) $\log_{10} Q_{\text{DA}}^2$ and (h) $\log_{10}(x_{\text{DA}})$ for the charm enriched region. The data (dots) are compared to the sum of all MC samples (yellow area). The individual MC samples are shown as solid lines.

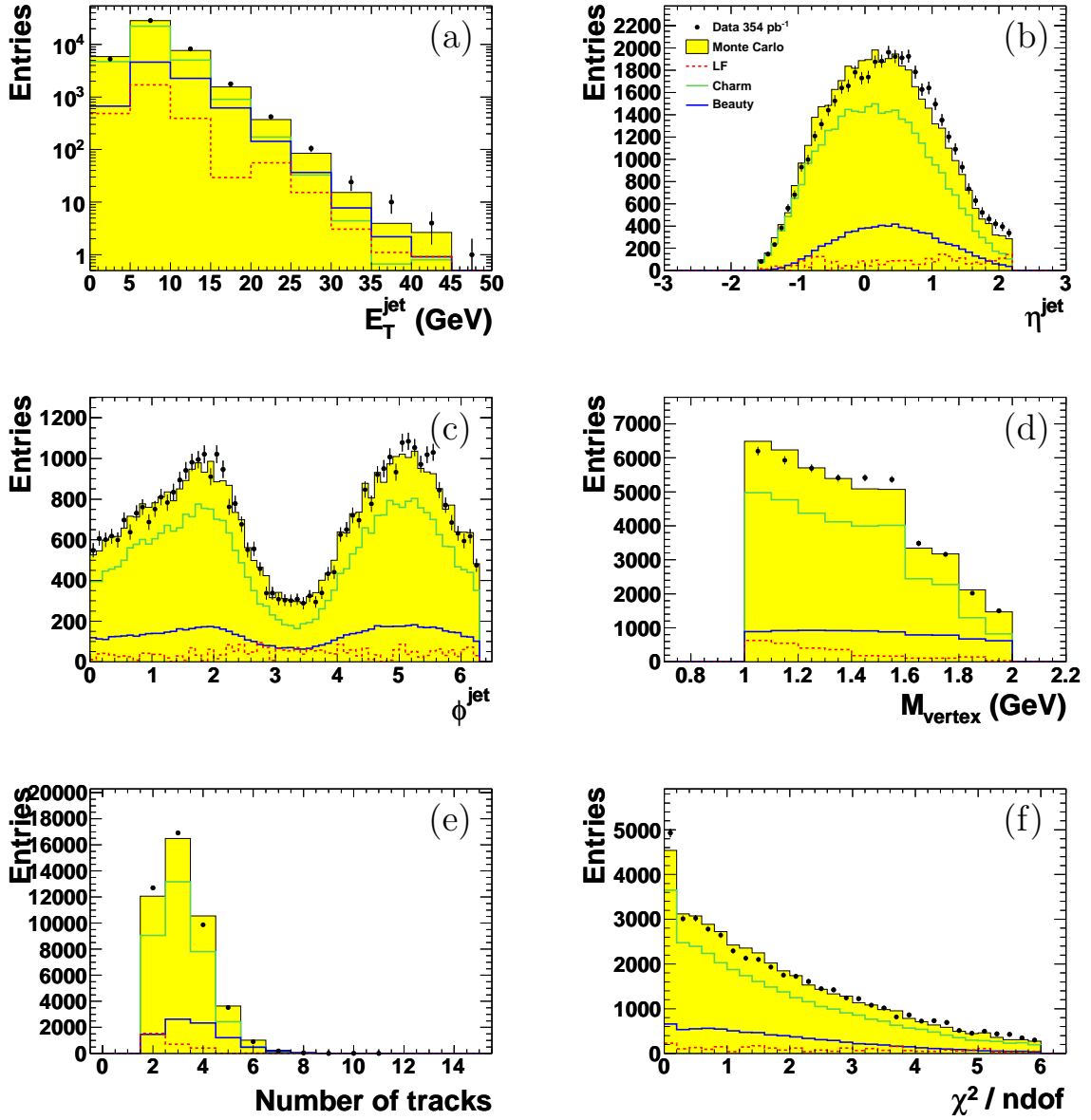


Figure F.4.: The jet and vertex variables (a) E_T^{jet} , (b) η^{jet} , (c) ϕ^{jet} , (d) m_{vtx} , (e) secondary vertex multiplicity and (f) χ^2/ndof for the charm enriched region. The data (dots) are compared to the sum of all MC samples (yellow area). The individual MC samples are shown as solid lines.

G. Uncertainties of the HVQDIS NLO QCD predictions

All sources of systematic uncertainty considered for the HVQDIS NLO QCD predictions for jet production in charm and beauty events are shown in the following.

$$\frac{d\sigma}{dE_T^{\text{jet}}} \text{ for beauty using } \mu_R = \mu_F = \frac{1}{2}\sqrt{Q^2 + p_T^2 + m_b^2}$$

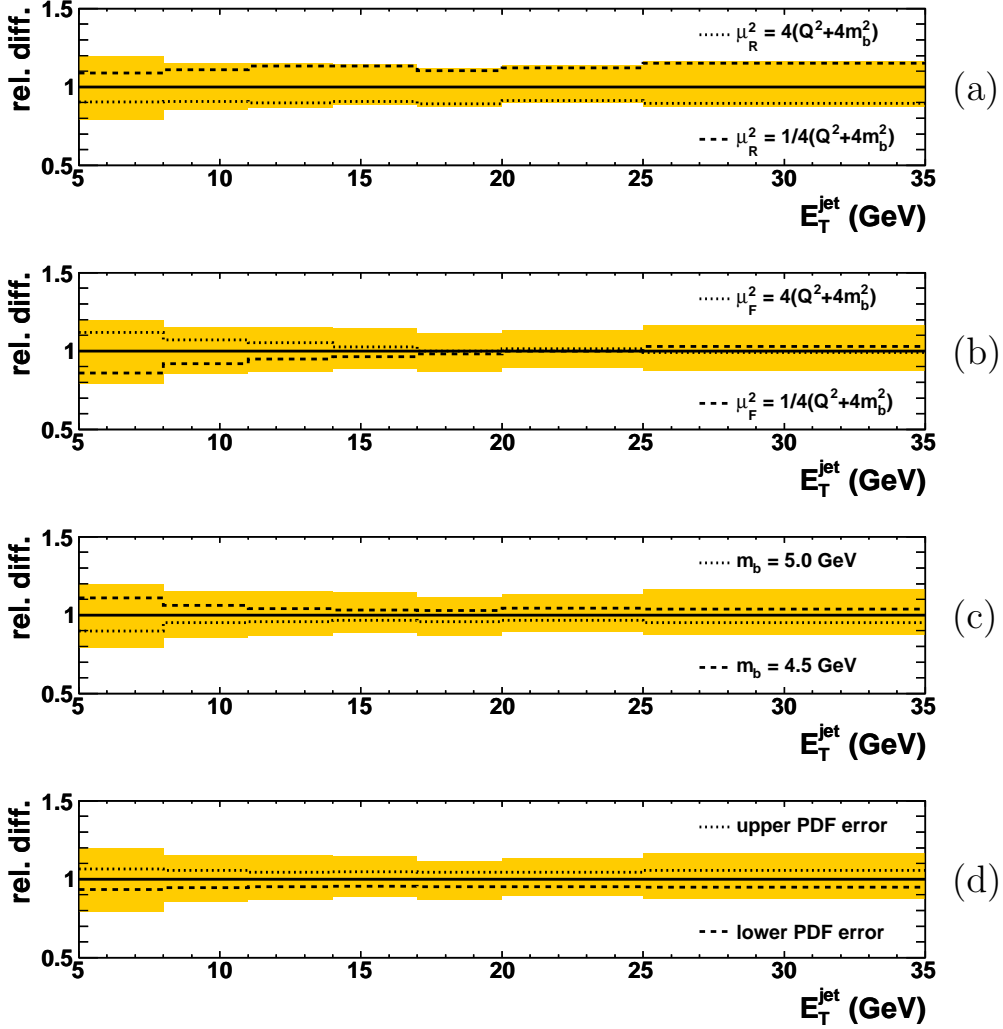


Figure G.1.: Ratio of the systematic variations of the HVQDIS NLO QCD predictions to the central value (lines) as a function of E_T^{jet} . The effects due to the (a) renormalisation scale variation, (b) factorisation scale variation, (c) mass variation and (d) PDF uncertainties are shown separately. The sum all all systematic uncertainties is shown by the yellow band.

$\frac{d\sigma}{d\eta^{\text{jet}}}$ for beauty using $\mu_R = \mu_F = \frac{1}{2}\sqrt{Q^2 + p_T^2 + m_b^2}$

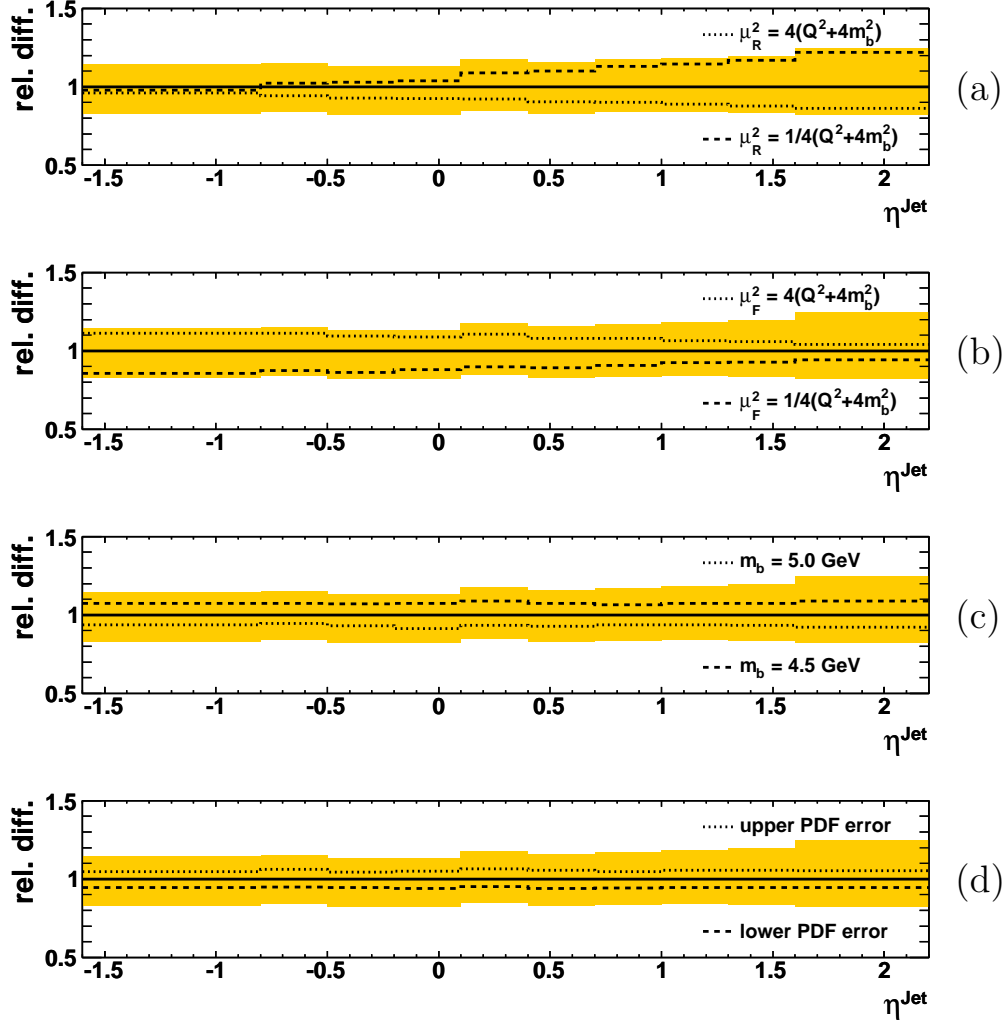


Figure G.2.: Ratio of the systematic variations of the HVQDIS NLO QCD predictions to the central value (lines) as a function of η^{jet} . The effects due to the (a) renormalisation scale variation, (b) factorisation scale variation, (c) mass variation and (d) PDF uncertainties are shown separately. The sum all all systematic uncertainties is shown by the yellow band.

$$\frac{d\sigma}{dx} \text{ for beauty using } \mu_R = \mu_F = \frac{1}{2}\sqrt{Q^2 + p_T^2 + m_b^2}$$

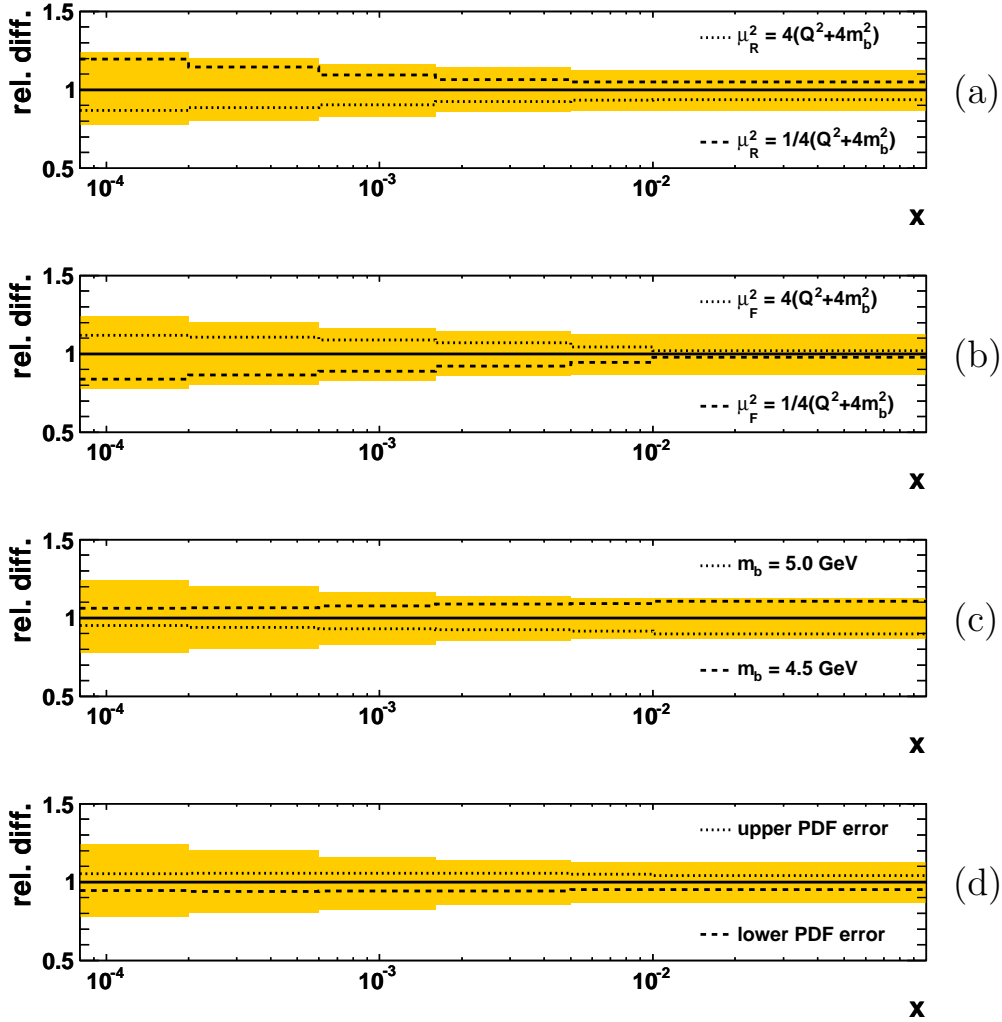


Figure G.3.: Ratio of the systematic variations of the HVQDIS NLO QCD predictions to the central value (lines) as a function of x . The effects due to the (a) renormalisation scale variation, (b) factorisation scale variation, (c) mass variation and (d) PDF uncertainties are shown separately. The sum all all systematic uncertainties is shown by the yellow band.

$$\frac{d\sigma}{dE_T^{\text{jet}}} \text{ for beauty using } \mu_R = \mu_F = \frac{1}{2}\sqrt{Q^2 + 4m_b^2}$$

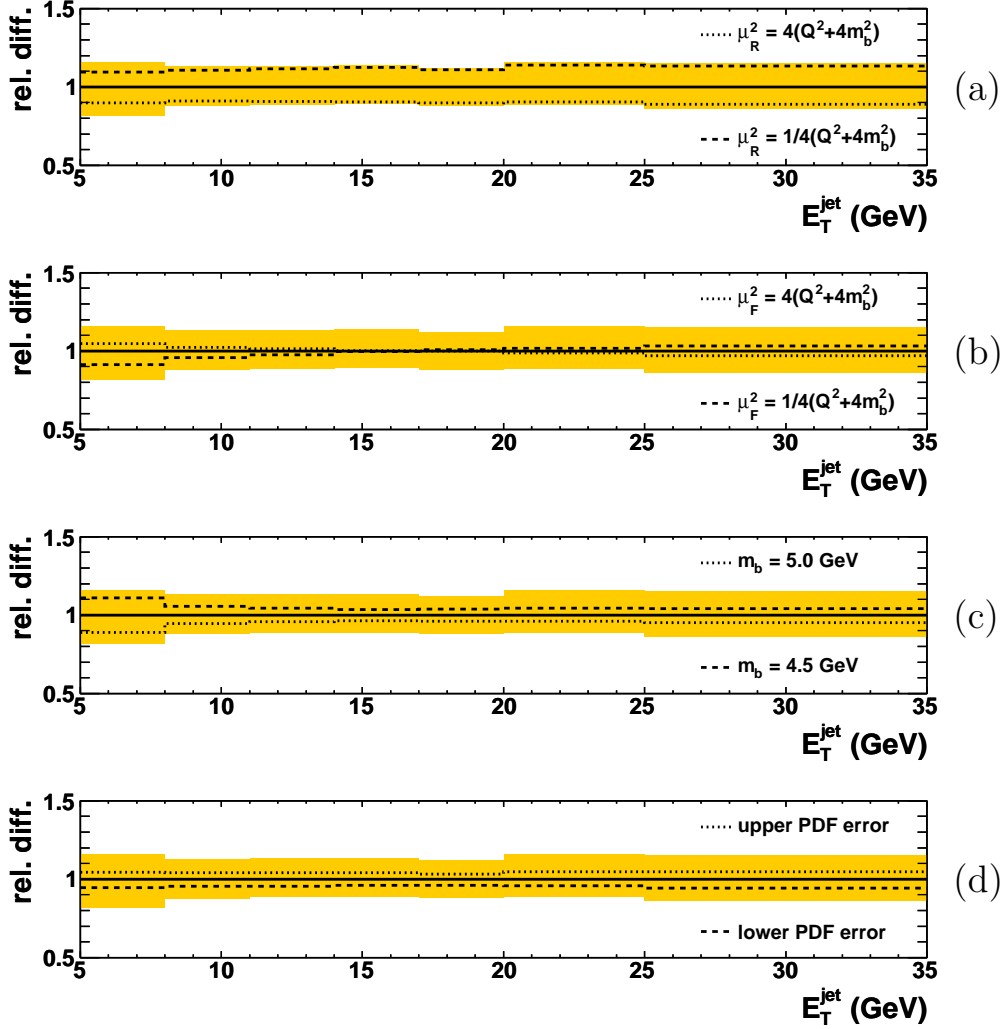


Figure G.4.: Ratio of the systematic variations of the HVQDIS NLO QCD predictions to the central value (lines) as a function of E_T^{jet} . The effects due to the (a) renormalisation scale variation, (b) factorisation scale variation, (c) mass variation and (d) PDF uncertainties are shown separately. The sum all all systematic uncertainties is shown by the yellow band.

$$\frac{d\sigma}{d\eta^{\text{jet}}} \text{ for beauty using } \mu_R = \mu_F = \frac{1}{2}\sqrt{Q^2 + 4m_b^2}$$

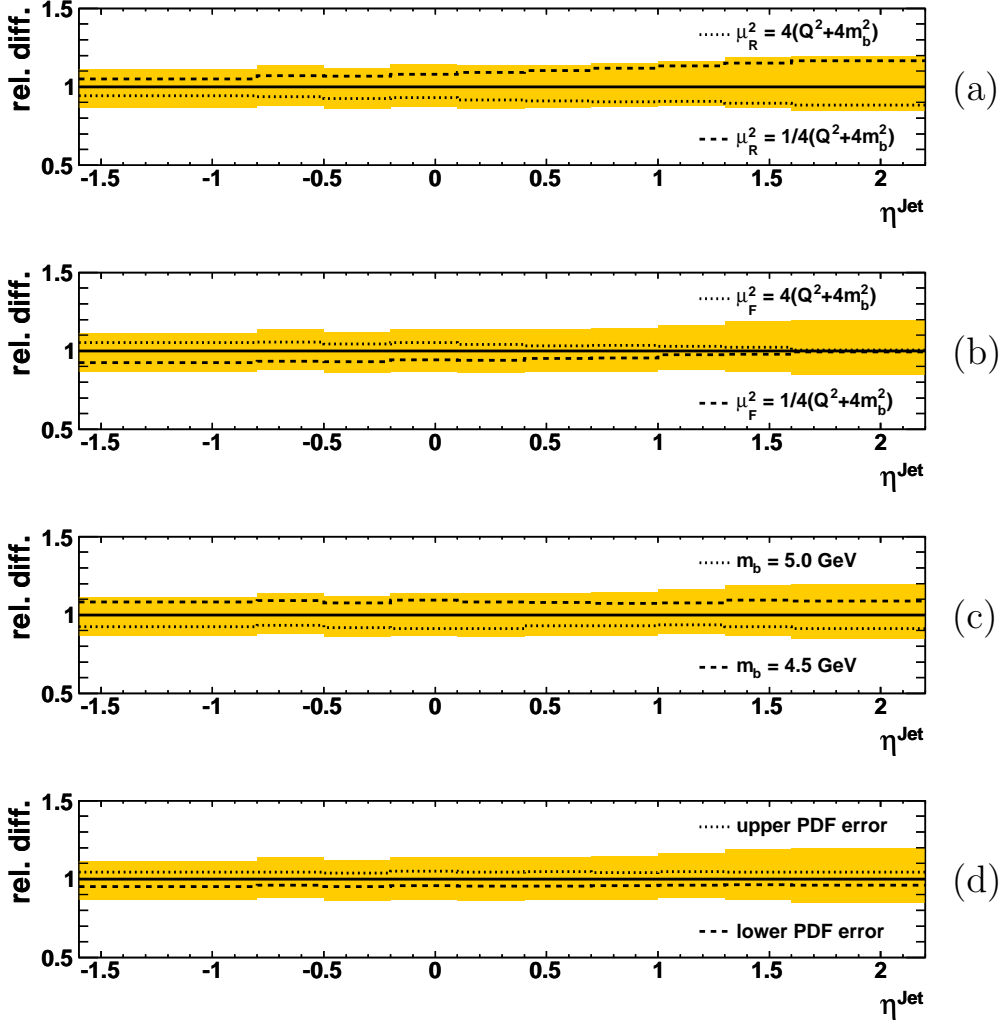


Figure G.5.: Ratio of the systematic variations of the HVQDIS NLO QCD predictions to the central value (lines) as a function of η^{jet} . The effects due to the (a) renormalisation scale variation, (b) factorisation scale variation, (c) mass variation and (d) PDF uncertainties are shown separately. The sum all all systematic uncertainties is shown by the yellow band.

$\frac{d\sigma}{dQ^2}$ for beauty using $\mu_R = \mu_F = \frac{1}{2}\sqrt{Q^2 + 4m_b^2}$

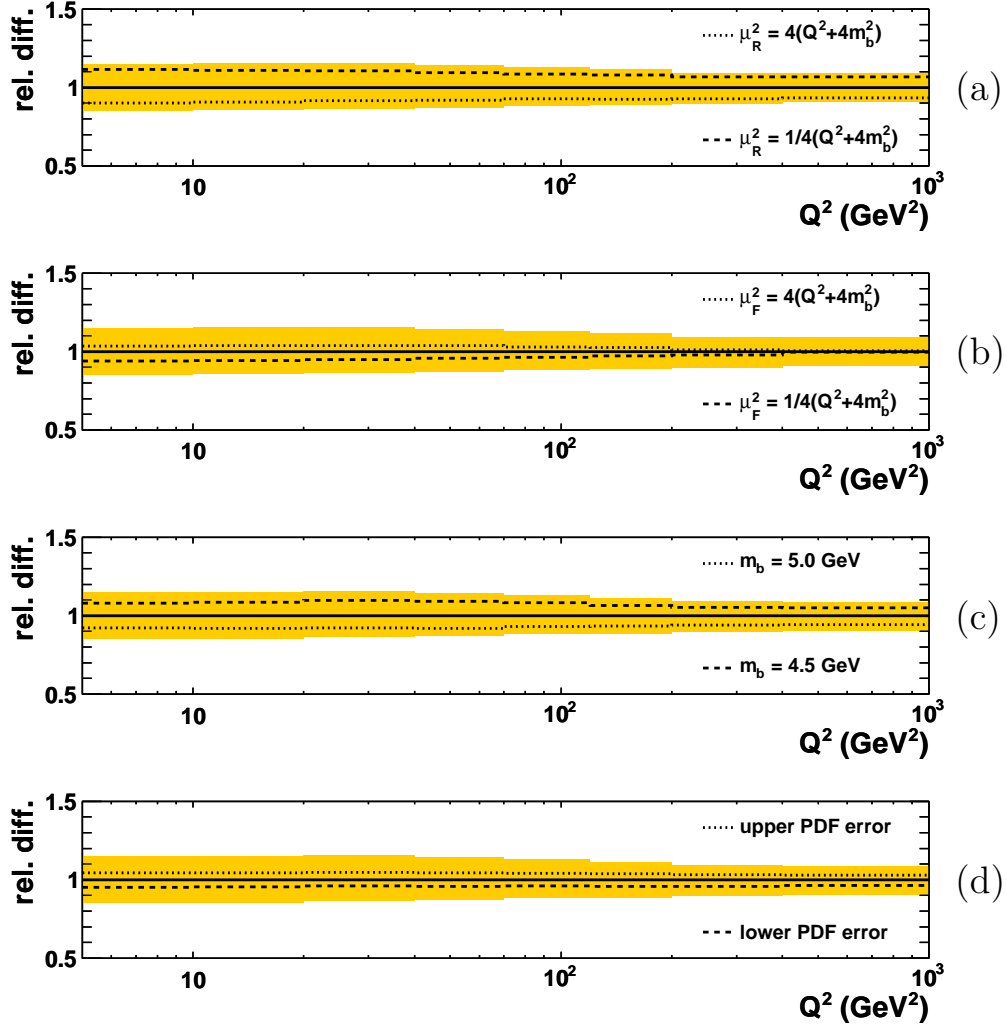


Figure G.6.: Ratio of the systematic variations of the HVQDIS NLO QCD predictions to the central value (lines) as a function of Q^2 . The effects due to the (a) renormalisation scale variation, (b) factorisation scale variation, (c) mass variation and (d) PDF uncertainties are shown separately. The sum all all systematic uncertainties is shown by the yellow band.

$$\frac{d\sigma}{dx} \text{ for beauty using } \mu_R = \mu_F = \frac{1}{2}\sqrt{Q^2 + 4m_b^2}$$

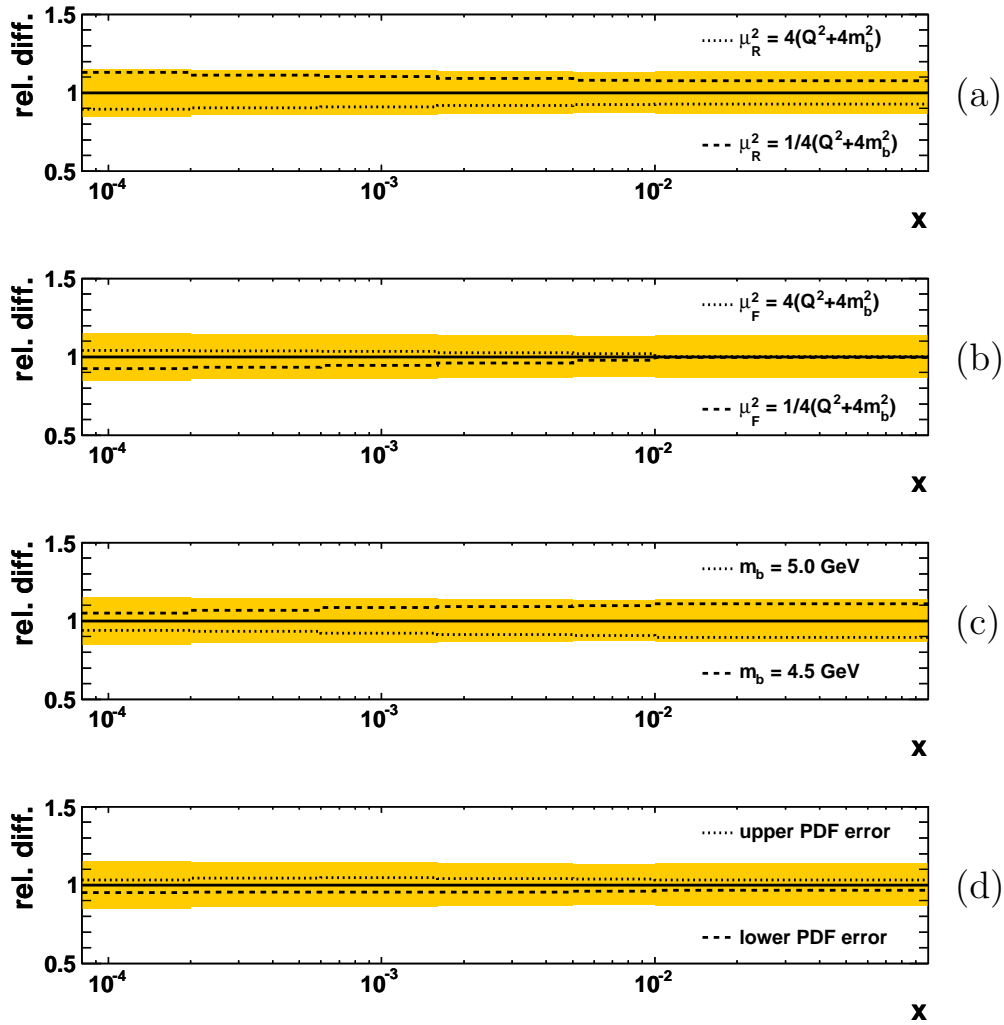


Figure G.7.: Ratio of the systematic variations of the HVQDIS NLO QCD predictions to the central value (lines) as a function of x . The effects due to the (a) renormalisation scale variation, (b) factorisation scale variation, (c) mass variation and (d) PDF uncertainties are shown separately. The sum all all systematic uncertainties is shown by the yellow band.

$$\frac{d\sigma}{dE_T^{\text{jet}}} \text{ for charm using } \mu_R = \mu_F = \frac{1}{2}\sqrt{Q^2 + 4m_c^2}$$

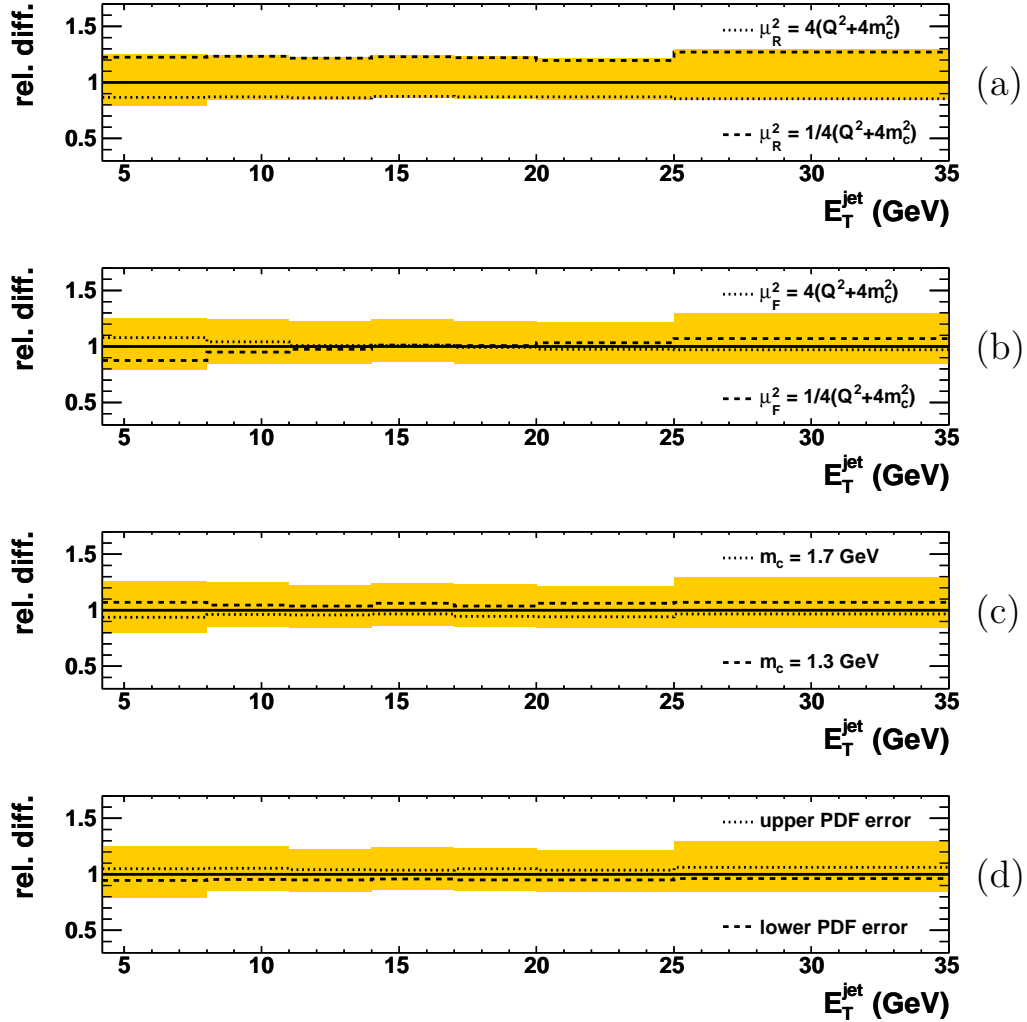


Figure G.8.: Ratio of the systematic variations of the HVQDIS NLO QCD predictions to the central value (lines) as a function of E_T^{jet} . The effects due to the (a) renormalisation scale variation, (b) factorisation scale variation, (c) mass variation and (d) PDF uncertainties are shown separately. The sum all all systematic uncertainties is shown by the yellow band.

$$\frac{d\sigma}{d\eta^{\text{jet}}} \text{ for charm using } \mu_R = \mu_F = \frac{1}{2}\sqrt{Q^2 + 4m_c^2}$$

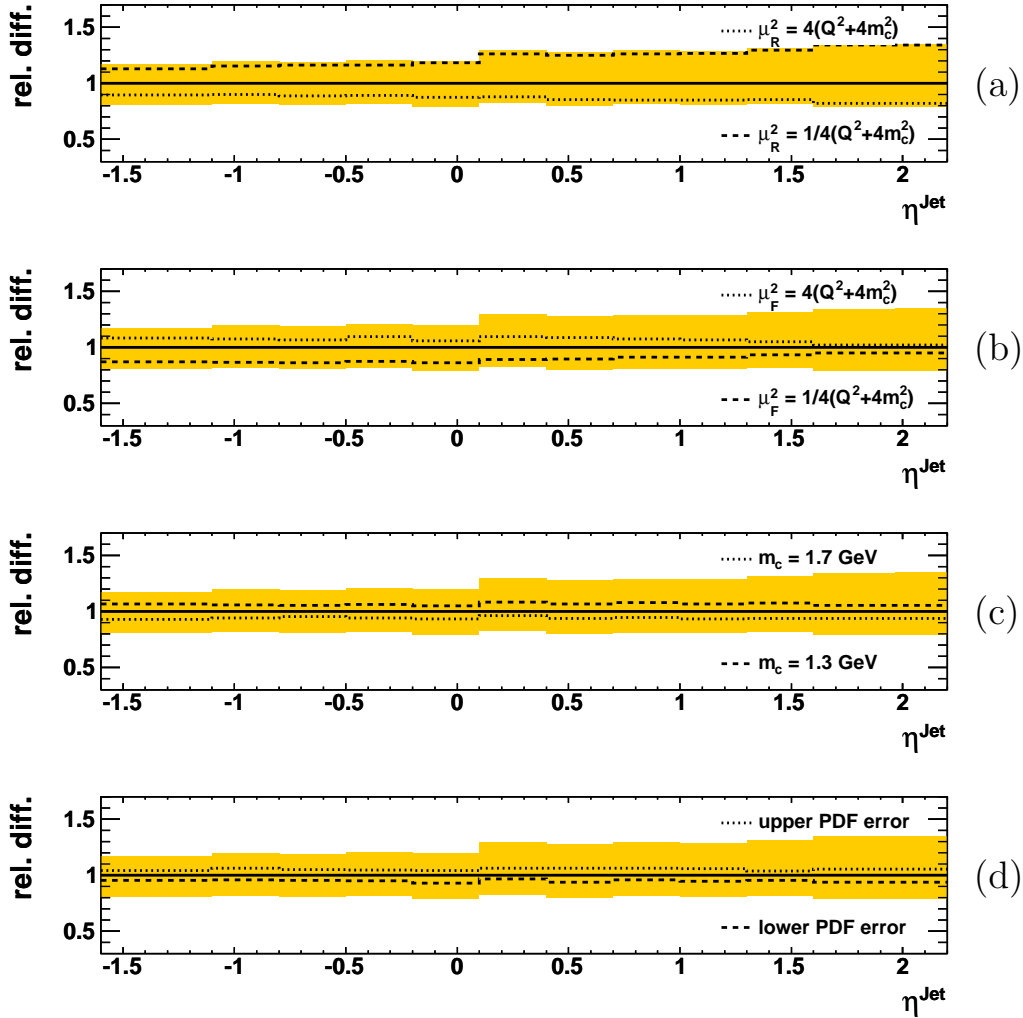


Figure G.9.: Ratio of the systematic variations of the HVQDIS NLO QCD predictions to the central value (lines) as a function of η^{jet} . The effects due to the (a) renormalisation scale variation, (b) factorisation scale variation, (c) mass variation and (d) PDF uncertainties are shown separately. The sum all all systematic uncertainties is shown by the yellow band.

$$\frac{d\sigma}{dQ^2} \text{ for charm using } \mu_R = \mu_F = \frac{1}{2}\sqrt{Q^2 + 4m_c^2}$$

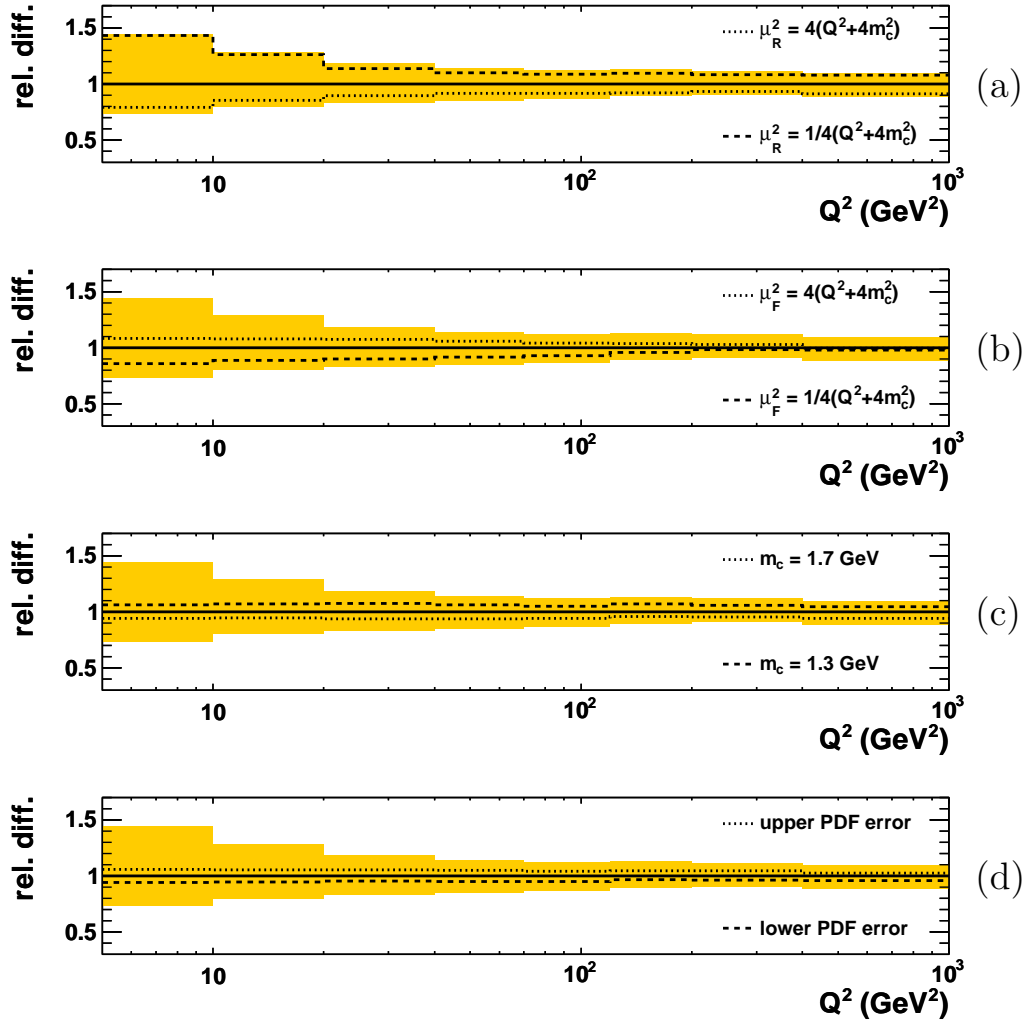


Figure G.10.: Ratio of the systematic variations of the HVQDIS NLO QCD predictions to the central value (lines) as a function of Q^2 . The effects due to the (a) renormalisation scale variation, (b) factorisation scale variation, (c) mass variation and (d) PDF uncertainties are shown separately. The sum of all systematic uncertainties is shown by the yellow band.

$\frac{d\sigma}{dx}$ for charm using $\mu_R = \mu_F = \frac{1}{2}\sqrt{Q^2 + 4m_c^2}$

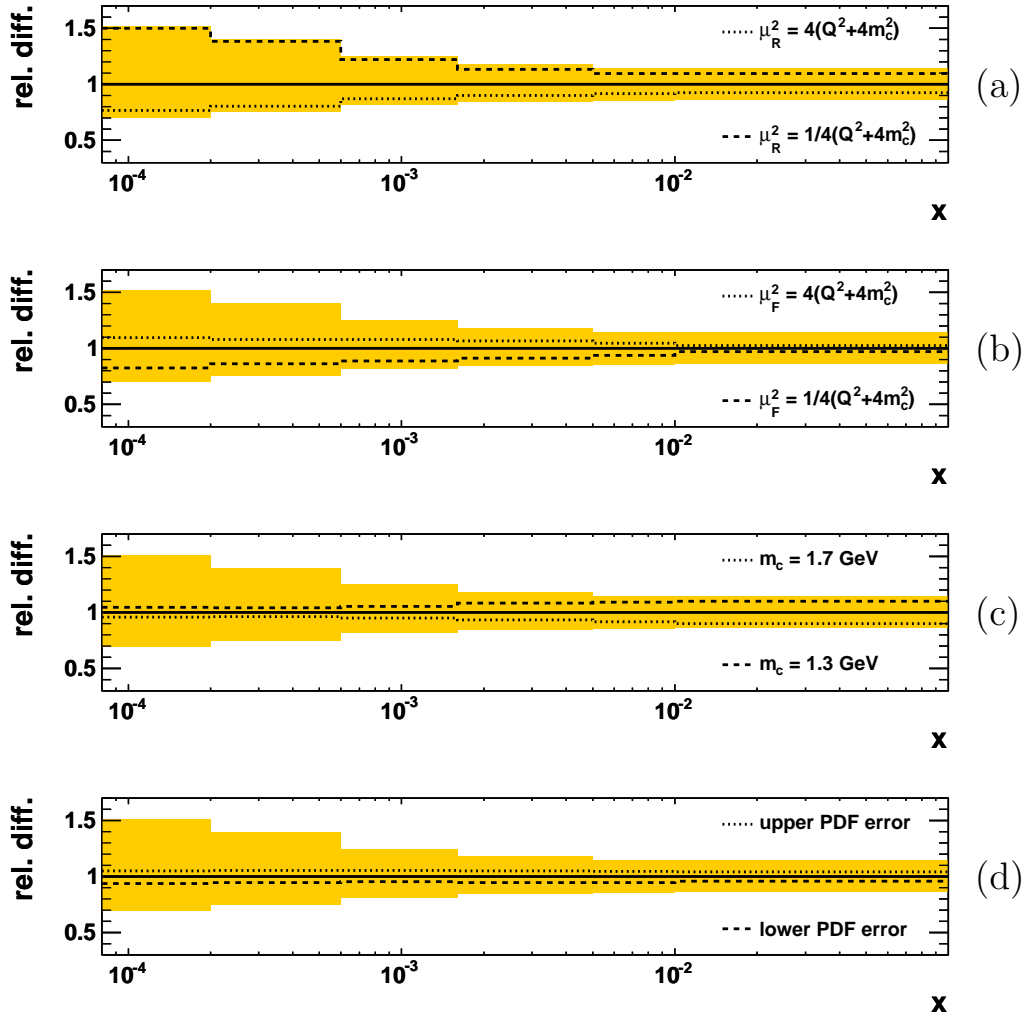


Figure G.11.: Ratio of the systematic variations of the HVQDIS NLO QCD predictions to the central value (lines) as a function of x . The effects due to the (a) renormalisation scale variation, (b) factorisation scale variation, (c) mass variation and (d) PDF uncertainties are shown separately. The sum all all systematic uncertainties is shown by the yellow band.

Bibliography

- [1] F. Halzen and A.D. Martin, *Quarks and Leptons: Introductory Course in Modern Particle Physics*, John Wiley & Sons, New York (1984);
C. Berger, *Elementarteilchenphysik*, Springer, Berlin (2006).
- [2] S.L. Glashow, *Partial-symmetries of weak interactions*, Nucl. Phys. **22**, 579 (1961);
A. Salam, *Renormalizability of Gauge Theories*, Phys. Rev. **127**, 331 (1962);
S. Weinberg, *A Model of Leptons*, Phys. Rev. Lett. **19**, 1264 (1967)
- [3] F. Englert and R. Brout, *Broken Symmetry and the Mass of Gauge Vector Mesons*, Phys. Rev. Lett. **13**, 321 (1964);
P.W. Higgs, *Broken Symmetries and the Masses of Gauge Bosons*, Phys. Rev. Lett. **13**, 508 (1964);
G.S. Guralnik, C.R. Hagen, and T.W.B. Kibble, *Global Conservation Laws and Massless Particles*, Phys. Rev. Lett. **13**, 585 (1964).
- [4] P. Roloff, *Measurement of the charm cross section using D^+ and Λ_c^+ decays in ep collisions at HERA*, Diploma Thesis, Universität Hamburg, 2007.
- [5] H. Abramowicz et al. [ZEUS Coll.], *Measurement of D^+ and Λ_c^+ production in deep inelastic scattering at HERA*, JHEP **11**, 009 (2010).
- [6] J. Brau, Y. Okada and N. Walker (eds.), *International Linear Collider Reference Design Report*, Volume 1: Executive Summary (2007);
N. Phinney, N. Toge and N. Walker (eds.), *International Linear Collider Reference Design Report*, Volume 3: Accelerator (2007).
- [7] R. Tomás, *Overview of the Compact Linear Collider*, Phys. Rev. ST Accel. Beams **13**, 014801 (2010).
- [8] A.M. Cooper-Sarkar, R.C.E. Devenish and A. De Roeck, *Structure functions of the nucleon and their interpretation*, Int. J. Mod. Phys. **A 20**, 3385 (1998).
- [9] H1 Coll. and ZEUS Coll., *Compiled H1+ZEUS NC and CC plots for conferences*, ZEUS-prel-09-001, also H1prelim-09-043 (2009).
- [10] J.D. Bjorken, *Inequality for Backward Electron- and Muon-Nucleon Scattering at High Momentum Transfer*, Phys. Rev. **163**, 1767 (1967);
J.D. Bjorken, *Asymptotic Sum Rules at Infinite Momentum*, Phys. Rev. **179**, 1547 (1969).

- [11] F.D. Aaron et al. [H1 Coll. and ZEUS Coll.], *Combined measurement and QCD analysis of the inclusive $e^\pm p$ scattering cross sections at HERA*, JHEP **01**, 109 (2010).
- [12] A.C. Benvenuti et al. [BCDMS Coll.], *A high statistics measurement of the proton structure functions $F_2(x, Q^2)$ and R from deep inelastic muon scattering at high Q^2* , Phys. Lett. **B 223**, 485 (1989);
M. Arneodo et al. [NMC Coll.], *Measurement of the proton and deuteron structure functions, F_2^p and F_2^d , and of the ratio σ_L/σ_T* , Nucl. Phys. **B 483**, 3 (1997).
- [13] C.G. Callan and D. Gross, *High-Energy Electroproduction and the Constitution of the Electric Current*, Phys. Rev. Lett. **22**, 156 (1969).
- [14] A. Bodek et al., *Experimental studies of the neutron and proton electromagnetic structure functions*, Phys. Rev. **D 20**, 1471 (1979).
- [15] T. Eichten, *Measurement of the neutrino-nucleon and antineutrino-nucleon total cross sections*, Phys. Lett. **B 46**, 274 (1973).
- [16] R. Brandelik et al. [TASSO Coll.], *Evidence for planar events in e^+e^- annihilation at high energies*, Phys. Lett. **B 86**, 243 (1979);
D.P. Barber et al. [MARK-J Coll.], *Discovery of Three-Jet Events and a Test of Quantum Chromodynamics at PETRA*, Phys. Rev. Lett. **43**, 830 (1979);
Ch. Berger et al. [PLUTO Coll.], *Evidence for gluon bremsstrahlung in e^+e^- annihilations at high energies*, Phys. Lett. **B 86**, 418 (1979);
W. Bartel et al. [JADE Coll.], *Observation of planar three-jet events in e^+e^- annihilation and evidence for gluon bremsstrahlung*, Phys. Lett. **B 91**, 142 (1980).
- [17] R. Brock et al. [CTEQ Coll.], *Handbook of Perturbative QCD*, Reviews of Modern Physics **67**, 157 (1995);
R.K. Ellis, W.J. Stirling and B.R. Webber, *QCD and collider physics*, Cambridge Monographs on Particle Physics, Nuclear Physics and Cosmology **8** (1996);
G. Dissertori, I.G. Knowles and M. Schmelling, *High energy experiments and theory*, Clarendon Press, Oxford, United Kingdom (2003);
G. Dissertori and G.P. Salam, *Quantum chromodynamics*, in K. Nakamura et al., J. Phys. **G 37**, 075021 (2010).
- [18] G. 't Hooft and M. Veltman, *Regularization and renormalization of gauge fields*, Nucl. Phys. **B 44**, 189 (1972).
- [19] W.A. Bardeen et al., *Deep inelastic scattering beyond the leading order in asymptotically free gauge theories*, Phys. Rev. **D 18**, 3998 (1978).
- [20] D.J. Gross and F. Wilczek, *Ultraviolet Behavior of Non-Abelian Gauge Theories*, Phys. Rev. Lett. **30**, 1343 (1973);
H.D. Politzer, *Reliable Perturbative Results for Strong Interactions?*, Phys. Rev. Lett. **30**, 1346 (1973);
G. 't Hooft, Report at the Marseille Conference on Yang-Mills Fields (1972).

- W.E. Caswell, *Asymptotic Behavior of Non-Abelian Gauge Theories to Two-Loop Order*, Phys. Rev. Lett. **33**, 244 (1974);
D.R.T. Jones, *Two-loop diagrams in Yang-Mills theory*, Nuclear Physics **B 75**, 531 (1974);
E.Sh. Egoryan and O.V. Tarasov, *Renormalization of quantum chromodynamics in the two-loop approximation in an arbitrary gauge*, Theor. Math. Phys. **41**, 863 (1979);
O.V. Tarasov, A.A. Vladimirov and A.Yu. Zharkov, *The gell-mann-low function of QCD in the three-loop approximation*, Phys. Lett. **B 93**, 429 (1980);
S.A. Larin and J.A.M. Vermaseren, *The three-loop QCD β -function and anomalous dimensions*, Phys. Lett. **B 303**, 334 (1993).
- [21] S. Bethke, *The 2009 world average of α_s* , Eur. Phys. J. **C 64**, 689 (2009).
- [22] G. Grunberg, *Renormalization group improved perturbative QCD*, Phys. Lett **B 95**, 70 (1980);
P.M. Stevenson, *Optimized perturbation theory*, Phys. Rev. **D 23**, 2916 (1981);
P.M. Stevenson, *Resolution of the renormalisation-scheme ambiguity in perturbative QCD*, Phys. Lett. **B 100**, 61 (1981).
- [23] I.I. Bigi et al., *Pole mass of the heavy quark: Perturbation theory and beyond*, Phys. Rev. **D 50**, 2234 (1994).
- [24] N. Gray et al., *Three-loop relation of quark $\overline{\text{MS}}$ and pole masses*, Z. Phys. **C 48**, 673 (1990);
K.G. Chetyrkin and M. Steinhauser, *The relation between the $\overline{\text{MS}}$ and the on-shell quark mass at order α_s^3* , Nucl. Phys. **B 573**, 617 (2000);
K. Melnikov and T. van Ritbergen, *The three-loop relation between the $\overline{\text{MS}}$ and the pole quark masses*, Phys. Lett. **B 482**, 99 (2000).
- [25] B. Bistrovic et al., *Understanding hadron structure from lattice QCD in the SciDAC era*, Journal of Physics: Conference Series **16**, 150 (2005);
J.D. Bratt et al., *Ab initio Hadron Structure from Lattice QCD*, Journal of Physics: Conference Series **78**, 012019 (2007);
J.M. Zanotti, *Investigations of hadron structure on the lattice*, PoS(LATTICE 2008)007 (2008);
D.B. Renner, *Status and prospects for the calculation of hadron structure from lattice QCD*, PoS(LAT2009)018, also DESY 10-019 (2010).
- [26] J.C. Collins and D. Soper, *The theorems of perturbative QCD*, Annual Review of Nuclear and Particle Science **37**, 383 (1987).
- [27] V.N. Gribov and L.N. Lipatov, *Deep inelastic ep scattering in perturbation theory*, Sov. J. Nucl. Phys. **15**, 438 (1972);
G. Altarelli and G. Parisi, *Asymptotic freedom in parton language*, Nucl. Phys. **B 126**, 298 (1977);
Y.L. Dokshitzer, *Calculation of the structure functions for deep inelastic scattering*

- and e^+e^- annihilation by perturbation theory in Quantum Chromodynamics., Sov. Phys. JETP **46**, 641 (1977).
- [28] E.A. Kuraev, L.N. Lipatov and V.S. Fadin, *Multi-Reggeon Processes in the Yang-Mills Theory*, Sov. Phys. JETP **44**, 443 (1976);
E.A. Kuraev, L.N. Lipatov and V.S. Fadin, *The Pomeron Singularity in Non-abelian Gauge Theories*, Sov. Phys. JETP **45**, 199 (1977);
I.I. Balitsky and L.N. Lipatov, *The Pomeron Singularity in Quantum Chromodynamics*, Sov. J. Nucl. Phys. **28**, 822 (1978).
- [29] M. Ciafaloni, *Coherence Effects in Initial Jets at Small Q^2/s* , Nucl. Phys. **B 296**, 49 (1988);
S. Catani, F. Fiorani and G. Marchesini, *QCD Coherence in Initial State Radiation*, Phys. Lett. **B 234**, 339 (1990);
S. Catani, F. Fiorani and G. Marchesini, *Small x Behaviour of Initial State Radiation in Perturbative QCD*, Nucl. Phys. **B 336**, 18 (1990);
G. Marchesini, *QCD coherence in the structure function and associated distributions at small x* , Nucl. Phys. **B 445**, 49 (1995).
- [30] P.M. Nadolsky et al., *Implications of CTEQ global analysis for collider observables*, Phys. Rev. **D 78**, 013004 (2008);
- [31] H.-L. Lai et al., *New parton distributions for collider physics*, Phys. Rev. **D 82**, 074024 (2010).
- [32] A.D. Martin et al., *Parton distributions for the LHC*, Eur. Phys. J. **C 63**, 189 (2009).
- [33] S. Alekhin et al., *3-, 4-, and 5-flavor next-to-next-to-leading order parton distribution functions from deep-inelastic-scattering data and at hadron colliders*, Phys. Rev. **D 81**, 014032 (2010).
- [34] M. Glück, P. Jimenez-Delgado and E. Reya, *Dynamical parton distributions of the nucleon and very small- x physics*, Eur. Phys. J. **C 53**, 355 (2008).
- [35] R.D. Ball et al. [NNPDF Coll.], *A first unbiased global NLO determination of parton distributions and their uncertainties*, Nucl. Phys. **B 838**, 136 (2010).
- [36] M.R. Whalley, D. Bourilkov and R.C. Group, *The Les Houches accord PDFs (LHAPDF) and LHAGLUE*, hep-ph/0508110 (2005).
- [37] E. Witten, *Heavy quark contributions to deep inelastic scattering*, Nucl. Phys. **B 104**, 445 (1976);
M. Glück and E. Reya, *Deep inelastic quantum chromodynamic charm lepton production*, Phys. Lett. **B 83**, 98 (1979).
- [38] G. Ingelman, G.A. Schuler, *Characteristics of heavy flavour production in ep collisions*, Z. Phys. **C40**, 299 (1988).

- [39] E. Laenen et al., *Complete $O(\alpha_s)$ corrections to heavy-flavour structure functions in electroproduction*, Nucl. Phys. **B 392**, 162 (1993);
E. Laenen et al., *$O(\alpha_s)$ corrections to heavy-flavour inclusive distributions in electroproduction*, Nucl. Phys. **B 392**, 229 (1993).
- [40] B.W. Harris and J. Smith, *Heavy-quark correlations in deep-inelastic electroproduction*, Nucl. Phys. **B 452**, 109 (1995);
B.W. Harris and J. Smith, *Invariant mass distributions for heavy quark-antiquark pairs in deep inelastic electroproduction*, Phys. Lett. **B 353**, 535 (1995). Erratum-
ibid **B 359**, 423 (1995).
- [41] B.W. Harris and J. Smith, *Charm quark and $D^{*\pm}$ cross sections in deeply inelastic scattering at DESY HERA*, Phys. Rev. **D 57** 2806 (1998).
- [42] E. Laenen and S.-O. Moch, *Soft gluon resummation for heavy quark electroproduction*, Phys. Rev. **D 59**, 034027 (1999);
N.A. Lo Presti et al., *Threshold-improved predictions for charm production in deep-inelastic scattering*, PoS(DIS 2010)163 (2010).
- [43] M. Buza et al., *Heavy quark coefficient functions at asymptotic values $Q^2 \gg m^2$* , Nucl. Phys. **B 472**, 611 (1996);
I. Bierenbaum, J. Blümlein and S. Klein, *Two-loop massive operator matrix elements and unpolarized heavy flavor production at asymptotic values $Q^2 \gg m^2$* , Nucl. Phys. **B 780**, 40 (2007).
- [44] I. Bierenbaum, J. Blümlein and S. Klein, *Mellin moments of the $O(\alpha_s^3)$ heavy flavor contributions to unpolarized deep-inelastic scattering at $Q^2 \gg m^2$ and anomalous dimensions*, Nucl. Phys. **B 820**, 417 (2009).
- [45] W.-K. Tung, S. Kretzer and C. Schmidt, *Open heavy flavour production: conceptual framework and implementation issues*, J. Phys. **G 28**, 983 (2002);
S. Kretzer et al., *CTEQ6 parton distributions with heavy quark mass effects*, Phys. Rev. **D 69**, 114005 (2004).
- [46] R.S. Thorne and R.G. Roberts, *A practical procedure for evolving heavy flavour structure functions*, Phys. Lett. **B 421**, 303 (1998);
R.S. Thorne and R.G. Roberts, *Ordered analysis of heavy flavor production in deep-inelastic scattering*, Phys. Rev. **D 57**, 6871 (1998).
- [47] M. Buza et al., *Comparison between the various descriptions for charm electroproduction and the HERA-data*, Phys. Lett. **B 411**, 211 (1997);
M. Buza et al., *Charm electroproduction viewed in the variable-flavour number scheme versus fixed-order perturbation theory*, Eur. Phys. J. **C 1**, 301 (1998).
- [48] A. Chuvakin, J. Smith and W.L. van Neerven, *Comparison between variable flavor number schemes for charm quark electroproduction*, Phys.Rev. **D 61**, 096004 (2000);
R.S. Thorne and W.K. Tung, *PQCD Formulations with Heavy Quark Masses and*

- Global Analysis*, arXiv:0809.0714 (2009);
R.S. Thorne, *The Effect of Variable Flavour Number Scheme Variations on PDFs and Cross Sections*, PoS(DIS 2010)053 (2010).
- [49] R.S. Thorne, *A Variable-Flavour Number Scheme for NNLO*, Phys. Rev. **D 73**, 054019 (2006).
- [50] H1 Coll. and ZEUS Coll., *The Rôle of the Charm Mass Parameter in the QCD Analysis of the Combined HERA Data and Implications for the LHC*, ZEUS-prel-10-019, also H1-prelim-10-143 (2010).
- [51] T. Sjöstrand, *Monte Carlo Generators*, arXiv:hep-ph/0611247 (2006).
- [52] C. Peterson et al., *Scaling violations in inclusive e^+e^- annihilation spectra*, Phys. Rev. **D 27**, 105 (1983).
- [53] V.G. Kartvelishvili, A.K. Likhoded and V.A. Petrov, *On the fragmentation functions of heavy quarks into hadrons*, Phys. Lett. **B 78**, 615 (1978).
- [54] M.G. Bowler, *e^+e^- Production of Heavy Quarks in the String Model*, Z. Phys. **C 11**, 169 (1981).
- [55] X. Artru and G. Mennessier, *String model and multiproduction*, Nucl. Phys. **B 70**, 93 (1974).
- [56] B. Andersson, G. Gustafson and B. Söderberg, *A General Model for Jet Fragmentation*, Z. Phys. **C 20**, 317 (1983).
- [57] B. Andersson et al., *Parton fragmentation and string dynamics*, Physics Reports **97**, 31 (1983);
T. Sjöstrand, *Jet fragmentation of multiparton configurations in a string framework*, Nucl. Phys. **B 248**, 469 (1984).
- [58] K. Charchuła, G.A. Schuler and H. Spiesberger, *Combined QED and QCD radiative effects in deep inelastic lepton-proton scattering: the Monte Carlo generator DJANGO6*, Computer Physics Communications **81**, 381 (1994);
H. Spiesberger, *HERACLES and DJANGO6: Event Generation of ep Interactions at HERA Including Radiative Processes* (2005), available on <http://wwwthep.physik.uni-mainz.de/~hspiesb/djangoh/djangoh.html>.
- [59] A. Kwiatkowski, H. Spiesberger and H.-J. Möhring, *HERACLES: an event generator for ep interactions at HERA energies including radiative processes*, Computer Physics Communications **69**, 155 (1992);
H. Spiesberger, *HERACLES. An Event Generator for ep Interactions at HERA Including Radiative Processes - Version 4.6* (1996), available on <http://www.desy.de/~hspiesb/heracles.html>.

- [60] G. Ingelman, A. Edin and J. Rathsman, *LEPTO 6.5 - A Monte Carlo generator for deep inelastic lepton-nucleon scattering*, Computer Physics Communications **101**, 108 (1997).
- [61] L. Lönnblad, *Ariadne version 4 - A program for simulation of QDC cascades implementing the colour dipole model*, Computer Physics Communications **71**, 15 (1992);
L. Lönnblad, *Rapidity gaps and other final state properties in the colour dipole model for deep inelastic scattering*, Z. Phys. **C 65**, 285 (1994).
- [62] Ya.I. Azimov, *The string effect and QCD coherence*, Phys. Lett. **B 165**, 147 (1985);
G. Gustafson, *Dual description of a confined colour field*, Phys. Lett. **B 175**, 453 (1986);
G. Gustafson and U. Pettersson, *Dipole formulation of QCD cascades*, Nucl. Phys. **B 306**, 746 (1988);
B. Andersson et al., *Coherence effects in deep inelastic scattering*, Z. Phys. **C 43**, 625 (1989).
- [63] T. Sjöstrand, *High-energy-physics event generation with PYTHIA 5.7 and JETSET 7.4*, Computer Physics Communications **82**, 74 (1994).
- [64] H. Jung, *Hard diffractive scattering in high energy ep collisions and the Monte Carlo Generator RAPGAP*, Computer Physics Communications **86**, 147 (1995);
H. Jung, *The RAPGAP Monte Carlo for Deep Inelastic Scattering - version 3.2* (2010), available on <http://projects.hepforge.org/rapgap/>.
- [65] T. Sjöstrand et al., *High-energy-physics event generation with PYTHIA 6.1*, Computer Physics Communications **135**, 238 (2001);
T. Sjöstrand et al., *PYTHIA 6.2 - Physics and Manual*, hep-ph/0108264, also LU TP 01-21 second edition (2002).
- [66] K. Nakamura et al. [Particle Data Group], *The Review of Particle Physics*, J. Phys. **G 37**, 075021 (2010).
- [67] C. Chang, K.W. Chen and A. Van Ginneken, *Dimuon and Trimuon Final States in Deep Inelastic Muon Scattering*, Phys. Rev. Lett. **39**, 519 (1977);
D. Bauer et al., *Multimuon Final States in Muon-Nucleon Scattering at 270 GeV*, Phys. Rev. Lett **43**, 1551 (1979);
J.J. Aubert et al. [EMC Coll.], *A study of dimuon events in 280 GeV muon interactions*, Phys. Lett. **B 94**, 96 (1980);
J.J. Aubert et al. [EMC Coll.], *Production of charmed particles in 250 GeV μ^+ -iron interactions*, Nucl. Phys. **B 213**, 31 (1983);
M. Arneodo et al. [EMC Coll.], *Charm production in deep inelastic muon-iron interactions at 200 GeV/c*, Z. Phys. **C 35**, 1 (1987).
- [68] C. Adloff et al. [H1 Coll.], *Inclusive D^0 and $D^{*\pm}$ production in neutral current deep inelastic ep scattering at HERA*, Z. Phys. **C 72**, 593 (1996);
J. Breitweg et al. [ZEUS Coll.], *D^* Production in Deep Inelastic Scattering at HERA*,

- Phys. Lett. **B 407**, 402 (1997);
C. Adloff et al. [H1 Coll.], *Measurement of D^* meson cross sections at HERA and determination of the gluon density in the proton using NLO QCD*, Nucl. Phys. **B 545**, 21 (1999);
J. Breitweg et al. [ZEUS Coll.], *Measurement of $D^{*\pm}$ production and the charm contribution to F_2F_2 in deep inelastic scattering at HERA*, Eur. Phys. J **C 12**, 35 (2000);
C. Adloff et al. [H1 Coll.], *Measurement of $D^{*\pm}$ meson production and F_2^c in deep inelastic scattering at HERA*, Phys. Lett. **B 528**, 199 (2002);
S. Chekanov et al. [ZEUS Coll.], *Measurement of $D^{*\pm}$ production in deep inelastic $e^\pm p$ scattering at DESY HERA*, Phys. Rev. **D 69**, 012004 (2004);
A. Aktas et al. [H1 Coll.], *Inclusive $D^{*\pm}$ meson and associated dijet production in deep-inelastic scattering at HERA*, Eur. Phys. J **C 51**, 271 (2007);
S. Chekanov et al. [ZEUS Coll.], *Measurement of $D^{*\pm}$ meson production in $e^\pm p$ scattering at low Q^2* , Phys. Lett. **B 649**, 111 (2007);
F.D. Aaron et al. [H1 Coll.], *Measurement of the $D^{*\pm}$ meson production cross section and F_2^c at high Q^2 in ep scattering at HERA*, Phys. Lett. **B 686**, 91 (2010).
- [69] S. Nussinov, *Possible Effects of Decays of Charmed-Particle Resonances*, Phys. Rev. Lett. **35**, 1672 (1975).
- [70] G.J. Feldman et al., *Observation of the Decay $D^{*+} \rightarrow D^0\pi^+$* , Phys. Rev. Lett **38**, 1313 (1977).
- [71] S. Chekanov et al. [ZEUS Coll.], *Measurement of D^\pm and D^0 production in deep inelastic scattering using a lifetime tag at HERA*, Eur. Phys. J. **C 63**, 171 (2009).
- [72] S. Chekanov et al. [ZEUS Coll.], *Measurement of D mesons production in deep inelastic scattering at HERA*, JHEP **07**, 074 (2007).
- [73] A. Aktas et al. [H1 Coll.], *Inclusive production of D^+ , D^0 , D_s^+ and D^{*+} mesons in deep inelastic scattering at HERA*, Eur. Phys. J. **C 38**, 447 (2005).
- [74] L. Gladilin, *Charm Hadron Production Fractions*, arXiv:hep-ex/9912064 (1999).
- [75] H1 Coll. and ZEUS Coll., *Combination of $F_2^{c\bar{c}}$ from DIS measurements at HERA*, ZEUS-prel-09-015, also H1prelim-09-171 (2009).
- [76] S. Chekanov et al. [ZEUS Coll.], *Measurement of charm fragmentation ratios and fractions in photoproduction at HERA*, Eur. Phys. J. **C 44**, 351 (2005).
- [77] W.-M. Yao et al. [Particle Data Group], *Review of Particle Physics*, J. Phys. **G 33**, 1 (2006).
- [78] S. Eidelman et al. [Particle Data Group], *Review of Particle Physics*, Phys. Lett. **B 592**, 1 (2004).
- [79] S. Chekanov et al. [ZEUS Coll.], *Measurement of the charm fragmentation function in D^* photoproduction at HERA*, JHEP **04**, 082 (2009).

-
- [80] S. Frixione et al., *Total cross sections for heavy flavour production at HERA*, Phys. Lett. **B 348**, 633 (1995);
S. Frixione, P. Nason and G. Ridolfi, *Differential distributions for heavy flavour production at HERA*, Nucl. Phys. **B 454**, 3 (1995).
- [81] F.D. Aaron et al. [H1 Coll.], *Study of charm fragmentation into $D^{*\pm}$ mesons in deep-inelastic scattering at HERA*, Eur. Phys. J. **C 59**, 589 (2009).
- [82] A. Aktas et al. [H1 Coll.], *Measurement of beauty production at HERA using events with muons and jets*, Eur. Phys. J. **C 41**, 453 (2005).
- [83] S. Chekanov et al. [ZEUS Coll.], *Measurement of beauty production in deep inelastic scattering at HERA*, Phys. Lett. **B 599**, 173 (2004).
- [84] H. Abramowicz et al. [ZEUS Coll.], *Measurement of beauty production in DIS and F_2^{bb} extraction at ZEUS*, Eur. Phys. J. **C**, doi:10.1140/epjc/s10052-010-1423-2 (2010).
- [85] H. Abramowicz et al. [ZEUS Coll.], *Measurement of beauty production in deep inelastic scattering at HERA using decays into electrons*, DESY-11-005 (2011), also arXiv:1101.3692.
- [86] A. Aktas et al. [H1 Coll.], *Measurement of $F_2^{c\bar{c}}$ and $F_2^{b\bar{b}}$ at high Q^2 using the H1 vertex detector at HERA*, Eur. Phys. J. **C 40**, 349 (2005);
A. Aktas et al. [H1 Coll.], *Measurement of $F_2^{c\bar{c}}$ and $F_2^{b\bar{b}}$ at low Q^2 and x using the H1 vertex detector at HERA*, Eur. Phys. J. **C 45**, 23 (2006);
F.D. Aaron et al. [H1 Coll.], *Measurement of the charm and beauty structure functions using the H1 vertex detector at HERA*, Eur. Phys. J. **C 65**, 89 (2010).
- [87] S. Chekanov et al. [ZEUS Coll.], *Measurement of charm and beauty production in deep inelastic ep scattering from decays into muons at HERA*, Eur. Phys. J. **C 65**, 65 (2010).
- [88] F.D. Aaron et al. [H1 Coll.], *Measurement of Charm and Beauty Jets in Deep Inelastic Scattering at HERA*, DESY 10-083 (2010).
- [89] *HERA, A proposal for a large electron-proton colliding beam facility at DESY*, DESY-HERA-81-10 (1981).
- [90] U. Schneekloth (ed.), *The HERA luminosity upgrade*, DESY-HERA-98-05 (1998).
- [91] A.A. Sokolov and I.M. Ternov, *On polarization and spin effects in synchrotron radiation theory*, Sov. Phys. Dokl. **8**, 1203 (1964);
V.N. Baier and V.A. Khoze, *Determination of the transverse polarization of high-energy electrons*, Sov. J. Nucl. Phys. **9**, 238 (1969).
- [92] D.P. Barber et al., *The first achievement of longitudinal spin polarization in a high energy electron storage ring*, Phys. Lett. **B 343**, 436 (1995).

- [93] D.P. Barber et al., *The HERA polarimeter and the first observation of electron spin polarization at HERA*, Nucl. Inst. Meth. **A 329**, 79 (1993).
- [94] M. Beckmann et al., *The Longitudinal Polarimeter at HERA*, Nucl. Inst. Meth. **A 479**, 334 (2002).
- [95] D. Bailey et al. [ZEUS Background Working Group], *Study of beam-induced backgrounds in the ZEUS detector from 2002 HERA running*, ZEUS-02-018 (2002);
Abbandum, ZEUS-02-020 (2002);
Abbandum, ZEUS-02-027 (2002).
- [96] S. Chekanov et al. [ZEUS Coll.], *Measurement of the longitudinal proton structure function at HERA*, Phys. Lett. **B 682**, 8 (2009);
F.D. Aaron et al. [H1 Coll.], *Measurement of the Proton Structure Function $F_L(x, Q^2)$ at Low x* , Phys. Lett. **B 665**, 139 (2008);
F.D. Aaron et al. [H1 Coll.], *Measurement of the Inclusive $e^\pm p$ Scattering Cross Section at High Inelasticity y and of the Structure Function F_L* , DESY 10-228, also arXiv:1012.4355 (2010).
- [97] U. Holm (ed.) [ZEUS Coll.], *The ZEUS Detector*, Status Report (unpublished), DESY (1993), available on <http://www-zeus.desy.de/bluebook/bluebook.html>.
- [98] A. Bamberger et al., *The small angle rear tracking detector of ZEUS*, Nucl. Instr. Meth. **A 401**, 63 (1997).
- [99] A. Polini et al., *The design and performance of the ZEUS micro vertex detector*, Nucl. Inst. Meth **A 581**, 656 (2007).
- [100] D. Dannheim et al. *Design and tests of the silicon sensors for the ZEUS micro vertex detector*, Nucl. Inst. Meth. **A 505**, 663 (2003).
- [101] M. Milite, *The internal structure of charmed jets in photoproduction at HERA and tests of the ZEUS microvertex silicon sensor*, Ph.D. Thesis, Universität Hamburg, DESY-THESIS-2001-050 (2001);
V. Chiochia, *Measurement of beauty quark production in deep inelastic scattering at HERA*, Ph.D. Thesis, Universität Hamburg, DESY-THESIS-2003-031 (2003).
- [102] M. Feuerstack-Raible, *Overview of microstrip read-out chips*, Nucl. Inst. Meth. **A 447**, 35 (2000).
- [103] N. Harnew et al., *Vertex triggering using time difference measurements in the ZEUS Central Tracking Detector*, Nucl. Inst. Meth. **A 279**, 290 (1989);
B. Foster et al., *The performance of the ZEUS central tracking detector z-by-timing electronics in a transputer based data acquisition system*, Nucl. Phys. Proc. Suppl. **B 32**, 181 (1993);
B. Foster et al., *The design and construction of the ZEUS central tracking detector*, Nucl. Inst. Meth. **A 338**, 254 (1994).

-
- [104] R. Hall-Wilton et al., *The CTD Tracking Resolution*, ZEUS-Note-99-024 (1999).
- [105] A. Spiridonov, *Tracking Status*, Talk at the ZEUS Collaboration Meeting, DESY Hamburg, Germany, February 2011.
- [106] S. Fourletov, *Straw tube tracking detector (STT) for ZEUS*, Nucl. Inst. Meth. **A 535**, 191 (2004).
- [107] M. Derrick et al., *Design and construction of the ZEUS barrel calorimeter*, Nucl. Inst. Meth. **A 309**, 77 (1991);
A. Andresen et al., *Construction and beam test of the ZEUS forward and rear calorimeter*, Nucl. Inst. Meth. **A 309**, 101 (1991);
A. Caldwell et al., *Design and implementation of a high precision readout system for the ZEUS calorimeter*, Nucl. Inst. Meth. **A 321**, 356 (1992);
A. Bernstein et al., *Beam tests of the ZEUS barrel calorimeter*, Nucl. Inst. Meth. **A 336**, 23 (1993).
- [108] H. Bethe and W. Heitler, *On the Stopping of Fast Particles and on the Creation of Positive Electrons*, Proc. R. Soc. Lond. **A 146**, 83 (1934).
- [109] T. Haas and V. Makarenko, *Title: Precision calculation of processes used for luminosity measurement at the ZEUS experiment*, arXiv:1009.2451 (2010).
- [110] R.L. Gluckstern and M.H. Hull, *Polarization Dependence of the Integrated Bremsstrahlung Cross Section*, Phys. Rev. **90**, 1030 (1953).
- [111] J. Andruszkóv et al., *First Measurement of HERA Luminosity by ZEUS Lumi Monitor*, DESY-92-066 (1992);
M. Derrick et al., *Measurement of total and partial photon proton cross sections at 180 GeV center of mass energy*, Z. Phys. **C 63**, 391 (1994);
J. Andruszkóv et al., *Luminosity Measurement in the ZEUS Experiment*, Acta Phys. Pol. **B 32**, 2025 (2001).
- [112] M. Helbich et al., *The spectrometer system for measuring ZEUS luminosity at HERA*, Nucl. Inst. Meth. **A 565**, 572 (2006).
- [113] W.H. Smith, T. Tokushuku and P. Kooijman, *The ZEUS trigger system*, Proc. Computing in High-Energy Physics (CHEP), Annecy, France, Sept. 1992, C. Verkerk and W. Wojcik (eds.), CERN, Geneva, Switzerland, 222 (1992), also in DESY 92-150B.
- [114] W.H. Smith et al., *The ZEUS calorimeter first level trigger*, Nucl. Inst. Meth. **A 355**, 278 (1995);
G.P. Heath et al., *The ZEUS first level tracking trigger*, Nucl. Inst. Meth. **A 315**, 431 (1992).
- [115] A. Quadt et al., *The design and performance of the ZEUS central tracking detector second-level trigger*, Nucl. Inst. Meth **A 438**, 472 (1999).

- [116] U. Behrens, L. Hagge and W.O. Vogel, *The Eventbuilder of the ZEUS experiment*, Nucl. Inst. Meth **A 332**, 253 (1993).
- [117] S.M. Fischer and P. Palazzi, *ADAMO Reference Manual*, CERN (1993), available on <http://adamo.web.cern.ch/adamo/refmanual/Document.html>.
- [118] P.D. Allfrey et al., *The design and performance of the ZEUS global tracking trigger*, Nucl. Inst. Meth. **A 580**, 1257 (2007).
- [119] S. Bhadra et al., *The ZEUS third-level trigger system*, Computer Physics Communications **57**, 321 (1989).
- [120] R. Brun et al., *GEANT3*, CERN-DD/EE/84-1 (1987).
- [121] G.F. Hartner et al., *VCTRAK (3.07/04): Offline Output Information*, ZEUS-Note 97-064 (1997);
G.F. Hartner, *VCTRAK Briefing: Program and Math*, ZEUS-Note 98-058 (1998).
- [122] P. Billoir and S. Qian, *Fast vertex fitting with a local parametrization of tracks*, Nucl. Inst. Meth. **A 311**, 139 (1992).
- [123] G. Hartner, *VCTRAK: STT(+CTD)+MVD combined pattern recognition*, talk at the ZEUS collaboration meeting, October 2005;
G. Hartner, *VCTRAK: STT(+CTD)+MVD combined pattern recognition*, talk at the ZEUS collaboration meeting, February 2006.
- [124] A. Spiridonov, *Mathematical Framework for Fast and Rigorous Track Fit for the ZEUS Detector*, DESY 08-182 (2008).
- [125] R.E. Kalman, *A New Approach to Linear Filtering and Prediction Problems*, Transactions of the ASME Journal of Basic Engineering, **D 82**, 35 (1960).
- [126] R. Frühwirth and A. Strandlie, *Track fitting with ambiguities and noise: a study of elastic tracking and nonlinear filters*, Comp. Phys. Comm. **120**, 197 (1999).
- [127] D. Nicholass, *The study of D^\pm and D^0 meson production in deep inelastic scattering at HERA II with the ZEUS detector*, Ph.D. Thesis, University College London, DESY-THESIS-08-046 (2008).
- [128] A. Spiridonov, *Evaluation of Beam Spot Size*, talk at the ZEUS collaboration meeting, October 2009.
- [129] J. Breitweg et al. [ZEUS Coll.], *Measurement of inclusive (D_s^\pm) production at HERA*, Phys. Lett. **B 481**, 213 (2000);
J. Breitweg et al. [ZEUS Coll.], *Measurement of open beauty production in photoproduction at HERA*, Eur. Phys. J. **C 18**, 625 (2000);
D. Bartsch, *Energy-loss measurement with the ZEUS Central Tracking Detector*, Ph.D. Thesis, Universität Bonn, BONN-IR-2007-05 (2007);

-
- S. Chekanov et al. [ZEUS Coll.], *Beauty photoproduction using decays into electrons at HERA*, Phys. Rev. **78**, 072001 (2008).
- [130] G.M. Briskin, *Diffraction Dissociation in ep Deep Inelastic Scattering*, Ph.D. Thesis, Tel Aviv University, DESY-THESIS-1998-036 (1998);
N. Tuning, *ZUFOS: Hadronic final state reconstruction with calorimeter, tracking and backplash correction*, ZEUS-01-021 (2001).
- [131] T.C. Awes et al., *A simple method of shower localization and identification in laterally segmented calorimeters*, Nucl. Inst. Meth **A 311**, 130 (1992).
- [132] H. Abramowicz, A. Caldwell and R. Sinkus, *Neural network based electron identification in the ZEUS calorimeter*, Nucl. Inst. Meth. **A 365**, 508 (1995);
R. Sinkus and T. Voss, *Particle identification with neural networks using a rotational invariant momentum representation*, Nucl. Inst. Meth. **A 391**, 360 (1997).
- [133] J.E. Huth et al., *Toward a Standardization of Jet Definitions*, Proc. of the 1990 Summer Study on High Energy Physics, Research Directions for the Decade, Snowmass, Colorado, USA, also FERMILAB-Conf-90/249-E [E-741/CDF] (1990).
- [134] S. Catani, Y.L. Dokshitzer and B.R. Webber, *The k_T -clustering algorithm for jets in deep inelastic scattering and hadron collisions*, Phys. Lett. **B 285**, 291 (1992);
S. Catani et al., *Longitudinally-invariant k_\perp -clustering algorithms for hadron-hadron collisions*, Nucl. Phys. **B 406**, 187 (1993);
S.T. Ellis and D.E. Soper, *Successive combination jet algorithm for hadron collisions*, Phys. Rev. **D 48**, 3160 (1993).
- [135] M. Corradi and M. Turcato, *Beauty production in dijet events*, ZEUS-Note 04-005 (2004).
- [136] B. Kahle, *Measurement of Beauty-Production in Deep Inelastic Scattering at HERA II*, Ph.D. Thesis, Universität Hamburg, DESY-THESIS-2006-011 (2006).
- [137] S. Bentvelsen, J. Engelen and P. Kooijman, *Reconstruction of (x, Q^2) and extraction of structure functions in neutral current scattering at HERA*, Proc. Workshop on Physics at HERA, C. Verkerk and W. Wojcik (eds.), CERN, Geneva, Switzerland, also DESY 92-152B (1992).
- [138] F. Jacquet and A. Blondel, *Detection and study of the charged current event*, Proc. of the Study for an ep Facility for Europe, U. Amaldi (ed.), Hamburg, Germany, also DESY 79/48 (1979).
- [139] H.L. Lai et al., *Global QCD analysis of parton structure of the nucleon: CTEQ5 parton distributions*, Eur. Phys. J. **C 12**, 375 (2000).
- [140] S. Chekanov et al. [ZEUS Coll.], *Measurement of the neutral current cross section and F_2 structure function for deep inelastic e^+p scattering at HERA*, Eur. Phys. J. **C 21** 443 (2001).

- [141] M.J. Wodarczyk, *Measurement of the F_2 structure function of the proton at HERA from 1996 and 1997 ZEUS data*, Ph.D. Thesis, University of Wisconsin (1999).
- [142] N. Tuning, *Proton structure functions at HERA*, Ph.D. Thesis, University of Amsterdam (2001).
- [143] C. Amsler et al. [Particle Data Group], *The Review of Particle Physics*, Phys. Lett. **B 667**, 1 (2008).
- [144] S. Chekanov et al., *ZEUS next-to-leading-order QCD analysis of data on deep inelastic scattering*, Phys. Rev. **D 67**, 012007 (2003).
- [145] P. Roloff, *D^+ , D^0 and Λ_c^+ production in deep inelastic scattering at HERA*, PoS(ICHEP 2010)170, also arXiv:1012.1198 (2010).
- [146] P. Roloff, *$F_2^{b\bar{b}}$ measurement at ZEUS*, PoS(DIS 2010)174, also arXiv:1007.0748 (2010).
- [147] ZEUS Coll., *Measurement of beauty production from inclusive secondary vertices in DIS and $F_2^{b\bar{b}}$ extraction at ZEUS*, Write-up of result for the ICHEP 2010 conference (2010), available on http://www-zeus.desy.de/physics/hfla/public/PublicPlots/Zeus-prel-10-004/f2b_ichep2010.pdf.
- [148] A.G. Yagües Molina, *Study of Beauty Photoproduction with the ZEUS Experiment at the Electron-Proton Collider HERA*, Ph.D. Thesis, Humboldt Universität zu Berlin (2008).
- [149] V.E. Schönberg, *Measurement of beauty and charm photoproduction using inclusive secondary vertexing with the ZEUS detector at HERA*, Ph.D. Thesis, Universität Bonn, BONN-IR-2010-05 (2010).
- [150] O. Viazlo, Bachelor Thesis, University of Kiev (2010).
- [151] O. Behnke, *Track efficiency tests with K_S^0 decays*, Talk at the ZEUS Heavy Flavour Meeting, DESY Hamburg, Germany, 25.03.2010.
- [152] S. Lammers and D. Chapin, *Jet Energy Scale Uncertainty*, ZEUS-01-006 (2001).
- [153] J. Blümlein, Private communication (2010).
- [154] S. Alekhin and S. Moch, *Higher order QCD corrections to charged-lepton deep inelastic scattering and global fits of parton distributions*, Phys. Lett. **B 672**, 166 (2009);
S. Alekhin, J. Blümlein and S.-O. Moch, *Update of the NNLO PDFs in the 3-, 4-, and 5-flavour schemes*, PoS(DIS 2010)021 (2010).
- [155] S. Alekhin and S. Moch, *Heavy-quark deep-inelastic scattering with a running mass*, DESY 10-212, also arXiv:1011.5790 (2010).

-
- [156] ZEUS Coll., *Measurement of D^\pm production and F_2^c extraction in deep inelastic scattering at ZEUS*, ZEUS-prel-10-005 (2010).
- [157] I. Bloch, *Measurement of beauty production from dimuon events at HERA/ZEUS*, PhD Thesis, Universität Hamburg, DESY-THESIS-05-034 (2005).
- [158] J. Hofestädt, *Study of different reference axes for secondary vertexing in DIS at ZEUS*, Summer student report, DESY (2010).
- [159] I.-M. Gregor, *The EUDET research infrastructure for detector R&D*, Nucl. Inst. Meth. **A 623**, 397 (2010).
- [160] V. Boudry et al., *Summary of the Linear Collider Testbeam Workshop 2009 - LCTW09*, LC-DET-2010-002, also arXiv:1010.1337 (2010).
- [161] J. Alozy et al., *First Version of the PCMAG Field Map*, EUDET-Memo-2007-51 (2007), available on <http://www.eudet.org/e26/e28/e182/e599/eudet-memo-2007-51.pdf>.
- [162] P. Roloff, *The EUDET high resolution pixel telescope*, Nucl. Inst. Meth. **A 604**, 265 (2009).
- [163] L. Reuen, *The DEPFET sensor as the first device under test using the EUDET JRA1 telescope*, EUDET-Memo-2007-40 (2007), available on <http://www.eudet.org/e26/e28/e182/e429/eudet-memo-2007-40.pdf>.
- [164] C. Grah et al., *Towards a Measurement of the Mean Number of Charge Carriers Created by a MIP in sCVD Diamond using the EUDET Telescope*, EUDET-Memo-2007-58 (2007), available on <http://www.eudet.org/e26/e28/e182/e614/eudet-memo-2007-58.pdf>;
T. Bergauer et al., *Resolution studies on silicon strip sensors with fine pitch*, EUDET-Memo-2008-15 (2008), available on <http://www.eudet.org/e26/e28/e615/e782/EUDET-Memo-2008-15.pdf>;
I. Laktineh, *Report on the use of the EUDET telescope in the CALICE DHCAL test beam of July 2008 at CERN*, EUDET-Memo-2008-35 (2008), available on <http://www.eudet.org/e26/e28/e615/e797/eudet-memo-2008-35.pdf>;
J. Furltova and L. Reuen, *JRA1 - The DEPFET sensor as the first fully integrated DUT in the EUDET pixel telescope: The PS test beam 2008*, EUDET-Memo-2008-33 (2008), available on <http://www.eudet.org/e26/e28/e615/e794/eudet-memo-2008-33.pdf>;
J. Furltova and L. Reuen, *JRA1 - The DEPFET sensor as the first fully integrated DUT in the EUDET pixel telescope: The SPS test beam 2008*, EUDET-Memo-2008-34 (2008), available on <http://www.eudet.org/e26/e28/e615/e795/eudet-memo-2008-34.pdf>;
J.J. Velthuis, *ISIS1 beam test using the EUDET telescope*, EUDET-Memo-2008-36 (2008), available on <http://www.eudet.org/e26/e28/e615/e812/eudet-memo-2008-36.pdf>;

- J. Furltova, *DEPFET SPS beam test using the EUDET telescope*, EUDET-Memo-2009-19 (2009), <http://www.eudet.org/e26/e28/e42441/e68289/EUDET-MEMO-2009-19.pdf>.
- [165] E. Corrin, *The EUDET High Resolution Beam Telescope - The Final Digital Readout*, EUDET-Report-2009-06 (2009), available on <http://www.eudet.org/e26/e26/e27/e71570/eudet-report-09-06.pdf>;
J. Behr, *Test Beam Measurements with the EUDET Pixel Telescope*, EUDET-Report-2010-01 (2010), available on <http://www.eudet.org/e26/e26/e27/e107291/eudet-report-2010-01.pdf>, also DESY-THESIS-2010-038.
- [166] I.-M. Gregor and C. Muhl, *JRA1 - Status of Mechanics, Cooling and Infrastructure*, EUDET-Memo-2007-26, (2007), <http://www.eudet.org/e26/e28/e182/e406/eudet-memo-2007-26.pdf>.
- [167] B. Dierickx, G. Meynants and D. Scheffer, *Near 100% fill factor CMOS active pixel*, Proc. of the 1997 IEEE Workshop on Charged-Coupled Devices & Advanced Image Sensors, Brugge, Belgium (1997);
R. Turchetta et al., *A monolithic active pixel sensor for charged particle tracking and imaging using standard VLSI CMOS technology*, Nucl. Inst. Meth. **A 458**, 677 (2001).
- [168] Yu. Gornushkin et al., *Tracking performance and radiation tolerance of monolithic active pixel sensors*, Nucl. Inst. Meth. **A 513**, 291 (2003).
- [169] C. Colledani et al., *MimoTEL - User Manual*, available on http://www.iphc.cnrs.fr/IMG/MimoTEL_1.0.pdf (2006);
W. Dulinski: *Status of pixel sensors for the demonstrator phase of EUDET beam telescope*, EUDET-Memo-45 (2007), available on <http://www.eudet.org/e26/e28/e182/e431/EUDET-MEMO-2007-45.pdf>.
- [170] W. Dulinski et al., *Beam telescope for medium energy particles based on thin, sub-micron precision MAPS*, IEEE Nuclear Science Symposium Conference Record, 26 October 2007 - 3 November 2007, Honolulu, USA, 995 (2008)
- [171] A. Dorokhov, *Optimization of amplifiers for Monolithic Active Pixel Sensors*, Proc. of the Topical Workshop on Electronics for Particle Physics - TWEPP 2007, Prague, Czech Republic (2007);
M. Deveaux et al., *Radiation tolerance of CMOS monolithic active pixel sensors with self-biased pixels*, Nucl. Inst. Meth. **A 624**, 428 (2010).
- [172] A. Cotta Ramusino, *The EUDET Data Reduction Board (EUDRB)*, EUDET-Memo-2007-36 (2007), available on <http://www.eudet.org/e26/e28/e182/e436/eudet-memo-2007-36.pdf>.
- [173] D. Cussans, *Description of the JRA1 Trigger Logic Unit (TLU)*, EUDET-Memo-2007-02 (2007), available on <http://www.eudet.org/e26/e28/e182/e291/eudet-memo-2007-02.pdf>.

-
- [174] E. Corrin, *EUDAQ Software User Manual*, EUDET-Memo-2010-01 (2010), available on <http://www.eudet.org/e26/e28/e86887/e86890/EUDET-Memo-2010-01.pdf>.
- [175] J. Behr, *The JRA-1 Online Monitor*, EUDET-Memo-2008-19 (2008), available on <http://www.eudet.org/e26/e28/e615/e800/EUDET-Memo-2008-19.pdf>.
- [176] A. Bulgheroni et al., *EUTelescope: tracking software*, EUDET-Memo-2007-20 (2007), available on <http://www.eudet.org/e26/e28/e182/e425/eudet-memo-2007-20.pdf>;
A. Bulgheroni et al., *EUTelescope, the JRA1 tracking and reconstruction software: a status report (Milestone)*, EUDET-Memo-2008-48 (2008), available on <http://www.eudet.org/e26/e28/e615/e835/eudet-memo-2008-48.pdf>.
- [177] F. Gaede and J. Engels, *Marlin et al - A Software Framework for ILC detector R&D*, EUDET-Report-2007-11 (2007), available on <http://www.eudet.org/e26/e27/e584/eudet-report-2007-11.pdf>.
- [178] V. Blobel and C. Kleinwort, *A New Method for the High-Precision Alignment of Track Detectors*, DESY 02-077, also arXiv:hep-ex/0208021 (2001);
V. Blobel, *Millepede II - Linear Least Squares Fits with a Large Number of Parameters* (2007), available on <http://www.desy.de/~blobel/Mptwo.pdf>
- [179] E. Belau et al., *Charge collection in silicon strip detectors*, Nucl. Inst. Meth. **214**, 253 (1983);
R. Turchetta, *Spacial resolution of silicon microstrip detectors*, Nucl. Inst. Meth. **A 355**, 44 (1993);
C. Colledani et al., *A submicron precision silicon telescope for beam test purposes*, Nucl. Inst. Meth. **A 372**, 379 (1996).
- [180] T. Behnke et al., *Test Beams at DESY*, EUDET-Memo-2007-11 (2007), available on <http://www.eudet.org/e26/e28/e182/e283/eudet-memo-2007-11.pdf>;
A. Cagil, *Characterisation of the Test Beam Lines T21 and T24 at DESY II*, EUDET-Memo-2007-50, available on <http://www.eudet.org/e26/e28/e182/e580/eudet-memo-2007-50.pdf>.
- [181] A. Bulgheroni, *First Test Beam Results from the EUDET Pixel Telescope*, IEEE Nuclear Science Symposium Conference Record, 26 October 2007 - 3 November 2007, Honolulu, USA, 1878 (2008), also EUDET-Report-2007-006.
- [182] V. Blobel and E. Lohrmann, *Statistische und numerische Methoden der Datenanalyse*, Teubner, Stuttgart (1998).
- [183] I.-M. Gregor, Private communication (2008).
- [184] J.J. Velthuis et al., *DEPFET, a monolithic active pixel sensor for the ILC*, Nucl. Inst. Meth. **A 579**, 685 (2007).

- [185] A.F. Żarnecki and P. Niezurawski, *EUDET Telescope Geometry and Resolution Studies*, arXiv:physics/07030581 (2007), also EUDET-Report-2007-01.

Acknowledgements

The results presented in this thesis could never have been achieved without the combined efforts of the members of the ZEUS collaboration and of the EUDET JRA1 group. I would like to express my special gratitude to:

- Achim Geiser for his excellent support during all stages of this thesis. I enjoyed our many discussions about heavy flavour production and physics in general a lot;
- Robert Klanner for very valuable comments on the thesis;
- Olaf Behnke for many interesting discussions on the lifetime analysis;
- Vladyslav Libov for providing the second analysis for the $F_2^{b\bar{b}}$ measurement and for generating many missing Monte Carlo samples;
- Mykhailo Lisovyi for preparing the second analysis for the D^+ and Λ_c^+ measurement;
- the members and coordinators of the ZEUS heavy flavour working group for many helpful comments and discussions;
- Ingrid Gregor for her guidance during the technical part of this thesis and for proof-reading parts of the text;
- Antonio Bulgheroni for his help understanding the EU Telescope software;
- Daniel Haas and Emlyn Corrin for our good collaboration during the EUDET test beam campaign in 2008.